UNIVERSIDAD DE CANTABRIA

E.T.S. DE INGENIEROS DE CAMINOS, CANALES Y PUERTOS

Departamento de Ciencias y Técnicas del Agua y del Medio Ambiente

TESIS DOCTORAL

Modelado experimental y numérico de la interacción del oleaje con ecosistemas naturales para la protección costera

---

Experimental and numerical modelling of flow interaction with natural ecosystems for coastal protection

---

Presentada por: **MARIA EMILIA MAZA FERNANDEZ**

Dirigida por: **ÍÑIGO J. LOSADA RODRÍGUEZ**
JAVIER LÓPEZ LARA

Santander, Enero 2015

A mis padres, hermanos y sobrinos

Agradecimientos

Antes de mostrar el trabajo realizado en la presente tesis me gustaría agradecer a cuantos han hecho posible este estudio, compartiendo con ellos el crédito del mismo. Muchos son los que han colaborado en el desarrollo de la tesis ya sea complementado el esfuerzo de la autora con el suyo propio o simplemente facilitándole la vida. Todos ellos merecen un agradecimiento expreso y por supuesto el consiguiente reconocimiento. Pido disculpas de antemano, a quienes por despiste no haga mención en lo que sigue. A ellos les ruego acepten estas palabras como reconocimiento de su ayuda.

En primer lugar me gustaría agradecer a mi director de tesis Dr. Iñigo J. Losada por las oportunidades que me ha brindado. Porque me dio la oportunidad de comenzar mi carrera investigadora dentro del Instituto de Hidráulica Ambiental, IH Cantabria, y porque desde ese momento siempre me ha ayudado a seguir formándome como investigadora. Gracias por los consejos y correcciones llenos de experiencia y saber hacer.

Quiero agradecerle a mi codirector de tesis Dr. Javier L. Lara su constante apoyo y todas las horas y horas de dedicación. Gracias por tus múltiples correcciones porque sin ellas este documento no sería tan completo. Gracias por cuestionar mis hipótesis, por plantearme nuevas cuestiones, por la orientación para afrontar los problemas y por los consejos que han hecho posible este trabajo y que me han formado como investigadora.

Quiero agradecerle a toda la gente del IH su cariño, su apoyo y los buenos momentos compartidos. A Raúl Medina por gestionar la gran familia del IH Cantabria de la que me han permitido formar parte. Al grupo de eco-hidráulica sin los cuales los ensayos realizados en el Cantabria Coastal and Ocean Basin no habrían sido posibles. Especialmente a Bárbara Ondiviela y a Nerea Gordejuela, por su gran implicación en el trabajo, por la cantidad de horas y horas invertidas en conseguir las plantas sin las cuales los ensayos no se habrían podido realizar, por la búsqueda de soluciones cada vez que había un problema y por todo lo que me enseñaron. I am also especially grateful to Tjeerd J. Bouma and Juliane Trinogga for their help in these experiments. A todo el personal del laboratorio por la ayuda en la realización de los diferentes ensayos llevados a cabo en la tesis. A mis compañeros del grupo de Hidrodinámica e Infraestructuras Costeras, especialmente a Pablo Higuera y Manuel del Jesus, que me han ayudado en tantas ocasiones en el desarrollo de esta tesis y con los que tantas risas y momentos he compartido. A la gente de administración e informática por hacernos la vida más fácil. A todos aquellos que me han ayudado cuando lo he necesitado. Y no menos importante, a todos aquellos que día tras día me han regalado una sonrisa, una conversación o unas palabras de apoyo.

Quiero agradecer también al Ministerio de Educación, Cultura y Deporte por el Programa de Formación de Profesorado Universitario (FPU) que me ha proporcionado la financiación necesaria para llevar a cabo mi formación doctoral. En este apartado también quiero agradecer al IH Cantabria por la financiación extra aportada al desarrollo de mi tesis, sin la cual el presente estudio no podría haber sido tan completo.

Esta tesis está dedicada, como no podía ser de otra manera, a mi familia. Es sólo un pequeño reconocimiento a todo el amor, el apoyo y la dedicación que siempre me han brindado. Quiero agradecer a mis padres, Adolfo y Emilia, su plena dedicación a formarme como persona, su apoyo incondicional, todas las oportunidades que me han dado a lo largo de mi vida, su paciencia y el inmenso amor que siempre me han transmitido. Porque sin ellos no sería la persona que soy hoy, gracias. A mis hermanos, Adolfo, Mariola y Osmar y a los que considero como tales, Yolanda, Javi y Ana, por sus constantes palabras de ánimo, por ayudarme siempre que lo he necesitado, por quererme con locura y siempre desear lo mejor para mí y por sus sabios consejos. A mis cuatro tesoros, Marcos, María, Andrea y Claudia, por darme siempre un cariño desmesurado, por su maravillosa inocencia, curiosidad e ilusión contagiosa y porque con ellos todo es alegría. Gracias a todos porque me siento tremendamente afortunada por tener esta familia que supone siempre mi punto de apoyo y de referencia para seguir avanzando.

CONTENTS

NOTATION

A_C: field area

A_E: envelope square area

A_0: base field area

A_w: vegetation element wet area

a: width of the vegetation element perpendicular to the flow direction

C: damping coefficient

C_D: drag coefficient

C_{kp}: empirical constant

C_M: inertia coefficient

C_m: added mass coefficient

C_α: factor specified by the user to calculate $\bar{u}_{c,i}$

$C_{\varepsilon p}$: empirical constant

C_μ: empirical constant

c_g: group velocity

dA: differential area along the vegetation element

E: young's modulus

E_S: spectral wave energy

$\bar{F}_{D,i}$: drag force

Notation

$\overline{F_{I,\,i}}$: inertia force

F_{max}: maximum force exerted over the vegetation element

f_p: peak frequency

g: gravity acceleration

H: wave height

H_i: incident wave height

H_0: wave height at the beginning of the vegetation field

H_{rms}: root mean square wave height

H_s: significant wave height

h: water depth

h_r: relative water depth

I: inertia moment of the cross section of the plant

KC: Keulegan Carpenter number

kh: relative wave number

$khSR$: depth wave number

kL_eSR: field wave number

k: turbulent production

LAI: leaf area index

L_e: equivalent field length

$m0$: spectrum zero moment

N: number of plants per unit area

N_c: total number of cylinders

Notation

n: field porosity

n_0: base field porosity

$\bar{p}$: mean pressure

p^*: pseudo-dynamic pressure

Re: Reynolds number

Re_S^{Le}: field Reynolds number

$\bar{S}_{ij}$: mean strain-rate tensor

S_d: energy dissipation due to vegetation

SR: submergence ratio

s_0: vegetation elements spacing

T: wave period

T_p: peak wave period

t: time

$\bar{u}_i$: mean flow velocity

u'_i: turbulent flow velocity

$\overline{(u'_\iota u'_J)}$: Reynolds stresses

$\bar{u}_{c,i}$: artificial compression term

$\bar{u}_{rel,i}$: relative velocity defined as the difference between the plant and flow velocities

V_c: characteristic velocity

V_p: plant volume per unit area

x_i: spatial coordinate

α: single phase function

α_0: empirical parameter

α_1: empirical parameter

β: damping coefficient

β': damping coefficient for random waves

δ_{ij}: Kronecker delta function

ε: turbulent dissipation

η: free surface elevation

θ: wave angle

μ: dynamic viscosity

μ_{eff}: efficient dynamic viscosity

μ_t: eddy viscosity

ν: kinematic viscosity

ν_t: turbulent kinematic viscosity

ξ_i: plant displacement

ρ: flow density

ρ_p: vegetation density

$\bar{\sigma}_{ij}$: mean flow deformation rate

σ_k: closure coefficient

$\bar{\tau}_{ij}$: mean viscous tensor

ϕ: solid volume fraction

LIST OF FIGURES

LIST OF TABLES

*"**N**ecesito del mar porque me enseña:*
no sé si aprendo música o conciencia:
no sé si es ola sola o ser profundo
o sólo ronca voz o deslumbrante
suposición de peces y navíos.
El hecho es que hasta cuando estoy dormido
de algún modo magnético circulo
en la universidad del oleaje."

Pablo Neruda

0

RESUMEN EN ESPAÑOL

0.1 Introducción y motivación

Las zonas costeras de todo el mundo están cambiando muy rápidamente. Su tasa de cambio está aumentado debido al desarrollo costero y al cambio climático que, de forma combinada, conducen a un incremento espectacular del riesgo de daños catastróficos en los sistemas naturales y socioeconómicos ubicados en la costa. Las inundaciones, la erosión y los eventos meteorológicos extremos afectan a millones de personas así como a infraestructuras críticas, la industria, el turismo y el comercio con consecuencias económicas y ambientales importantes. El último informe del IPCC, AR5 (Wong et al., 2014), pone de manifiesto que las proyecciones climáticas y el incremento de la exposición y vulnerabilidad en zonas costeras indican un incremento del riesgo. Éste, que es debido tanto a los eventos meteorológicos extremos como al cambio climático, será una realidad a no ser que se potencie la introducción de nuevas medidas de gestión del riesgo o de adaptación en las estrategias de la gestión de la costa. Por ejemplo, Hallegatte et al. (2013) establece que el aumento del nivel del mar y de la subsidencia pueden conducir a que las consecuencias económicas de la inundación en ciudades costeras puedan incrementarse globalmente hasta en un billón de euros/año a no ser que se introduzcan medidas específicas de adaptación. En la actualidad se están destinando miles de millones de

euros en el todo el mundo a la reducción del riesgo en la costa y a la adaptación al cambio climático. La mayor parte de estos fondos se han destinado tradicionalmente a soluciones ingenieriles conocidas como "infraestructura gris". Sin embargo, tras los huracanes Katrina (2005) o Sandy (2012), o a partir del tsunami de Indonesia (2004), los gestores de la costa han comenzado a preguntarse sobre la viabilidad y eficiencia económica de soluciones alternativas basadas en opciones más naturales o híbridas que disminuyan la degradación de ésta.

La inversión en soluciones basadas en los servicios que nos proveen los ecosistemas costeros, ya sea a través de mejoras en su conservación o restauración, es una opción efectiva económicamente para aumentar la resiliencia frente a eventos extremos y el cambio climático. Los arrecifes (de coral o de moluscos), los humedales caracterizados por su vegetación (manglares, zostera, etc.) o la vegetación sumergida (posidonia) o las macroalgas cumplen importantes funciones que influyen en cada una de las componentes de la ecuación del riesgo. Estos ecosistemas regulan la peligrosidad controlando el oleaje o la marea meteorológica y retienen el sedimento, reduciendo, entre otros, la exposición de la población. Además, reducen la vulnerabilidad a través de la provisión de servicios adicionales. Los ecosistemas vegetales costeros tienen la ventaja de cumplir una triple función: contribuir a la reducción de riesgos frente a eventos extremos, favorecer la adaptación al cambio climático, y por último mitigar sus efectos, éste último gracias a su capacidad de capturar CO_2 (Duarte et al. 2013). En las últimas décadas se ha demostrado la importancia de los ecosistemas costeros en la adaptación y mitigación de los efectos del cambio climático (Borsje et al., 2011; Duarte et al., 2013). Por este motivo, se han buscado opciones basadas en soluciones naturales para la protección de la costa como las presentadas en las costas de los Países Bajos (http://www.ecoshape.nl/en_GB/delfland-sand-engine.html) o los presentados en el proyecto Global Restoration Network de la Society for Ecological Restoration International (http://www.globalrestorationnetwork.org/ecosystems/coastal/estuaries-marshes-mangroves/case-studies/) basados en todo tipo de vegetación costera. Sin embargo, los ecosistemas costeros aún no se han considerado de manera firme en el portfolio de adaptación al cambio climático y protección costera y se sigue optando mayoritariamente por medidas artificiales de protección. Esto se debe fundamentalmente a la complejidad del problema y a la falta de medidas cuantitativas.

La interacción del flujo con ecosistemas naturales es un problema que abarca diferentes escalas temporales y espaciales. La problemática parte desde la pequeña escala, en la que el flujo interacciona con las plantas individuales dando lugar a procesos como la deformación y movimiento de las plantas, la separación del flujo o la formación de turbulencia. Estos proceso a pequeña escala determinarán otros a mayor escala como la disipación de energía producida por el campo o los procesos de transporte de sedimento a su alrededor. Por lo tanto, un buen conocimiento de los procesos de pequeña escala puede dar lugar a la obtención de parámetros

y formulaciones que nos permitan cuantificar la protección costera proporcionada por la vegetación. Sin embargo, estos procesos son muy complejos y además se pueden dar en un gran número de especies de vegetación que pueden estar afectadas por un amplio abanico de condiciones de flujo.

La vegetación costera se desarrolla en un amplio rango de profundidades. Encontramos desde vegetación sumergida, como las fanerógamas marinas, hasta especies que viven en el intermareal, como la vegetación de marisma en zonas templadas y los bosques de manglares en zonas tropicales. Además, las propiedades biomecánicas asociadas a las distintas especies pueden ser muy diferentes, así como su geometría. Existen especies muy flexibles que presentan una sección casi contante a lo largo de toda su longitud y especies que son rígidas y están formadas por estructuras complejas formadas por raíces, troncos y ramas. Pero no solo estos parámetros influyen en la disipación de energía que pueden proporcionar los distintos ecosistemas. También las propiedades de todo el campo como la densidad de pies por metro cuadrado o la distribución espacial de los mismos condiciona en gran medida la atenuación inducida. Por lo tanto, existe una amplia variedad de campos de vegetación dependientes de muchas variables lo que conduce a que su caracterización no sea fácil de realizar.

Dada la complejidad de las plantas y la aleatoriedad en la forma de los campos de vegetación, muchos estudios han recurrido al uso de réplicas (Augustin et al., 2009; Anderson y Smith, 2014) realizadas de acuerdo a parámetros como el número de Cauchy (Ghisalberti y Nepf, 2002). Sin embargo, estos materiales muchas veces no pueden replicar el comportamiento mecánico de las plantas adecuadamente y la geometría de las mismas es a menudo simplificada. En cuanto a la reproducción de la distribución espacial de las plantas, ésta se hace normalmente de manera uniforme y continua (Stratigaki et al. 2011; Huang et al., 2011). Todo este conjunto de simplificaciones se adoptan debido a la falta de medidas de las propiedades de las plantas (flexibilidad, flotabilidad, distribución espacial) o de la geometría de las mismas, como en el caso de los manglares que presentan geometrías complejas. Además, la selección del material para crear las plantas no es sencilla y muchas veces limitante. Por todo esto, una opción muy interesante para estudiar la atenuación producida por la vegetación es el uso de plantas reales (Bouma et al., 2005; Fonseca et al., 2006). Sin embargo, son pocos los estudios (Bouma et al., 2010) que se han realizado con vegetación real debido a las dificultades asociadas a la obtención de las plantas y los consiguientes costes. Además, trabajar con organismos vivos siempre conlleva mayores dificultades como adoptar las medidas necesarias para que no se vean alteradas sus características en el transcurso del estudio. Por lo tanto, es necesaria una mejor caracterización y parametrización de las plantas y de su distribución espacial ya que ello servirá de base para el desarrollo de modelos que permitan estudiar y cuantificar la capacidad de atenuación de energía de las mismas.

Otro aspecto determinante en la protección costera proporcionada por la vegetación es la hidrodinámica involucrada en el problema. Dado que los ecosistemas costeros de desarrollan en áreas afectadas por diferentes dinámicas, la definición de las mismas no es sencilla. Podemos encontrar ecosistemas afectados por condiciones de oleaje con alturas de ola y periodos muy diferentes que se ven transformados no linealmente en su aproximación a la costa por procesos como la rotura del oleaje. La vegetación costera también puede verse afectada por eventos extremos que pueden llevar a la rotura o arranque de las plantas. Además, no sólo encontramos oleaje en las zonas costeras sino que las corrientes pueden tener un papel muy relevante, especialmente en zonas intermareales. La reproducción de todas estas dinámicas y su interacción con la vegetación es un problema muy complejo y altamente no lineal.

Muchos autores han realizado estudios considerando flujo unidireccional (Arbele and Järvelä, 2013; Bouma et al., 2013). Otros se han centrado en el estudio del flujo oscilatorio (Bouma et al., 2010; Yoon et al., 2011) y la influencia que tienen en la atenuación los parámetros del oleaje (Manca et al. 2012; Anderson y Smith, 2014). Sin embargo, no se ha alcanzado un acuerdo en la influencia que dichos parámetros tienen en la atenuación registrada. Además, se han realizado muy pocos estudios que consideren oleaje y corriente de forma simultánea (Paul et al., 2012; Hu et al., 2014). Por lo tanto, se pone de manifiesto la necesidad de realizar nuevos estudios en los que se observe, cuantifique y caracterice la interacción de las diferentes condiciones de flujo con la vegetación. De esta forma se podrá analizar la influencia de los diferentes parámetros en la atenuación obtenida.

Esta tesis busca mejorar nuestro conocimiento de la interacción del flujo con la vegetación para poder cuantificar y caracterizar la protección costera proporcionada por este tipo de ecosistemas. El estudio pretende contribuir a resolver parte de esta compleja problemática, para ayudar a los gestores costeros en la integración de soluciones naturales, como parte de las estrategias de protección. Para hacer esto, se proporcionarán nuevos parámetros, formulaciones y modelos que caractericen la interacción flujo-vegetación y que ayuden a cuantificar la protección costera bajo diferentes condiciones de vegetación y flujo.

0.2 Objetivos y metodología

0.2.1 Objetivos y metas

El objetivo principal de esta tesis es avanzar en el análisis de la protección costera proporcionada por la vegetación a partir del análisis, caracterización y cuantificación de la capacidad que tienen estos ecosistemas en atenuar la energía de las dinámicas costeras. El primer capítulo ha puesto

de manifiesto algunos de los aspectos que están aún por estudiar o aún no han sido estudiados suficientemente como la representación de las propiedades de las plantas y del campo de vegetación; el análisis de la influencia de los parámetros del oleaje; el estudio de condiciones combinadas de oleaje y corriente; o el efecto de eventos extremos sobre la vegetación. Para poder cubrir estos aspectos, se definen un conjunto de objetivos que se detallan a continuación.

Objetivo 1 – Análisis de la influencia de la flexibilidad de la vegetación en la atenuación del oleaje. Es muy importante una correcta definición de las propiedades de la vegetación si queremos estudiar su capacidad de atenuación. La mayoría de la vegetación presente en zonas costeras es flexible y su flexibilidad determinará su capacidad de disipación. Por ello, es necesario profundizar en la influencia de este parámetro en la interacción flujo - vegetación y, por lo tanto, en la protección costera.

Objetivo 2 – Cuantificación de la protección costera proporcionada por vegetación real de marisma. Una gran cantidad de zonas intermareales están ocupadas por vegetación de marisma. Estos ecosistemas reducen los riesgos de erosión e inundación de estas áreas. Sin embargo, en la mayoría de los estudios realizados para cuantificar su protección se han utilizado réplicas. Además, sólo unos pocos han considerado la acción del oleaje y la corriente de forma simultánea. Por lo tanto, existe una clara necesidad de determinar el efecto de olas y corrientes sobre vegetación real bajo condiciones controladas.

Objetivo 3 – Modelo semi-empírico de la disipación de energía producida por la vegetación bajo condiciones combinadas de oleaje y corriente. Debido a los pocos estudios realizados considerando oleaje y corriente simultáneamente, la atenuación producida por la vegetación bajo estas condiciones no está bien definida y no existen modelos analíticos que permitan cuantificarla de una manera rápida. Aunque se pueden encontrar formulaciones para condiciones de oleaje, es necesario profundizar en el desarrollo de una nueva formulación para casos en los que tenemos oleaje y corrientes.

Objetivo 4 – Modelo numérico para vegetación rígida emergida. Se han realizado muchos estudios para estudiar el efecto de la vegetación sobre el flujo pero muy pocos para analizar el efecto del flujo sobre los elementos del campo de vegetación, ya que para ello, se precisa de un modelo de alta resolución que no esté basado en parametrizaciones. Este problema es especialmente importante en la interacción de tsunamis con bosques de manglares. Para poder estudiarlo es necesario un modelo que permita resolver el flujo entre los diferentes elementos y las fuerzas ejercidas por el flujo sobre los mismos, como primer elemento para establecer estrategias de regeneración de áreas costeras mediante el uso de estructuras naturales.

Objetivo 5 – Análisis de las características del campo de vegetación en la protección proporcionada por este. No sólo las características de las plantas son importantes en la protección costera sino que las características del campo también influyen, en gran medida, en la disipación de energía. Aunque la vegetación no crece de manera uniforme y continua en la naturaleza la mayoría de los estudios realizados consideran campos homogéneos. Por lo tanto, es importante estudiar campos no uniformes y cómo la disipación, los patrones de flujo y las fuerzas sufridas por la vegetación se ven afectadas por estas heterogeneidades.

0.2.2 Metodología

A continuación, se presentan los diferentes pasos y métodos seguidos para la consecución de los objetivos citados en el apartado anterior. Para conseguir cada uno de los objetivos se utilizan diferentes aproximaciones y desarrollos dependiendo de la escala del problema y su complejidad. Por lo tanto, se consideran aproximaciones experimentales, analíticas y numéricas. Por todo esto la metodología se presenta dividida por objetivos.

Objetivo 1 – Análisis de la influencia de la flexibilidad de la vegetación en la atenuación del oleaje. Para estudiar la influencia de la flexibilidad de la vegetación en su capacidad de atenuación, es necesario caracterizar la interacción entre el flujo y las plantas. En esta tesis este problema se aborda numéricamente mediante el desarrollo de un modelo que resuelva el movimiento acoplado entre el flujo y las plantas. Dicho modelo se obtiene siguiendo dos pasos. En primer lugar, un algoritmo que represente de forma adecuada el flujo es necesario. Para el presente trabajo, se ha seleccionado el modelo IH-2VOF como código base en el que se implementará el modelo de vegetación. Esta selección se realiza debido a que el modelo permite resolver las componentes verticales de flujo y contiene implementado un modelo de turbulencia.

En segundo lugar, se desarrolla un modelo mecánico de movimiento de la planta que considera el movimiento acoplado producido entre el flujo y la vegetación. Dicho modelo se formula en función de las características del flujo y de la planta. El movimiento de la planta se representa basándose en la ecuación de Morison y en la ecuación de movimiento oscilatorio amortiguado (Ikeda et al., 2001; Mendez et al., 1999). Esta ecuación de movimiento permite obtener el desplazamiento de la planta y, por tanto, su velocidad de movimiento que será utilizada para obtener la velocidad relativa producida respecto del flujo. Esta velocidad relativa es la utilizada para obtener la fuerza de arrastre corregida que se introduce en la ecuación de momento del modelo IH-2VOF para considerar la pérdida de energía producida por la vegetación. Además, se considera la producción y disipación de turbulencia producida por la vegetación. Por ello, se

introducen dos términos adicionales en el modelo k-ε ya implementado en el IH-2VOF, uno en la ecuación de producción turbulenta y otro en la ecuación de disipación.

Objetivo 2 – Cuantificación de la protección costera proporcionada por vegetación real de marisma. Para conseguir este objetivo se plantea una aproximación experimental debido a la falta de trabajos realizados con vegetación real y bajo condiciones de flujo de oleaje y corriente y a la dificultad de representar con métodos numéricos y analíticos la vegetación real. Por lo tanto, se plantea un estudio experimental en el que: 1) se trabaje a gran escala; 2) se utilicen diferentes plantas reales; 3) se generen de forma controlada condiciones de oleaje y corriente.

Para la realización de los ensayos se selecciona el Cantabria Coastal and Ocean Basin (CCOB) ya que esta instalación permite estudiar la interacción tridimensional de oleaje y corrientes con la vegetación. Se consideran dos especies de vegetación de marisma con diferentes propiedades biomecánicas, biomasa y densidad con el fin de estudiar cuál es la influencia de los diferentes parámetros en la atenuación de energía producida. Para la realización de los ensayos se deben cubrir diferentes pasos, desde el cultivo o recolección de las plantas hasta la selección de las condiciones hidrodinámicas a simular. Todo ese proceso lleva al desarrollo de una metodología y a un conjunto de recomendaciones obtenidas a partir de la propia experiencia. Además, el análisis de los datos de laboratorio permitirá estudiar la compleja interacción entre oleaje, corriente y vegetación así como evaluar la influencia que, tanto las características del flujo como de la vegetación, tienen en la atenuación obtenida.

Objetivo 3 – Modelo semi-empírico de la disipación de energía producida por la vegetación bajo condiciones combinadas de oleaje y corriente. La cuantificación de la disipación de energía proporcionada por la vegetación bajo condiciones de oleaje y corriente es una tarea difícil ya que la interacción olas-corriente-vegetación es un proceso complejo y altamente no lineal. Por lo tanto, como primera aproximación se considera el desarrollo de un modelo analítico que proporcione una nueva formulación para la atenuación de energía producida bajo estas condiciones. Para la obtención de la nueva formulación se toma como base las aproximaciones basadas en la conservación de la energía presentadas por autores como Dalrymple et al. (1984) o Méndez y Losada (2004).

Objetivo 4 – Modelo numérico para vegetación rígida emergida. El estudio de la interacción del flujo con elementos rígidos y las fuerzas ejercidas sobre los mismos es un problema complejo que exige la utilización de un modelo avanzado y una alta resolución espacial para definir los elementos que forman la vegetación que no es posible realizar en el laboratorio. Por lo tanto, el problema se aborda numéricamente utilizando un modelo tridimensional basado en las ecuaciones de Navier-Stokes. El modelo seleccionado es el IHFOAM ya que permite simular la componente vertical del flujo y el flujo desarrollado entre los diferentes elementos rígidos

considerando los consiguientes efectos turbulentos. El modelo IHFOAM se desarrolló en IH Cantabria y permite simular todo tipo de oleajes así como medios porosos. Además el modelo incorpora un conjunto de algoritmos que permite generar y absorber el oleaje evitando zonas de disipación y, por lo tanto, disminuyendo el coste computacional.

Siguiendo las simplificaciones adoptadas por muchos autores, la vegetación se representa a partir de cilindros. El campo de cilindros se resuelve considerando dos aproximaciones. En primer lugar, se realiza una simulación directa de los diferentes elementos utilizando un modelo de turbulencia $\kappa - \omega$ SST. La segunda aproximación se basa en un enfoque macroscópico y el flujo en el campo de vegetación se resuelve como la combinación de la introducción de una fuerza de arrastre en la ecuación de momento y un modelo de turbulencia $\kappa - \varepsilon$ modificado.

Objetivo 5 – Análisis de las características del campo de vegetación en la protección proporcionada por este. El estudio de la influencia de los parámetros del campo de vegetación en la disipación de energía se hace considerando dos aproximaciones. En primer lugar, el modelo desarrollado para la consecución del Objetivo 4 se utiliza para estudiar distintas distribuciones espaciales dentro de un mismo campo de vegetación. Tomando como base unas distribuciones de cilindros uniformes se construyen unas distribuciones aleatorias con la misma densidad de cilindros y distribuyéndolos cumpliendo un espacio mínimo entre ellos. Posteriormente, ambas distribuciones se simulan bajo las mismas condiciones de flujo. Esto permite estudiar la influencia de la distribución de los elementos que representan el campo de vegetación en la disipación de energía proporcionada por los mismos y en las fuerzas que experimentan.

En segundo lugar, se estudia la influencia de las características del campo a mayor escala. En este caso, se opta por una aproximación experimental para estudiar cómo se modifica la disipación de energía cuando el campo no es continuo y uniforme. Para ello, se consideran varias configuraciones de campo y se toman medidas de superficie libre y velocidad. Posteriormente, los ensayos se reproducen numéricamente utilizando el modelo desarrollado en el Objetivo 4 con el fin de analizar variables que no han sido medidas en los ensayos físicos.

0.2.3 Estructura del documento

En los siguientes capítulos del presente documento se abordarán los objetivos expuestos en la sección anterior. Por lo tanto, el presente documento ha sido organizado en función de los objetivos arriba expuestos como se detalla a continuación.

En el capítulo 3 se ha desarrollado el trabajo necesario para completar el Objetivo 1. Este capítulo presenta un modelo bidimensional para la interacción del flujo con vegetación flexible

sumergida basado en las ecuaciones de Navier Stokes y considerando el movimiento acoplado entre flujo y vegetación.

Los capítulos 4 y 5 exponen el trabajo realizado para completar el Objetivo 2. El capítulo 4 presenta un conjunto de directrices a tener en cuenta a la hora de hacer ensayos a gran escala con vegetación real. En ese capítulo, se describen los ensayos y se detallan un conjunto de pasos que deben ser considerados cuando se realizan este tipo de ensayos. Finalmente, se recogen un conjunto de recomendaciones basadas en la propia experiencia. En el capítulo 5 se describe el análisis de los datos de laboratorio. Se analiza la influencia de los parámetros del oleaje, el calado, la interacción ola-corriente, la densidad de la vegetación, la biomasa y la rigidez de la vegetación en la disipación de energía obtenida.

El capítulo 6 se desarrolla íntegramente para cubrir el Objetivo 3. El capítulo 6 presenta el nuevo modelo analítico de disipación para condiciones de oleaje y corriente para oleaje regular e irregular. Asimismo se obtienen unas nuevas formulaciones del coeficiente de arrastre en función de un nuevo número de Reynolds que considera el comportamiento de la vegetación bajo la acción el flujo.

En el capítulo 7 se completa el Objetivo 4. Este capítulo presenta dos aproximaciones tridimensionales para resolver la interacción del flujo con elementos rígidos basados en las ecuaciones de Navier-Stokes. Asimismo, se presentan las ventajas e inconvenientes de ambas aproximaciones.

Por último, el Objetivo 5 se aborda en los capítulos 7 y 8. En el capítulo 7 se presenta un apartado en el que se estudia la influencia de la distribución de los elementos que representan la vegetación estudiando configuraciones uniformes y aleatorias y comparándolas entre sí. El capítulo 8 describe los ensayos realizados para estudiar diferentes configuraciones de parches de vegetación y su influencia en la disipación de energía. Además, el capítulo 8 muestra un conjunto de simulaciones numéricas de estos ensayos realizadas para analizar fuerzas en los cilindros.

Finalmente, el capítulo 9 presenta un conjunto de conclusiones generales y las futuras líneas de trabajo.

Los diferentes capítulos comienzan con una descripción del estado del arte del tema que se trata en cada uno de ellos. Posteriormente, se presenta el trabajo realizado para la consecución de los diferentes objetivos marcados en esta tesis. Por lo tanto, cada uno de los capítulos es autocontenido.

0.3 Modelo bidimensional de vegetación sumergida bajo la acción de flujo oscilatorio

En el capítulo 3 se presenta el modelo bidimensional para oleaje y vegetación sumergida que acopla el movimiento del fluido con la deformación sufrida por la planta. Se introduce el efecto de la vegetación en el modelo IH-2VOF, de tal manera que en la zona fuera del campo de vegetación se resuelven las ecuaciones RANS (Reynolds Averaged Navier-Stokes equations), mientras que en la zona ocupada por la vegetación se introduce una fricción adicional en la ecuación de momento que induce pérdida de momento. Esta fricción se representa a través de la fuerza de arrastre:

$$\bar{F}_{D,i} = \frac{1}{2} C_D a N \bar{u}_{rel,i} \left| \bar{u}_{rel,i} \right| \tag{1}$$

donde a es la anchura de la planta perpendicular a la dirección del flujo, $C_D$es el coeficiente de arrastre, N es el número de plantas por unidad de área y $\bar{u}_{rel,i}$ la velocidad relativa, definida como la diferencia entre la velocidad del flujo y de la planta. El subíndice i representa las componentes de la velocidad y de las fuerzas. Por lo tanto, las ecuaciones RANS dentro del campo de vegetación son de la forma:

$$\frac{\partial \bar{u}_i}{\partial x_i} = 0 \tag{2}$$

$$\frac{\partial \bar{u}_i}{\partial t} + \bar{u}_j \frac{\partial \bar{u}_i}{\partial x_j} = -\frac{1}{\rho} \frac{\partial \bar{p}}{\partial x_i} + g_i + \frac{1}{\rho} \frac{\partial \bar{\tau}_{ij}}{\partial x_j} - \frac{\partial \overline{\left(u'_\iota u'_\jmath\right)}}{\partial x_j} - \bar{F}_{D,i} \tag{3}$$

donde ρ es la densidad del flujo, $\bar{u}_i$ es la velocidad media del flujo, t es el tiempo, $\bar{p}$ es la presión media, x_i es la coordenada especial, u'_i la velocidad turbulenta y $\bar{\tau}_{ij} = 2\mu\bar{\sigma}_{ij}$ el tensor viscoso, siendo μ la viscosidad molecular y $\bar{\sigma}_{ij} = \frac{1}{2}\left(\frac{\partial \bar{u}_i}{\partial x_j} + \frac{\partial \bar{u}_j}{\partial x_i}\right)$ el ratio de deformación del flujo. El término $\overline{\left(u'_\iota u'_\jmath\right)}$ representa las tensiones de Reynolds que consideran el flujo turbulento.

Para poder calcular la ecuación (1), la velocidad de la planta debe ser modelada para determinar la velocidad relativa, $\bar{u}_{rel,i}$. Para ello, se formula un modelo mecánico de movimiento basado en la ecuación de Morison y en la ecuación de movimiento oscilatorio amortiguado (Mendez et al., 1999; Ikeda et al., 2001). La ecuación que gobierna el movimiento de la planta bajo la acción del flujo es de la forma:

$$m_0 \frac{\partial^2 \xi_i}{\partial t^2} + C \frac{\partial \xi_i}{\partial t} + EI \frac{\partial^4 \xi_i}{\partial z^4} =$$

$$= \frac{1}{2}\rho C_D a\left(\bar{u}_i - \frac{\partial \xi_i}{\partial t}\right)\left|\bar{u}_i - \frac{\partial \xi_i}{\partial t}\right| + \left(\rho_p - \rho\right) g_i V_p \frac{\partial \xi_i}{\partial z} + \rho V_p \frac{\partial \bar{u}_i}{\partial t} + \rho C_m V_p \left(\frac{\partial \bar{u}_i}{\partial t} - \frac{\partial^2 \xi_i}{\partial t^2}\right) \quad (4)$$

donde $m_0 = \left(\rho_p - \rho C_m\right) V_p$, ρ_p es la densidad de la vegetación, C_m es el coeficiente de masa añadida, V_p es el volumen de la planta por unidad de área, ξ_i es el desplazamiento de la planta, C es el coeficiente de amortiguamiento, E es el módulo de Young e I es el momento de inercia de la sección transversal de la planta. El primer y segundo término a la izquierda de la ecuación se corresponden con las fuerzas de inercia y amortiguamiento y los dos últimos con la fuerza restauradora. Los términos de la derecha se corresponden con la fuerza de arrastre, gravitacional, Froude-Krylov y la de masa hidrodinámica, respectivamente. La ecuación (4) es un modelo simplificado que considera deformación lineal para el cálculo del movimiento oscilatorio mediante una integración vertical a lo largo de la planta como propone Dupont et al. (2011). Esta hipótesis permite obtener la deformación de la planta a lo largo de su longitud en función del ángulo de deformación de su extremo. Mientras la deformación de la planta no sea muy grande esta aproximación proporciona buenos resultados y el coste computacional para resolver el movimiento de la planta es muy bajo. Sin embargo, para casos con vegetación muy flexible esta aproximación permitiría obtener el desplazamiento del extremo pero no la deformación de la planta a lo largo de su longitud. Cuando se desea calcular dicha deformación se debe considerar un modelo de grandes deformaciones (Maza, 2012).

Una vez el movimiento de la planta está calculado la velocidad relativa (Ecuación 1) se obtiene de la forma:

$$\bar{u}_{rel,i} = \bar{u}_i - \frac{\partial \xi_i}{\partial t} \quad (5)$$

La diferencia de este modelo con el planteado por Méndez et al. (1999) es que éste está basado en teoría lineal de ondas sobre fondo plano mientras que el presentado aquí resuelve las ecuaciones de Navier-Stokes para profundidad variable. Además, el modelo propuesto permite resolver no sólo casos de vegetación sumergida sino también casos de vegetación emergida. El modelo presentado por Ikeda et al. (2001) resuelve las mismas ecuaciones que el presentado aquí pero de una forma diferente. Ikeda et al. (2001) resuelve la fuerza restauradora considerando un perfil de velocidades exponencial que determina los valores de desplazamiento. En el modelo presentado, la fuerza restauradora se aproxima considerando el desplazamiento del extremo de un voladizo bajo la acción de una carga uniforme utilizando las velocidades del flujo como forzamientos.

Otro aspecto que se considera en el modelo propuesto es la influencia de la vegetación en el modelo de turbulencia. Para la modelización de la turbulencia se opta por un modelo k-ε en el que k es la energía turbulenta y ε es la tasa de disipación. Se considera el efecto de la vegetación

mediante la introducción de dos términos adicionales, uno en la ecuación de producción turbulenta, k_w, y otro en la de disipación, ε_w. Estos términos consideran la contribución turbulenta de la vegetación a partir de una aproximación de flujos dispersivos función de la fuerza de arrastre basada en Hiraoka et al. (2006). Por lo tanto, las ecuaciones del modelo de turbulencia modificado k-ε son:

$$\rho\frac{\partial k}{\partial t}+\rho\bar{u}_j\frac{\partial k}{\partial x_j}=\frac{\partial}{\partial x_j}\left[\left(\frac{\mu_t}{\sigma_k}+\mu\right)\frac{\partial k}{\partial x_j}\right]+\bar{\tau}_{ij}\frac{\partial \bar{u}_i}{\partial x_j}-\rho\varepsilon+\underbrace{\rho C_{kp}C_D aN\sqrt{\bar{u}_{rel,i}\bar{u}_{rel,i}}k}_{k_w} \quad (6)$$

$$\rho\frac{\partial \varepsilon}{\partial t}+\rho\bar{u}_j\frac{\partial \varepsilon}{\partial x_j}=\frac{\partial}{\partial x_j}\left[\left(\frac{\mu_t}{\sigma_\varepsilon}+\mu\right)\frac{\partial \varepsilon}{\partial x_j}\right]+C_{\varepsilon 1}\frac{\varepsilon}{k}\bar{\tau}_{ij}\frac{\partial \bar{u}_i}{\partial x_j}-C_{\varepsilon 2}\rho\frac{\varepsilon^2}{k}+\underbrace{\rho C_{\varepsilon p}C_D aN\sqrt{\bar{u}_{rel,i}\bar{u}_{rel,i}}\varepsilon}_{\varepsilon_w} \quad (7)$$

En las ecuaciones (6) y (7) μ_t es la viscosidad turbulenta, μ la viscosidad dinámica y σ_k un coeficiente de cierre. C_{kp} y $C_{\varepsilon p}$ son constant empíricas y toman los valores propouestos por Hiraoka et al. (2006) (Tabla 0.1) . El coeficiente de arrastre, C_D, es el mismo que el que aparece en la ecuación de momento.

Adicionalmente a estas ecuaciones, hay dos relaciones que son necesarias para poder utilizar el modelo k-ε. La primera introduce la aproximación de Boussinesq que considera que las tensiones de Reynolds ($\bar{\tau}_{ij}$) son directamente proporcionales al tensor medio de deformación ($\bar{S}_{ij}$). La constante de proporcionalidad es la viscosidad turbulenta, μ_t:

$$\rho\overline{\left(u'_\iota u'_\jmath\right)}=2\mu_t\bar{S}_{ij}-\frac{2}{3}\rho k\delta_{ij} \quad (8)$$

donde el último término se introduce por razones de consistencia. La única variable que queda por definir es la viscosidad turbulenta. Con base en consideraciones dimensionales la viscosidad turbulenta se define como:

$$\mu_t=\rho C_\mu\frac{k^2}{\varepsilon} \quad (9)$$

donde C_μ es una constante empírica (Tabla 0.1).

$\boldsymbol{\kappa}$	0.4
$\boldsymbol{\sigma_k}$	1.0
$\boldsymbol{\sigma_\varepsilon}$	1.3
$\boldsymbol{C_\mu}$	0.09

$C_{\varepsilon 1}$	1.44
$C_{\varepsilon 2}$	1.92
C_{kp}	1
$C_{\varepsilon p}$	3.5
C_D	Calibration

Tabla 0.1 Valores de las constantes empíricas del modelo de turbulencia k-ε

El modelo IH-2VOF utiliza un esquema de diferencias finitas para la discretización de las ecuaciones. Para la resolución de las ecuaciones utiliza un método en dos pasos y el modelo de turbulencia se resuelve mediante un esquema de diferencias finitas explícito.

Para introducir las condiciones de oleaje en el dominio se impone un campo de velocidades y la evolución de la superficie libre en uno de los contornos del dominio. Asimismo, se aplica la absorción activa presentada por Torres-Freyermuth et al. (2009), tanto en el contorno de generación como en el final del dominio, para permitir que el oleaje salga del dominio.

El procedimiento de resolución seguido considera el acoplamiento entre el flujo y el movimiento de la planta. Las velocidades del flujo se utilizan como forzamiento para resolver el movimiento de la planta utilizando la ecuación (4) siguiendo un esquema explícito en el tiempo. Una vez está resuelto el movimiento de la planta, se aplica la ecuación (5) para obtener la velocidad relativa. Esta velocidad relativa se usa para actualizar la velocidad utilizada en el método de resolución en dos pasos en el siguiente paso de tiempo. De esta manera, las velocidades relativas obtenidas en un paso de tiempo permiten obtener el movimiento de la planta que será utilizado para calcular, a su vez, las velocidades relativas del siguiente paso de tiempo. El diagrama de flujo del esquema de resolución se muestra en la Figura 0.1.

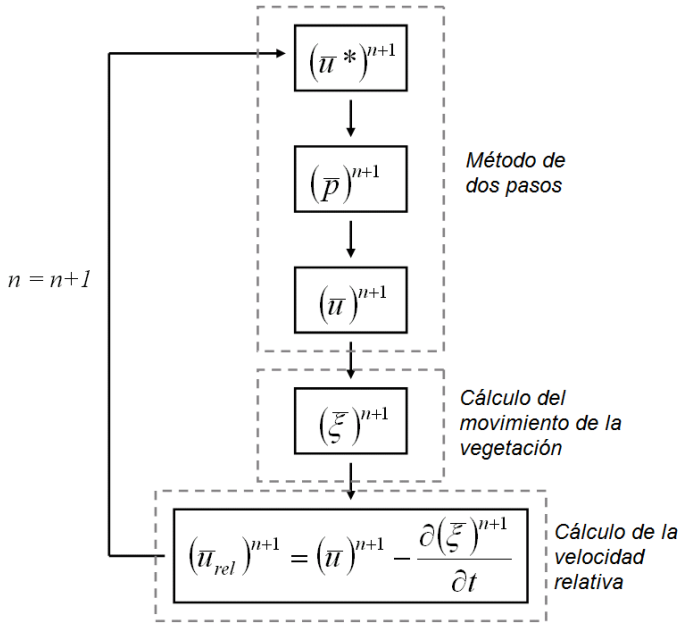

Figura 0.1 Diagrama de flujo del esquema de resolución

Una vez presentado el modelo es necesario su validación. Para ello se utilizan dos grupos de ensayos presentes en la literatura, Asano et al. (1988) y Stratigaki et al. (2011). Los ensayos presentados por Asano et al. (1988) se realizaron con réplicas de polipropileno, tomando medidas de superficie libre en cuatro puntos dentro del campo de vegetación. Se ejecutaron un total de sesenta experimentos considerando dos densidades de vegetación, dos calados, ocho frecuencias de oleaje regular y seis alturas de ola. Los ensayos presentados en Stratigaki et al. (2011) son unos ensayos a mayor escala en los que se consideran réplicas de plástico de Posidonia oceanica. En estos ensayos se tomaron medidas de superficie libre delante y a lo largo del campo de vegetación aís como medidas de velocidad, dentro y fuera del mismo. Se ejecutaron experimentos con diferentes condiciones de oleaje. Aunque no sólo se ejecutó oleaje regular, el presente estudio se centra en los 54 experimentos realizados con ese tipo de oleaje. Se ensayaron dos densidades de vegetación y cuatro calados.

La validación del modelo se realiza considerando dos aproximaciones. En la primera no se considera el movimiento de las plantas mientras que en la segunda sí se resuelve, siguiendo el esquema presentado en la Figura 0.1. En ambos casos el único parámetro de ajuste es el coeficiente de arrastre ya que el resto de variables se fijan de acuerdo con las características de la vegetación que se vaya a resolver.

La primera aproximación muestra un buen acuerdo entre los resultados de evolución de altura de ola numéricos y de laboratorio como se muestra en la Figura 0.2 para los ensayos de Asano et al. (1988) y en la Figura 0.3 para los ensayos de Stratigaki et al. (2011).

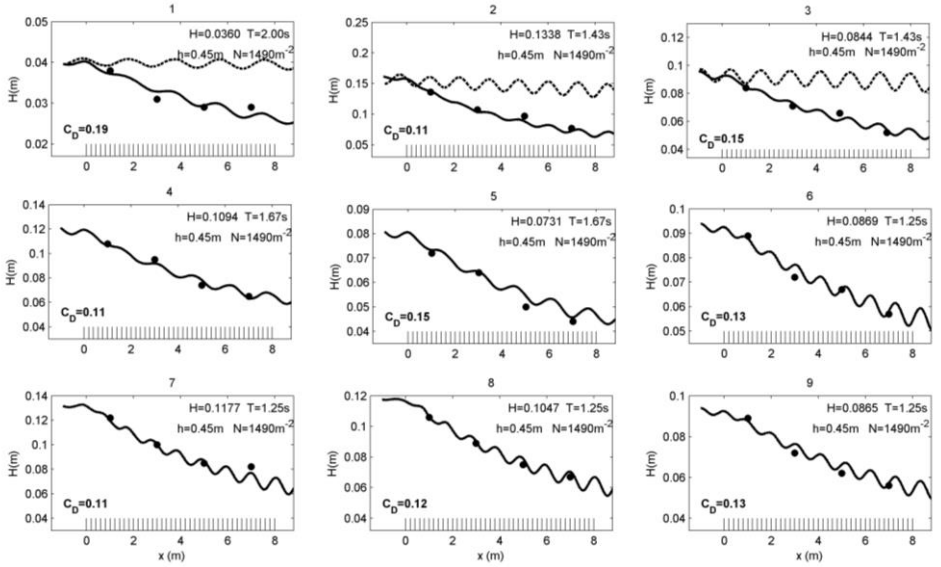

Figura 0.2 Evolución de la altura de ola (H) a lo largo del campo de vegetación. Resultados numéricos (línea continua) y medidas de laboratorio de los ensayos de Asano et al. (1988) (puntos negros). La evolución de la altura de ola sin vegetación se muestra en línea punteada en las imágenes 1-3.

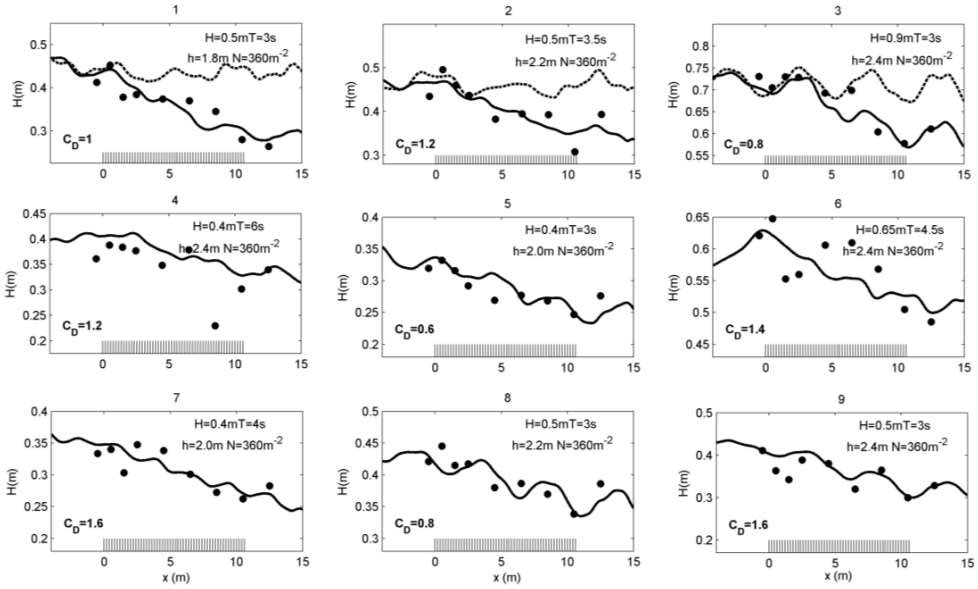

Figura 0.3 Evolución de la altura de ola (H) a lo largo del campo de vegetación. Resultados numéricos (línea continua) y medidas de laboratorio de los ensayos de Stratigaki et al. (2011) (puntos negros). La evolución de la altura de ola sin vegetación se muestra en línea punteada en las imágenes 1-3.

Asimismo, se validan las velocidades fuera y dentro del campo para los ensayos de Stratigaki et al. (2011). De nuevo se observa un buen acuerdo entre los resultados numéricos y los datos de laboratorio como se muestra en la Figura 0.4.

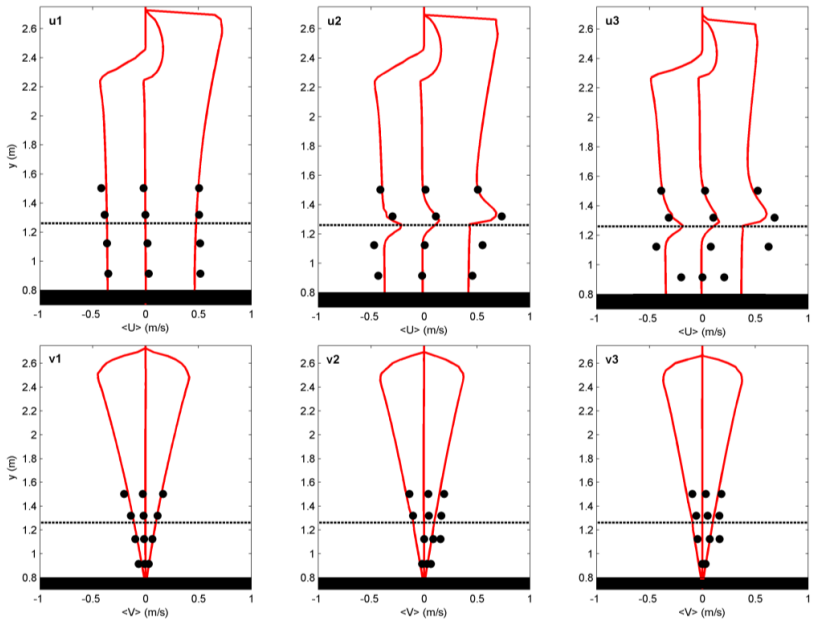

Figura 0.4 Perfiles de velocidad promediada horizontal (arriba) y vertical (abajo) mínima, media y máxima 0.7 m antes del campo de vegetación (u1 y v1), 2 m tras su comienzo (u2 y v) y 2.7 m antes de su final (u3 y v3). Resultados numéricos (líneas rojas) y medidas de laboratorio (círculos negros). La línea punteada representa el límite superior del campo. Resultados para un ensayo con N=180 m-2, h = 2.4m, H = 0.5m y T = 3.5s.

El ajuste del coeficiente de arrastre para cada uno de los ensayos da lugar a establecer una nueva relación de éste con el número de Reynolds ($Re = a\frac{V_c}{\nu}$ siendo a el ancho de la replica, V_c la velocidad característica definida como la máxima velocidad en el extremo superior del comienzo del campo y ν la viscosidad cinemática). Los coeficientes obtenidos para los ensayos de Asano et al. (1988) son muy similares a los obtenidos con la formulación de Kobayashi et al. (1993) y a la de Méndez et al. (1999). Este resultado no es sorprendente ya que dichas formulaciones se obtuvieron con base en dichos ensayos. Sin embargo, los coeficientes obtenidos para los ensayos de Stratigaki et al. (2011) no se ajustan a las formulaciones existentes y se propone una nueva formulación basada en el mayor índice de correlación entre los coeficientes de arrastre obtenidos y el Re tal y como se muestra en la Figura 0.5.

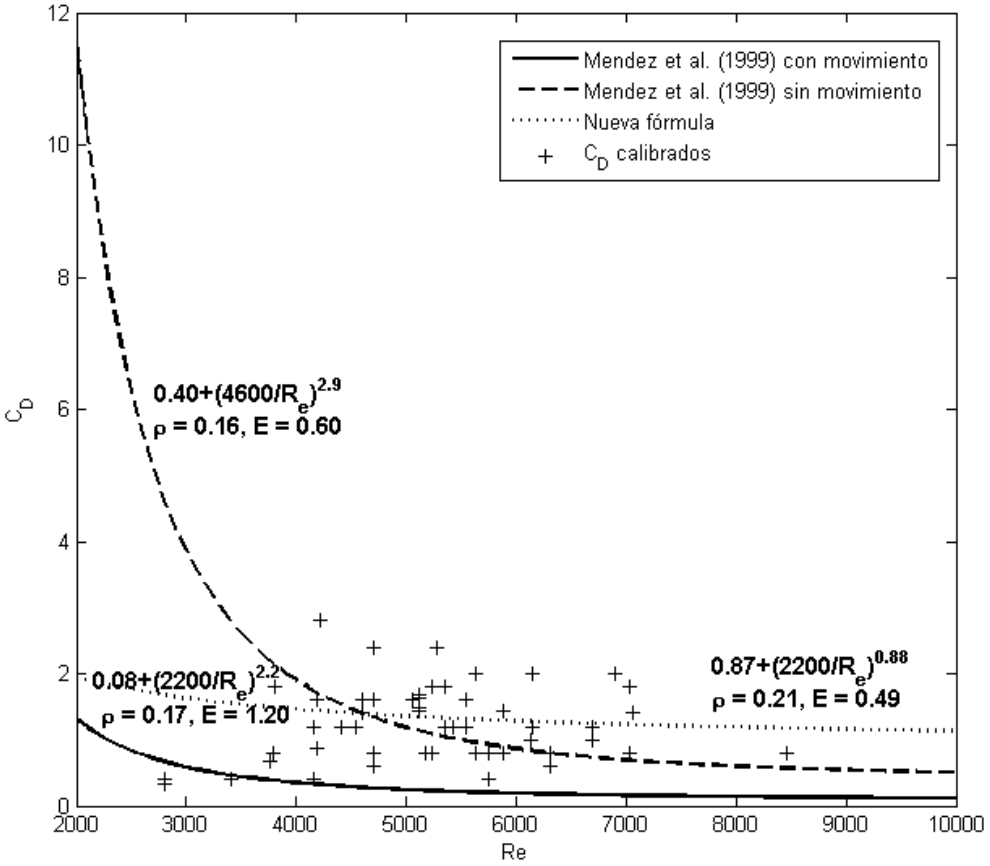

Figura 0.5 Coeficientes de arrastre obtenidos en la validación llevada a cabo considerando los ensayos de Stratigaki et al. (2011) y sin considerar el movimiento de la vegetación. Se muestran las formulaciones de Méndez et al. (1999) así como un nuevo ajuste (línea punteada gris).

La nueva formulación para el coeficiente de arrastre propuesta para casos en los que no se considera el movimiento de las plantas este se puede expresar como:

$$C_D = 0.87 + \left(\frac{2200}{Re}\right)^{0.88} \tag{10}$$

La segunda aproximación considera el movimiento de la planta. La validación de esta segunda aproximación se realiza de la misma manera que en el caso de la primera con la única excepción de que se deben fijar las diferentes variables y parámetros del modelo de movimiento de la planta. Las variables geométricas y de elasticidad se fijan de acuerdo con las características de las réplicas utilizadas en los ensayos. El coeficiente de masa añadida se toma igual a la unidad basándose en estudios anteriores (Ikeda et al., 2001). El coeficiente de amortiguamiento, C, despreciado en modelos anteriores como el presentado por Mendez et al. (1999) se obtiene a partir de unos ensayos de laboratorio realizados para medir el movimiento experimentado por las réplicas bajo condiciones controladas. Una vez fijado el valor de C en 12 Ns/m, el único parámetro de ajuste del modelo es el coeficiente de arrastre.

De nuevo se realiza el ajuste del coeficiente de arrastre para los ensayos presentados en Stratigaki et al. (2011), obteniendo acuerdos muy similares a los obtenidos en la primera aproximación. Sin embargo, los valores del coeficiente de arrastre obtenidos son diferentes dado que se está resolviendo el movimiento acoplado entre flujo y vegetación. La Figura 0.6 muestra los diferentes coeficientes de arrastre obtenidos de nuevo en función del número de Reynolds.

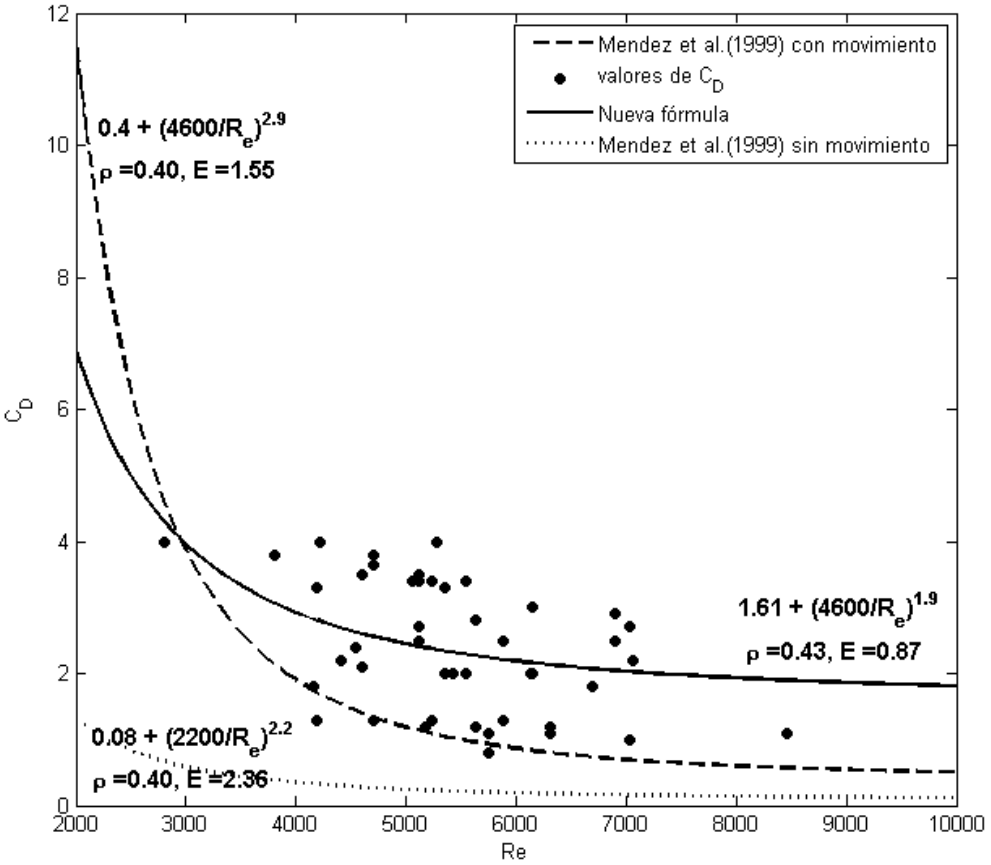

Figura 0.6 Coeficientes de arrastre obtenidos en la validación llevada a cabo considerando los ensayos de Stratigaki et al. (2011) considerando el movimiento de la vegetación. Se muestran las formulaciones de Méndez et al. (1999) así como un nuevo ajuste (línea continua negra).

Como se observa en la figura anterior, las formulaciones existentes no se ajustan a los valores de coeficiente de arrastre obtenidos. Por ello, se propone una nueva formulación para el coeficiente de arrastre en función de Re para casos en los que se resuelve el movimiento de la vegetación:

$$C_D = 1.61 + \left(\frac{4600}{Re}\right)^{1.9} \tag{11}$$

El trabajo realizado en el capítulo 3 muestra el modelo desarrollado para interacción de oleaje con vegetación flexible, resolviendo numéricamente las ecuaciones RANS e incluyendo la

presencia de la vegetación mediante una fuerza de arrastre y un modelo de turbulencia k-ε modificado. Asimismo, se muestran dos aproximaciones, una en la que se considera la vegetación rígida y una segunda en la que se resuelve el movimiento acoplado entre flujo y vegetación.

Ambas aproximaciones son capaces de reproducir la evolución de la altura de ola a lo largo del campo de vegetación y las velocidades desarrolladas dentro y fuera del mismo, como se ha demostrado mediante la validación realizada utilizando ensayos de laboratorio. La segunda aproximación permite obtener la fuerza de arrastre en función de la velocidad relativa producida entre el flujo y la vegetación.

A partir de la validación llevada a cabo despreciando o considerando el movimiento de las plantas, se han propuesto dos nuevas formulaciones del coeficiente de arrastre, una para cada uno de los escenarios. De esta forma se ha extendido el rango del número de Reynolds para el que se habían obtenido este tipo de formulaciones y se ha demostrado las diferencias en el coeficiente de arrastre que se debe considerar, dependiendo de si se tiene en cuenta o no el movimiento de la vegetación.

0.4 Recomendaciones para la realización de ensayos físicos con vegetación real de marisma

El creciente interés en integrar soluciones naturales, como parte de las estrategias de protección de la costa, ha llevado a la realización de una gran cantidad de estudios enfocados a estudiar la protección costera proporcionada por ecosistemas naturales. Debido a la complejidad del problema, la mayoría de estos estudios se han realizado en canales de laboratorio utilizando réplicas de vegetación. Sin embargo, estos estudios llevan asociadas simplificaciones que limitan la comprensión del problema real por el diferente comportamiento de las réplicas respecto a las plantas reales. Por ello, en los últimos años se ha evidenciado la necesidad de realizar ensayos con vegetación real y a una escala que sea representativa de las condiciones a las que estas plantas están sometidas en el medio físico. Por este motivo, en el capítulo 4 se plantean unos nuevos ensayos que permitan estudiar la interacción de oleaje y corriente con vegetación real a gran escala y que son pioneros en el campo.

Los ensayos se realizaron en el Cantabria Coastal and Ocean Basin (CCOB) del Instituto de Hidráulica Ambiental de Cantabria (IH Cantabria). El tanque tiene 44 m de anchura, 30 m de largo y 4.75 m de altura. En él se pueden generar simultáneamente oleaje y corriente, considerando distintas direcciones y ángulos de interacción entre las dos dinámicas. Además sus grandes dimensiones permiten realizar ensayos tridimensionales a gran escala. La vegetación

seleccionada para los ensayos fue dos especies de marisma de propiedades biomecánicas muy diferentes: Spartina anglica y Puccinellia maritima (Figura 0.7). Ambas especies se cultivaron a partir de semillas recogidas en campo en cajas de plástico que posteriormente se introdujeron en el tanque formando un campo de vegetación de 6 m de diámetro (Figura 0.8).

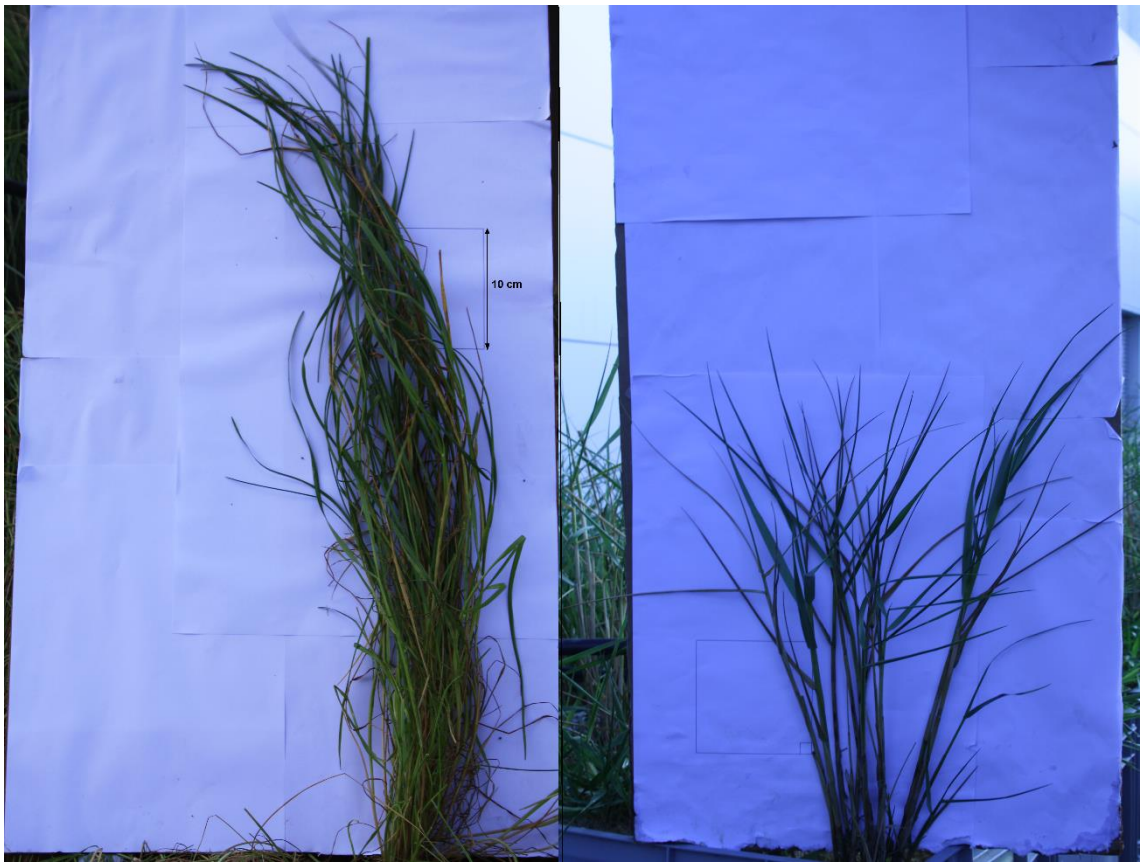

Figura 0.7 Puccinellia maritima (left) and Spartina anglica (right).

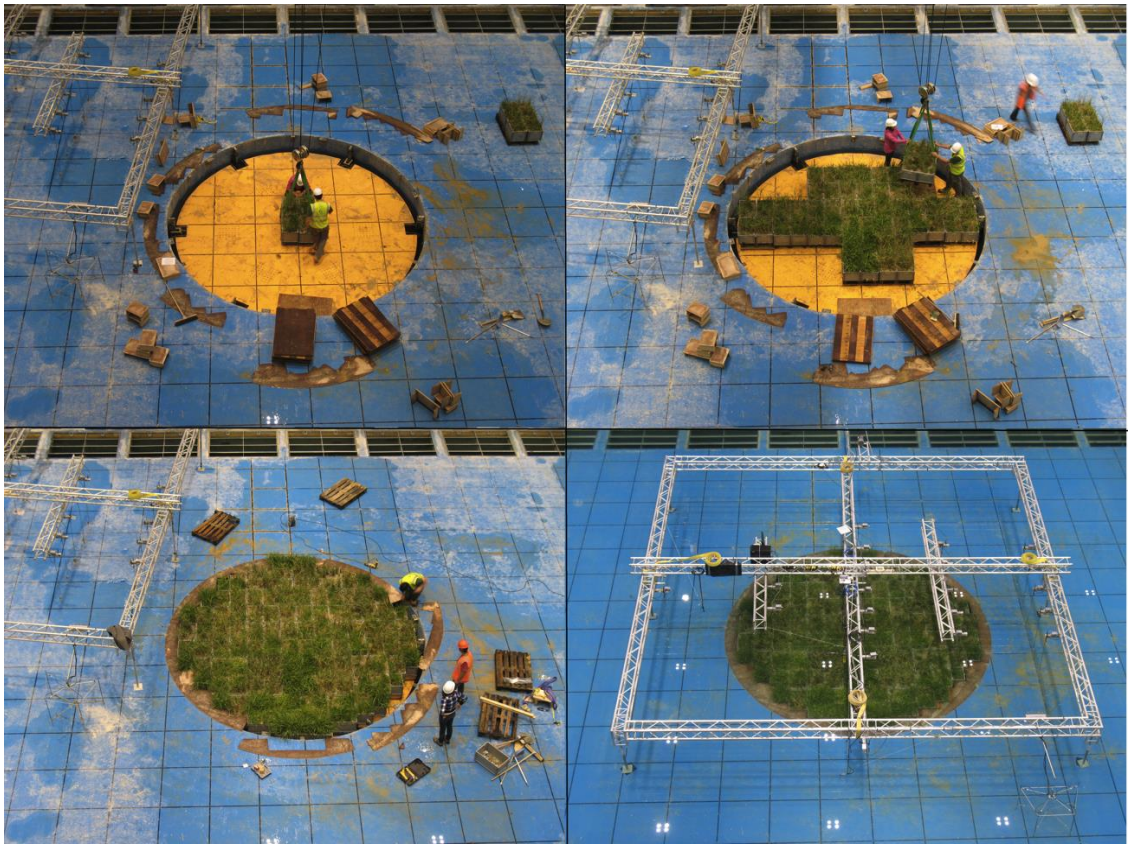

Figura 0.8 Colocación de las cajas de Spartina anglica en el tanque.

Para la realización de los ensayos se tuvo que realizar un conjunto de trabajos como el cultivo y recolección de plantas, el diseño experimental incluyendo la monitorización de los ensayos y la definición de las condiciones hidrodinámicas o el almacenamiento y eliminación de las plantas ensayadas tras los experimentos. Todo ello llevó al establecimiento de metodologías y a la definición de variables importantes a tener en cuenta en cada uno de los pasos.

Por lo tanto, con base en la experiencia obtenida mediante la realización de los ensayos, se presenta a continuación un conjunto de recomendaciones que pueden ser de gran utilidad para el desarrollo de nuevos ensayos, en los que se pretende analizar el efecto de vegetación real sobre diferentes dinámicas de flujo.

La primera parte de los ensayos consistió en cultivar durante cuatro meses las dos especies que iban a ser ensayadas. De todo este proceso se pueden extraer las siguientes lecciones aprendidas:

- Uno de los factores determinantes es la germinación de las plantas. Este paso se debe controlar en la medida de lo posible ya que de él depende obtener el número suficiente de plántulas para la realización de los ensayos. En el caso de *S. anglica*, se llevaron a

cabo dos tandas de germinación, utilizando semillas recogidas en la misma zona, aunque en años diferentes. Pese a que, en ambos casos, se siguió el mismo proceso de germinación, la germinación en el segundo fue muy inferior a la del primero. Puede que factores adicionales inherentes al proceso de germinación, como la aparición de hongos en las placas Petri o un cambio en el porcentaje de humedad o en la temperatura de la zona de germinación, fuesen los responsables de esta diferencia. En cuanto a la germinación de *P. maritima*, se consideraron dos procesos, uno llevado a cabo con semillas secas y otro con semillas húmedas. En el primer caso, ninguna de las semillas germinó.

- Es muy recomendable tener una segunda opción para la consecución de plantas, debiendo considerar los tiempos y costes asociados a la misma. En los ensayos descritos en este capítulo, fue necesario recolectar del campo 6000 plantas de *S. Anglica,* dado que la segunda tanda de germinación fue muy baja y no se obtuvo la densidad de campo necesaria para realizar los ensayos. La recogida y almacenamiento de dichas plantas llevó asociadas unas 100 horas de trabajo.

- El cultivo se puede llevar a cabo en un invernadero. Sin embargo, en ese caso se deben considerar los costes asociados. Por otro lado, puede ser más conveniente cultivar las plantas cerca de la instalación en la que se van a realizar los ensayos. Para ello es necesario disponer de una zona lo suficientemente grande y con unas condiciones climáticas adecuadas. Además, se debe proteger las plantas de hongos, insectos y pájaros. Con este propósito, en nuestros ensayos se construyó un invernadero con alambres y malla anti mosquitos, regando las plantas con agua salada dos veces por semana. Además, se utilizaron pesticidas ecológicos, una vez a la semana, durante tres meses, en horas de baja insolación.

- El sistema de irrigación se debe diseñar atendiendo a las condiciones climáticas del lugar de cultivo y a las necesidades de las plantas. Es aconsejable utilizar un sistema de riego por goteo que cubra todo el área ocupada por las plantas. De esta forma se puede suministrar el agua necesaria, sin desperdiciar parte de ella. En los ensayos realizados se utilizó agua dulce y el crecimiento de las plantas fue adecuado, confirmando así que se pueden cultivar sin necesidad de agua salada.

- La selección del sustrato para el cultivo de las plantas también es un factor determinante. El sustrato se debe elegir dependiendo del tipo de planta a cultivar y de sus necesidades de agua. Es común añadir al sustrato seleccionado fertilizantes que favorezcan el crecimiento. En nuestros ensayos se dispusieron dos capas de fertilizante y se añadieron fertilizantes líquidos dependiendo del color de las hojas de las plantas a lo largo de su

crecimiento. Este aspecto es muy importante ya que el color de las hojas es un buen indicador de las necesidades de la planta. Por ejemplo, la aparición de hojas de color morado indica falta de fósforo y de color amarillo falta de nitrógeno. Cuando se añaden fertilizantes se debe controlar el pH del sustrato ya que cambios importantes en el mismo puede producir la muerte de las plantas.

- Un aspecto muy importante cuando se cultivan plantas es saber si éstas son especies autóctonas o no. Cuando no lo son es extremadamente importante evitar que se puedan introducir en el entorno. En nuestro caso, *S. anglica* no es una especie autóctona por lo que se recogieron todas las pantas y se tamizaron todos los sustratos en los que se habían cultivado para eliminar cualquier trozo de raíz. Todos los restos se las plantas se almacenaron y se secaron para posteriormente incinerarlos.

La segunda parte de los experimentos consistió en la propia realización de los ensayos en el laboratorio. Durante el mes en el que se trabajó de continuo para realizar todo el conjunto de ensayos se consideraron varios aspectos clave que se detallan a continuación:

- Se debe estudiar cuál es la mejor opción para introducir las plantas en el tanque donde se realizaran los ensayos teniendo en cuenta tiempo, costes y su localización respecto de las zonas de generación de flujo. En los ensayos realizados se optó por bajar el nivel de la tapa del foso central del tanque y disponer las cajas en ese espacio permitiendo así una transición suave desde el fondo del tanque a la zona vegetada.

- Una vez colocadas las cajas en el tanque es aconsejable ejecutar un primer ensayo para eliminar hojas sueltas o sedimento no consolidado de la zona vegetada. De esta forma se limpiará la zona de ensayos para empezar posteriormente los mismos.

- Es importante que el campo de vegetación cultivado tenga una densidad uniforme. En nuestro caso, se distinguieron cinco tipos de densidades en las cajas de *S. anglica*. La disposición de las cajas en el tanque se realizó considerando los diferentes tipos y buscando un campo lo más uniforme posible para evitar caminos de flujo preferentes.

- Para poder identificar los patrones de flujo desarrollados en superficie de forma visual se pueden utilizar cuerpos flotantes. En nuestro caso se utilizaron naranjas distribuidas paralelamente a la zona de generación del oleaje para observar los patrones de flujo bajo condiciones de oleaje y corriente.

- Se deben seleccionar el número y tipo de sensores que se van a utilizar en los ensayos de acuerdo con las variables que se quieran medir y la disponibilidad de los mismos. Cuando se quiere tomar medidas dentro del campo de vegetación pueden surgir varios

problemas. Si se utilizan sensores resistivos para la medida de la superficie libre, las hojas de las plantas falsearán las medidas cuando toquen dichos sensores. Los sensores capacitivos son más estables en este sentido y además no necesitan una calibración diaria, por lo que fueron los seleccionados en nuestro caso. Para tomar medidas de velocidad se pueden utilizar ADVs, pero de nuevo, las plantas no deben interferir la zona de medida. Para ello, se pueden cortar todas las plantas alrededor del ADV que puedan introducirse en la zona de medida. En nuestro caso se optó por construir una pequeña estructura que protegía el área de medida reduciendo el número de plantas que tuvieron que ser cortadas.

- Es aconsejable calibrar las condiciones hidrodinámicas que se van a generar en los ensayos, especialmente cuando se van a generar simultáneamente olas y corriente. En nuestros ensayos, dada la magnitud de las olas y la de las corrientes, las olas se activaban en primer lugar y posteriormente la corriente ya que en caso opuesto la corriente no permitía que se desarrollase el oleaje.

- Cuando se quiere cambiar la densidad del campo para poder realizar ensayos con diferentes densidades, los cortes se deben realizar sin dañar las plantas. Esta tarea de corte puede ser muy laboriosa dependiendo del tamaño del campo, ya que si éste es grande, no se podrá acceder desde los bordes a las plantas del interior del mismo. En ese caso se deberán mover las cajas para poder abrir caminos o crear una estructura que permita acceder a las plantas del centro. Otra alternativa es la que se utilizó en nuestros ensayos. El corte de las plantas se realizó dejando un nivel de agua suficiente para poder cortar las plantas buceando. De esta forma se podía acceder al centro del campo sin dañar las plantas de una forma rápida y barata.

- Es muy importante mantener las características de las plantas a lo largo de los ensayos. Es aconsejable tomar medidas de biomasa durante los ensayos para chequear el estado de las plantas. En nuestro caso, se tomaron medidas al comienzo y al final de los ensayos para las dos especies, obteniendo una reducción de biomasa del 6% para *S. anglica* y del 11% para *P. marítima*.

Todas estas recomendaciones son de utilidad para la realización de futuros ensayos con vegetación real.

0.5 Experimentos 3D a gran escala de la interacción de oleaje y corriente con vegetación real

El capítulo 5 presenta el análisis de los ensayos realizados en el CCOB con vegetación real. Estos ensayos se realizaron con dos especies de vegetación, Spartina anglica y Puccinellia maritima (Figura 0.7), que se presentan en la zona baja y media del estuario, respectivamente, y que poseen propiedades biomecánicas muy diferentes. P. maritima es una especie muy flexible mientras que S. anglica es mucho más rígida. Esto permite analizar la influencia que tiene la rigidez de la vegetación en la atenuación de energía. Así mismo, se llevaron a cabo varios ensayos considerando distintos valores de densidad del campo. La densidad del campo de P. maritima se redujo dos veces, dando lugar a tres valores de densidad: 100, 66 y 33%. En el caso de S. anglica la densidad se redujo una sola vez, por lo que se obtuvieron dos densidades: 100 y 66%. Para ambas especies las densidades iniciales, 100%, se corresponden con características propias de campo. De esta forma se puede analizar la influencia de la densidad del campo de vegetación en la atenuación.

Los ensayos se realizaron considerando diferentes condiciones de oleaje regular e irregular (Tabla 0.2) y corrientes de 0.30 m/s que se generan a favor y en contra de la propagación del oleaje con incidencia normal y con un ángulo de 20º.

Oleaje	Tipo	H(m)|Hs(m)	T(s)|Tp(s)
R1	Regular	0.15	2
R2	Regular	0.20	2
R3	Regular	0.20	1.2
R4	Regular	0.20	1.7
R5	Regular	0.20	2.2
IR	Irregular	0.12	1.7

Tabla 0.2 Condiciones de oleaje.

Todo el conjunto de oleajes y corrientes se generaron para cuatro calados: 0.40, 0.60, 0.80 y 1.0 m. La Tabla 0.3 muestra las diferentes combinaciones de oleaje, corriente (+C: corriente de 0.30 m/s a favor de la propagación de las olas, -C: misma corriente en contra), calado y vegetación (P: P. maritima, S: S. anglica, 100, 66 y 33 se refieren al % de densidad). El número total de ensayos fue de 276 y se ejecutaron durante 30 días seguidos.

Vegetación	Oleaje	Ángulo del oleaje (θ)	Corriente	Calado (h)
P100 y S100	R1 – R5, IR	0	+C, -C	0.40 m

P100 y S100	R1 – R5, IR	0	+C, -C	0.60 m
P100 y S100	R1 y R3	0	+C, -C	0.80 m
P100 y S100	R1 y R3	0	+C, -C	1.00 m
P100 y S100	R1, R3 y IR	20º	+C, -C	0.40 m
P100 y S100	R1, R3 y IR	20º	+C, -C	0.60 m
P66, P33 y S66	R1, R3 y IR	0	+C, -C	0.40 m
P66, P33 y S66	R1, R3 y IR	0	+C, -C	0.60 m
P66, P33 y S66	R1 y R3	0	+C, -C	0.80 m
P66, P33 y S66	R1 y R3	0	+C, -C	1.00 m
P66, P33 y S66	R1, R3 y IR	20º	+C, -C	0.40 m
P66, P33 y S66	R1, R3 y IR	20º	+C, -C	0.60 m

Tabla 0.3 Ensayos ejecutados

Para medir la influencia del campo de vegetación en las distintas condiciones de flujo se dispuso un total de 28 sensores de superficie libre y tres ADVs para medir la velocidad. La Figura 0.9 muestra la localización de los distintos sensores, así como la localización del campo de vegetación dentro del tanque y los generadores de corrientes y oleaje.

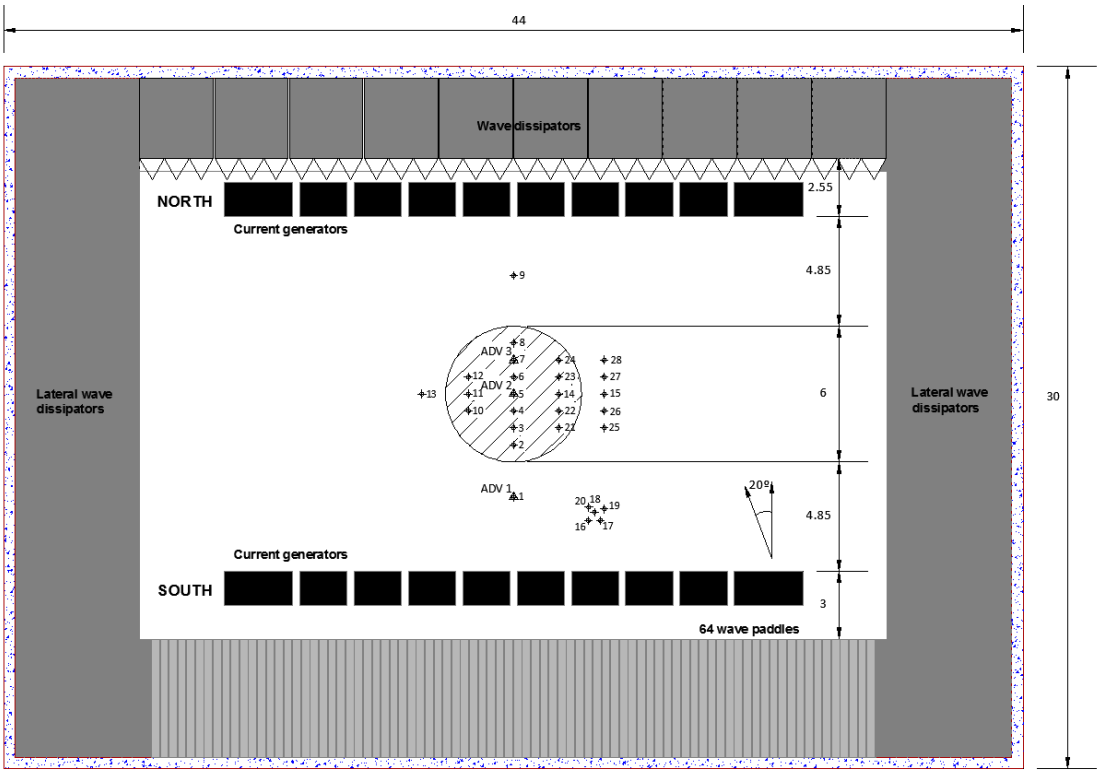

Figura 0.9 Localización de los sensores de superficie libre (1 – 28) y los 3 ADVs dentro del CCOB

El análisis de los resultados de los ensayos se realizó con base en la atenuación de oleaje medida. Para ello, se tomó la formulación de atenuación de energía de Dalrymple et al. (1984) para oleaje regular y posteriormente extendida a oleaje irregular por Méndez y Losada (2004) y se aplicó a las medidas de altura de ola registradas en la línea central de sensores dispuesta en los ensayos. Estas formulaciones son,

$$\frac{H}{H_0} = \frac{1}{1+\beta x} \tag{12}$$

$$\frac{H_{rms}}{H_{rms,0}} = \frac{1}{1+\beta' x} \tag{13}$$

donde H es la altura de ola para oleaje regular y H_{rms} es la altura de ola media cuadrática para oleaje irregular, β y β' son los coeficientes de atenuación, x la distancia longitudinal a lo largo del campo y 0 se refiere a las condiciones de oleaje incidente.

La Figura 0.10 muestra los ajustes obtenidos para 3 condiciones de oleaje considerando sólo olas, olas + corriente (corriente generada a favor de la propagación de las olas) y olas – corriente (corriente generada en sentido opuesto al oleaje) para dos calados (0.40 y 0.60 m) y P100.

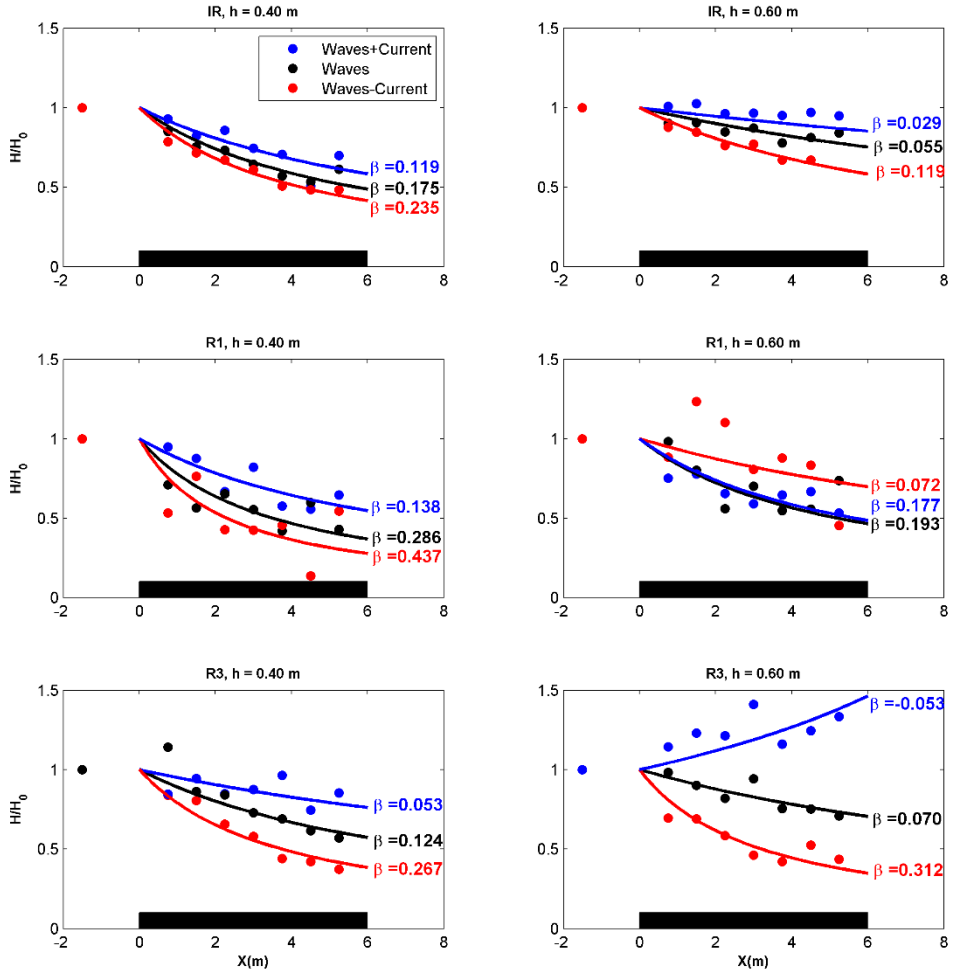

Figura 0.10 Atenuación obtenida para P100 y condiciones de oleaje (negro), oleaje+corriente (azul) y oleaje-corriente (rojo) para IR, R1 y R3 y h = 0.40 y 0.60 m.

La Figura 0.10 muestra, en términos generales, un aumento del coeficiente de atenuación para condiciones de oleaje y corriente en contra, con respecto al obtenido sólo con olas, mientras que el coeficiente disminuye cuando la corriente se genera en el mismo sentido que las olas. Las discrepancias con esta tendencia general observadas en R1 y R3 y h = 0.60 m se deben a los patrones de flujo producidos alrededor del campo de vegetación para este calado que hacen que la corriente influya, en gran medida, en oleajes poco energéticos modificando así sus características (Figura 5.9). Esto se muestra a partir de las medidas de velocidad (Figuras 5.10, 5.11 y 5.12). El análisis de los casos de oleaje oblicuo interaccionando con corriente indican una disminución de la atenuación producida por el campo respecto a los casos de incidencia normal (Figura 5.14).

También se estudia la influencia del calado en la atenuación producida. Para ello, se representan los coeficientes de atenuación en función de la profundidad relativa definida como: $h_r = h/h_v$

donde h_v es la altura de la vegetación. La Figura 0.11 muestra estos resultados junto con los ajustes logarítmicos que establecen la relación de las dos variables para las dos especies estudiadas.

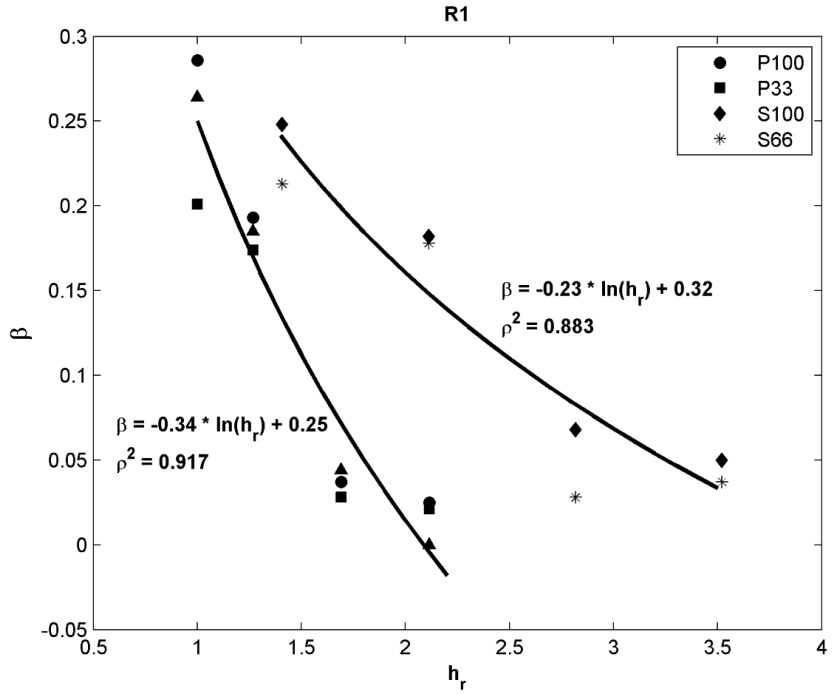

Figura 0.11 Coeficientes de atenuación para todas las densidad de vegetación de ambas especies en función de la profundidad relativa para R1.

La influencia de los parámetros de la vegetación también se estudia de acuerdo con los coeficientes de atenuación obtenidos. Los ensayos realizados considerando diferentes densidades muestran una mayor atenuación cuanto mayor es la densidad del campo (Figuras 5.15 y 5.16) . Para tener en cuenta, además de la densidad horizontal, la estructura vertical de las dos especies se utilizan medidas de biomasa. La biomasa se define como el peso seco por metro cuadrado y, por lo tanto, es diferente, dependiendo del número de plantas por metro cuadrado y de la estructura vertical de las mismas. La Figura 0.12 muestra la gran correlación que existe entre este parámetro y la atenuación obtenida para tres condiciones de oleaje (R1, R3 e IR), con y sin corriente.

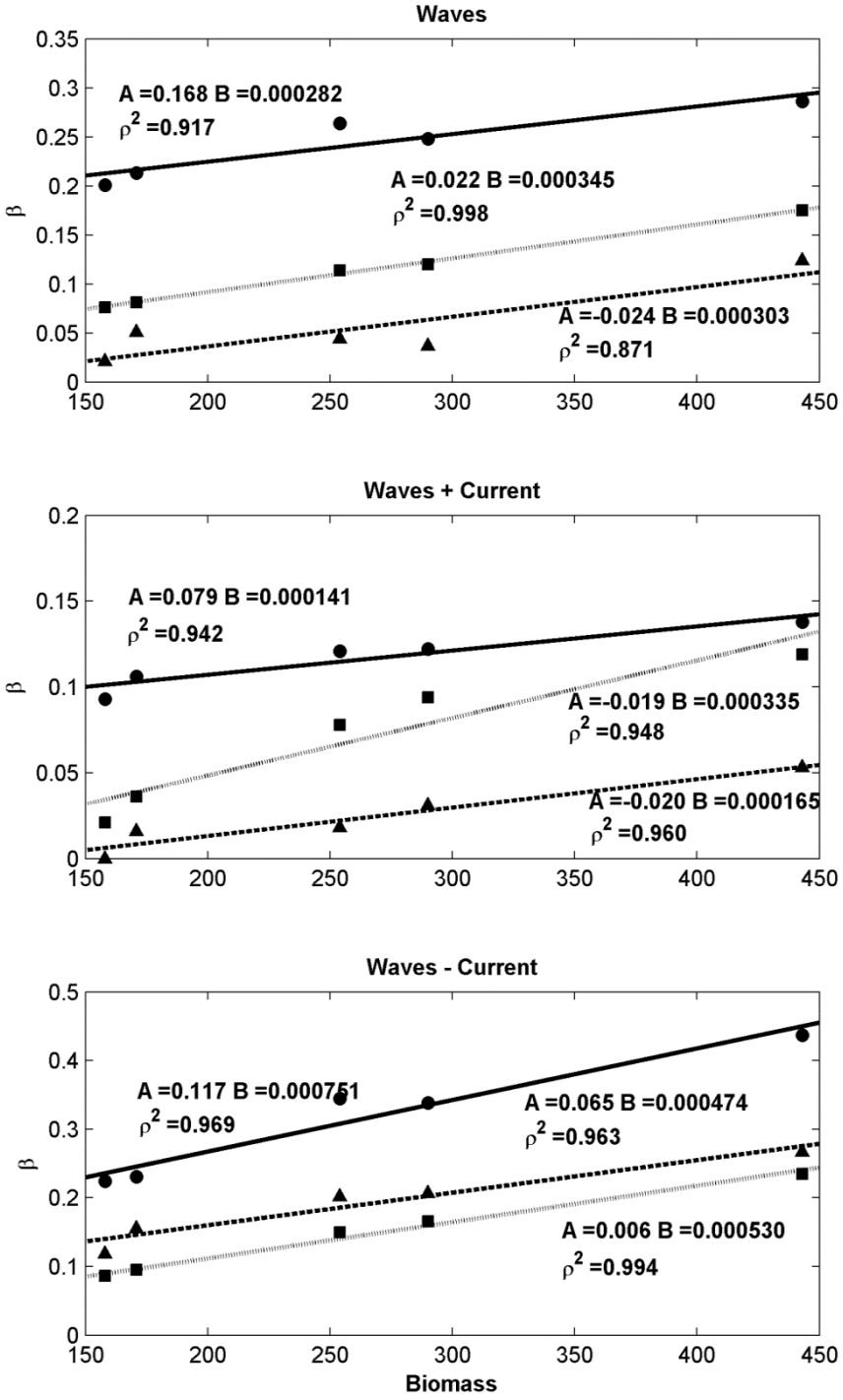

Figura 0.12 Coeficientes de atenuación para distintos valores de biomasa asociados a la vegetación y oleaje R1 (círculos), R3 (triángulos) y IR (cuadrados) y condiciones de solo oleaje, oleaje +corriente y oleaje-corriente.

En la Figura 0.12 se muestran los ajustes lineales obtenidos para todos los casos, considerando la biomasa asociada a las dos especies. Por lo tanto, los coeficientes de atenuación se relacionan linealmente con los valores de biomasa de ambas especies.

El análisis de los ensayos realizados en el CCOB ha permitido estudiar el efecto que tienen sobre la disipación de energía los parámetros del flujo y de la vegetación. Asimismo, se ha conseguido un mayor conocimiento de la interacción ola-corriente-vegetación.

0.6 Nueva formulación de la disipación de energía producida por vegetación bajo la acción de oleaje y corriente

El capítulo 6 muestra las nuevas formulaciones obtenidas para la disipación de energía producida por la vegetación bajo la acción combinada de oleaje y corriente. Dichas formulaciones se calibran con la ayuda de los ensayos descritos en el capítulo 5. En dichos ensayos se ha observado que la longitud de la planta que afecta realmente al flujo no es la longitud real de la misma sino una longitud deflectada que varía dependiendo de las propiedades de la planta y las del flujo que la afecta. La Figura 0.13 muestra un esquema del movimiento experimentado por las dos especies consideradas en los ensayos (Puccinellia maritima y Spartina anglica) bajo la acción del oleaje y de la acción combinada de olaje y corriente.

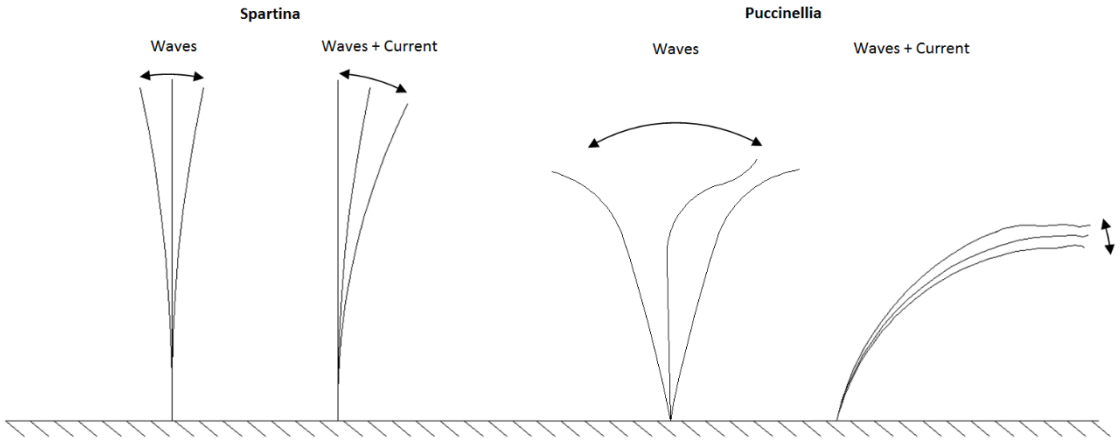

Figura 0.13 Representación esquemática del movimiento experimentado por una vegetación flexible (Puccinellia marítima) y una más rígida (Spartina anglica) bajo la acción del oleaje (izquierda) y de oleaje+corriente (derecha).

A partir de la formulación propuesta por Luhar y Nepf (2011) para la obtención de la longitud deflectada (l_D) y los ángulos de deflexión observados en el laboratorio se considera que, para S. anglica, l_D es igual a la longitud de la planta (l) y para P. maritima $l_D = 0.8\, l$ bajo la acción del oleaje y $l_D = 0.6\, l$ bajo la acción combinada de olas y corriente. Estas longitudes son las que se consideran en el desarrollo de las nuevas formulaciones.

Las nuevas formulaciones se obtienen con base en la aproximación presentada por Dalrymple et al. (1984) y considerando las siguientes hipótesis:

1. La corriente es uniforme en la columna de agua y a lo largo del campo.
2. Oleaje y corriente se propagan con incidencia normal.
3. Teoría lineal de ondas.
4. Campo de oleaje-corriente irrotacional y uniforme.
5. Efecto Doppler en el campo de velocidades del oleaje.
6. El movimiento de la vegetación es despreciable y la disipación es únicamente producida por la fuerza de arrastre.
7. La componente horizontal de la fuerza de arrastre es la predominante.
8. El coeficiente de arrastre es constante en la columna de agua.
9. Calado constante y fondo horizontal.
10. Condiciones de vegetación densa.

Considerando estas hipótesis la ecuación de conservación de la energía se expresa como:

$$\frac{\partial E_{wc} c_{g_{wc}}}{\partial x} = -\varepsilon_{D_{wc}} \tag{14}$$

donde E_{wc} es la densidad de energía asociada a olas y corriente, $c_{g_{wc}}$ la celeridad de grupo de olas y corriente, x la coordenada a lo largo del campo de vegetación y $\varepsilon_{D_{wc}}$ es la tasa de disipación, por unidad de área horizontal, inducida por la vegetación y promediada en el periodo de la ola. Considerando las hipótesis 1 – 5 la celeridad de grupo (Peregrine, 1976) es:

$$c_{g_{wc}} = \frac{\partial \sigma_{wc}}{\partial k} = U_0 + \frac{1}{2}\left(1 + \frac{2kh}{sinh2kh}\right)\left(\frac{g}{k} tanhkh\right)^{1/2} \tag{15}$$

donde σ_{wc} es la frecuencia angular de olas y corriente ($\sigma_{wc} = \sigma - U_0 k$), k es el número de onda, U_0 es la velocidad de la corriente, σ la frecuencia angular de las olas, h el calado y g la aceleración de la gravedad. La densidad de energía para olas y corriente (Baddour & Song, 1990) se expresa como:

$$E_{wc} = \frac{\rho}{16} g \left(1 + \frac{2kh}{sinh2kh}\right) \left(\frac{g}{k} tanhkh\right)^{1/2} H^2 + \frac{\rho}{16} g U_0 \left(3 + \frac{4kh}{sinh2kh}\right) H^2 + \frac{3\rho}{16} k U_0^2 \left(\frac{g}{k} cothkh\right)^{1/2} H^2 + \frac{\rho}{2} h U_0^3 \quad (16)$$

donde el primer término representa el transporte de energía realizado por las olas, el último el realizado por la corriente y el segundo y tercer término representan la energía transportada debida a la interacción no lineal de las olas y la corriente.

La disipación de energía promediada en el tiempo e integrada en vertical, considerando que el fondo se encuentra en $z = -h$, es:

$$\varepsilon_{D_{wc}} = \overline{\int_{-h}^{-h+l_D} F_{wc} u_{wc} dz} \quad (17)$$

donde F_{wc} es la fuerza actuando sobre la vegetación por unidad de volumen expresada como:

$$F_{wc} = \frac{1}{2} \rho C_{D_{wc}} a N u_{wc} |u_{wc}| \quad (18)$$

donde $C_{D_{wc}}$ es el coeficiente de arrastre, N el número de plantas por unidad de área y a el ancho de la planta normal a u_{wc} que representa la velocidad horizontal y se expresa como:

$$u_{wc} = U_0 + \frac{gk}{2\sigma_{wc}} H \frac{coshk(h+z)}{coshkh} sin(kx - \sigma t) \quad (19)$$

Basados en las medidas de velocidad tomadas en los ensayos realizados en el CCOB y la visualización de patrones de flujo (Figura 6.3), así como en trabajos anteriores (Zong y Nepf, 2010; Nepf, 2012) se considera que, dado que nos encontramos ante condiciones de campo denso, la velocidad que se registra dentro del campo es solo debida a la componente de las olas. Por lo tanto, la velocidad se expresa como:

$$u_{wc} = \frac{gk}{2\sigma_{wc}} H \frac{coshk(h+z)}{coshkh} sin(kx - \sigma t) \quad (20)$$

Considerando esta velocidad la disipación de energía se expresa como:

$$\varepsilon_{D_{wc}} = \overline{\int_{-h}^{-h+l_D} \frac{1}{2} \rho C_{D_{wc}} a N \left(\frac{gk}{2(\sigma - U_0 k)} H \frac{coshk(h+z)}{coshkh} sın(kx - \sigma t)\right)^2 \left|\frac{gk}{2(\sigma - U_0 k)} H \frac{coshk(h+z)}{coshkh} sın(kx - \sigma t)\right| dz} \quad (21)$$

Resolviendo la integración vertical la tasa de disipación de energía queda de la forma:

$$\varepsilon_{D\,wc} = -\frac{2}{3\pi}\rho C_{D\,wc} aN \left(\frac{gk}{2(\sigma - U_0 k)}\right)^3 \frac{sinh^3 kl_D + 3sinhkl_D}{3kcosh^3 kh} H^3 \tag{22}$$

El análisis de conservación de energía ha sido usado por autores como Dalrymple et al. (1984) para obtener la reducción de altura de ola a lo largo del campo. En este caso considerando condiciones de oleaje y corriente, esta reducción de la altura de ola se expresa como:

$$H = \frac{H_0}{1 + \beta_{wc} x} \tag{23}$$

donde β_{wc} es el coeficiente de disipacion para oleaje y corriente expresado como:

$$\beta_{wc} = \frac{A_0 H_0}{B} \tag{24}$$

$$A_0 = \frac{2}{3\pi}\rho C_{D\,wc} aN \left(\frac{gk}{2(\sigma - U_0 k)}\right)^3 \frac{sinh^3 kl_D + 3sinhkl_D}{3kcosh^3 kh} \tag{25}$$

$$B = \left[\frac{\rho g}{8}\left(1 + \frac{2kh}{sinh2kh}\right)\left(\frac{g}{k} tanhkh\right)^{\frac{1}{2}} + \frac{\rho g}{8} U_0 \left(3 + \frac{4kh}{sinh2kh}\right) + \frac{3\rho k}{8} U_0^2 \left(\frac{g}{k} cothkh\right)^{\frac{1}{2}}\right]\left[U_0 + \frac{1}{2}\left(1 + \frac{2kh}{sinh2kh}\right)\left(\frac{g}{k} tanhkh\right)^{\frac{1}{2}}\right] \tag{26}$$

Esta formulación permite obtener una expresión para el coeficiente de arrastre para oleaje regular y corriente de la forma:

$$C_{Dwc} = \frac{3\pi}{2aN\left(\frac{gk}{2(\sigma - U_0 k)}\right)^3 H_0} \frac{3kcosh^3 kh}{sinh^3 kl_D + 3sinhkl_D}\left[\frac{g}{8}\left(1 + \frac{2kh}{sinh2kh}\right)\left(\frac{g}{k} tanhkh\right)^{\frac{1}{2}} + \frac{g}{8} U_0 \left(3 + \frac{4kh}{sinh2kh}\right) + \frac{3k}{8} U_0^2 \left(\frac{g}{k} cothkh\right)^{\frac{1}{2}}\right]\left[U_0 + \frac{1}{2}\left(1 + \frac{2kh}{sinh2kh}\right)\left(\frac{g}{k} tanhkh\right)^{\frac{1}{2}}\right]\beta_{wc} \tag{27}$$

Siguiendo a Méndez y Losada (2004) estas expresiones obtenidas para oleaje regular se extienden a oleaje irregular de la forma:

$$H_{rms} = \frac{H_{rms,0}}{1 + \beta'_{wc} x} \tag{28}$$

donde H_{rms} es la altura de ola media cuadrática y β'_{wc} es el coeficiente de disipación obtenido como:

$$\beta'_{wc} = \frac{A'_0 H_{rms,0}}{B} \tag{29}$$

$$A_0 = \frac{1}{2\sqrt{\pi}} \rho C_{D_{wc}} aN \left(\frac{gk}{2(\sigma - U_0 k)}\right)^3 \frac{sinh^3 kl + 3sinhkl}{3kcosh^3 kh} \tag{30}$$

De nuevo se puede obtener una expresión para el coeficiente de arrastre que queda de la forma:

$$C'_{Dwc} = \frac{2\sqrt{\pi}}{aN\left(\frac{gk}{2(\sigma - U_0 k)}\right)^3 H_{rms,0}} \frac{3kcosh^3 kh}{sinh^3 kl_D + 3sinhkl_D} \left[\frac{g}{8}\left(1 + \frac{2kh}{sinh2kh}\right)\left(\frac{g}{k} tanhkh\right)^{\frac{1}{2}} + \frac{g}{8} U_0 \left(3 + \frac{4kh}{sinh2kh}\right) + \frac{3k}{8} U_0^2 \left(\frac{g}{k} cothkh\right)^{\frac{1}{2}}\right]$$

$$\left[U_0 + \frac{1}{2}\left(1 + \frac{2kh}{sinh2kh}\right)\left(\frac{g}{k} tanhkh\right)^{\frac{1}{2}}\right] \beta'_{wc} \tag{31}$$

Estas formulaciones del coeficiente de arrastre, para condiciones de oleaje y corrientes, para oleaje regular e irregular se aplican a los coeficientes de disipación obtenidos en el análisis experimental de los ensayos realizados en el CCOB (capítulo 5). Para aquellos casos en los que sólo se generan olas se toma la formulación presentada por Dalrymple et al. (1984) para oleaje regular y la de Méndez y Losada (2004) para oleaje irregular. De esta forma, se obtiene el coeficiente de arrastre para cada uno de los ensayos. Dichos coeficientes de arrastre se representan en función de un nuevo número de Reynolds (Re_{wc}^D) obtenido considerando como longitud característica la longitud deflectada de la planta y como velocidad característica la velocidad máxima horizontal en el extremo superior del comienzo del campo para condiciones de oleaje y u_{wc} para casos de ola-corriente. La Figura 0.14 muestra los ajustes obtenidos para relacionar los coeficientes de arrastre obtenidos para condiciones de oleaje y corriente en función del nuevo número de Reynolds. La Figura 0.15 muestra el ajuste obtenido para condiciones de oleaje regular.

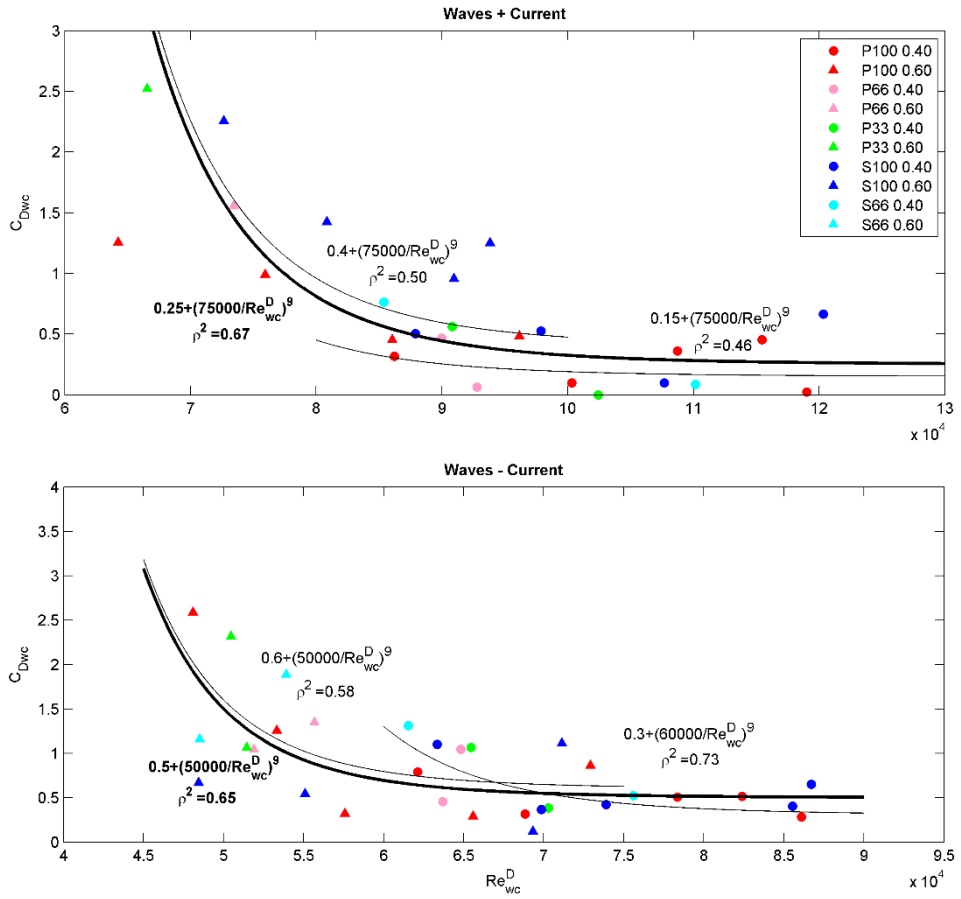

Figura 0.14 Coeficientes de arrastre para oleaje y corriente a favor (panel superior) y en contra (panel inferior) en función de Re_{wc}^{D}.

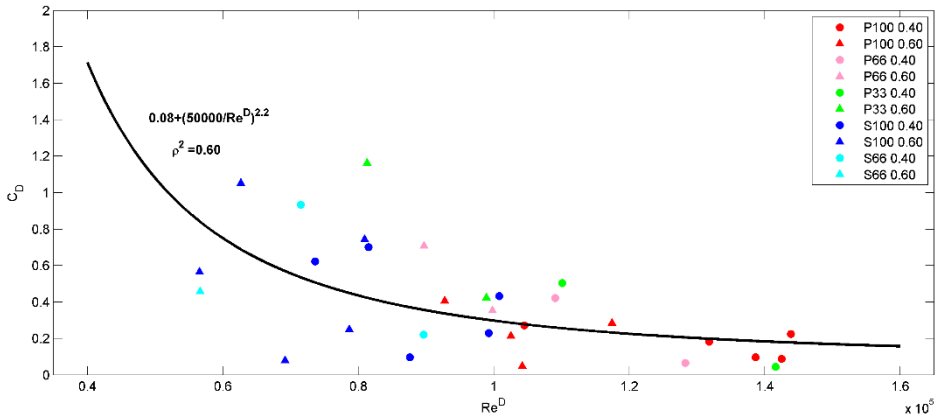

Figura 0.15 Coeficientes de arrastre para oleaje en función de Re^{D}.

Los ajustes mostrados en las Figuras 0.14 y 0.15 dan lugar a unas nuevas formulaciones para el coeficiente de arrastre, para oleaje regular, en función del numero de Reynolds obtenido con la longitud deflectada de la planta y para condiciones combinadas de oleaje y corriente:

$$C_D = 0.08 + \left(\frac{50000}{Re^D}\right)^{2.2} \qquad oleaje\ regular \qquad (32)$$

$$C_{Dwc+} = 0.25 + \left(\frac{75000}{Re_{wc}^D}\right)^9 \quad oleaje\ regular + corriente \quad (33)$$

$$C_{Dwc-} = 0.50 + \left(\frac{50000}{Re_{wc}^D}\right)^9 \quad oleaje\ regular - corriente \quad (34)$$

El mismo tipo de análisis se realiza para oleaje irregular. La Figura 0.16 muestra los ajustes encontrados en este caso.

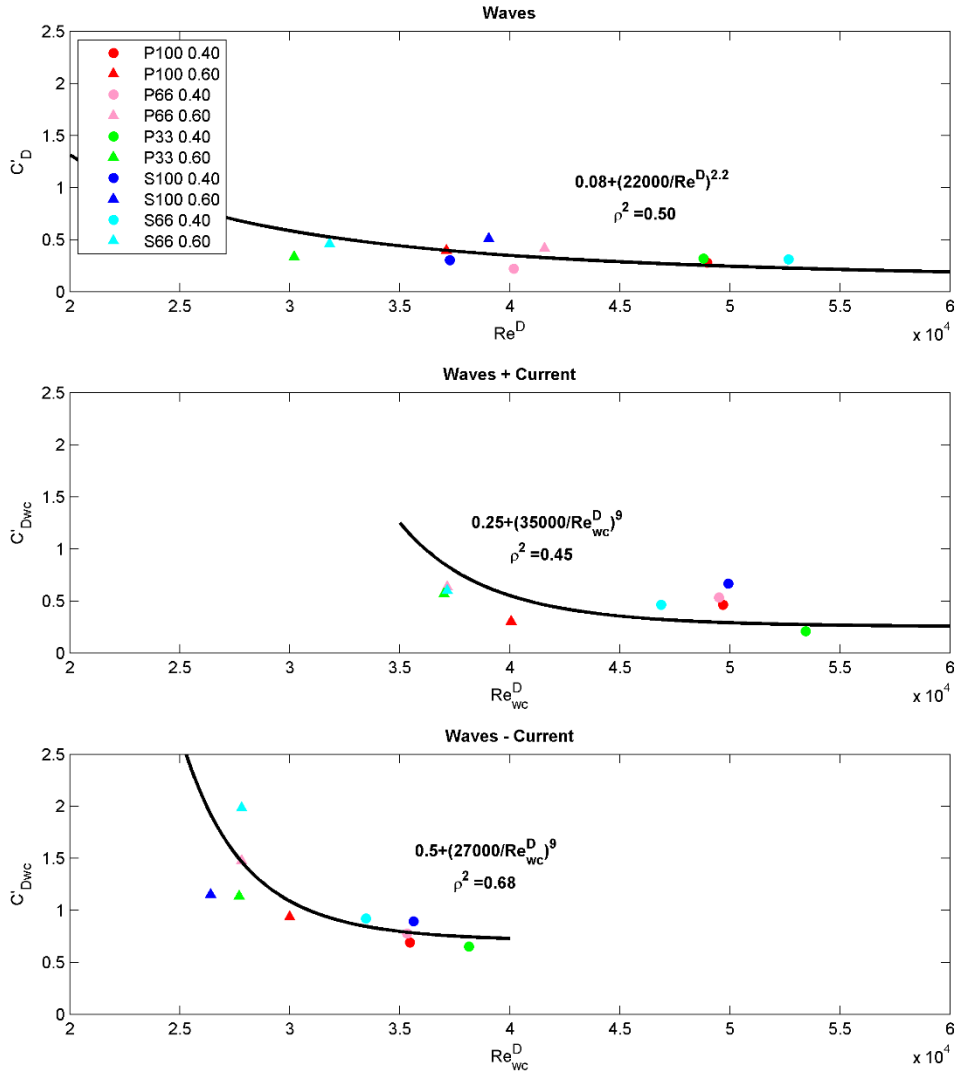

Figura 0.16 Coeficientes de arrastre para solo oleaje irregular (panel superior), oleaje irregular y corriente a favor (panel central) y en contra (panel inferior) en función del número de Reynolds calculado con la longitud deflectada.

Dichos ajustes responden a las ecuaciones:

$$C'_D = 0.08 + \left(\frac{22000}{Re'^D}\right)^{2.2} \qquad oleaje\ irregular \qquad (35)$$

$$C'_{Dwc+} = 0.25 + \left(\frac{35000}{Re'^D_{wc}}\right)^{9} \qquad oleaje\ irregular + corriente \quad (36)$$

$$C'_{Dwc-} = 0.50 + \left(\frac{27000}{Re'^{D}_{wc}}\right)^{9} \qquad oleaje\ irregular - corriente \quad (37)$$

En este capítulo se ha presentado un nuevo modelo analítico de disipación de energía para oleaje y corriente, tanto para oleaje regular como irregular. Además, se han presentado una nuevas formulaciones para la obtención del coeficiente de arrastre teniendo en cuenta la longitud deflectada de la planta y no sólo condiciones de oleaje sino también condiciones de oleaje y corriente.

0.7 Modelo tridimensional de la interacción de ondas de tsunami con bosques de manglares

El capítulo 7 presenta dos aproximaciones para la resolución de la interacción de ondas de tsunami, representadas con ondas solitarias, con bosques de manglares, aproximados a su vez por cilindros rígidos. La primera aproximación se basa en la simulación directa de la interacción del flujo con los cilindros, introduciendo la geometría de los mismos en el dominio. El modelo utilizado es IHFOAM que resuelve las ecuaciones de Navier Stokes tridimensionalmente. Para la modelización de la turbulencia se utiliza un modelo κ – ω SST. La segunda aproximación se lleva a cabo considerando una escala mayor en la que el campo de vegetación se introduce disminuyendo la cantidad de movimiento en la zona ocupada por los cilindros, mediante una fuerza de arrastre y una fuerza de inercia de la forma:

$$\frac{\partial \langle \bar{u}_i \rangle}{\partial x_i} = 0 \quad (38)$$

$$\frac{\partial \rho \langle \bar{u}_i \rangle}{\partial t} + \langle \bar{u}_j \rangle \frac{\partial \rho \langle \bar{u}_i \rangle}{\partial x_j} - \frac{\partial}{\partial x_j}\left(\langle \mu_{eff} \rangle \frac{\partial \langle \bar{u}_i \rangle}{\partial x_j} \right) = \frac{\partial \langle p^* \rangle}{\partial x_i} - g_i x_j \frac{\partial \langle \rho \rangle}{\partial x_j} - \overline{F_{D,\,i}} - \overline{F_{I,\,i}} \quad (39)$$

donde ρ es la densidad calculada como $\rho = \alpha \rho_{water} + (1-\alpha)\rho_{air}$, α es una función del modelo IHFOAM utilizada para resolver la interfaz entre las dos fases del modelo, ρ_{water} es la densidad del agua y ρ_{air} la del aire. p^* es la presión pseudo-dinámica, x_i el vector de posición, $\bar{u}_i$ son las componentes de velocidad del flujo, g_i la aceleración de la gravedad y μ_{eff} la viscosidad dinámica efectiva que tiene en cuenta la viscosidad molecular y los efectos turbulentos. Los corchetes implican promediación en el volumen. $\overline{F_{D,\,i}}$ es la fuerza de arrastre y $\overline{F_{I,\,i}}$ la de inercia, expresadas como:

$$\overline{F_{D,\,i}} = \frac{1}{2}\langle \rho \rangle C_D a N \langle \bar{u}_i \rangle |\langle \bar{u}_i \rangle| \quad (40)$$

$$\overline{F_{I,\,i}} = \langle\rho\rangle C_M \frac{\pi a^2}{4} N \frac{\partial\langle\bar{u}_i\rangle}{\partial t} \tag{41}$$

donde a es el ancho de los elementos, C_D el coeficiente de arrastre, N el número de elementos por unidad de área y C_M el coeficiente de inercia. Tras un análisis de sensibilidad realizado para ver la influencia de la fuerza de arrastre y la de inercia se puede considerar que la segunda es despreciable (Figura 7.2).

El modelo de turbulencia utilizado en esta segunda aproximación es un modelo k-ε modificado que tienen en cuenta un término adicional en la ecuación de producción turbulenta y uno en la ecuación de disipación turbulenta. Este modelo es el mismo que el presentado en el capítulo 3.

Ambas aproximaciones se validan utilizando los ensayos de laboratorio presentados por Huang et al. (2011). En ambos casos la reproducción de la superficie libre es adecuada (Figura 7.3, 7.4 y 7.9). Sin embargo, los tiempos de computación asociados son muy diferentes. En la primera aproximación, tras un análisis de sensibilidad de la malla, se recurre a una discretización mucho menor que en la segunda aproximación ya que es necesario reproducir la geometría de los cilindros. Esto conlleva un mayor coste computacional aunque por otro lado permite evaluar el flujo producido entre los distintos elementos, aspecto que no es posible con la segunda aproximación.

Por lo tanto, la segunda aproximación supone una herramienta muy útil para el estudio de la evolución de la superficie libre a lo largo de un campo de vegetación con un bajo coste computacional. La primera aproximación, sin embargo, nos permite evaluar más variables al margen a la superficie libre. Una de estas variables es la fuerza ejercida sobre los diferentes cilindros que forman el campo. Dado que el modelo permite introducir la geometría de los distintos cilindros, se plantea el estudio de la influencia de la distribución espacial de los mismos. Para ello, se toman como base las distribuciones (A, B y C) ensayadas por Huang et al. (2011) (Figura 7.1) que constan de 2228, 1108 y 560 cilindros, respectivamente, distribuidos en una longitud de 0.545 m y un ancho del mismo valor. El campo de velocidades experimentado por una onda solitaria de H = 0.10 m sobre un calado de h = 0.15 m se muestra en la Figura 0.17 para las tres configuraciones.

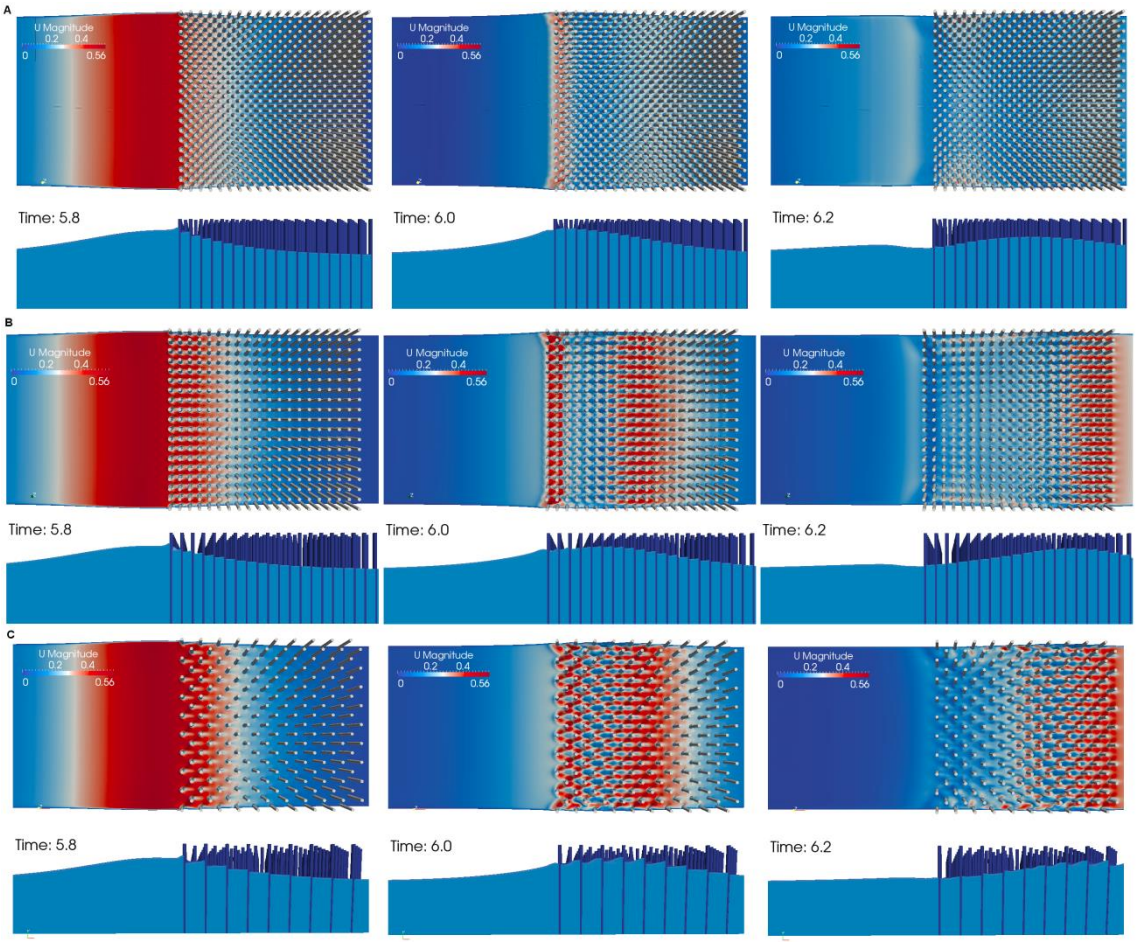

Figura 0.17 Campo de velocidad y superficie libre para tres pasos de tiempo y las tres configuraciones, A (panel superior), B (panel intermedio) y C (panel inferior).

Los campos de velocidad mostrados en la Figura 0.17 reflejan la atenuación producida a lo largo del campo. Asimismo, se puede observar como el flujo se canaliza entre las filas de cilindros para la configuración B en la que los cilindros forman una cuadrícula. Tomando estas densidades y dimensiones del campo, y estableciendo una distancia mínima entre cilindros igual a la mitad del diámetro de los mismos, se crean las distribuciones aleatorias mostradas en la Figura 0.18.

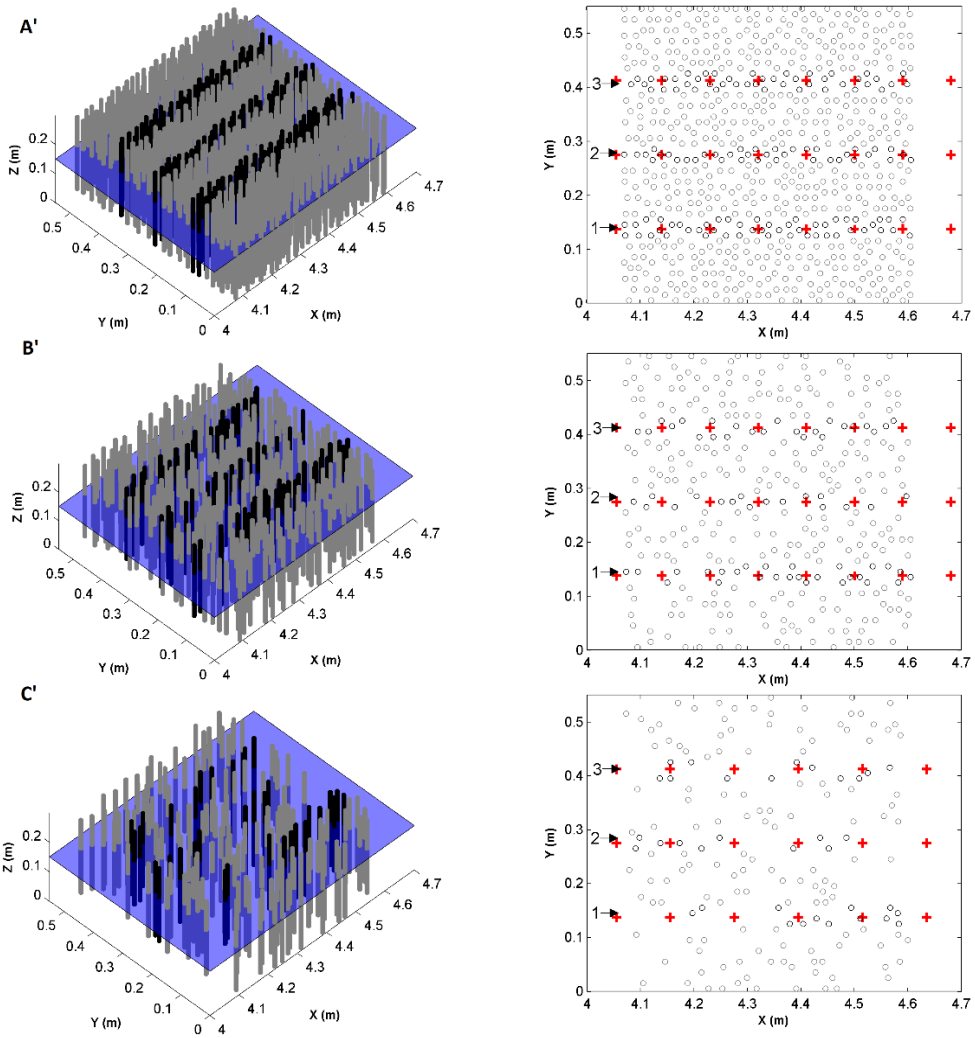

Figura 0.18 Distribuciones aleatorias A', B' y C'. Los cilindros dentro de las secciones de control se marcan en color negro.

La evolución de la altura de ola obtenida para las configuraciones uniformes en el centro del campo, se comparan con la evolución obtenida en las tres secciones de control seleccionadas en las configuraciones aleatorias localizadas en el centro del campo, y a un tercio y dos tercios del mismo. Los puntos en los que se evalúa la altura de ola para las secciones aleatorias se muestran en la Figura 0.18 con cruces rojas. Los resultados de evolución de altura de ola relativa (H / H_I), a lo largo del campo para los diferentes casos de muestran en la Figura 0.19.

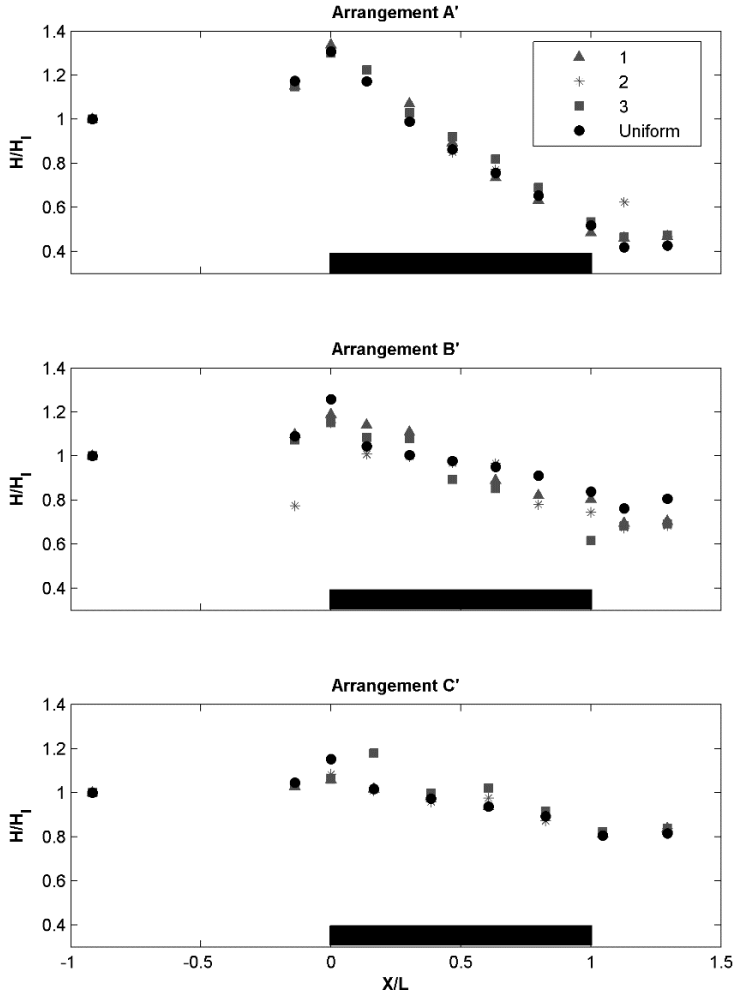

Figura 0.19 Evolución de la altura de ola relativa para las configuraciones uniformas (puntos negros) y las tres secciones de control (1, 2 y 3) de las configuraciones aleatorias (puntos grises).

La evolución de la altura de ola a lo largo del campo no se ve influenciada, en gran medida, por la distribución de los cilindros, como se muestra en la Figura 0.19. Asimismo, se comparan las fuerzas ejercidas sobre los cilindros de la fila central de las distribuciones uniformes y de las tres secciones de control de las distribuciones aleatorias. Los resultados de la fuerza máxima en cada cilindro, normalizada con la fuerza hidrostática ($\rho g(H_I + h)A_w$ donde A_w es el área mojada del cilindro), se muestran en la Figura 0.20.

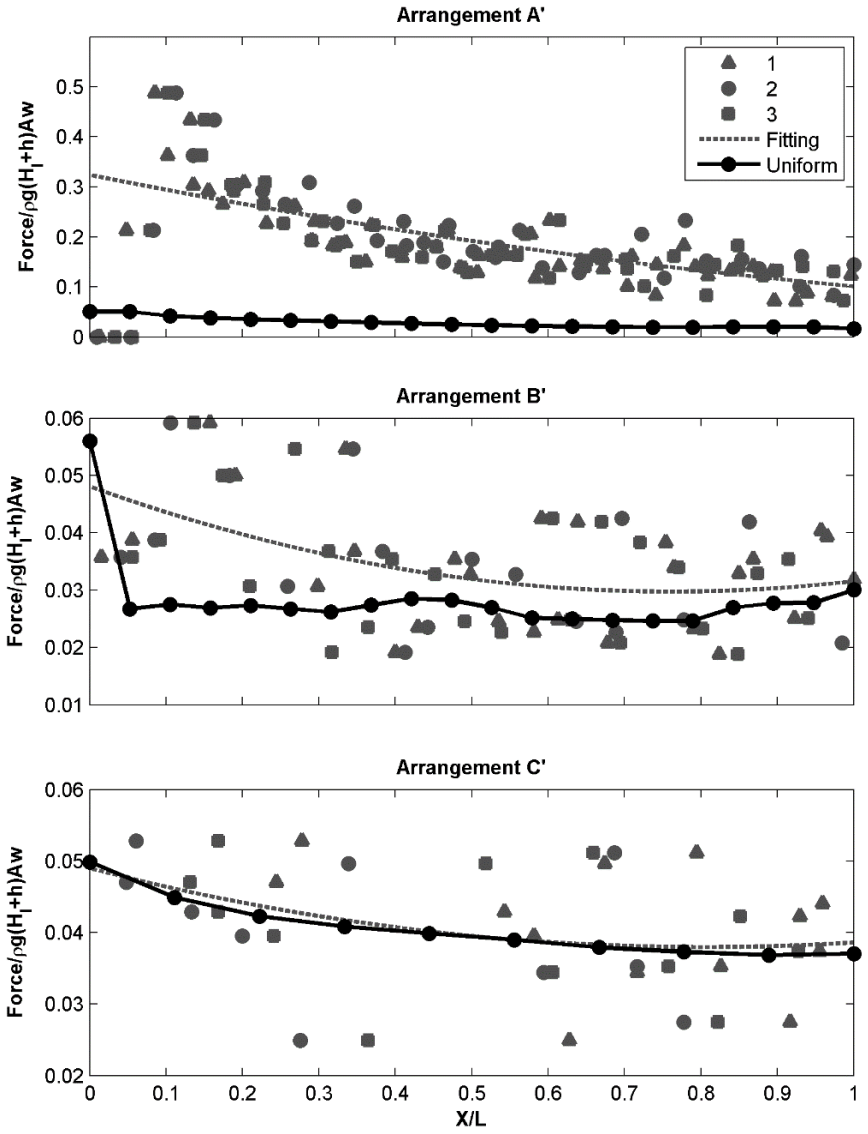

Figura 0.20 Máximas fuerzas normalizadas para las configuraciones uniformes (puntos negros) y las tres secciones de control (1, 2 y 3) de las configuraciones aleatorias (puntos grises).

A diferencia de lo observado en la evolución de la altura de ola, la distribución espacial de los cilindros tiene una gran influencia en las fuerzas ejercidas sobre los mismos. Lo mismo ocurre para los patrones de flujo, como se observa en la Figura 0.21, mediante los campos de velocidad representados en la superficie libre de las tres configuraciones aleatorias.

Por lo tanto, la distribución espacial de los distintos elementos que forman el campo de vegetación influye, en gran medida, en las fuerzas ejercidas sobre las plantas y los patrones de flujo desarrollados, mientras que no son tan relevantes en la evolución de la altura de ola a lo largo del campo.

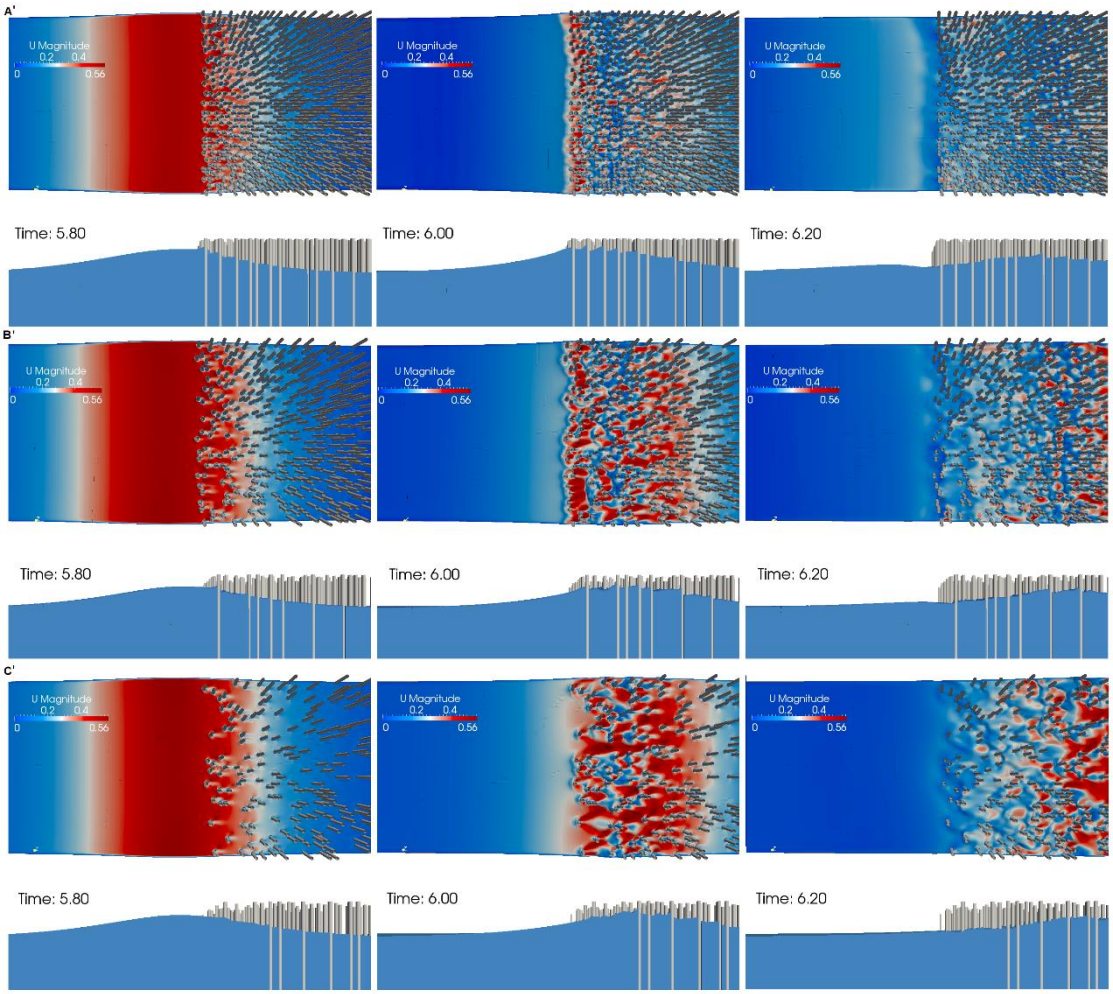

Figura 0.21 Campo de velocidad y superficie libre para tres pasos de tiempo y las tres configuraciones aleatorias, A' (panel superior), B' (panel intermedio) y C' (panel inferior).

En este capítulo se han presentado dos aproximaciones para resolver la interacción del flujo con elementos rígidos. Se ha demostrado que, el uso de una aproximación que parametrice el campo de elementos, permite reproducir la evolución de la superficie libre pero no permite resolver el flujo dentro del campo con exactitud. La aproximación que resuelve los distintos cilindros que forman el campo ha permitido evaluar la influencia de la distribución espacial de estos, revelando una gran influencia en los patrones de flujo desarrollados y las fuerzas ejercidas sobre los cilindros individuales.

0.8 Análisis experimental y numérico de la atenuación del oleaje producida por parches de vegetación

El capítulo 8 muestra el análisis experimental y numérico de los ensayos realizados para analizar la influencia de tener campos de vegetación no continuos. En estos ensayos se consideran tres configuraciones: la primera formada por un único parche de vegetación circular de 3 m de diámetro, la segunda formada por 8 parches circulares de 1 m de diámetro y la tercera por 4 de estos parches. Para la toma de medidas se utilizaron 29 sensores de superficie libre y 8 ADVs que se mantienen en la misma posición para las tres configuraciones de forma que los resultados obtenidos con ellas se pueden comparar directamente (Figura 8.2). La Figura 0.22 muestra una vista de las tres configuraciones donde se puede ver la estructura utilizada para colocar los sensores de superficie libre y un detalle de los ADVs.

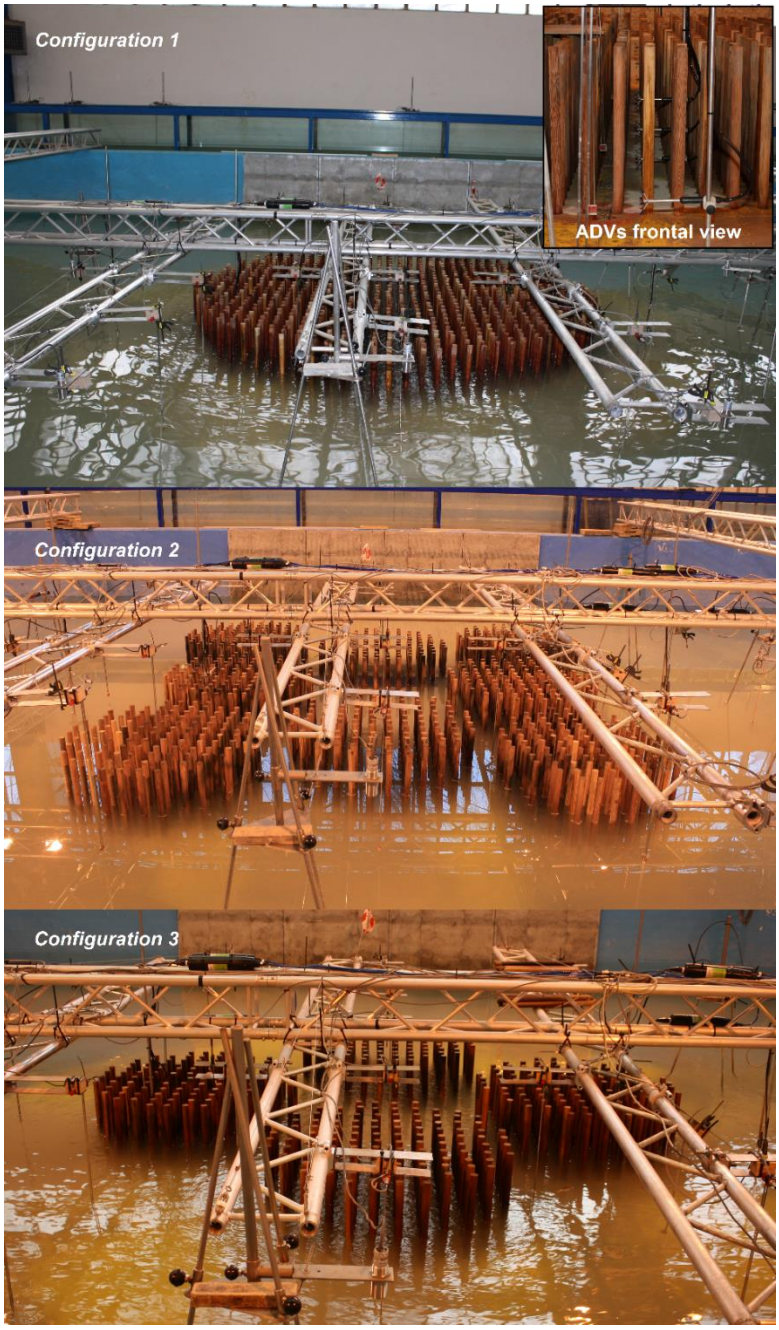

Figura 0.22 Vista de las tres configuraciones ensayadas. En la primera configuración se puede ver un detalle de los ADVs.

Para poder comparar estas tres configuraciones, se define un parámetro que tenga en cuenta el número de cilindros de cada una y su distribución, la longitud de campo equivalente, L_e. Esta longitud se define a partir de un campo de vegetación uniforme creado tomando el espaciamiento medio de los cilindros que forman las distintas configuraciones (en este caso dicho espaciamiento es constante, $s_0 = 9\ cm$) y con un área igual a 1 m^2. La porosidad de este

campo de referencia se define como $1 - \frac{A_C}{A_0}$, donde A_C es el área ocupada por los cilindros y A_0 el área del campo (1 m^2). Esta porosidad se relaciona con la de cada una de las configuraciones para así tener en cuenta la cantidad de área ocupada por la vegetación en cada una de ellas. Para ello, se considera el cuadrado envolvente de cada configuración (línea negra en la Figura 0.23). La porosidad se calculará como $1 - \frac{A_C}{A_E}$, donde A_E es el área del cuadrado envolvente para cada configuración. Con todas estas variables y considerando el número total de cilindros que forman cada configuración (N_C), la longitud de campo equivalente se define como:

$$L_e = s_0\sqrt{N_C}\frac{n_0}{n} \tag{42}$$

La Figura 0.23 muestra esta longitud para cada una de las configuraciones en línea punteada. Para la Configuración 1, $L_e = 2.62\,m$, y para las Configuraciones 2 y 3, $L_e = 2.61\,m$ y $1.8\,m$, respectivamente.

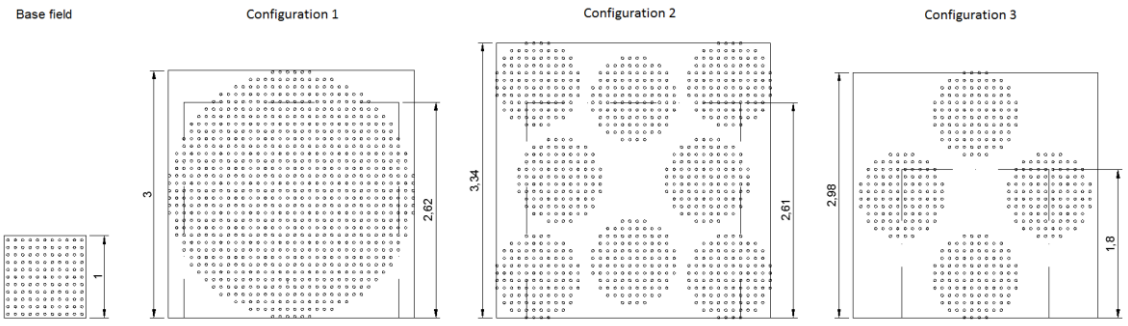

Figura 0.23 Campo de vegetación base (izquierda) y cuadrado envolvente (línea negra) y longitud equivalente (línea punteada) para cada una de las configuraciones.

Esta longitud equivalente se utiliza para poder comparar los resultados de las tres configuraciones. Los ensayos se realizan considerando distintos grados de sumergencia y varios tipos de ondas. En primer lugar, se consideran oleajes regulares. Para analizar la disipación producida por las distintas configuraciones se evalúa la disipación de la altura de ola producida en el eje central de cada uno de los campos, ajustando la formulación de Dalrymple et al. (1984) y obteniendo así el coeficiente de disipación β.

Los coeficientes de disipación de todos los casos se relacionan con distintos parámetros del campo y del oleaje. En primer lugar, se evalúa su relación con la altura de ola, obteniendo un mayor coeficiente para mayores alturas de ola (Figura 8.8). Posteriormente, se analiza su relación con el número de onda relativo que se modifica para establecer un parámetro que tenga en cuenta las características de las tres configuraciones. Para ello, se multiplica el número de onda por la longitud equivalente. Dado que el grado de sumergencia de un campo influye

fuertemente a la disipación producida, este nuevo número de onda relativo se multiplica por el grado de sumergencia, definido como el cociente entre la altura de la vegetación y el calado ($SR = h_v/h$). La Figura 0.24 muestra la relación entre los coeficientes de disipación y kL_eSR, encontrando mayores valores de disipacion para mayores kL_eSR que implican un menor periodo del oleaje, un campo más largo y una mayor parte de la columna de agua ocupada por la vegetación.

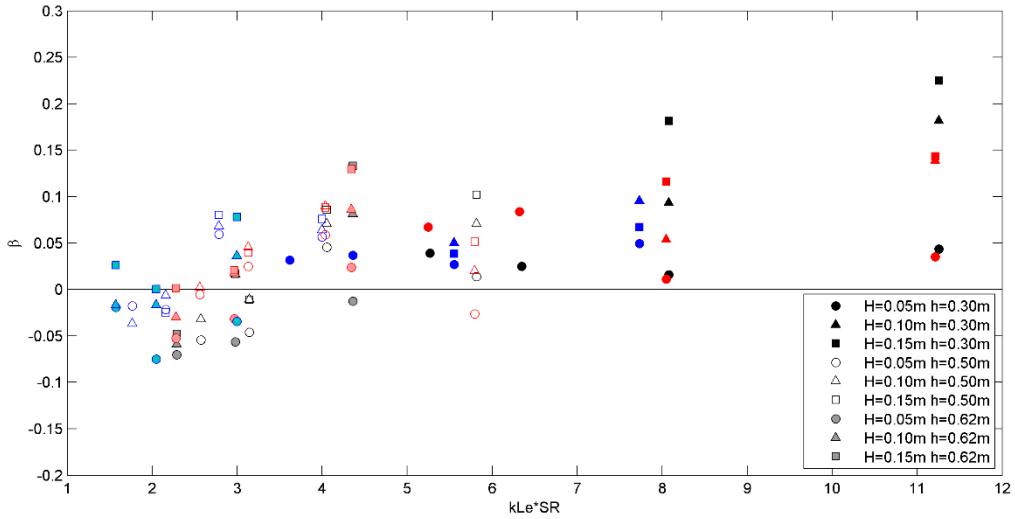

Figura 0.24 Coeficientes de disipación en función de kL_eSR para la Configuracion 1 (negro), Configuracion 2 (rojo) y Configuración 3 (azul). Las diferentes alturas de ola se muestran con distinto símbolo y los diferentes calados con distinta intensidad de color.

También se estudia la relación de los coeficientes de disipación con el número de Reynolds. Para ello se define un nuevo número de Reynolds que considera las propiedades del campo a través de la longitud característica seleccionada. Esta longitud se define como $L^* = Le\frac{h_v}{h} = LeSR$ y representa el área en la que la vegetación afecta al flujo, por unidad de longitud. Por lo tanto, el nuevo número de Reynolds, llamado número de Reynolds del campo equivalente, se define como:

$$Re_s^{Le} = \frac{L^* V_c}{\upsilon} \tag{43}$$

La Figura 0.25 muestra la relación entre los coeficientes de disipación y este nuevo número de Reynolds mostrando un aumento del coeficiente de disipación con Re_s^{Le}.

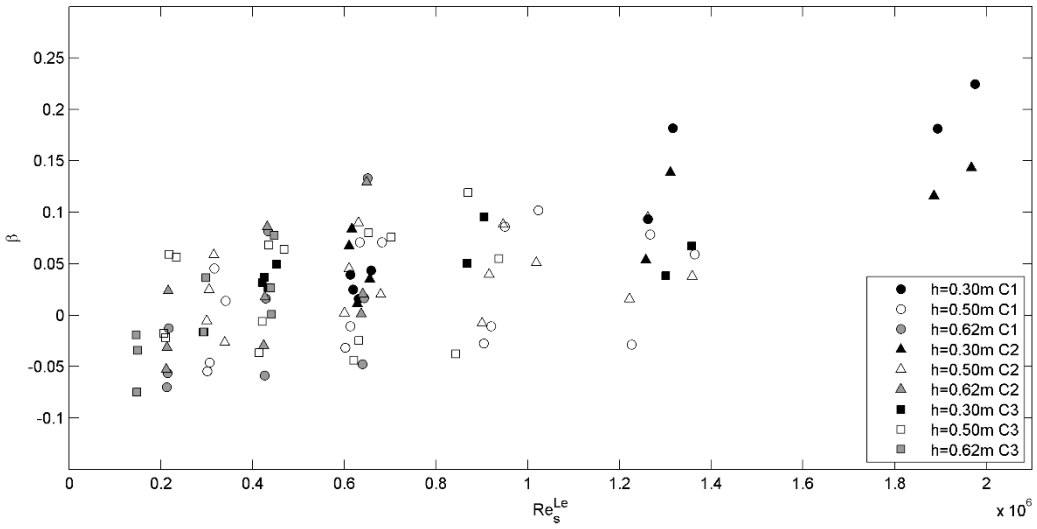

Figura 0.25 Coeficientes de disipación en funciones del Re_s^{Le}.

En los ensayos también se generan diferentes condiciones de oleaje irregular. Para caracterizar la disipación producida bajo estas condiciones, se realiza un análisis basado en la energía del espectro del oleaje. Asumiendo teoría lineal, la evolución de un oleaje irregular a lo largo de un campo de vegetación se puede expresar en términos de balance de energía como (Jadhav et al., 2013):

$$\frac{\Delta\left(E_{S,j}C_{g,j}\right)}{\Delta X} = -S_{d,j} \tag{44}$$

donde j representa la componente de frecuencia jth del espectro de oleaje, E es la densidad de energía espectral, C_g es la celeridad de grupo calculada como $C_g = nc = (1/2)[1 + (2kh/sinh2kh)]\sqrt{(g/k)tanh(kh)}$, X es la coordenada a lo largo del campo y S_d es la disipación de energía debida a la vegetación. La cantidad total de disipación de energía se obtiene integrando la disipación obtenida para cada frecuencia en el rango de frecuencias del espectro. La energía incidente se calcula como el momento de orden cero, $m0$, en el sensor que se encuentra offshore del campo.

El cálculo de la energía disipada se realiza considerando un conjunto de bandas de frecuencia de anchura $f_p/4$ donde f_p es la frecuencia de pico. La celeridad de grupo se calcula considerando la frecuencia central de cada banda. La Figura 0.26 muestra la disipación obtenida para un caso de H_s=0.10 m y T_p=2s, para las tres profundidades ensayadas (h = 0.30, 0.50 y 0.62 m) y las tres configuraciones de cilindros. Los resultados se muestran en términos de altura de ola media cuadrática, H_{rms}.

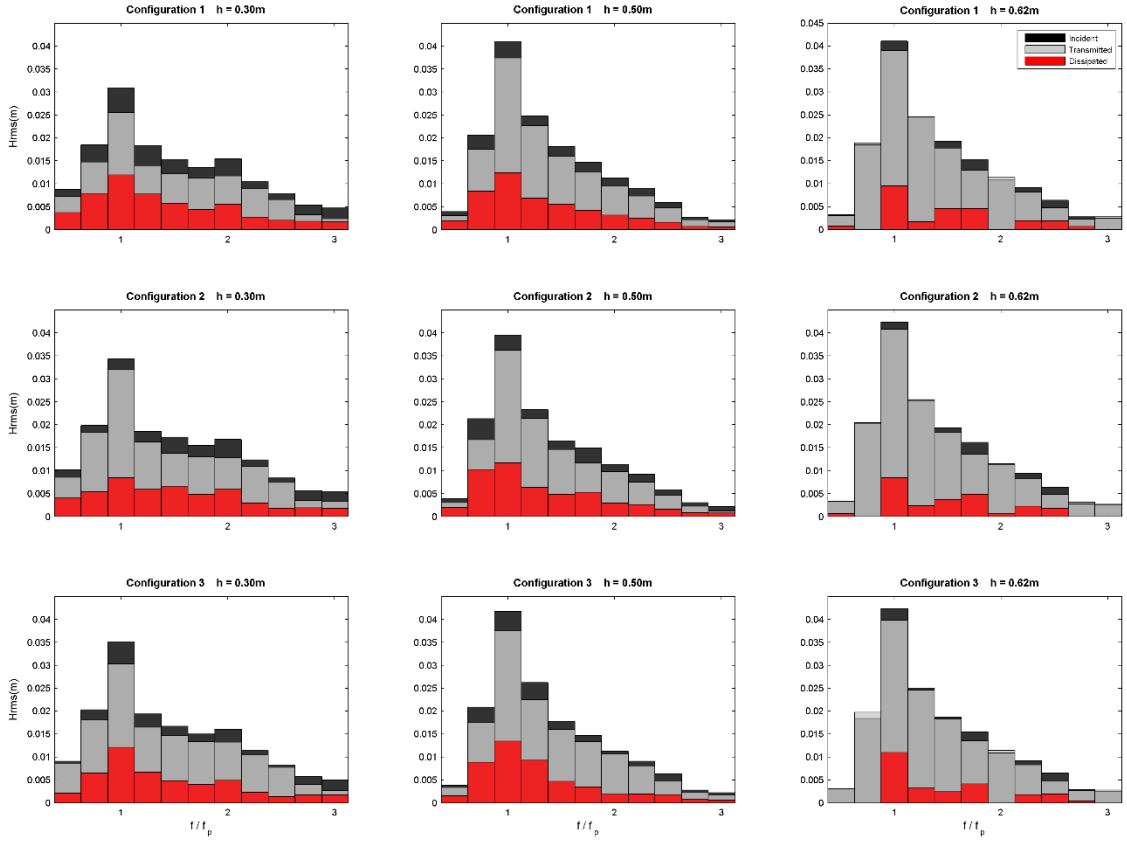

Figura 0.26 Espectros de oleaje (Hs = 0.10 m y Tp = 2 s) para los tres calados y las tres configuraciones.

Los valores de disipación obtenidos se representan en la Figura 0.27 normalizados, utilizando la energía incidente y en función del nuevo número de Reynolds, Re_s^{Le}. Al igual que para oleajes regulares la disipación aumenta para valores de Re_s^{Le} mayores.

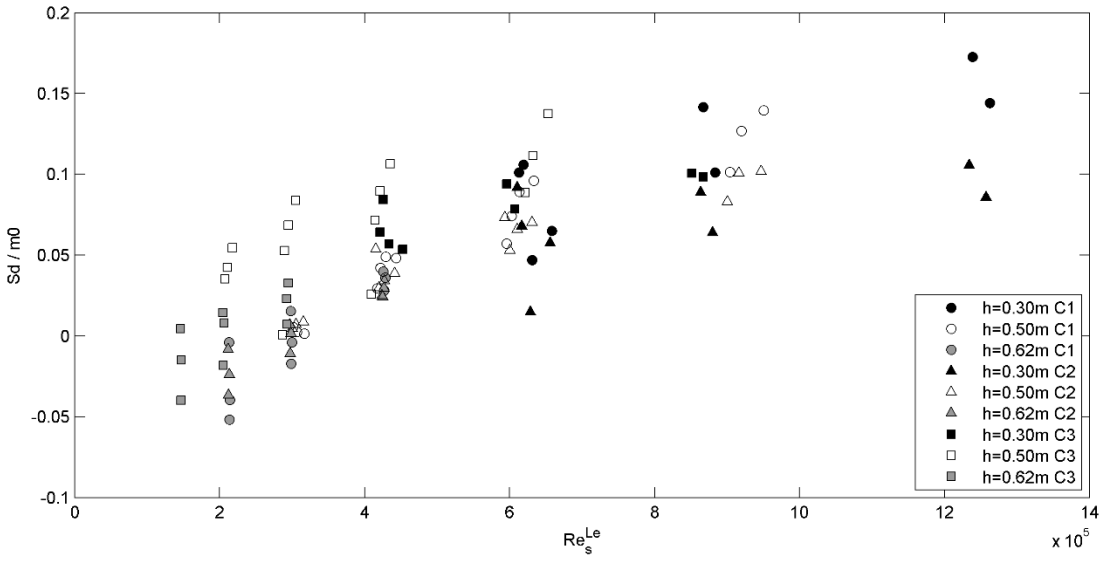

Figura 0.27 Disipación de energía de los oleajes irregulares en función de Re_s^{Le}.

En los ensayos también se consideran ondas solitarias. Los coeficientes de atenuación para estas ondas se obtienen, como para el caso de los oleajes regulares, en función de la evolución de la altura de ola a lo largo del campo. De nuevo se estudia la relación entre los coeficientes obtenidos y kL_eSR. La Figura 0.28 muestra la relación lineal que se da entre las dos variables para las ondas solitarias.

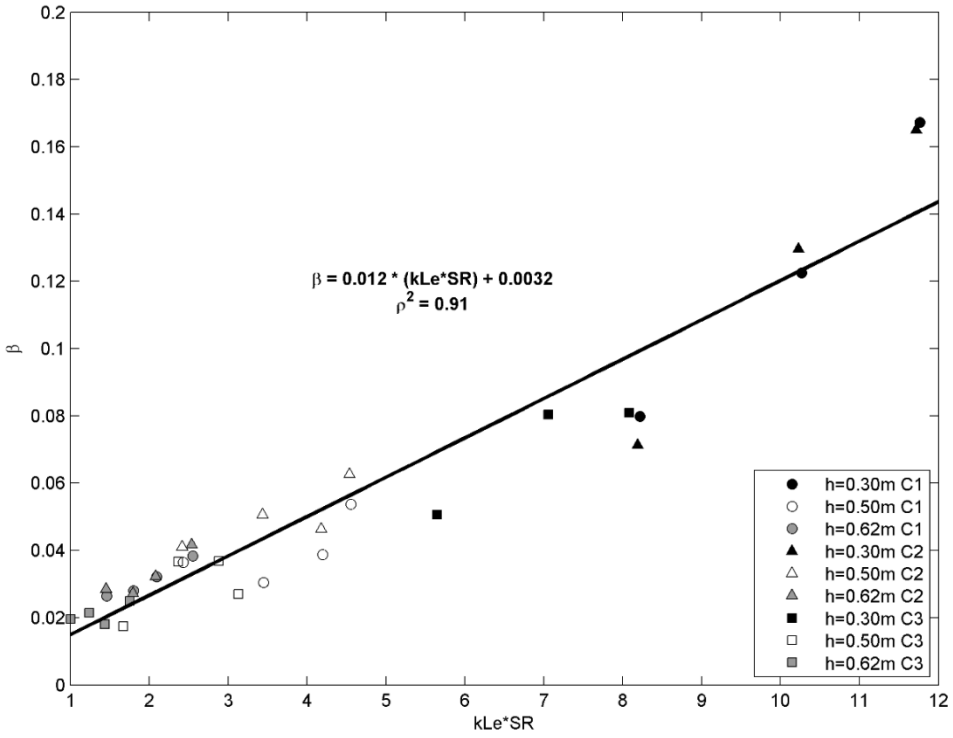

Figura 0.28 Coeficientes de disipación en función de kL_eSR para la Configuración 1 (círculos), Configuración 2 (triángulos) y Configuración 3 (cuadrados) y distintos calados.

Asimismo, se estudia la relación con el nuevo número de Reynolds. La Figura 0.29 muestra la relación entre los coeficientes de disipación y el número de Reynolds clásico, Re, obtenido considerando el ancho de los cilindros y la relación existente con el nuevo número de Reynolds Re_s^{Le}. Los ajustes mostrados en la Figura 0.29 muestran una mejor correlación entre los coeficientes de disipación y Re_s^{Le} en comparación con la obtenida para Re expresado de forma tradicional.

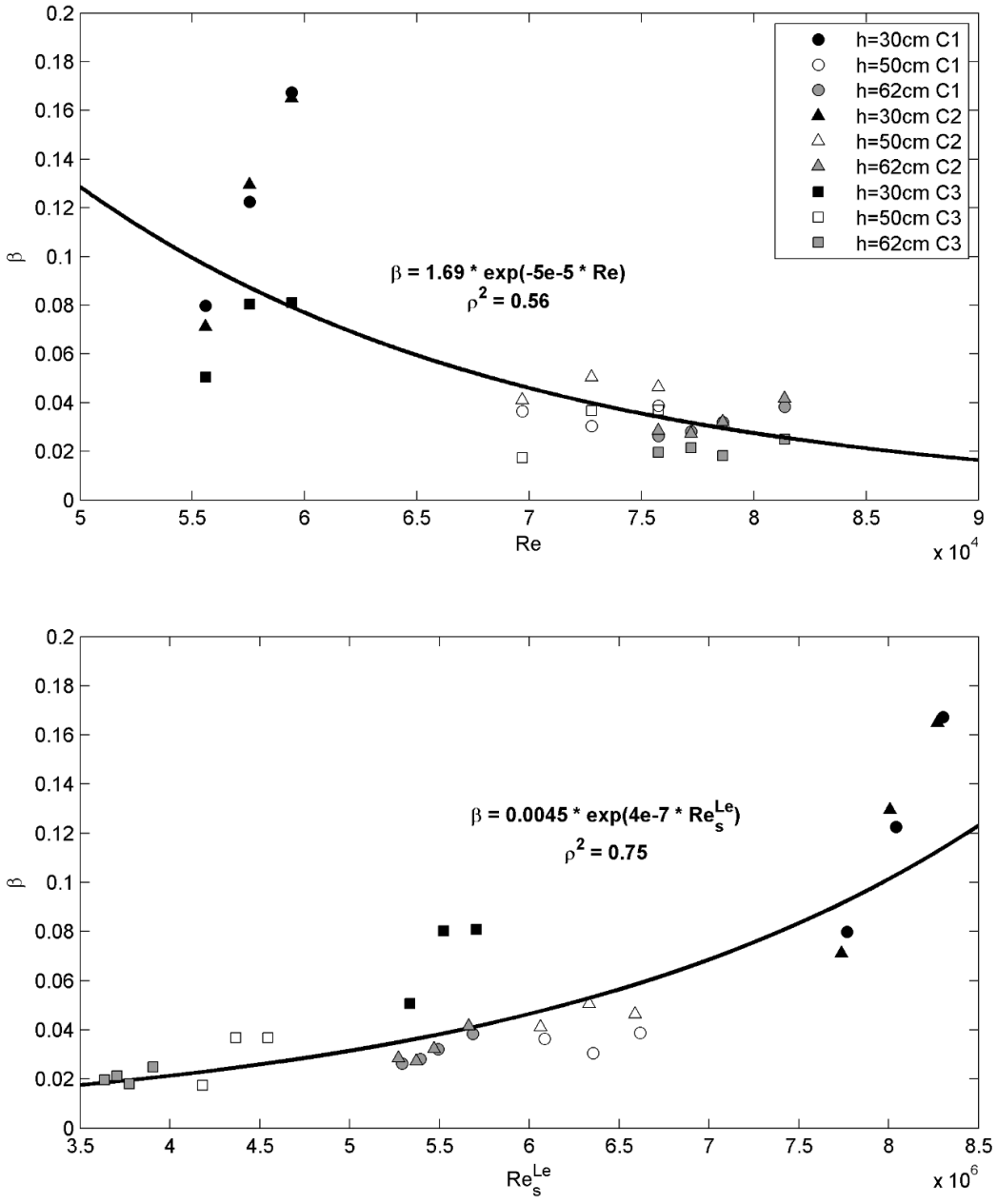

Figura 0.29 Coeficientes de disipación en función de Re (panel superior) y Re_s^{Le} (panel inferior).

Para extender el análisis de los resultados obtenidos en el laboratorio, el modelo numérico descrito en el capítulo 7 se utiliza para simular estos casos de laboratorio. En primer lugar, se valida el modelo con las medidas de superficie libre y velocidad del laboratorio (Figures 8.26 y 8.28). Una vez obtenido un buen acuerdo entre los resultados numéricos y de laboratorio se realizan las simulaciones considerando las geometrías de las tres configuraciones de cilindros ensayadas. La Figura 0.30 muestra un ejemplo de los resultados de fuerzas obtenidos para la Configuración 2. La mitad superior muestra los valores de las fuerzas máximas en cada cilindro,

normalizadas con la fuerza hidrostática. En la parte inferior se muestran las flechas que definen la dirección de estas fuerzas.

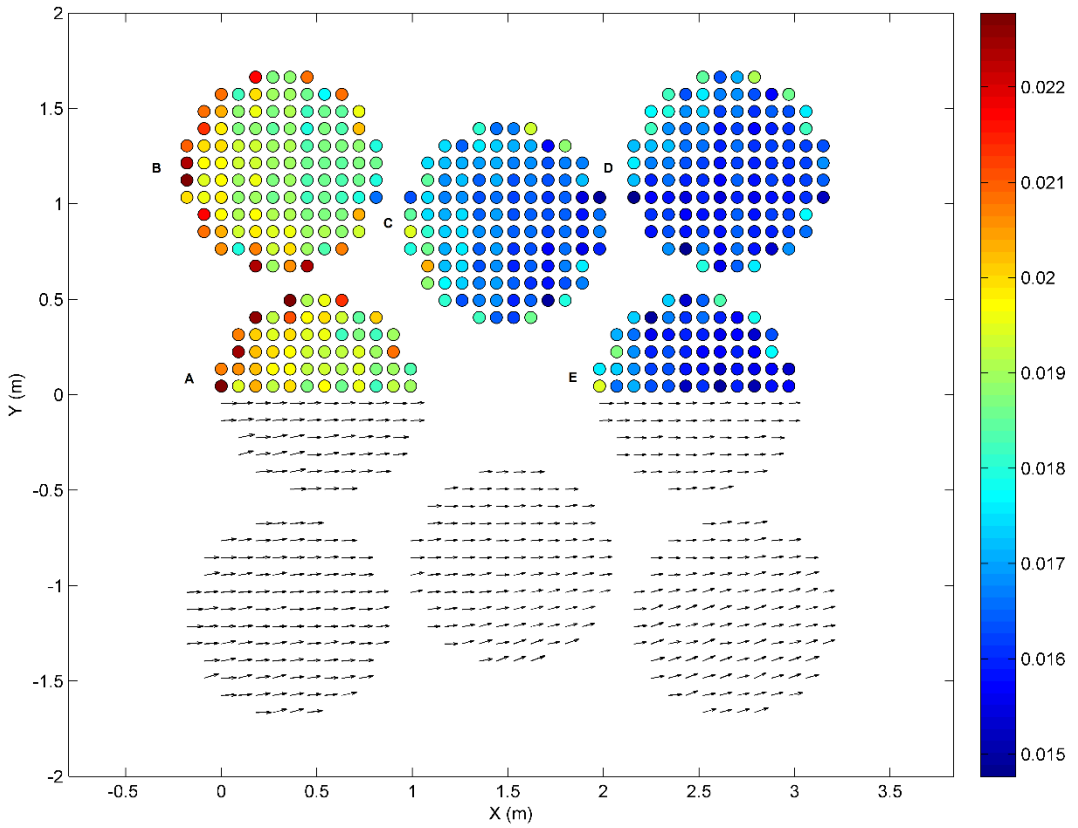

Figura 0.30 Fuerza máxima normalizada sobre cada cilindro (barra de color) para la Configuración 2 (mitad superior) y flechas direccionales de las fuerzas máximas (mitad inferior).

Los valores de las fuerzas máximas permiten ver qué cilindros sufren las mayores fuerzas. Estos cilindros son los que se encuentran en las primeras filas de los parches A y B y que tienen a ambos lados otros cilindros. Asimismo, se puede observar, que se produce una concentración de flujo entre los cilindros A y B, dado el mayor valor de las fuerzas experimentado por los cilindros que se encuentran en torno a esa zona.

Por lo tanto, el capítulo 8 presenta el análisis de los datos experimentales de los ensayos realizados para estudiar la influencia de la distribución espacial del campo. Se ha presentado un nuevo parámetro para definir estas características del campo y se ha estudiado su efecto y el de los parámetros del flujo en la disipación de energía. Finalmente, las simulaciones numéricas realizadas permiten extender el análisis obteniéndose e las fuerzas sobre los cilindros.

0.9 Conclusiones y futuras líneas de trabajo

En el primer capítulo de la tesis se puso de manifiesto la necesidad de mejorar el conocimiento de la interacción del flujo con la vegetación costera para poder cuantificar y caracterizar la protección del litoral proporcionada por estos ecosistemas. Para poder mejorar ese conocimiento, se marcaron un conjunto de objetivos como punto de partida, que engloban el uso de diferentes métodos de análisis y cuantificación de los procesos físicos a estudiar. Los objetivos a desarrollar en esta tesis fueron: análisis de la influencia de la flexibilidad de la vegetación en la atenuación del oleaje; cuantificación de la protección costera proporcionada por vegetación real de marisma; desarrollo de un modelo semi-empírico para la cuantificación de la disipación de energía producida por la vegetación bajo condiciones combinadas de oleaje y corriente; desarrollo de un modelo numérico de alta resolución para la caracterización de la disipación producida por vegetación rígida emergida bajo la acción del oleaje y la estimación de los esfuerzos de este en las plantas; y análisis de las características del campo de vegetación en la protección proporcionada por este.

A lo largo de los distintos capítulos presentados en esta tesis se ha pretendido cubrir los diferentes objetivos realizando en primer lugar una revisión del estado del arte de cada una de las temáticas específicas abordadas en cada capítulo para establecer cuáles eran los aspectos a cubrir y el punto de partida del trabajo a desarrollar.

0.9.1 Conclusiones

En el desarrollo de la tesis se han obtenido varios resultados relevantes que se presentan de forma resumida a continuación:

Modelo bidimensional para vegetación flexible: a nuestro entender, es la primera vez que se ha desarrollado un modelo RANS que resuelve el movimiento acoplado entre flujo del oleaje y la vegetación. El modelo permite estimar la velocidad relativa producida en dicho movimiento y la velocidad del flujo del oleaje, para así caracterizar de una manera más precisa la perdida de energía que produce la vegetación. La velocidad relativa se utiliza así mismo para desarrollar un nuevo modelo de turbulencia para vegetación basado en el modelo κ-ε. Además se ha presentado una ecuación de coeficiente de arrastre para casos en los que se considera el movimiento de la vegetación, que amplía el espectro de aplicación de las existentes en la literatura, cubriendo un rango de números de Reynolds mayor.

Recomendaciones para el modelado físico de vegetación real: se han presentado un conjunto de recomendaciones a tener en cuenta para la realización de ensayos físicos con vegetación real. Estas directrices se han obtenido basadas en la experiencia adquirida en la realización de los

primeros ensayos a gran escala con vegetación real de marisma bajo condiciones de oleaje y corriente.

Cuantificación de la protección costera proporcionada por vegetación de marisma: los primeros ensayos a gran escala desarrollados con vegetación real y condiciones de flujo de ola y corriente han dado lugar a una base de datos experimentales que permite estudiar la influencia de los parámetros de la vegetación y del flujo en la disipación de energía. Algunos de los aspectos más relevantes obtenidos en el análisis de estos datos experimentales son: se ha encontrado una relación logarítmica entre el coeficiente de disipación y el calado; la disipación de energía aumenta para corriente en contra de la propagación del oleaje y aumenta cuando la corriente fluye en el mismo sentido que las olas; los ensayos realizados con incidencia oblicua entre olas y corriente dan lugar a menores tasas de disipación; y la biomasa de la vegetación influye fuertemente la disipación de energía, observándose una relación lineal entre ambos parámetros.

Modelo semi-empírico de atenuación de energía bajo condiciones de ola-corriente: se presenta una nueva formulación de atenuación de energía producida por la vegetación para condiciones de oleaje y corriente. Es la primera vez que la formulación se realiza considerando condiciones de corriente a favor y en contra de la propagación del oleaje. Además se obtiene una formulación para oleaje regular y una para irregular. Estas formulaciones se aplican a los ensayos realizados con vegetación real para obtener, a partir de los coeficientes de disipación medidos, unas nuevas formulaciones de arrastre para condiciones de oleaje y corriente.

Modelo numérico avanzado para la interacción de flujo con elementos rígidos: es la primera vez que se presentan dos aproximaciones tridimensionales basadas en las ecuaciones de Navier-Stokes para resolver en detalle la interacción del flujo con elementos rígidos. La primera aproximación permite evaluar la disipación de energía producida por el campo, el flujo entre los distintos elementos y la fuerza ejercida sobre los mismos considerando un modelo de turbulencia κ-ω SST. La segunda aproximación reproduce el campo mediante una fuerza de arrastre que induce pérdida de momento en la zona vegetada un modelo de turbulencia κ-ε modificado. Esta segunda aproximación permite obtener la evolución de la superficie libre a lo largo del campo con un menor coste computacional.

Análisis de la distribución espacial de las plantas: el modelo tridimensional desarrollado para resolver la interacción de flujo con elementos rígidos se aplica a distribuciones uniformes y distribuciones aleatorias de cilindros. El análisis de dichas simulaciones numéricas muestra que la atenuación de la altura de ola a lo largo del campo no se ve fuertemente influenciada por la disposición de los cilindros. En cambio, si que existe una gran influencia en las fuerzas ejercidos sobre ellos debido a los diferentes patrones de flujo obtenidos.

Análisis de las características macro-escala de los campos de vegetación: se presentan unos nuevos ensayos en los que se ensayan por primera vez tres configuraciones de campo bajo las mismas condiciones de flujo para posteriormente compararlas. Para realizar esta comparación se propone un nuevo número, llamado longitud equivalente, que parametriza las características de la distribución espacial de los distintos parches de vegetación considerados en las distintas configuraciones. Este número permite encontrar una única relación para las tres configuraciones entre los parámetros del oleaje y la disipación de energía. Así se obtiene una mayor tasa de disipación para mayores valores del producto del número de onda, el grado de sumergencia y la longitud equivalente y lo mismo ocurre para mayores números de Reynolds calculados considerando la longitud equivalente. Además las simulaciones numéricas realizadas reproduciendo los ensayos de laboratorio muestran la gran influencia que tienen sobre las fuerzas ejercidas sobre los elementos la disposición de los parches de vegetación.

0.9.2 Futuras líneas de trabajo

Una vez satisfechos parte de los objetivos planteados se presentan las siguientes futuras líneas de investigación:

- Análisis mecánico de la interacción de flujo con vegetación flexible considerando un modelo de grandes deformaciones.

- Modelado numérico para la resolución de la interacción de vegetación con condiciones combinadas de oleaje y corriente.

- Representación de la geometría real de los manglares y estudio de su influencia en el estudio de la protección costera.

- Patrones de flujo y transporte de sedimentos alrededor de campos de vegetación no uniformes espacialmente.

Algunas de estas líneas ya han comenzado a desarrollarse como se detalla en el capítulo 9 de la presente tesis.

UNIVERSIDAD DE CANTABRIA

E.T.S. DE INGENIEROS DE CAMINOS, CANALES Y PUERTOS

Departamento de Ciencias y Técnicas del Agua y del Medio Ambiente

---

Doctor of Philosophy Degree

Dissertation

Experimental and numerical modelling of flow interaction with natural ecosystems for coastal protection

---

Presentada por: **MARIA EMILIA MAZA FERNANDEZ**

Dirigida por: **ÍÑIGO J. LOSADA RODRÍGUEZ**
JAVIER LÓPEZ LARA

Santander, Enero 2015

"We ourselves feel that what we are doing is just a drop in the ocean. But the ocean would be less because of that missing drop"

Teresa de Calcuta

1

INTRODUCTION AND MOTIVATION

Coastal regions around the world are changing due to their continuous socioeconomic development and climate change, leading to an increased risk of environmental and socioeconomic damages. Millions of people are yearly affected by flooding and erosion and extreme meteorological events while sectors such as industry or tourism are suffering important economic losses. The last IPCC Assessment Report, AR5 (Wong et al., 2014), reveals an increased risk of flooding and erosion in coastal areas due to the continuous increase in exposure and vulnerability with important consequences to human lives and property. New risk management and adaptation measures are needed to reduce the effects of climate change and extreme events. If appropriate measures are not to be adopted, damages associated with global coastal areas flooding will yield to economic losses that can reach one billion euros per year (Hallegatte et al., 2013). During the last decades, millions of euros have been spent on reducing consequences of extreme event and to a lesser extent on climate change adaptation in coastal areas. Most of these funds have been devoted to the implementation of traditional engineering measures, so-called "grey infrastructures". However, after hurricane Katrina (2005) or Sandy (2012) or the tsunami in Indonesia (2004), coastal managers have become interested in

alternative low environmental impact solutions or nature based solutions. Hence, knowledge about the reduction of flooding and erosion risks using low environmental impact structures, “green structures”, is currently of great interest.

As a consequence, one stream of thinking has been oriented towards the quantification of the role played by natural coastal systems in coastal protection. Decades of research on how coastal vegetation can play a role on coastal protection suggests that these natural solutions have the capability of dissipating energy from waves and currents (Chapman, V.J., 1974; Gedan et al., 2010; Borsje et al., 2011). Furthermore, these ecosystems provide services with high ecological and economic values (Constanza et al., 1997) which in part are related to their capacity to dissipate hydrodynamic energy (Millenium Ecosystem assessment; United Nations 2005; Nagelkerken, 2000; Valentine and Heck, 1999). Therefore, coastal vegetation ecosystems serve a triple function: they contribute to disaster risk reduction from extreme events, promotes climate change adaptation and finally mitigate its effects, the latter thanks to its ability to capture CO2 (Duarte et al. 2013). All these benefits provided by natural ecosystems has motivate in the last years the use of natural-base solutions to address both adaptation and risk reduction. As an example we can cite solutions taken in the Netherlands (http://www.ecoshape.nl/en_GB/delfland-sand-engine.html) or the Global Restoration Network project of the Society for ecological restoration international (http://www.globalrestorationnetwork.org/ecosystems/coastal/estuaries-marshes-mangroves/case-studies/). Despite this, coastal ecosystems have not yet been considered firmly as part of the portfolio of climate change mitigation and coastal protection options, and artificial measures are still preferred. This is mainly due to the complexity of understanding and quantifying flow-vegetation interaction.

The interaction of flow conditions with coastal ecosystems constitute a problem that involves processes at different spatial and temporal scales. The problem starts from the small scale when flow interacts with individual plants inducing processes such as plant movement, flow separation or turbulence. These processes dominate others at larger scales such as energy dissipation provided by the vegetation field or the sediment transport around it. A proper understanding of small scale processes leads to parametrizations and formulations that allow quantifying the coastal protection provided by vegetation. However, all these processes are very complex and the high variety of vegetation species and flow conditions that can be involved in the problem increases the problematic.

Regarding vegetation, a large number of species is found in coastal ecosystems. Vegetation can cover a wide range of the coastal profile. Vegetation such as seagrasses or macro algae develops at intermediate – deep waters while salt marshes cover the intertidal areas in temperate zones

and mangroves grow in the same ecological niche in the tropics. These vegetation species present completely different biomechanical properties that determine their behavior under flow action (Paul et al., 2012). We can found very flexible vegetation with small Young modulus and small cross-sections and also rigid plants with large trunks. The structure of the different species is also highly diverse. Plants can be formed by simple shoots with an almost constant cross-section along their length, to complex geometries that involving different structures with diverse forms, sizes and flexibilities. Not only plant properties are important in terms of coastal protection. The field vegetation properties are also determinant. Plant growing is not uniform and homogeneous; it is influenced by many factors such as flow action or substratum characteristics. This leads to many different vegetation densities and spatial distributions. Consequently, the characterization of plants and vegetation fields is not an easy task but it is extremely important when studying coastal vegetation capacity to dissipate flow energy.

Several studies have been conducted working with simplified plant mimics (Augustin et al., 2009; Anderson and Smith, 2014) designed attending to dimensional parameters such as the Cauchy number (Ghisalberti and Nepf, 2002). However, the mechanical replication of plant characteristics has fundamental limitations and plant morphology is often simplified. The simulation of vegetation fields have been classically performed considering uniform and continuous plant distributions (Stratigaki et al. 2011; Huang et al., 2011). These simplifications have been made due to aspects such as the lack of standard measurements of plant properties (e.g.: flexibility, buoyancy, spatial distribution) or plant geometry for complex geometries like those of mangroves. In addition, some difficulties can be found in the selection of the appropriate material to recreate plan biomechanical properties or reproducing the exact geometry of complex plants. Another interesting option when studying vegetation attenuation capacity is the use of real plants (Bouma et al., 2005; Fonseca et al., 2006). However, only a few studies (Bouma et al., 2010) have been conducted with real vegetation since that entails having a sufficient number of plants that must be grown or collected with the corresponding time and costs. Furthermore, working with living plants is a sensitive task since plants must keep their properties while testing is taken place. Therefore, a better characterization and parametrization of the different vegetation species that can be used to protect the coast is necessary. That will be useful to develop models that allow quantifying coastal protection capacity of different vegetation species.

The importance of flow characteristics on the protection that coastal ecosystems can provide is also determining. Since coastal ecosystems develop in different coastal regions, they are affected by different complex hydrodynamic forcings. Vegetation ecosystems can be affected by very different wave regimens with varying wave heights and periods. These waves are transformed along their onshore propagation and highly nonlinear processes, such as wave

breaking, can be induced. These nonlinearities increase when waves interact with vegetation fields and wave dissipation is produced jointly with a turbulence enhancement process. Extreme events, such as tsunami waves, can also affect some vegetation ecosystems. These highly energetic waves may, in some cases, lead to their uproot or breaking, transforming them into dangerous debris. Besides, vegetation ecosystems are not only affected by waves. Currents are especially important in intertidal zones. Thus, it is common to have specific coastal areas where waves, currents and vegetation interact. Therefore, it can be concluded that a proper understanding and modelling of the complex flow conditions is needed since the coastal protection service is highly dependent on the widely different types of waves and currents nonlinear interactions taken place with the diverse vegetation ecosystems.

Many studies have been carried out to study the interaction between unidirectional flow and vegetation (Arbele and Järvelä, 2013; Bouma et al., 2013). Also, several studies have been conducted considering oscillatory flow (Bouma et al., 2010; Yoon et al., 2011), most of them focusing on the influence of wave parameters on wave attenuation (Manca et al. 2012; Anderson y Smith, 2014). However, contradictory results have been presented regarding the influence of parameters such as wave height and period. Another still open aspect is the consideration of waves and currents simultaneously. Only a few works have been presented to study their interaction with vegetation (Paul et al., 2012; Hu et al., 2014). Consequently, research devoted to observe, quantify and characterize the flow under controlled hydrodynamic conditions is needed. These studies allow analyzing the influence of different flow conditions on flow-vegetation interaction to asses coastal protection.

The present thesis aims to increase our knowledge of flow-vegetation interaction in order to quantify the coastal protection provided by coastal and intertidal ecosystems. This study seeks to contribute to resolving some of the issues that can help coastal managers to integrate natural solutions as part of their strategies for coastal protection. To do this, the study attempts to make progress in the understanding and characterization of flow-vegetation interaction providing new parametrizations, formulations and models. These tools should help to explain and quantify how the interaction of flow and vegetation characteristics determines the level of protection under different conditions.

"Life is like riding a bicycle. To keep your balance, you must keep moving"

Albert Einstein

2

OBJECTIVES AND METHODOLOGY

2.1 Scope and goals

The main objective of the present thesis is to make a step forward in the analysis of coastal protection provided by vegetation. Chapter 1 has revealed some unsolved questions in literature regarding the representation of plants and field properties; the analysis of the influence of wave parameters on the relevant processes; the role of the combined effect of waves and currents on vegetation and the effect of extreme events on vegetation elements. In order to address these gaps some specific objectives are set for this work.

Objective 1 – Analysis of the role of flexible vegetation on wave attenuation. A correct definition of plant properties to study their attenuation capacity is very important. Vegetation present in coastal areas is mostly flexible and the degree of flexibility is one of the relevant parameters that determines the plant dissipation capacity. Therefore, it is necessary to get a deeper understanding of the role of vegetation flexibility on wave attenuation and the interaction between the fluid and plant motion.

Objective 2 – Quantifying coastal protection provided by real salt marsh vegetation. A wide area of intertidal areas in temperate zones are vegetated. These vegetation ecosystems help to

reduce flooding and erosion hazards in these vulnerable areas. However, most of the studies found in literature have been performed using vegetation mimics. In addition, only a few have been carried out considering simultaneously waves and current conditions. There is a clear need, to determine how real vegetation responds to the combined effect of waves and currents under controlled conditions.

Objective 3 – Semi-empirical modelling of wave and current attenuation by vegetation. Due to the few studies performed considering waves and currents simultaneously, the attenuation provided by vegetation under those conditions is not well defined. Although some formulations can be found for wave damping, no specific formulation exists to predict the interaction of waves and currents with vegetation. Therefore, a new formulation for these conditions is desirable.

Objective 4 – Advanced numerical modelling of emergent rigid vegetation. Most of the studies found in the literature have been focused on the effect that vegetation has on flow. However, the impact of flow in vegetation elements remains unstudied due to the need of high resolution modelling combined with advanced flow processes not accounted for in models based on wave theory including a parametric modelling of the interaction. This problem is especially important for extreme events like tsunamis interacting with rigid vegetation. The correct definition of the interaction between flow and vegetation is essential to correctly define the flow inside the vegetation field. Therefore, a detailed study of the flow between the vegetation elements and the forces that these elements suffer under flow action is needed.

Objective 5 – Analysis of field vegetation large-scale characteristics on coastal protection. Not only individual plants characteristics are important to determine flow energy dissipation; the geometry and location of the vegetation field are also important aspects to be considered. Vegetation does not grow uniformly in nature, forming varying geometric patterns and located at different positions depending on a series of environmental parameters. However, most of the studies carried out have been conducted considering uniform and continuous fields or in real configuration but using simplified models of large-scale wave and vegetation field interaction. As a consequence, there is a need for improving our understanding on how non-uniform fields work and its implications on the developed flow patterns and the exerted forces over the vegetation elements.

2.2 Methodology

The present section describes the different steps and methods required to achieve the set of objectives summarized in the previous section. Accomplishing each of the objectives requires

different approaches and developments. Depending on the temporal and geometric scale and the complexity of the problem, an experimental, analytical, numerical or combined approach is adopted. Therefore, the methodology is structured by objectives.

Objective 1 – Analysis of the role of flexible vegetation on wave attenuation. In order to study the influence of vegetation flexibility on wave attenuation a proper characterization of the flow-vegetation interaction is needed. In this thesis, the approach is based on the development of a numerical model that allows the analysis of the coupled motion that results from the interaction of the flow and flexible plants. In order to formulate the model, two steps must be accomplished. In the first place, a hydrodynamic model to correctly represent the flow is required. In the present work, the IH-2VOF model has been selected as the base code to address the second part of the work, namely the implementation of a vegetation model. The choice has been motivated because IH-2VOF is an advanced RANS-based code fully validated for complex flow-structure problems that allows solving the vertical component of the flow and incorporates a turbulence model.

In the second place, a mechanical model that accounts for the coupled movement produced between flow and vegetation is needed. The model must be formulated in terms of flow and vegetation characteristics. The plant motion formulation, based on the Morison equation and the damped oscillatory movement equation (Ikeda et al., 2001; Mendez et al., 1999), is adopted as the starting point. This equation allows obtaining the plant movement and thus the relative velocity defined as the flow velocity minus the plant velocity. This relative velocity can used later to obtain the drag force that is introduced into the momentum equation of the IH-2VOF source code to account for the momentum damping induced by vegetation. This scheme allows considering the coupled movement between flow and vegetation and evaluating the induced energy damping. Furthermore, the presence of vegetation introduces an additional turbulence production and dissipation, requiring a modified k-ε turbulence model. Consequently, the classical k-ε turbulence model implemented into the IH-2VOF needs to be modified by introducing two additional terms: on in the turbulence production equation and another one in the dissipation equation.

Objective 2 – Quantifying coastal protection provided by real salt marsh vegetation. In this case and due to the lack of similar work, the approach taken aims at a better understanding of the relevant processes together with the development of a high quality data set useful to address some of the following objectives as well as future work. Consequently, it is opted for an experimental approach under controlled conditions with three singular characteristics, namely: 1) working at a large-scale; 2) using different species of real plants and 3) test the combined effect of waves and currents.

The Cantabria Coastal and Ocean Basin (CCOB) is selected to carry out the experiments since this hydraulic facility allows studying three dimensional wave and current interaction with real salt marshes, using both collinear and non-collinear waves and currents close to real conditions. Two different salt marsh plants with different biomechanical properties, standing biomass and field density are considered in order to study the influence of these parameters on their attenuation capacity. Different steps must be covered in order to perform the experiments, from collecting and growing the plants to the selection of the hydraulic conditions. This effort leads to the need of developing a general methodology or some standards to conduct this kind of experiments and the proposal of a set of recommendations. Furthermore, the analysis of this unique set of experiments allows studying the complex hydrodynamic processes developed in the waves and currents interaction with real vegetation. The experimental setup requires considering different flow and vegetation characteristics to allow analyzing the influence of these parameters on energy dissipation.

Objective 3 – Semi-empirical modelling of wave and current attenuation by vegetation. Quantifying the amount of energy damped by vegetation under the combined effect of waves and currents is not an easy task since waves-current-vegetation interaction is a highly nonlinear problem. Therefore, as a first step and considering a series of simplifying assumptions, an analytical approach is followed in order to find a new formulation that allows obtaining the wave damping under the combination of waves and currents. The formulation will be addressed following the energy conservation approach presented by previous authors (e.g.: Dalrymple et al., 1984; Mendez and Losada, 2004). The formulation is design to consider both regular and random waves propagating over an underlying current. Taking advantage of the unique experimental work carried out under Objective 2, the new formulations are calibrated based on the experimental results.

Objective 4 – Advanced numerical modeling of emergent rigid vegetation. The study of the flow interaction with rigid elements and the forces exerted on those elements is a complex problem, requiring an advance flow solver as well as a high resolution analysis to solve the individual plant hydrodynamics, not feasible experimentally. Consequently, in this work that analysis is carried out using a 3-D Navier-Stokes equations solver. Models based on NS equations allow simulating flow vertical components and the flow between individual elements, considering appropriate turbulence effects. IHFOAM is selected to include rigid vegetation. This model has been developed in IHCantabria and allows simulating gravity waves and porous media flows. It also incorporates a set of algorithms to generate and absorb waves at the boundaries without the use of relaxation zones, speeding-up the simulations and ensuring a correct representation of the wave-induced hydrodynamics in the numerical domain.

Following the simplifications adopted by previous authors rigid vegetation represented by cylinders is planned to be used. Two different mathematical approaches are considered: 1) a direct simulation of the wave-induced flow field around the vegetation elements considering a $\kappa - \omega$ SST model as the turbulence closure; 2) a macroscopic representation of the flow field within the vegetation, considering a drag force to represent wave damping. In the latter, a modified $\kappa - \varepsilon$ turbulence model is considered.

Objective 5 – Analysis of field vegetation large-scale characteristics on coastal protection. The study of vegetation horizontal spatial distribution is carried out considering two different approaches. First, the model developed in Objective 4, that allows resolving the flow field between the vegetation elements, is used to study different cylinder spatial distributions within a given vegetation field. Random configurations are also studied, keeping constant the field density. The same flow conditions are simulated for both uniform and random distributions. This allows comparing the results and studying the influence of vegetation elements distribution in free surface evolution along the field and in the forces exerted over the vegetation elements.

The influence of large-scale field characteristics on coastal protection is also study. In this case, an experimental approach is selected to gain a better understanding of how non-homogeneous spatial field distribution may affect to the flow and to the damping process. Several spatial field configurations are considered. At a second stage, these experiments are simulated numerically using the model develop under Objective 4 in order to analyze variables not measured during the physical experiments.

2.3 Document structure

The work developed in order to achieve the objectives presented are discussed in the following chapters that are structured as follows.

Objective 1 is completely addressed in chapter 3. This chapter presents a two dimensional numerical model for flow - vegetation interaction based on the Navier-Stokes equations accounting for the coupled movement between flow and vegetation.

The accomplishment of Objective 2 is covered in two chapters, 4 and 5. Chapter 4 presents a set of guidelines for the physical modelling of this innovative type of eco-hydraulic experiments. A description of the experiments is presented jointly with the general steps to be considered when preforming this type of experiments. Finally, some recommendations based on the experience are presented. Chapter 5 presents the analysis of the experimental data. The influence of wave

parameters, water depth, waves and current interaction, vegetation density, vegetation standing biomass and vegetation stiffness is analysed and a set of conclusions are drawn.

Objective 3 is fully accomplished in Chapter 6. This chapter presents the new semi-empirical damping model for combined waves and currents under regular and random waves. Furthermore, new formulations for the drag coefficient as a function of a new Reynolds number are presented. This new Reynolds number accounts for vegetation response under different flow conditions.

Chapter 7 deals with the work needed to addresses Objective 4. This chapter presents two three-dimensional approaches to resolve the flow interaction with rigid vegetation based on the Navier-Stokes equations. A comparison between both approaches is presented highlighting the weaknesses and advantages of them.

Objective 5 is achieved partly in Chapter 7 and mostly in 8. Chapter 7 presents the study of the vegetation elements distribution by considering three different random configurations and comparing them with the uniform configuration formed by the same number of vegetation elements in one single field, using numerical modelling. Chapter 8 describes the experiments run with different vegetation patches and the analysis of the experimental data in terms of wave attenuation. In addition, Chapter 8 shows the numerical tests performed to simulate these experiments and to study the forces exerted over the cylinders.

Finally, Chapter 9 presents the conclusions of the present work and the future research topics.

Due to the specific contents of each chapter, each of them begins with more detailed description of the “state of the art” about the corresponding topic extending the overall review found in Chapter 1. In this way, the new developments are contextualized and a more self-contained reading of the steps covered in each chapter is provided.

"Avoid modelling the differential equations rather than the physics"

David C. Wilcox

3

TWO DIMENSIONAL MODEL OF SUBMERGED VEGETATION UNDER OSCILLATORY FLOW

Summary

This chapter presents a new model for wave and submerged vegetation which couples the flow motion with the plant deformation. The IH-2VOF model is extended to solve the Reynolds Average Navier Stokes equations including the presence of a vegetation field by means of a drag force. Turbulence is modeled using a k-ε equation which takes into account the effect of vegetation by an approximation of dispersive fluxes using the drag force produce by the plant. The plant motion is solved accounting for inertia, damping, restoring, gravitational, Froude-Krylov and hydrodynamic mass forces. The resulting model is validated with small and large-scale experiments with a high degree of accuracy for both no swaying and swaying plants. Two new formulations of the drag coefficient are provided extending the range of applicability of existing formulas to lower Reynolds number.

3.1 Introduction

Vegetated coastal habitats, including seagrasses such as *Posidonia oceanica* and macroalgae such as *Kelp*, have received much attention in recent years for its role in providing several functions contributing to coastal protection. Among other factors their canopies contribute to dampen wave height and velocities (Koch et al, 2009; Fonseca and Cahalan, 1992; Mendez and Losada, 2004), reducing flow and turbulence (Nepf and Vivoni, 2000) and thereby promoting sedimentation and limiting sediment resuspension within the vegetation beds (Terrados and Duarte, 2000; Garcia and Duarte, 2001).

Researchers working on wave interaction with vegetation fields have recognized the complexity of the processes involved, especially due to the coupling between the waves and vegetation motion. Besides the fact that only through the integration of field work, physical experiments and theoretical/numerical models a detailed knowledge of said processes will be achieved, it has to be said that some progress has been achieved so far considering the different approaches.

Few examples of detailed field studies considering wave attenuation are present in the literature (Elwany et al., 1995; Lowe et al., 2007; Bradley and Houser, 2009). Although this approach is the best suited to improve our understanding of the relevant processes, unfortunately, the ample range of species and hydrodynamic conditions considered and the technical complexity of the work do not guarantee, so far, the generalization of the results.

A second more extended approach has been the performance of small and large- scale experiments in wave flumes and basins under a controlled environment. Most of the laboratory experiments have been devoted to show that wave damping is strongly affected by different submerged aquatic species mostly represented by mimics selected to simulated real vegetation properties such as buoyancy and stiffness, among others (Dubi, 1995) or even considering rigid artificial units (Lowe et al., 2005)

At a larger scale, Stratigaki et al. (2011), characterized wave attenuation produced by *Posidonia oceanica* using artificial flexible mimics. Some additional results on these experiments have been recently published in Koftis et al. (2013).

Only recently, a limited number of experiments with real vegetation have been presented in the literature (Bridges et al., 2011; Bouma et al., 2013; Maza et al., 2013). Although the existing experimental studies provide a good sensitivity analysis to different parameters involved in the wave interaction with wave vegetation, conclusions are restricted to inherent limitations associated to physical modelling.

Together with the main goal of improving our understanding of the relevant hydrodynamic processes, laboratory work has been the main source of validation for both theoretical and numerical models.

Early pioneering works provided the basis for the conceptual models of wave damping by submerged vegetation (Dalrymple et al., 1984; Kobayashi et al., 1993; Dubi and Torum, 1997; Mendez et al., 1999). This work has been later extended to consider random breaking and non breaking waves, Mendez et al. (2004) or wave and current interaction with vegetation, Ota et al. (2004).

In order to overcome most of the limitations associated to the initial models two lines of research have been followed over the last years. For those interested in the effects originated by submerged vegetation fields on waves, currents and associated sediment transport, the approach has been performed introducing expressions for vegetation drag as a function of characteristics such as shoot density and canopy width based on previous approaches or empirical formulations derived from physical modelling into phase averaged models. Some examples are the full spectrum model SWAN (Suzuki et al., 2011), including the damping model by Mendez and Losada (2004) or Chen et al. (2007) considering the effects of seagrass bed geometry on wave attenuation and suspended sediment transport using a modified Nearshore Community Model (NearCoM).

In order to solve the near field or the kinematics and dynamics within the vegetation field several researchers have used phase resolving models with vegetation damping such as Boussinesq equations based models (Augustin et al., 2009). Furthermore, several advances in the analysis of airflow interaction with terrestrial plants (DuPont et al., 2010) using full Navier-Stokes equations, has opened the possibility to address the complex turbulent interaction between waves and submerged vegetation in the marine environment.

It has to be said that some early works exist in this context. Two-dimensional applications using Navier-Stokes equations have been already presented by Ikeda et al. (2001) and Li and Yan, (2007). However, several aspects in their models are still undefined. Most of them are related to the correct definition of the horizontal and vertical velocities associated to the oscillatory flow, the treatment/lack of turbulence or of the coupled motion of fluid and plants as well as the definition of the drag force exerted by the flow on the individual plants.

During the last years much progressed has been achieved in the field in wave modelling based on RANS equations. Losada et al. (2008), Lara et al. (2008), Guanche et al. (2009), Torres-Freyermuth et al. (2007) or Lara et al. (2011) are a few examples of the capabilities of RANS

equations combined with a Volume of Fluid technique is able to deal with the modelling of wave interaction with different complex structures or surf zone processes.

Based on this work, the purpose of this chapter is to provide a new numerical coupled model able to improve the existing models by introducing a higher degree of complexity in simulating the processes governing the interaction between waves and vegetation. Based on an existing Reynolds Average Navier-Stokes (RANS) equation model (IH-2VOF, Losada et al., 2008; Lara et al., 2008), the governing equations area extended to include the presence of a vegetation field by considering an additional friction, inducing a loss of momentum represented by a drag force. The restoring force is approximated by including the displacement at the top of a cantilever beam using the flow velocities. Besides, turbulence is modeled using a k-ε model which takes into account the effect of vegetation by an approximation of dispersive fluxes using the drag force produce by the plant after Hiraoka et al. (2006). Comparisons between numerical and experimental results for small and large scale no swaying and swaying vegetation show a very high degree of agreement.

3.2 Equations and numerical model description

In this work, an extended version of the Navier-Stokes (NS) based model IH-2VOF is developed by introducing a coupled system of equations considering both the wave and plant motion. IH-2VOF (Losada et al., 2008; Lara et al., 2011) solves wave flow for hybrid two dimensional domains in a coupled NS-type equation system, in this case, at the clear-fluid region (outside the vegetation field) and inside the vegetation field. The movement of the free surface is tracked by the Volume of Fluid (VOF) method. This model based on the Reynolds Average Navier-Stokes (RANS) equations has been successfully applied in previous work for the study of wave-structure interaction and wave breaking on beaches. In particular, Torres-Freyermuth et al. (2007) employed the IH-2VOF model to investigate the nearshore processes associated with random wave breaking on a gently sloping natural beach. Further they studied long wave transformation in beaches using a high spatial resolution laboratory dataset (Torres-Freyermuth et al., 2009) and Lara et al. (2011) and Ruju et al. (2012) studied long waves induced by transient wave group on a beach. About validation in flow-structure interaction Losada et al. (2008), Lara et al. (2008) and Guanche et al. (2009) shows the satisfactory results obtained with this model.

At the clear-fluid region the 2DV RANS equations are considered. The flow inside the vegetation field is modelled considering an additional friction inducing a loss of momentum which is represented by a drag force, similar to Mendez et al. (1999):

$$\bar{F}_{D,i} = \frac{1}{2} C_D a N \bar{u}_{rel,i} \left| \bar{u}_{rel,i} \right| \tag{1}$$

where a is the width of the vegetation element perpendicular to the flow direction, C_D is the drag coefficient, N is the number of plants per unit area and $\bar{u}_{rel,i}$ the relative velocity defined as the difference between the plant and flow velocities. Sub-index i represents the components of the velocity and force vectors. Therefore the RANS equations inside the vegetation field are formulated by introducing this force in the momentum balance equation:

$$\frac{\partial \bar{u}_i}{\partial x_i} = 0 \tag{2}$$

$$\frac{\partial \bar{u}_i}{\partial t} + \bar{u}_j \frac{\partial \bar{u}_i}{\partial x_j} = -\frac{1}{\rho} \frac{\partial \bar{p}}{\partial x_i} + g_i + \frac{1}{\rho} \frac{\partial \bar{\tau}_{ij}}{\partial x_j} - \frac{\partial \overline{\left(u'_\iota u'_j \right)}}{\partial x_j} - \bar{F}_{D,i} \tag{3}$$

Where ρ is the flow density, $\bar{u}_i$ is the mean flow velocity, t is the time, $\bar{p}$ the mean pressure, $x_i$the spatial coordinate, $u'_i$the turbulent flow velocity and $\bar{\tau}_{ij} = 2\mu\bar{\sigma}_{ij}$ the mean viscous tensor, μ being the molecular viscosity and $\bar{\sigma}_{ij} = \frac{1}{2}\left(\frac{\partial \bar{u}_i}{\partial x_j} + \frac{\partial \bar{u}_j}{\partial x_i} \right)$ the mean flow deformation rate. The term $\overline{\left(u'_\iota u'_j \right)}$ represents the Reynolds stresses, which take into account the turbulent flow.

In order to close equation (1), the plant velocity is modelled to calculate the relative velocity, $\bar{u}_{rel,i}$. A vegetation mechanical model, following the Morison equation and based on the damped oscillatory movement equation (Méndez et al., 1999; Ikeda et al., 2001) is formulated accordingly. The governing equation of the plant motion is given by:

$$m_0 \frac{\partial^2 \xi_i}{\partial t^2} + C \frac{\partial \xi_i}{\partial t} + EI \frac{\partial^4 \xi_i}{\partial z^4} =$$

$$= \frac{1}{2} \rho C_D a \left(\bar{u}_i - \frac{\partial \xi_i}{\partial t} \right) \left| \bar{u}_i - \frac{\partial \xi_i}{\partial t} \right| + \left(\rho_p - \rho \right) g_i V_p \frac{\partial \xi_i}{\partial z} + \rho V_p \frac{\partial \bar{u}_i}{\partial t} + \rho C_m V_p \left(\frac{\partial \bar{u}_i}{\partial t} - \frac{\partial^2 \xi_i}{\partial t^2} \right) \tag{4}$$

where $m_0 = \left(\rho_p - \rho C_m \right) V_p$, ρ_p is the vegetation density, $C_m$is the added mass coefficient, $V_p$is the volume of the plant per unit area, $\xi_i$is the plant displacement, C is the damping coefficient, E is the young's modulus and I is the inertia moment of the cross section of the plant. The first and second terms on the left-hand side are the inertia and damping forces and the last two terms correspond to the restoring force. The terms on the right-hand side are the drag, gravitational, Froude-Krylov and hydrodynamic mass forces, respectively. Equation (4) is a simplified model which considers a linear deformation of the plant in order to solve its oscillatory motion by a vertically integrating over the plant length as proposed by Dupont et al. (2011). This

assumption allows obtaining the plant deformation along its length as a function of the tip deformation angle as a first approximation. As long as the vegetation deformation is not very large this approximation gives good results and the computational cost used to solve the plant motion is very low. However, for very flexible vegetation this approach allows obtaining the maximum plant displacements but not the deformation along the vegetation length. When this deformation is desired a model based on large deformations must be taken into account (Maza, 2012).

The integration of the plant motion is solved considering a linear deformation of the plant and the relative velocity is obtained as:

$$\bar{u}_{rel,i} = \bar{u}_i - \frac{\partial \xi_i}{\partial t} \tag{5}$$

The relative velocity presented in equation (5) is also present in the first term of the right hand side of equation (4) which represents the drag force contribution.

This model differs from the one presented by Mendez et al. (1999) which is based on linear wave theory on a flat bottom whereas the presented model solves Navier-Stokes equations for variable depth. Furthermore, the proposed model allows modelling cases with submerged but also emerged vegetation. The model proposed in Ikeda et al (2001) also differs from the one presented here. Although the same equations are used, the solving procedure is different. Ikeda et al. (2001) solves the restoring force considering an exponential velocity profile which determines the displacement values. In this model, the restoring force is approximated considering the displacement at the top of a cantilever beam under uniform loading using the flow velocities as the forcing loads. Ikeda et al. (2001) prescribes the plant deformation following an exponential deformation, therefore limiting the solutions.

Moreover, unlike in previous models (Mendez et al., 1999; Ikeda et al., 2001), turbulence is considered. Turbulence is modelled using a k-ε equation for the turbulent kinetic energy (k), and the turbulent dissipation rate (ε) which takes into account the effect of vegetation. The influence of turbulence fluctuations on the mean flow field is represented by the Reynolds stresses. The governing equations for k-ε are derived from the Navier-Stokes equations, and higher order correlations of turbulence fluctuations in k and ε equations are replaced by closure conditions. The effect of the vegetation field is considered by two additional terms, one in the turbulent kinetic budget, kw, and the other one in the turbulent dissipation rate, εw. These terms take into account the production of turbulent kinetic energy and the energy dissipation produced inside the vegetation field by an approximation of dispersive fluxes using the drag force produce by the plant. The equations are based on the turbulence model presented by Hiraoka et al.

(2006), but closure terms are modified in order to consider the relative velocity developed only inside the vegetation meadow. Terms related to turbulent production and dissipations are considered only using the shear stress tensor according to the ensemble velocity. Therefore, the new k-ε model is presented as:

$$\rho\frac{\partial k}{\partial t}+\rho\bar{u}_j\frac{\partial k}{\partial x_j}=\frac{\partial}{\partial x_j}\left[\left(\frac{\mu_t}{\sigma_k}+\mu\right)\frac{\partial k}{\partial x_j}\right]+\bar{\tau}_{ij}\frac{\partial \bar{u}_i}{\partial x_j}-\rho\varepsilon+\underbrace{\rho C_{kp}C_D aN\sqrt{\bar{u}_{rel,i}\bar{u}_{rel,i}}k}_{k_w} \quad (6)$$

$$\rho\frac{\partial \varepsilon}{\partial t}+\rho\bar{u}_j\frac{\partial \varepsilon}{\partial x_j}=\frac{\partial}{\partial x_j}\left[\left(\frac{\mu_t}{\sigma_\varepsilon}+\mu\right)\frac{\partial \varepsilon}{\partial x_j}\right]+C_{\varepsilon 1}\frac{\varepsilon}{k}\bar{\tau}_{ij}\frac{\partial \bar{u}_i}{\partial x_j}-C_{\varepsilon 2}\rho\frac{\varepsilon^2}{k}+\underbrace{\rho C_{\varepsilon p}C_D aN\sqrt{\bar{u}_{rel,i}\bar{u}_{rel,i}}\varepsilon}_{\varepsilon_w} \quad (7)$$

In the equations above μ_t is the eddy viscosity, μ the dynamic viscosity and σ_k a closure coefficient. Values given by Hiraoka et al. (2006) for the empirical constants C_{kp} and $C_{\varepsilon p}$ are used (see Table 3.1). The drag coefficient, C_D, is the same coefficient used in the momentum equation.

Besides the equations presented above, there are two additional relations needed to make use of the k-ε model. The first introduces the Boussinesq approximation which assumes that Reynolds stresses ($\bar{\tau}_{ij}$) are directly proportional to the mean strain-rate tensor ($\bar{S}_{ij}$). The proportionality constant is the eddy or turbulent viscosity, μ_t,

$$\rho\overline{\left(u'_\iota u'_J\right)}=2\mu_t\bar{S}_{ij}-\frac{2}{3}\rho k\delta_{ij} \quad (8)$$

where the last term in the previous equation is introduced for consistency reasons. Having defined the Reynolds stresses, there is only the need to define the eddy viscosity in order to link the k-ε model with the momentum conservation equations. By dimensional considerations the eddy viscosity is defined as,

$$\mu_t=\rho C_\mu\frac{k^2}{\varepsilon} \quad (9)$$

where C_μ is an empirical constant (Table 3.1).

κ	0.4
σ_k	1.0
σ_ε	1.3
C_μ	0.09
$C_{\varepsilon 1}$	1.44
$C_{\varepsilon 2}$	1.92
C_{kp}	1
$C_{\varepsilon p}$	3.5
C_D	Calibration

Table 3.1 Values of empirical constant of k-ε turbulence model

IH-2VOF uses a finite difference scheme to discretize the equations. A forward time difference and a combined central difference and upwind schemes are considered for the time and spatial derivations, respectively. A two-step projection method is used in the resolution of the equations. The turbulence model is solved based on an explicit finite difference scheme.

Wave conditions are introduced in the model imposing a velocity field and a free surface time evolution at one side of the numerical domain. Active wave absorption, Torres-Freyermuth et al. (2009), is also considered, not only at the rear end of the numerical flume to allow waves leaving the domain but also at the wave generating boundary, so that they do not interfere with the generated waves.

The solving procedure consists of coupling both the fluid and the plant motion. Flow velocities are used to calculate the induced plant motion using equation (4) following an explicit time marching scheme using forward differencing. Once the plant motion is solved it is used to obtain the relative velocity, equation (5). This relative velocity is used to update the velocity used in the two step projection method at the next time step. In this way, the relative velocities calculated at a given time step allow obtaining the plant motion which will be used to evaluate the relative velocity at the next time step. Figure 3.1 shows a flow chart with the solving procedure.

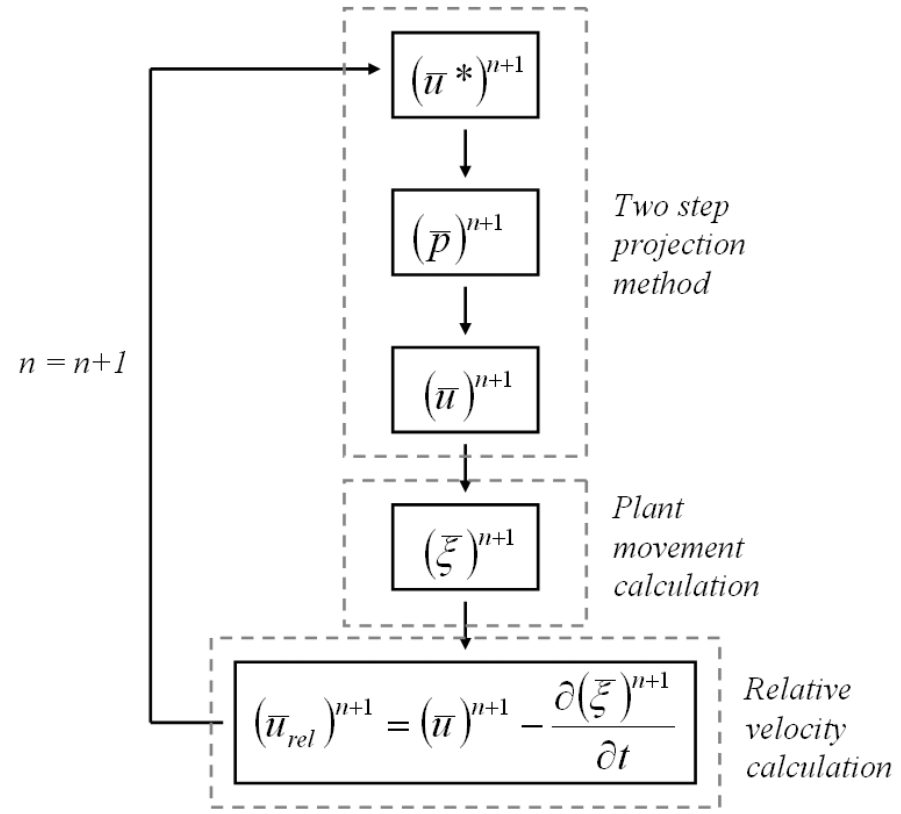

Figure 3.1 Flow chart of the solving procedure

3.3 Numerical model validation

Although an extensively validation of IH-2VOF model has been carried out for other flow conditions, validation for this new implementation is needed. In this work, the coupled motion of flow and vegetation is validated using experimental studies available in the literature. The validation is carried out in two steps. First, a simplified approach to the problem is considered by modelling the flow interaction with no swaying vegetation, see for instance Lowe et al. (2005). Secondly, the coupled movement between flow and vegetation is considered.

In the first case, the problem is simplified because the relative velocity is directly the flow velocity. The introduction of a new equation to describe the motion of the plants is not needed. Therefore, with no swaying elements the vegetation effect is reduced to evaluating the drag force presented in equation (1) obtained as a function of the flow velocity (Méndez et al., 1999; Lowe et al., 2005). In order to validate this approach numerical results are compared with experimental data from flume experiments developed by Asano et al. (1988). These experiments

have been previously used to validate similar models, Méndez et al. (1999). A second set of experiments with flexible vegetation is also considered to validate this approach. These experiments are the ones presented in Stratigaki et al. (2011).

Once this validation is completed, the second approach, which considers the coupled movement between the flow and the vegetation, is validated using Stratigaki et al. (2011) experimental data.

In order to carry out both validations the set of coefficients defined in the model must be specified. The k-ε model coefficients are kept constant. Considering no swaying vegetation the only parameter to be set is the drag coefficient, CD, which will be used as the calibration coefficient. Considering the coupled movement requires the added mass and the damping coefficients to be determined together with the drag coefficient which will be again the calibration coefficient. The values of these coefficients will be specified further on.

3.3.1 A brief description of the experiments used for validation

In the following a brief description of the experiments to be numerically modelled is given.

3.3.1.1 Asano et al. (1988)

Asano et al. (1988) experiments were carried out in a 27m long, 0.5m wide and 0.7m high flume. Vegetation mimics were made with polypropylene strips with a specific gravity of 0.9. Each of the strips was 25cm long, 5.2cm wide and 0.03mm thick. The artificial vegetation field had a length of 8m and was disposed in the middle of the flume width. For the entire test runs capacitance wave gages were used to measure the free surface oscillations at four locations over the artificial vegetation field. The first one was located 1m from the edge of the field and the distance between two adjacent gages was 2m, as it is shown in Figure 3.2.

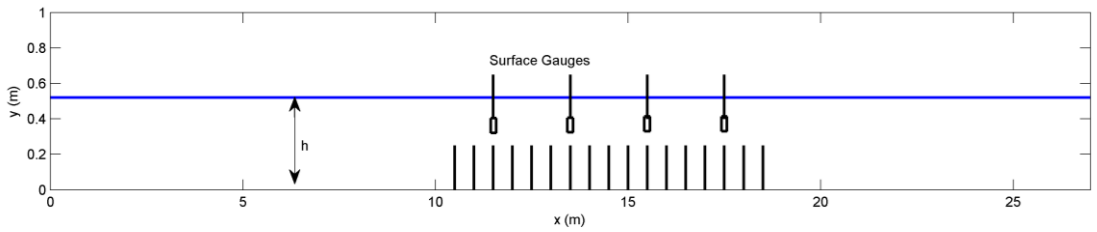

Figure 3.2 Asano et al. (1988) experimental set-up. Vegetation field is represented by vertical solid black lines and the positions of free surface gauges are displayed.

Two different seaweed densities, N, were tested. The sparse configuration had 0.110strips/cm2 whereas the dense configuration consisted of 0.149strips/cm2. Two different water depths (h), were evaluated, h = 45 and 52cm. For the different combinations of N and h, except for the case of N = 0.110strips/cm2 and h = 52cm different monochromatic waves were generated. Eight different wave frequencies were considered, f = 0.5, 0.6, 0.7, 0.8, 0.9, 1.0, 1.2 and 1.4Hz. Six different wave heights were tested for the frequency of 0.8Hz and two for the other cases. A total of sixty tests were carried out and for each one of them the values of the wave height in the different capacitance gauges was measured.

3.3.1.2 Stratigaki et al. (2011)

These experiments were carried in the UPC flume in Barcelona. Flume dimensions were 100m long, 3m wide and 5m deep. Due to these dimensions experiments were scaled. The flume bottom was covered by a sandy layer 0.7m thick and at a distance equal to 17.21m from wave paddle generation a 1/15 slope of 12m was located. Behind this slope, a 20m flat sandy beach was located and finally a beach of 37m to dissipate wave energy. Over the flat sandy beach a 10.7m long artificial vegetation field was placed. The beginning of this vegetation field was located at 38.36m from the wave paddle.

Vegetation mimics were composed of four PVC strips, one pair 45cm long and another pair of 27.5cm length, all inserted in a stiff 10cm long rod of the same material. PVC strips were 1mm thick and 1cm wide, with a Young's modulus equal to 2.9GPa and a density equal to 700 kg/m3.

Two densities were tested, 360mimics/m2 and 180mimics/m2. Free surface measurements were taken with fifteen resistive gauges, six before the meadow, seven over it and two after the field as shown in Figure 3.3. Velocity was measured using eight ADVs (Acoustic Doppler Velocimeters) and four EMCMs (Electro Magnetic Current-meters) positioned at three different distances from the paddle, at 37.66, 40.36 and 46.36m. EMCMs allowed measuring velocity inside the field.

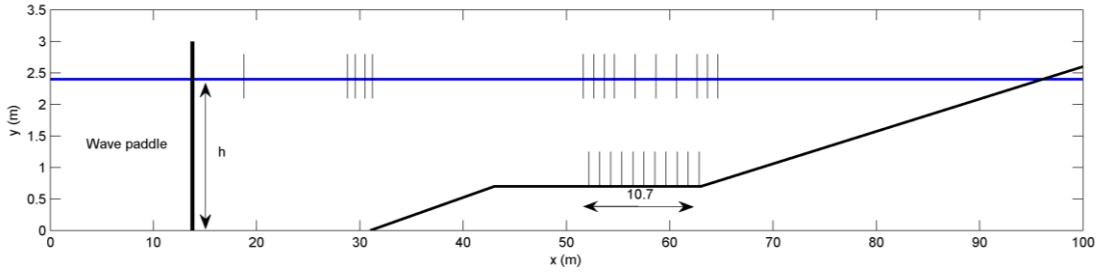

Figure 3.3 Stratigaki et al. (2011) experimental set-up. Vegetation field is represented by vertical solid lines and the positions of free surface gauges are displayed.

Different wave conditions were tested. As the present study is focused on regular waves, a total of 54 runs are available for the validation. These runs were the results of the combination of different wave heights, periods, water depths and meadow density. The tested wave conditions were the result of considering values of significant wave height between 0.4 and 0.5m, wave periods between 2 and 6s and water depths of 1.8, 2.0, 2.2 and 2.4m.

3.3.2 Validation for no swaying vegetation

The no swaying vegetation approach considers the vegetation effect as a loss of energy modelled by a drag force. For this propose, different wave and vegetation conditions are simulated with the model IH-2VOF.

For modelling Asano et al. (1988) experiments, a uniform grid size is chosen. In the horizontal direction the grid size is equal to 0.02m and in the vertical equal to 0.005m. In the case of Stratigaki et al. (2011) experiments, a large grid is used due to the experimental scale and a uniform grid system of variable grid size is used. The smallest discretization is used where the vegetation is located, having a grid size equal to 0.04m in the horizontal direction and half of this value, 0.02m, in the vertical one. The grid size has been selected on the basis of experience achieved in previous applications of the model.

To verify the simulated wave conditions the measurements of the first free surface gauges for both experiments is compared with the numerical results obtained at that position. Once the same wave conditions are obtained numerically all the variables involved in the problem are known except the drag coefficient. Therefore, this coefficient will be the calibration parameter of the model.

3.3.2.1 Wave height evolution

Sixty tests carried out by Asano et al. (1988) are simulated and the wave evolution over the plant meadow is compared. The results for eighteen of these tests are shown in Figure 3.4 and Figure 3.5. In each one of them the flow and vegetation conditions are displayed as well as the value of the drag coefficient used to fit the wave evolution along the field. As can be observed in the figure there is a good agreement in all cases. The model allows reproducing wave attenuation for different wave conditions, water depth and vegetation density. It is observed that wave attenuation is higher for larger relative depths (defined as the ratio between the vegetation height and the water depth) higher vegetation densities and larger Reynolds numbers (around 5000 - 7000) with wave height attenuations up to 60%. Small variations for the drag coefficient are shown with the largest values of the Reynolds number associated to the longer wave

periods. In order to evaluate the real dissipation produced by the vegetation some runs are selected and simulated without considering vegetation. Only cases with relevant wave attenuation are chosen. Three of these simulations are shown in Figure 3.4 in black dashed line. As can be seen the dissipation without vegetation is negligible whereas the simulations carried out with vegetation show a significant wave attenuation as the one measured in the experiments.

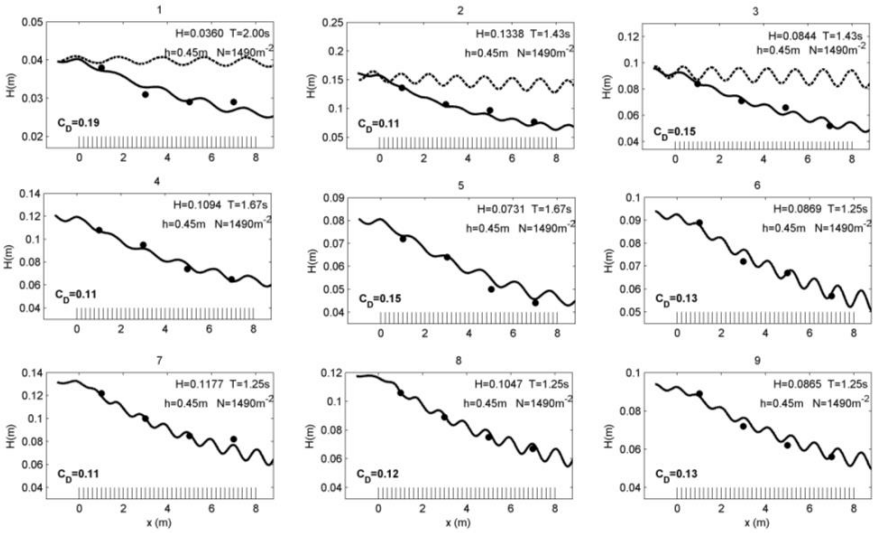

Figure 3.4 Numerical results(solid line) and Asano et al. (1988) laboratory data(black dots) of wave evolution along the meadow for experiments 1 - 9. Wave evolution without vegetation (dashed line) is presented in images 1-3

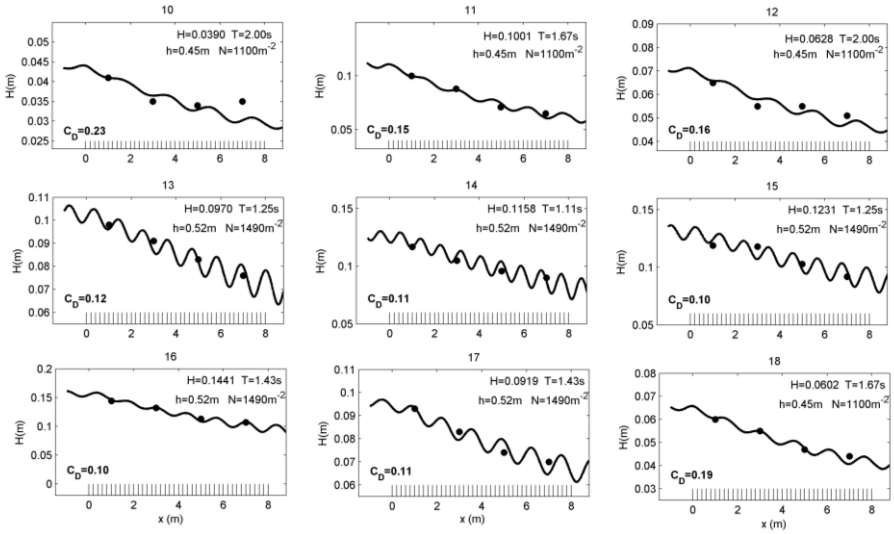

Figure 3.5 Numerical results(solid line) and Asano et al. (1988) laboratory data(black dots) of wave evolution along the meadow for experiments 10 - 18.

The experiments performed by Stratigaki et al. (2011) are also reproduced. In this case, the fifty four runs tested considering regular wave conditions are simulated. Eighteen of these runs are shown in Figure 3.6 and Figure 3.7. The numerical results fit the experimental measurements for different flow and vegetation conditions. Again, the drag coefficient used in each simulation is shown in each figure. This coefficient allows obtaining wave evolution along the field. This evolution leads to wave height attenuations up to 40% for cases with the largest vegetation density, the smallest water depth and large Reynolds numbers. Again three runs without vegetation are displayed in Figure 3.6 showing negligible wave attenuation during wave propagation.

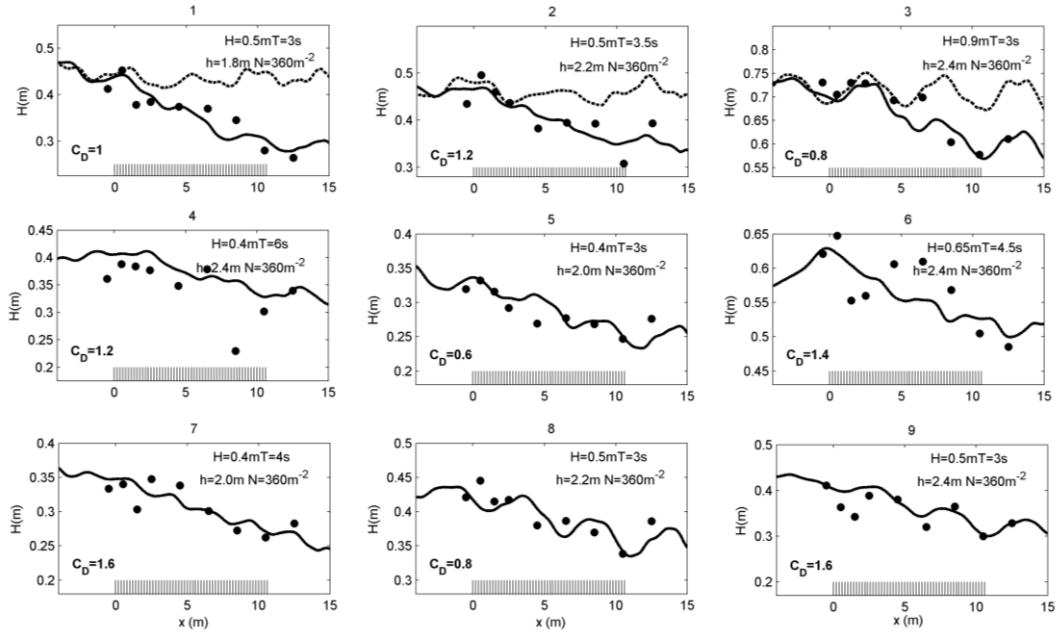

Figure 3.6 Numerical results(solid line) and Stratigaki et al. (2011) laboratory data(black dots) of wave evolution along the meadow for experiments 1 - 9. Wave evolution without vegetation (dashed line) is presented in images 1-3.

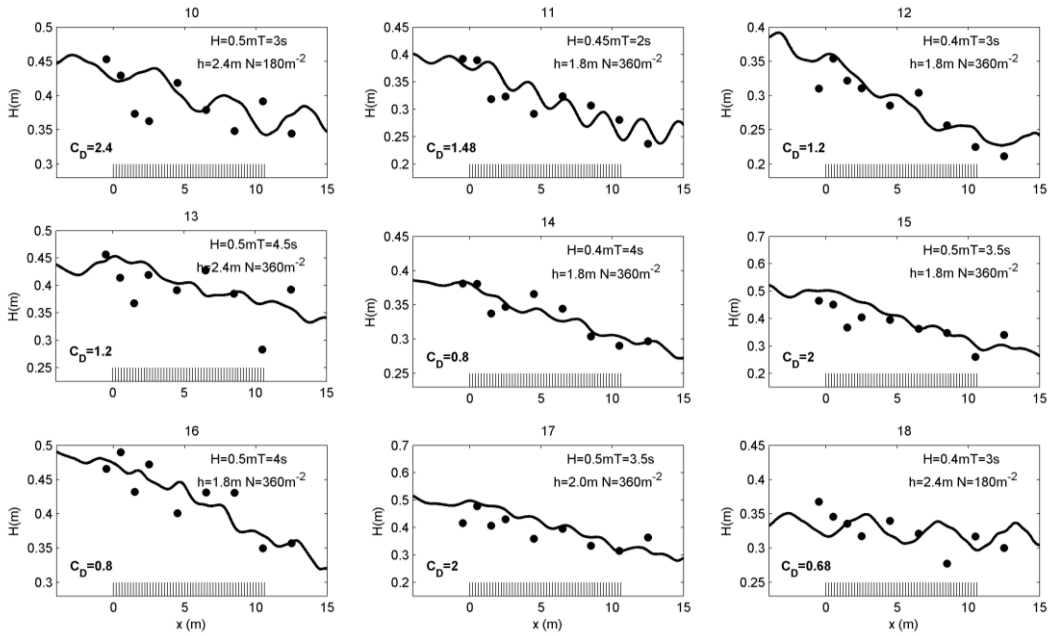

Figure 3.7 Numerical results(solid line) and Stratigaki et al. (2011) laboratory data(black dots) of wave evolution along the meadow for experiments 10 - 18.

As a conclusion assuming no swaying stems and calibrating the CD allows reproducing wave attenuation along the field using the convenient drag coefficient. The different complex processes produce in the interaction between flow and submerged vegetation are reproduced with a macroscopic approach based on a drag force.

From the different numerical experiments a set of drag coefficients has been found for Asano et al. (1988) and Stratigaki et al. (2011) experiments. The calculated values of the drag coefficient can be related with flow characteristics. Considering a Reynolds number, Re, defined as follows:

$$Re = a\frac{V_c}{\nu} \tag{10}$$

where a is the mimic width, V_c is the characteristic velocity, defined as the maximum value of the horizontal velocity at the top of the first mimic of the field and ν the kinematic viscosity. This number has been used for authors such as Mendez et al. (1999) to account for flow characteristics. Table 3.2 shows the values for the drag coefficient for the 18 cases displayed in Figure 3.4 and Figure 3.5 for Asano et al. (1988) experiments, and in Figure 3.6 and Figure 3.7 for Stratigaki et al. (2011) experiments, and their associated Reynolds number.

Case	**Asano et al. (1988)**		**Stratigaki et al. (2011)**	
	Re	***Cd***	***Re***	***Cd***
1	4763	0.19	4697	1.6
2	12367	0.11	5429	1.2
3	8520	0.15	4546	1.2
4	13263	0.11	8455	0.8
5	9441	0.15	4700	0.6
6	9373	0.13	7058	1.4
7	11642	0.11	4595	1.6
8	11165	0.12	5230	0.8
9	9373	0.13	5542	1.2
10	10469	0.10	4697	2.4
11	8461	0.11	5122	1.48
12	9981	0.10	5350	1.2
13	8652	0.12	6687	1
14	9429	0.11	5625	0.8
15	8075	0.16	6896	2
16	5164	0.23	7031	0.8
17	11455	0.15	6896	2

18	*7221*	*0.19*	*3758*	*0.68*

Table 3.2 Drag coefficient and Reynolds number values for 18 cases of Asano et al. (1988) and Stratigaki et al. (2011) experiments.

As can be observed in the table, Reynolds numbers associated to the 18 tests of Asano et al. (1988) are higher than the values for Stratigaki et al. (2011). The opposite relationship between drag coefficient and Reynolds number is observed, with higher drag coefficients for Stratigaki et al. (2011).

Free surface data from Stratigaki et al. (2011) experiments are used in order to compare experimental and numerical time series. The location of the different gauges is shown in Figure 3.8. Comparisons for two different cases are plotted in Figure 3.9 and Figure 3.10. Figure 3.9 shows a case with the lowest vegetation density, N = 180m-2, and the deepest water depth, h = 2.4m, with H = 0.5m and T = 3.5s. The numerical results reproduce with high accuracy the free surface measurements during the experiments, at both offshore (gauge AWG4), on the vegetation patch (gauges AWG10, 11, 8 and 9) and onshore (gauge AWG13). An additional case is shown in Figure 3.10 for a N = 360 m-2 vegetation density case and a water depth of h = 1.8m. The figure reveals larger wave deformation on the wave shape due to the higher influence of the vegetation meadow. Free surface attenuation and the nonlinearities produced by the interaction of the wave field with the vegetation meadow are well represented by the model as can be seen in the figure. The differences observed between laboratory and numerical results at the wave trough are due to unknown reflection patterns in the experiments at the rear end of the wave flume by the sandy beach, which is not simulated in the model.

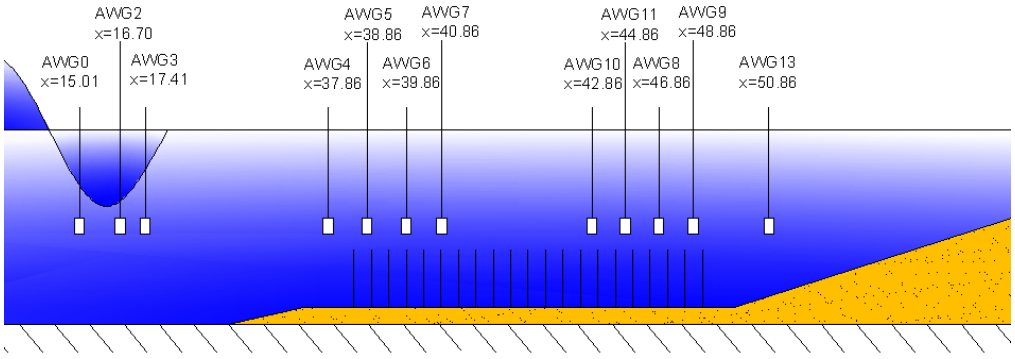

Figure 3.8 Scheme of the free surface gauges location for Stratigaki et al. (2011) experiments.

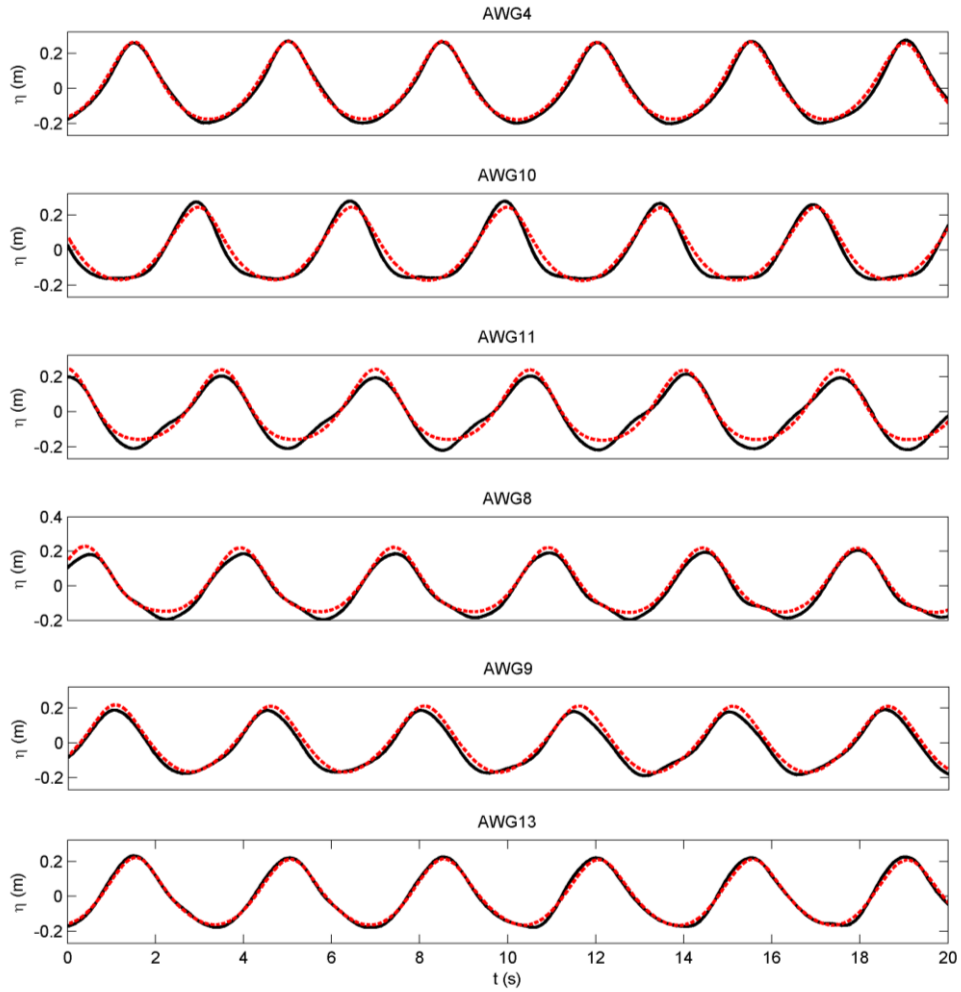

Figure 3.9 surface time series for 1 gauge located before the meadow and 5 inside it. Laboratory data (black line) and numerical results (red dashed line) for the experiment with N = 180m-2, h = 2.4m, H = 0.5m and T = 3.5s.

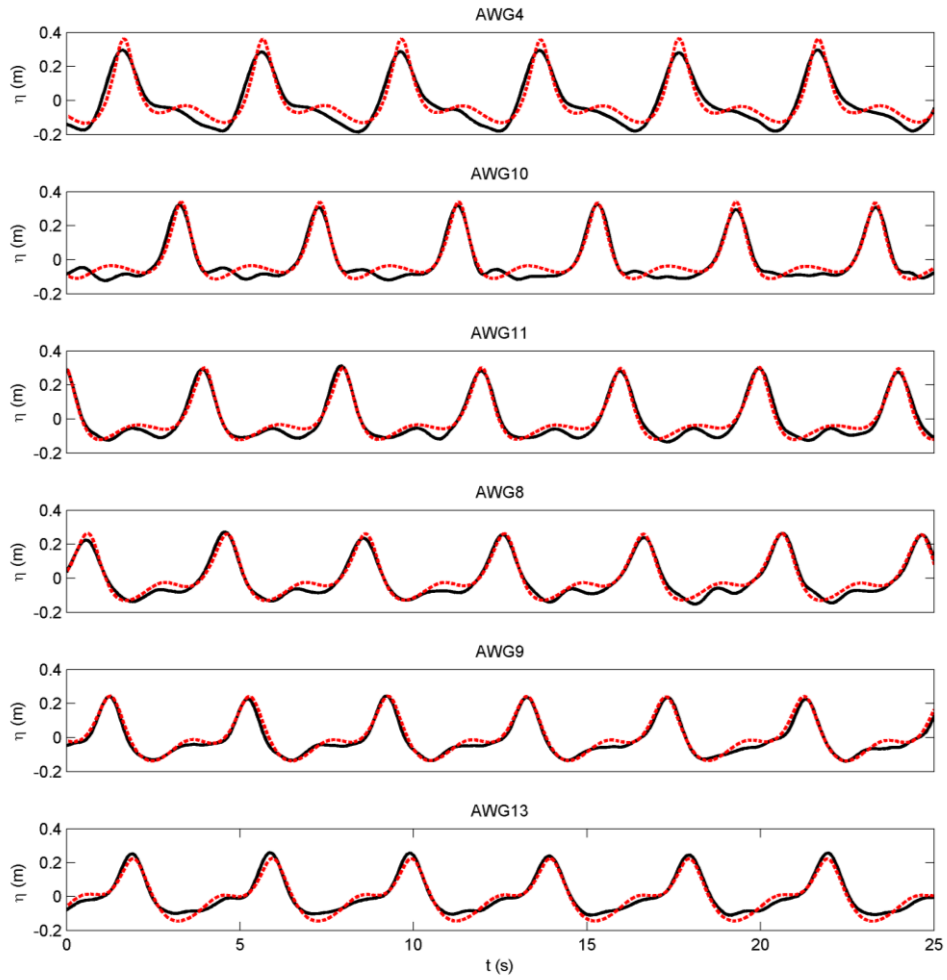

Figure 3.10 Free surface time series for 1 gauge located before the meadow and 5 inside it. Laboratory data (black line) and numerical results (red dashed line) for the experiment with N = 360m-2, h = 1.8m, H = 0.5m and T = 4s.

3.3.2.2 Velocities inside and outside the meadow

The proposed approach is also validated using velocity measurements. The model IH-2VOF allows obtaining both, vertical and horizontal velocity components in the entire water column. Velocities predicted by the model are compared with measurements by Stratigaki et al. (2011).

Measurements inside, using EMCMs, and outside the meadow, using ADVs, were taken. The measurements are located at 37.66m, 40.36m and 46.36m from the wave paddle which means at 0.7m before the meadow, at 2m from its beginning and at 2.7m from its end. Figure 3.11 shows a sketch of these locations. Numerical and experimental data are phase averaged over 20 waves for comparison. Figure 3.12 and Figure 3.13 show comparisons for horizontal velocity values, outside and inside the meadow respectively, and Figure 3.14 and Figure 3.15 vertical

velocity values, for a test with H = 0.5m, T = 3.5s, h = 2.4m and a vegetation density equal to 180 m-2. In Figure 3.12 and Figure 3.14 the nonlinearities generated above the meadow are well captured by the numerical model as is shown in the comparisons at points 5, 6, 7 and 8. The measured velocities inside the meadow displayed in Figure 3.13 show a good agreement in points a and b with small deviations in magnitude and a small phase shift. The results of point c and d show some discrepancies. Differences found in c and d can be due to a change in the sand bottom or local effects not captured by the model. Similar results are found in the velocity vertical components as presented in Figure 3.15. The irregularities in laboratory measurements found in points a, b and d in this figure can be due to EMCMs accuracy since very small values are registered.

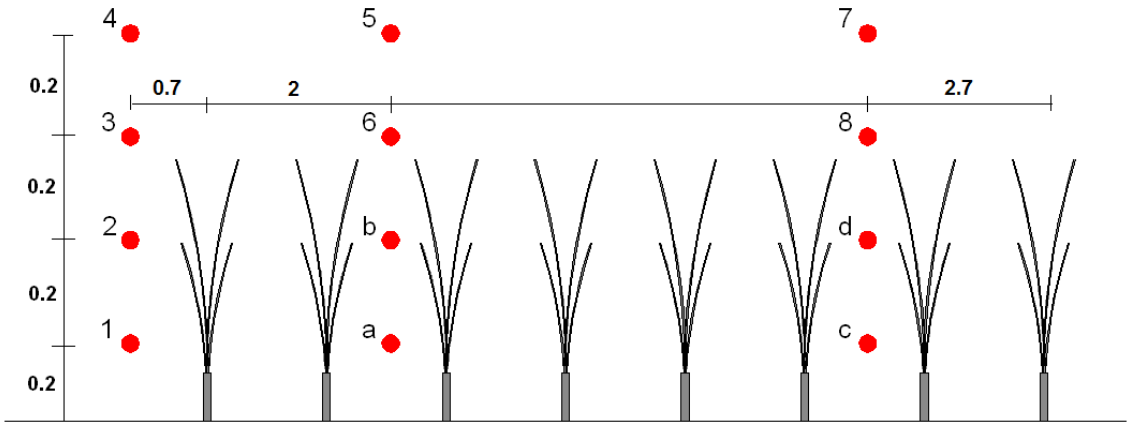

Figure 3.11 ADVs(1-8) and EMCMs (a-d) locations for Stratigaki et al. (2011) experiments.

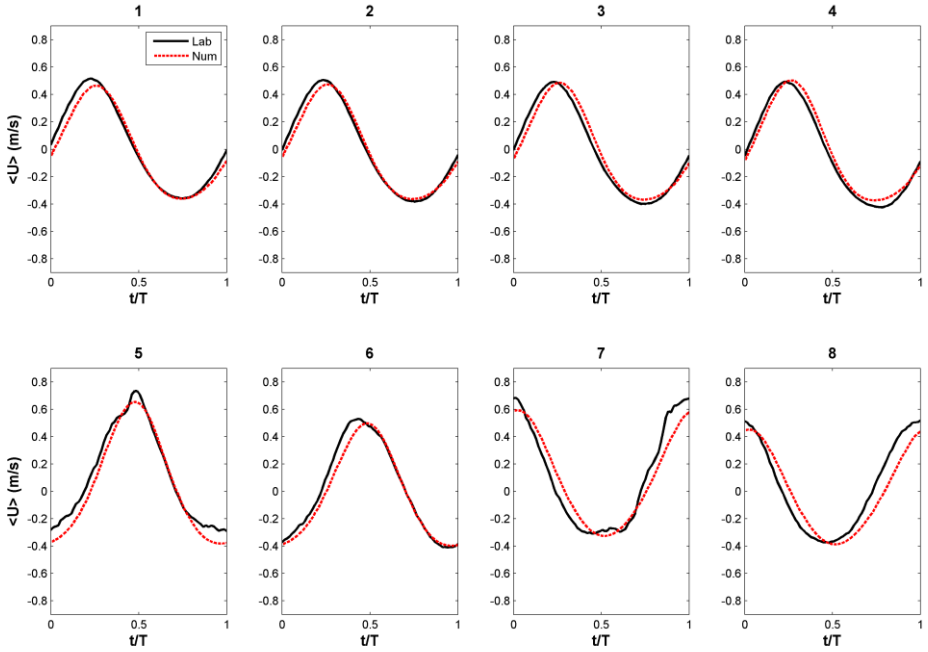

Figure 3.12 Phase-averaged horizontal velocities, <U>, in front, 1-4, and above the meadow, 5-8 for the experiment with N = 180m-2, h = 2.4m, H = 0.5m and T = 3.5s. Experimental data (black solid line) vs numerical results (red dashed line).

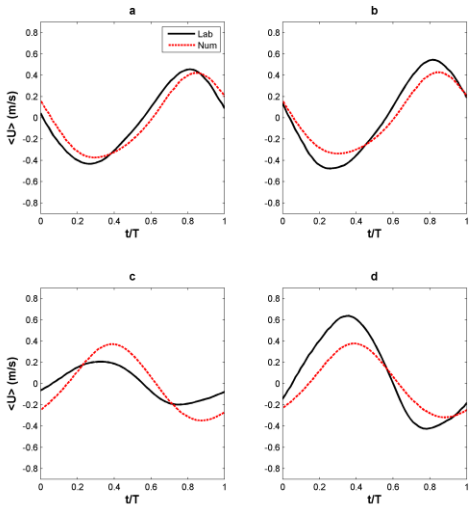

Figure 3.13 Phase-averaged horizontal velocities, <U>, inside the meadow for the experiment with N = 180m-2, h = 2.4m, H = 0.5m and T = 3.5s. Experimental data (black solid line) vs numerical results (red dashed line).

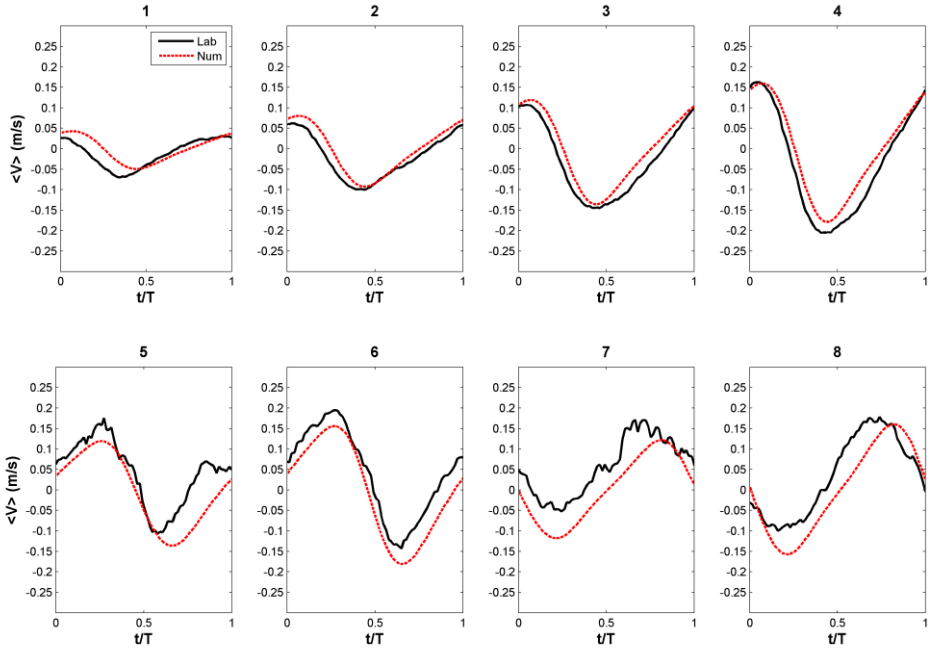

Figure 3.14 Phase-averaged vertical velocities, <V>, in front, 1-4, and above the meadow, 5-8 for the experiment with N = 180m-2, h = 2.4m, H = 0.5m and T = 3.5s. Experimental data (black solid line) vs numerical results (red dashed line).

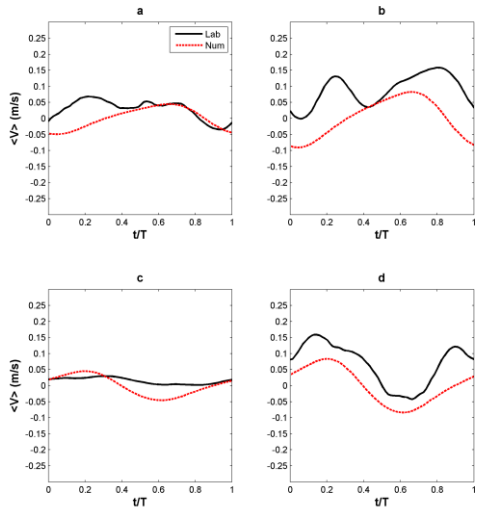

Figure 3.15 Phase-averaged vertical velocities, <V>, inside the meadow for the experiment with N = 180m-2, h = 2.4m, H = 0.5m and T = 3.5s. Experimental data (black solid line) vs numerical results (red dashed line).

Velocities are also validated by representing velocities profiles. Figure 3.16 and Figure 3.17 present minimum, mean and maximum velocity profiles for both, horizontal and vertical velocities for two different cases. Figure 3.16 shows the results for a case with H = 0.5m, T = 3.5s,

h = 2.4m and N = 180 m-2. This figure clearly indicates an increase in the horizontal velocity just above the meadow for both the numerical and experimental results. This is known as skimming flow and is the result of the strong discontinuity in the drag force between the area occupied by the meadow and the free flow over it. As can be observed the model is able to reproduce this phenomenon accurately. On the other hand, Figure 3.17 displays the results for a case with H = 0.5m, T = 4s, h = 1.8m and N = 360 m-2 in which the vegetation influence is stronger. In this case there is a larger velocity reduction inside the meadow and, again, the skimming flow is observed.

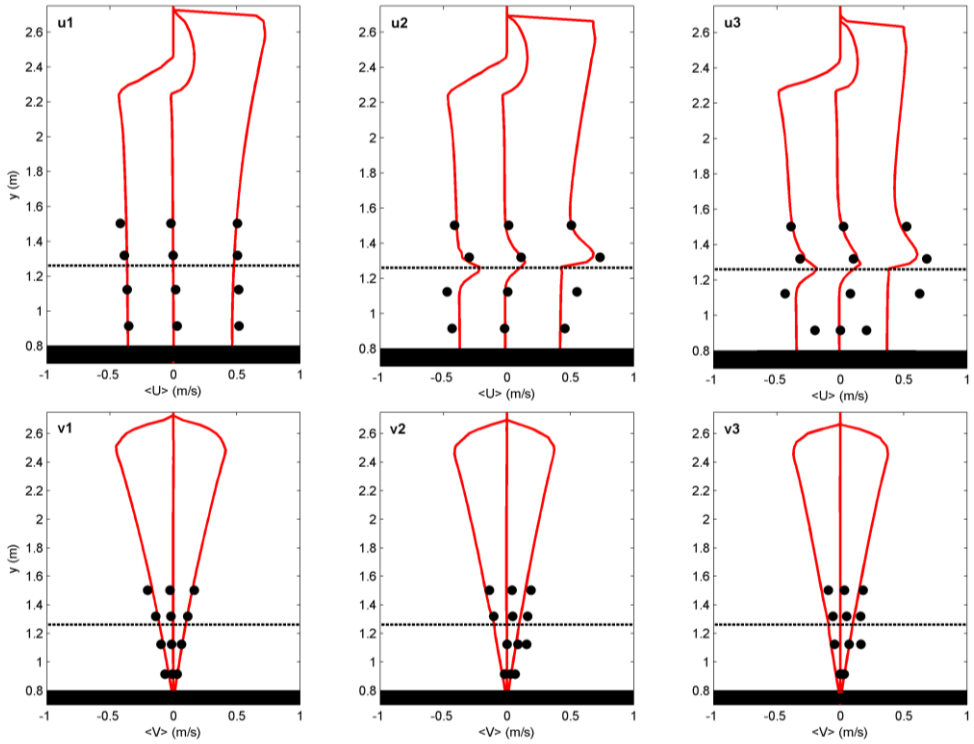

Figure 3.16 Minimum, mean and maximum average horizontal (above) and vertical (below) velocity profilesat 0.7m before the meadow, 2m after its beginning and 2.7m before its end. Experimental (black dots) and numerical results (red lines). The black dashed line represents the end of the meadow. Results for the experimentwith N = 180m-2, h = 2.4m, H = 0.5m and T = 3.5s.

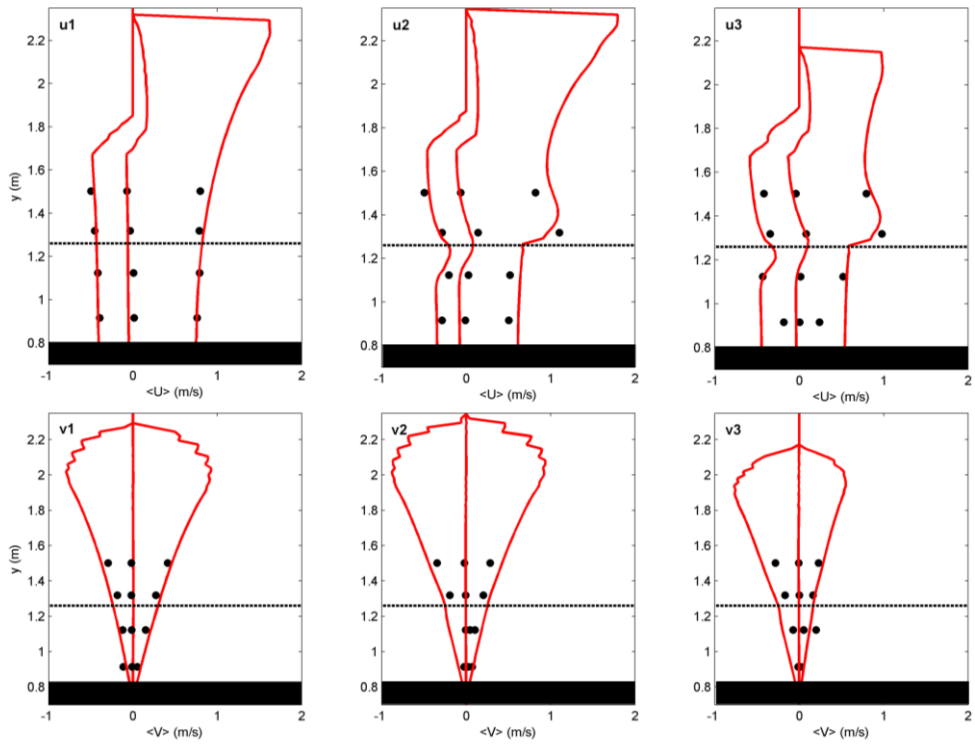

Figure 3.17 Minimum, mean and maximum average horizontal (above) and vertical (below) velocity profilesat 0.7m before the meadow, 2m after its beginning and 2.7m before its end. Experimental (black dots) and numerical results (red lines). The black dashed line represents the end of the meadow. Results for the experimentwithN = 360m-2, h = 1.8m, H = 0.5m and T = 4s.

In general, a good agreement is found between laboratory and numerical data reproducing especially well the mean values, even for cases in which the vegetation influence is very important. Values recorded at point c are very small in comparison with the values measured at the rest of the points. The differences between the predicted and measured velocities at point c can be due to local effects, not considered in the numerical simulations, such as possible ripples formation during the experiments since the mimics where placed over a sandy bottom. This can be seen in the last plots of Figure 3.16 and Figure 3.17 where the point closest to the bottom presents a very small velocity value.

3.3.2.3 Drag coefficient values and fitting formulation

Authors, as Kobayashi et al. (1993) and Mendez et al. (1999), developed new empirical relationships for drag coefficient as a function of the Reynolds number, Re. Those formulas are a function of three parameters, ζ, λ and γ, following the generic form:

$$C_D = \zeta + \left(\frac{\gamma}{Re}\right)^{\lambda} \tag{11}$$

Kobayashi et al. (1993) proposed values for these parameters based on the experimental data from Asano et al. (1988). Mendez et al. (1999) also proposed some values based on the same experiments using their own model considering both no swaying and swaying plants. Values in both papers are presented in Table 3.3.

Author	ζ	λ	γ
Kobayashi et al. (1993)	0.08	2.4	2200
Mendez et al. (1999) no swaying plants	0.08	2.2	2200
Mendez et al. (1999) swaying plants	0.40	2.9	4600

Table 3.3 Coefficient proposed by Kobayashi et al. (1993) and Mendez et al. (1999) to relate drag coefficient with Reynolds number.

As can be seen the values of Kobayashi et al. (1993) and Mendez et al. (1999) without plant swaying are almost identical whereas including plant swaying points to larger values of the drag coefficient.

In the calibration of the proposed model using Asano et al. (1988) and Stratigaki et al. (2011) experiments a set of drag coefficient values have been obtained. In order to relate these values with the empirical relationships described above the Reynolds number is obtained for each one of the runs. The calibrated drag coefficients obtained for Asano et al. (1988) experiments are represented in Figure 3.18. The formulations proposed by Kobayashi et al. (1993) and Mendez et al. (1999), without swaying, are also displayed in order to evaluate how the calibration drag coefficient values fit to these formulations. The correlation coefficients found for both cases are high with values about 0.54 and relative errors smaller than 4%. Therefore, the calibrated drag coefficient values obtained for Asano et al. (1988) experiments fit to existing formulations.

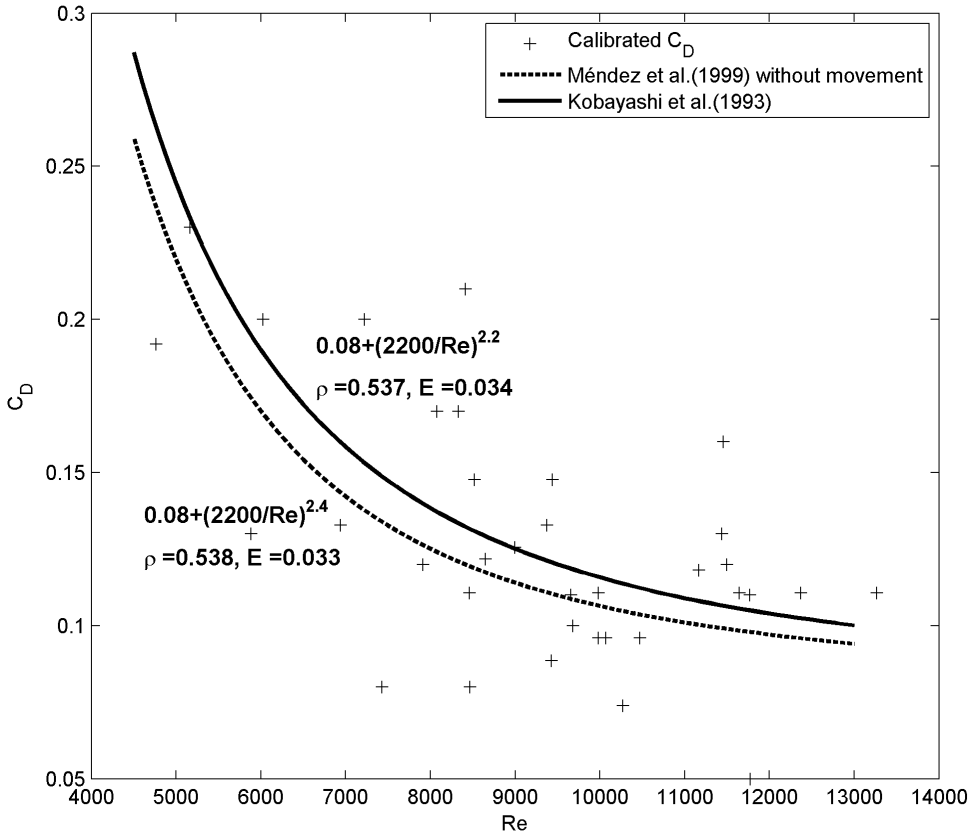

Figure 3.18 Calibrated drag coefficient values for Asano et al. (1988) experiments. Kobayashi et al. (1993) and Mendez et al. (1999), without considering vegetation movement, empirical relationships are shown.

Figure 3.19 shows the obtained drag coefficients versus the associated Reynolds numbers for the Stratigaki et al. (2011) experiments. In this case Mendez et al (1999) empirical relationships do not fit well to the obtained drag coefficient values. Although the formula for cases with movement fit well for Reynolds number between 4000 and 6000, large relative error and low correlation coefficient are found due to the discrepancies shown at low Reynolds numbers, range at which that formulation was not validated. Consequently, existing formulations are not appropriated for this case. This can be due to many different reasons: the larger experimental scale, the use of mimics with high flexibility and a range of Reynolds numbers not have been covered before. This points out the necessity of developing a new relationship for this type of cases where the flow conditions are different as well as the plant mechanical characteristics.

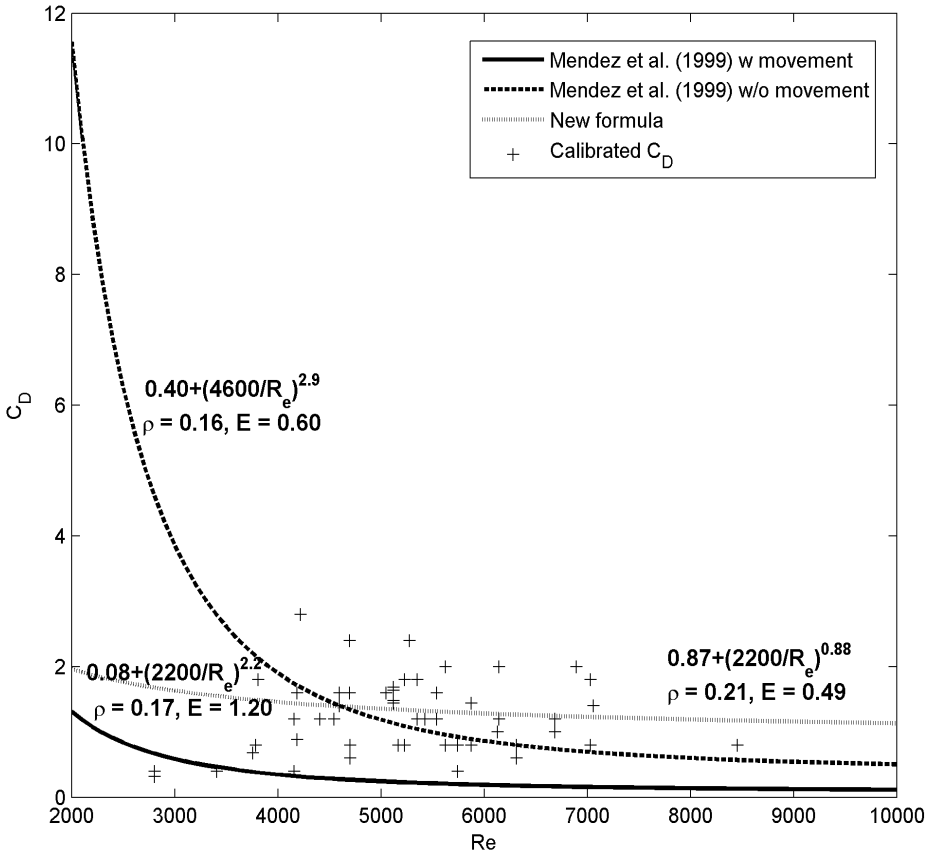

Figure 3.19 Calibrated drag coefficient values for Stratigakiet al. (2011) experiments. Mendez et al. (1999), with and without considering vegetation movement, empirical relationships and a new adjustment (dotted line) are shown.

A new formulation is proposed looking for the best fit to the calibrated drag coefficient values. That formulation is shown in Figure 3.19 and has the following expression:

$$C_D = 0.87 + \left(\frac{2200}{Re}\right)^{0.88} \tag{12}$$

Although a higher correlation coefficient and a smaller relative error than with Mendez et al. (1999) formulations are obtained, the values are still not good enough. Therefore, the drag coefficients achieved for Stratigaki et al. (2011) experiments do not fit to any existing formulation, neither to any formulation obtained using the based formula (11). For that reason, a new approach is needed in order to find the appropriate formulation for this case in which the vegetation is very flexible. The new approach, in which the vegetation movement is considered, is presented in the next section. Furthermore, the new approach allows estimating the relative

velocity developed inside the meadow and with that the drag force exerted by the flow in the plants.

3.3.3 Analysis of coupling modelling of vegetation motion and flow

Looking for a better representation of the interaction between flow and vegetation the model for coupled movement described in Section 2 is considered. With this approach not only the drag force is considered but also the inertia, damping, restoring, gravitational, Froude-Krylov and hydrodynamic mass forces. Stratigaki et al. (2011) experiments are simulated with this new approach looking for better results. Only Stratigaki et al. (2011) experiments have been simulated using a coupled model because velocity measurements outside and inside the vegetation meadow are available. With this approach the plant swaying is solved and the velocity of this movement is used to calculate the relative velocity necessary in the drag force calculation. As a result, a new set of drag coefficients are obtained.

The vegetation motion equation depends on a set of coefficients that must be defined according to the mechanical model proposed in equation (4). The value of the added mass coefficient, Cm, is assumed to be equal to 1, as in Mendez et al. (1999) and Ikeda et al. (2001). The damping coefficient, C, depends on the mimic's properties, on its rigidity and its mass. The balance between these two coefficients will define the appropriate plant velocity. As the drag coefficient depends on the flow properties but the damping coefficient depends on plant properties, which are constant, this second coefficient is set to a constant value. Therefore, the damping coefficient is set to simulate the swaying observed in the laboratory and the drag coefficient will be used as the calibration coefficient to match the energy attenuation in each one of the cases depending on flow characteristics.Unfortunately, plant movement was not directly measured in the experiments.

In order to determine the damping coefficient, a new set of laboratory experiments is carried at the University of Cantabria wave flume. It is 68.9m long, 2m wide and 2m deep. The objective of this new set of experiment is to measure the magnitude of the plant bending under wave action. The upper plant excursion is used to calibrate the damping coefficient in equation (4).

The same mimics used in Stratigaki et al. (2011) are tested. Five mimics are inserted in a wood panel 2 cm thick attached to the flume floor and parallel to the flume sidewalls. The space between mimics is 5 cm, the same used by Stratigaki et al. (2011). The reason to use five mimics is to get plant-plant interaction during the plant bending, as it occurs in Stratigaki et al. (2011). Different regular wave conditions are considered. Wave period of 3, 4 and 5 s and wave height

of 0.05, 0.10, 0.15 and 0.20 m are studied. The water depth is kept constant to 80 cm in all tests. The associated Reynolds number is between 1000 and 3500 for al the cases, in agreement with the range covered by Stratigaki et al. (2011).

Because the sidewalls of the flume are made of glass, plant motion can be measured by optical techniques. It is recorded by a 1 megapixel camera Marlin F131C of 8 bits of spectral resolution and with a frequency of 10Hz. The camera is positioned perpendicular to the plane of plant movement. A calibration plate located at the plants plane is used to determine the correlation between pixels and meters. Synchronous measurements of free surface motion are made at the plant location and 4.65m seaward this position, using a sampling frequency of 20Hz. The synchronization of both measurements was done using a trigger at 10 Hz.

Figure 3.20 presents an example of the maximum wave plant excursion for a regular wave case of H=0.2 m and T=4 s. The two upper panels represent the time history of the phase averaged free surface at the location of the plant. The lower pictures represent the maximum excursion onshore (left panel) and offshore (right panel). The corresponding wave phases when the maximum excursions are observed are represented using two dots in the free surface time series. The maximum excursion obtained for this case is of the order of 25-30 cm.

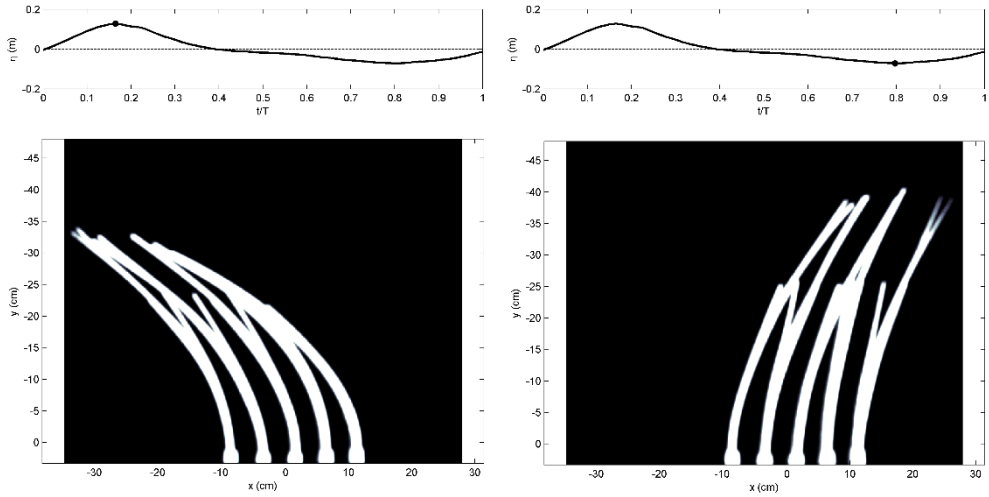

Figure 3.20 Maximum wave plant excursion for a regular wave case of H=0.2 m and T=4 s. Upper panels: Time history of phase averaged free surface at the plant location. Lower left panel: maximum onshore excursion. Lower right panel: maximum offshore excursion. Dots represent the time where both maxima occurs in the wave phase.

After sensitivity analysis made using wave excursion from the experiments and equation (4) a value of 12 Ns/m was chosen. This damping coefficient allows reproducing the plant movement

amplitude and is in agreement with values found in the literature as the one proposed by Ikeda et al. (2001), 12.64Ns/m for similar plant length and velocity regimes.

To calibrate the model, only the drag coefficient, Cd, in equation (4) is used to find the best fit to experimental data.

Figure 3.21 shows the instantaneous positions of the plants under wave action at six different time steps every 0.5s. The colour scale represents the horizontal velocity magnitude while vegetation is represented by black lines. For a better visualization the plant motion is multiplied by a factor of 5 in the figure. As can be seen vegetation sways forced by the flow velocities. Positive horizontal velocity values, in red, produce a displacement of vegetation plants in the positive x direction. The same effect is found with negative velocity values, in blue, although the displacement is smaller due to the smaller magnitude of the velocity in that direction. This pattern is consistent with the one observed in the experiments indicating that the numerical model allows representing flow vegetation interaction. As can be seen, just above the vegetation field there is an increase in the velocity, skimming flow, due to the discontinuity in the momentum balance. This effect was also observed in the velocity profiles shown in Figure 3.16 and Figure 3.17.

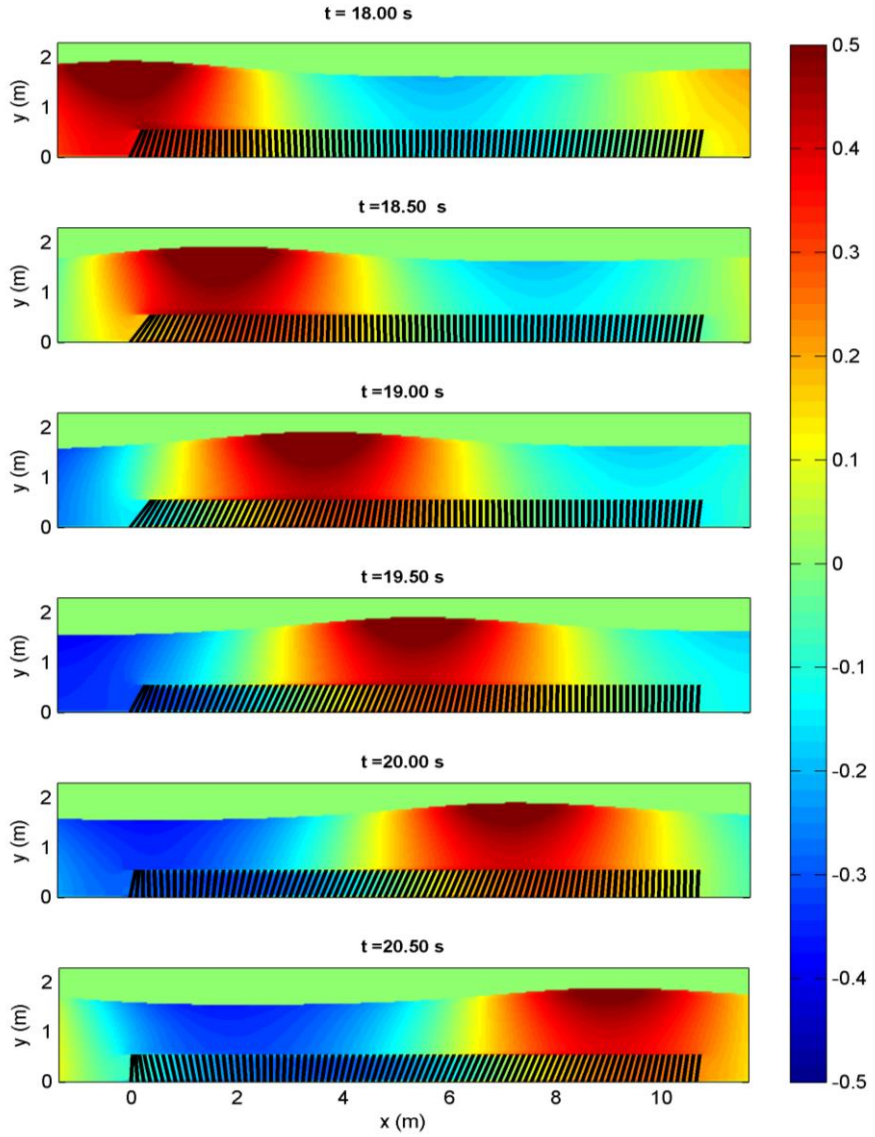

Figure 3.21 Instantaneous vegetation field, black lines, position under wave action at six different times for the case with H = 0.5m, T = 3.5s, N = 180 strips/m2 and h = 1.7m over the meadow. Colour scale represents the horizontal velocity magnitude. Vegetation motion is multiplied by a factor of 5 for better visualization.

Drag coefficients are set to obtain the best possible agreement between experimental and numerical wave height along the field. Numerical result for no swaying and swaying vegetation, is shown in Figure 3.22 for one of the tests. As can be seen numerical results are almost identical but with different drag coefficients. In the case of swaying, the drag force introduced in the momentum equation is a function of the relative velocity developed between the plant and the flow. Taking into account this phenomenon the drag coefficient must be higher in order to obtain the same momentum reduction as in the case of no swaying vegetation and,

consequently, the same wave attenuation along the vegetation field. The drag coefficient influence is shown in the same figure where two additional cases are displayed considering the drag coefficient for no swaying vegetation and a high drag coefficient. As can be observed, the drag coefficient which fits for no swaying vegetation is too small for the case in which the movement is considered and if this coefficient is too large the produced wave attenuation is also too high.

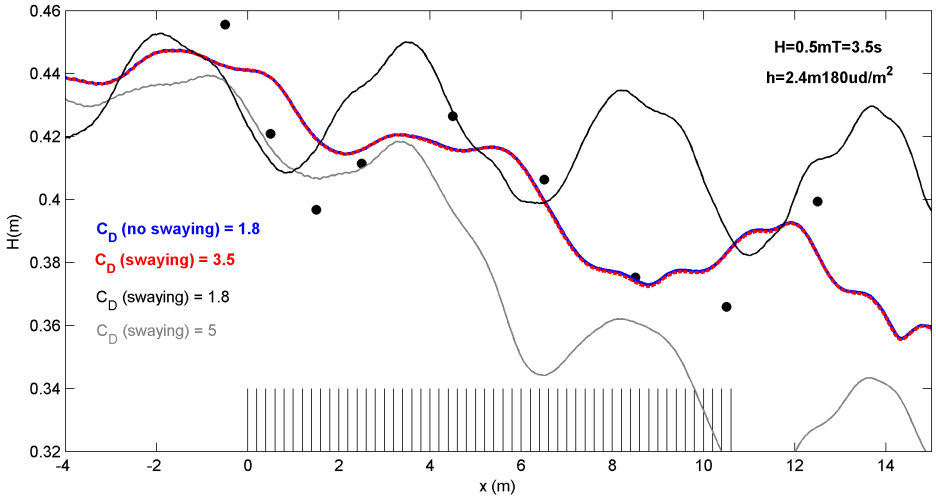

Figure 3.22 Wave height evolution achieved considering no swaying vegetation (blue solid line) and flexible vegetation (red solid line) for a case with H = 0.5m, T = 3.5s, h = 2.4m and N = 180 strips/m2. Experimental measurements (black dots)and two additional cases for flexible vegetation with different CD (solid black and gray line) are represented.

Wave velocities obtained with both approaches are also compared (Figure 3.23) and, again, the results are almost identical. The maximum, mean and minimum velocity profiles along the vegetation field obtained considering swaying show the same velocity reduction inside the meadow and the same skimming flow obtained considering no swaying vegetation since the momentum reduction inside the vegetation is set to be almost equal with the increase of the drag coefficient.

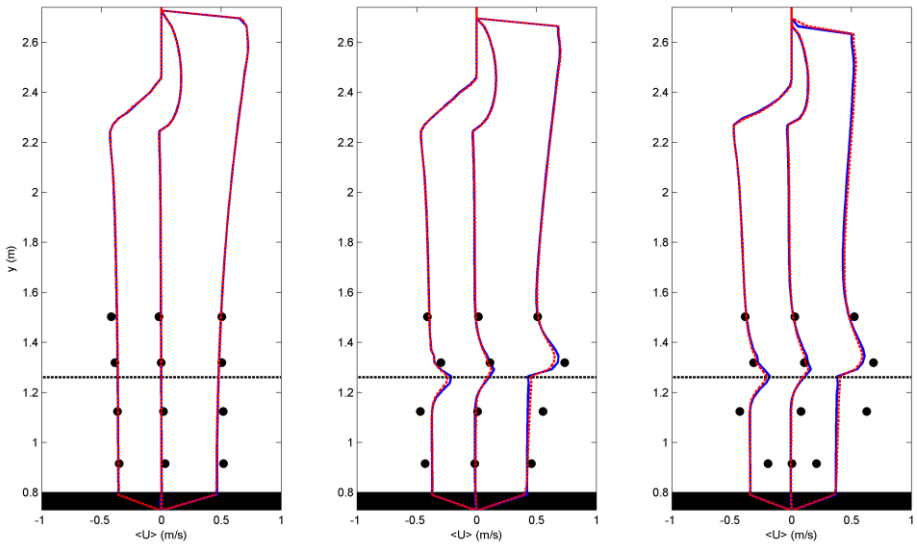

Figure 3.23 Horizontal velocity profiles for no swaying (blue lines) and swaying (red lines) plants for the case with H = 0.5m, T = 3.5s, h = 2.4m and N = 180 strips/m2.

Therefore, there are two approaches which can be used in order to obtain the wave attenuation produced by the meadow and the reduction in flow velocities. Both allow reproducing the problem taking into account the loss of energy produced by the vegetation meadow as a function of the drag coefficient but in the second case the physics involved in the coupled movement between the vegetation and the flow are considered. The drag coefficient is different for both approaches since the physics considered in each case is also different. Therefore, a different calibration of this coefficient is needed for the swaying approach. It can be concluded that in previous modelling efforts CD fitting has taken care of interaction processes that have not been either properly modelled or even considered.

Following the same methodology used in the case of no swaying vegetation approach a new set of drag coefficients is obtained. These drag coefficients are represented in Figure 3.24. The agreement of these new coefficients with existing formulas is evaluated by plotting them together with Mendez et al. (1999) formulations. Correlation coefficients and relative errors are calculated and displayed in the figure below the formulations. Although these estimators improve with this approach in comparison with the no swaying vegetation approximation for the formulation considering movement, the calculated relative error is very high. This disagreement is due to some different aspects. First, the experiments used to calibrate this coefficient are very different to the ones used by Mendez et al. (1999). The scale is larger and the vegetation is more flexible. Secondly, Méndez et al. (1999) swaying formulation was calibrated for Reynolds numbers between 2300 and 20000 with a small amount of data in the

low range. In this case, the range of Reynolds number varies mostly between 2000 and 7000 which means that the calibration is performed considering cases with less energetic wave conditions. Finally, the approach proposed by Mendez et al. (1999) to solve the problem of flow and vegetation interaction is based on a potential model whereas a model based on Navier-Stokes equations is proposed here, considering also the turbulent effects.

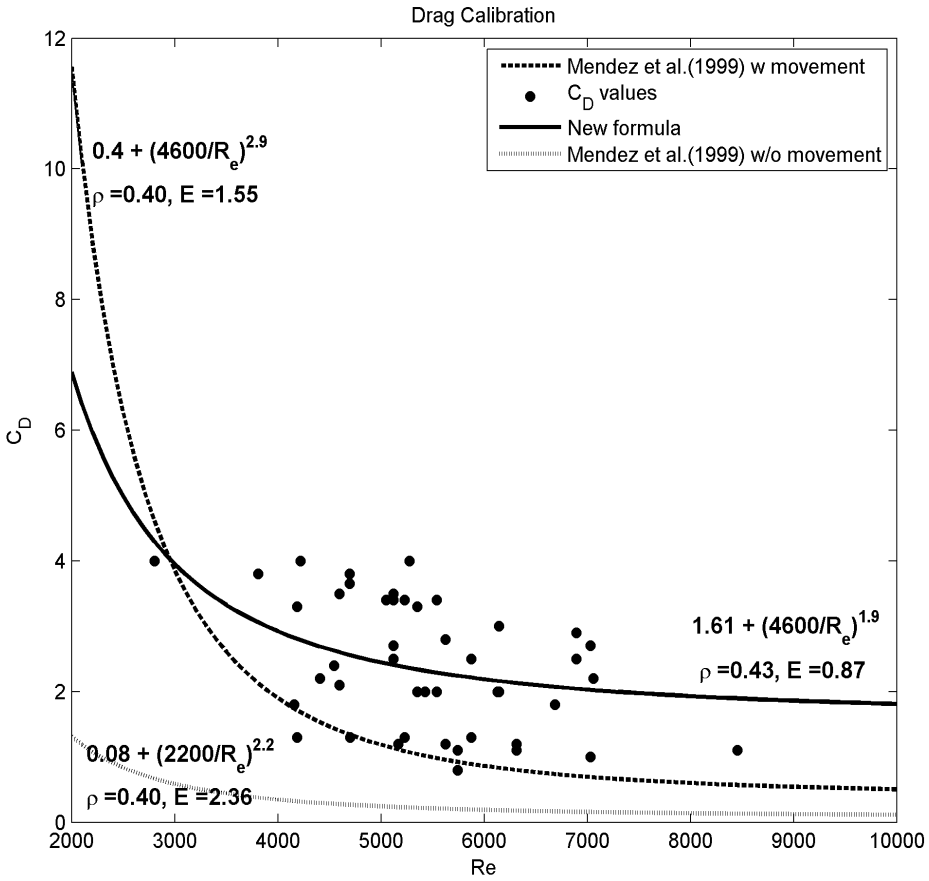

Figure 3.24 Calibrated drag coefficient values for Stratigaki et al. (2011) experiments considering vegetation movement(black dots). Mendez et al. (1999) empirical relationships and a new formula (black solid line) are shown with the associated correlation coefficient,ρ, and relative error, E.

Therefore, a new empirical relationship is proposed, based on the formulation given by Mendez et al. (1999) for cases with movement. This new relationship is as follows:

$$C_D = 1.61 + \left(\frac{4600}{Re}\right)^{1.9} \tag{13}$$

This formulation provides a relative error smaller than those ones obtained using Mendez et al. (1999) formulations and a higher correlation coefficient. It gives a better estimation of the drag coefficient for cases with low values of the Reynolds number and in which the plant movement is considered.

3.3.4 Analysis of drag force exerted by the flow on plants

A good estimation of the drag force produced by the flow on the plants can be used to study the vegetation survival or the possibility of having shoots torn off. As it has been demonstrated in previous sections, the modelling of the hydrodynamics processes produced by the plant on the fluid is very accurately considering vegetation with different mechanical properties. The difference lies on the value of the drag coefficient used to estimate the momentum damping exerted by the plants on the flow. However, when the effect of the fluid on the plant is calculated, flexible vegetation has to be considered in order to compute the wave plant excursion due to the waves since the velocity developed inside the meadow is the relative velocity between the flow and the plant motion and the drag force depends on this velocity.

Considering the coupled modelling the drag force is estimated as a function of the relative velocity. Therefore, the drag force exerted by the fluid on the plant is estimated more precisely with the presented model owing to including the plant motion.The drag force on the plant is estimated by vertically integrating the relative velocity determined by equation (5) using equation (1) to obtain the total force exerted over the plants. Figure 3.25, Figure 3.26, Figure 3.27 and Figure 3.28 display the drag force simulated numerically by the model. The force is presented in the plots per shoot and running meter.

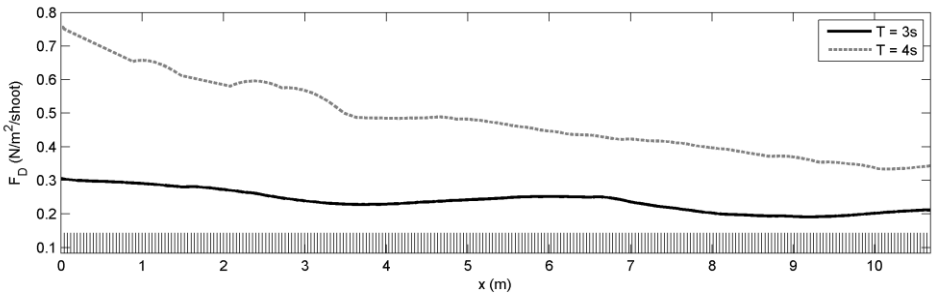

Figure 3.25 Drag force evolution along the vegetation meadow for two cases with different wave period: H = 0.4m, h = 2.2m, N = 360m-2, and T = 3s, black solid line, and T = 4s, gray dashed line.

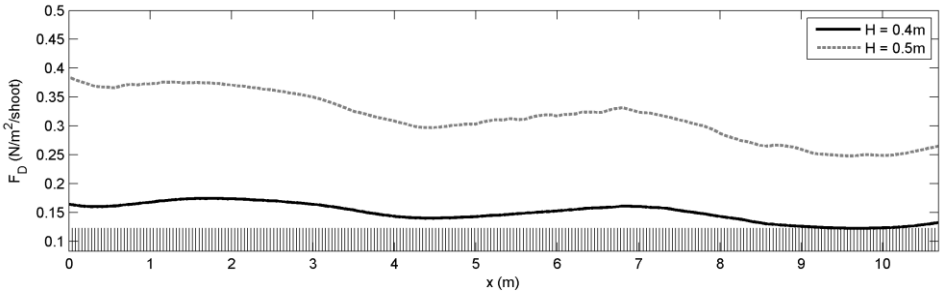

Figure 3.26 Drag force evolution along the vegetation meadow for two cases with different wave height: T = 3s, h = 2m, N = 360m-2, and H = 0.4m, black solid line, and H = 0.5m, gray dashed line.

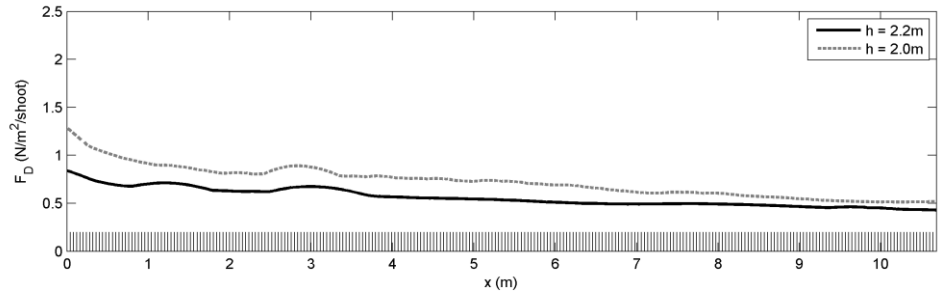

Figure 3.27 Drag force evolution along the vegetation meadow for two cases with different water depth: H = 0.5m, T = 3.5s, N = 360m-2, and h = 2.2m, black solid line, and h = 2m, gray dashed line.

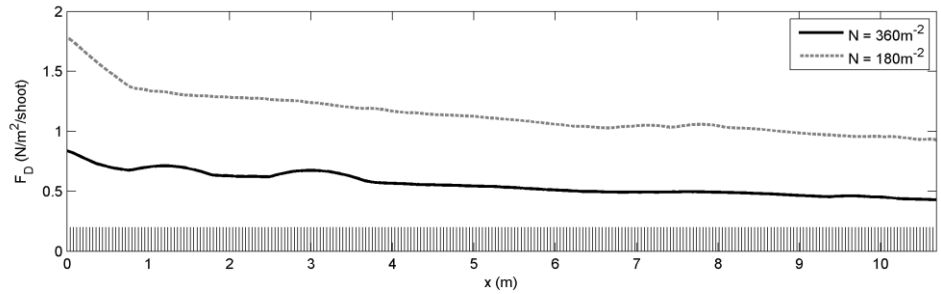

Figure 3.28 Drag force evolution along the vegetation meadow for two cases with different vegetation density: H = 0.5m, T = 3.5s, h = 2.2m and N = 360m-2, black solid line, and N = 180m-2, gray dashed line

Figure 3.25 shows the influence of wave period in the drag force evolution along the vegetation meadow. Two cases with a vegetation density equal to 360shoots/m2, h = 2.2m, H = 0.4m and T = 3 and 4s are considered. A direct relationship between the drag force and the wave period is observed obtaining larger values of the drag force with higher wave periods. A reduction in the drag force at the beginning of the meadow is observed, yielding a 35% reduction along the first four meters and a gross damping of 55% at the rear end of the vegetation field.

The influence of wave height is also evaluated in Figure 3.26 considering two cases with N = 360shoots/m2, h = 2m, T = 3s and H = 0.4 and 0.5m. Higher values of wave height induce larger drag forces in the field as expected.

The water depth influence is evaluated in Figure 3.27. Two cases with H = 0.5m, T = 3.5s and N = 360shoots/m2 are compared considering two different water depth, h = 2.2 and 2m. The increase in relative depth produces an increment of drag force on the plantdue to the higher velocities of the fluid at the meadow since there is not breaking waves.

Finally, the influence of the vegetation density is studied. Figure 3.28 shows the drag force evolution along the meadow for two different vegetation densities (180 and 360 shoots/m2) under the same wave conditions (H = 0.5m, T = 3.5s and h = 2.2m). The results shows that the force on the individual shoots is higher for cases with lower plant density as expected.

3.4 Conclusions

In this chapter the modelling of wave interaction with flexible swaying vegetation is addressed by solving numerically the RANS equations including the presence of the submerged plants in the model by a drag force and the turbulent flow by means of a k-ε model with closure equations incorporating the effect of vegetation in the flow. The fluid flow solution is coupled with a governing equation of the plant motion considering a linear deformation of the plant.

The new coupled model allows estimating the drag force exerted along the vegetation field as a function of the relative velocity between the fluid flow and the vegetation motion. The model ability to reproduce wave damping and the velocity field inside and outside the vegetation meadow is tested against different experimental setups, considering small and large-scale tests, swaying and no swaying plants.

Comparisons reveal a very good agreement between experimental and numerical results existing drag coefficient formulas for cases in which the vegetation swaying can be neglected. However, for flexible swaying plants it is shown that the best possible results can only be achieved by considering the coupling of the flow and the plant motion and by introducing a new drag coefficient formula which extends the range of Reynolds numbers previously explored.

In such a way, the new model provides very good comparisons with large-scale and flexible vegetation experiments for wave damping and velocity fields, inside and outside the meadow. Many of the limitations of existing models are overcome, opening the possibility to advance in

the understanding of the two-dimensional interaction of real sea states with aquatic vegetation of diverse mechanical characteristics and geometries.

"Remember when discoursing about water to induce first experience then reason"

Leonardo da Vinci

4

GUIDELINES FOR PHYSICAL MODELLING OF COASTAL SALT MARSH HYDRODYNAMICS USING REAL VEGETATION

Summary

The growing interest on incorporating nature based solutions and ecosystems services as part of the coastal protection schemes has resulted in a large amount of recent literature focused on the understanding and modelling of wave and current interaction with natural coastal landforms such as salt marshes. With this purpose, experimental modelling under controlled conditions, using flume or basins, has been one of the preferred options. However, due to the inherent complexities associated with this approach, to date most of the experiments available in the literature are based on wave flume experiments using vegetation mimics. The existing demand for understanding the relevant processes requires a step forward, being experimental modelling with real vegetation at both a relevant large scale and sufficiently large water depth. In response

to the needs foreseen, this chapter attempts to provide some useful guidance based on the experience gained from a unique set of experiments carried out at a large wave basin including wave and current interaction with real salt marsh vegetation. The chapter reports on the plant collection or growing strategies, plant properties, physical set-up, instrumentation, experimental strategy and dismantling, proving guidelines aimed at being helpful for future experimental efforts at the interface between engineering and ecology.

4.1 Introduction

During the present era of global change, sustainable coastal protection is of growing importance. Hence, knowledge about the mitigation of flooding and erosion hazards with low environmental impact structures is of great interest (Duarte et al. 2013; Temmerman et al. 2013; Möller et al. 2014). Coastal vegetation like salt marshes can play an important role in dissipating energy from waves and currents. They provide services with a high ecological and economical value (Constanza et al. 1997), which in part are related to their capacity to dissipate hydrodynamic energy (Millenium Ecosystem assesement; United Nations 2005; Nagelkerken 2000; Valentine & Heck 1999). An increasingly recognized, yet not fully understood service provided by coastal ecosystems, is their ability to contribute to coastal protection by attenuating waves, stabilizing shorelines and reducing flood surge propagation (Bouma at al, 2014). All of them will be relevant in the next decades due to the increasing storminess and the increment of the sea level rise (FitzGerald et al., 2008; Gedan et al., 2010).

The ability of tidal salt marshes in significantly attenuating wave energy has been broadly studied (Wayne, 1976; Knuston et al., 1982; Asano et al., 1996; Möller, 2006; Barbier et al., 2008; Koch et al., 2009), revealing that this may be of great importance for coastal defense (Leggett and Dixon, 1994; Möller et al., 1999; Yang et al., 2008; Barbier et al., 2008; Koch et al., 2009). Attenuating hydrodynamic energy is also essential for tidal marshes to follow sea-level rise by accreting sediment (Leonard and Reed, 2000; Bouma et al., 2005a; Wang et al., 2006; Yang et al., 2008). Hence, from the perspective of both coastal defense and nature conservation in terms of salt-marsh management, there exists the need for an in-depth understanding on the way in which wave and current energy is attenuated by salt marshes. Compared with the large number of studies that have investigated currents in tidal wetlands (e.g. Leonard and Luther 1995; 2002; Shi et al., 1995; Allen, 2000; Christiansen et al., 2000; Neumeier and Ciavola, 2004; Bouma et al., 2005b; and references therein), relatively few studies have been focused on wave attenuation (Wayne 1976; Knutson et al. 1982; Möller et al., 1996; Yang et al. 2009), or even lower on the

study of the attenuation combining the action of waves and currents (Ota et al., 2004; Li and Yan, 2007; Paul et al., 2012).

Although most of the works existing in literature have been focused on addressing the energy damped by salt marshes, it is difficult to lead to generalizations due to the difficulty of reproducing both realistic hydrodynamic conditions, including waves and currents, and a good representation of the mechanical behavior and geometrical characteristics of the plants. In the field, both vegetation characteristics and hydrodynamic conditions cannot be properly controlled. As a result, the conclusions from the available field studies on wave attenuation attend to specific locations on how different vegetation types affect wave attenuation, and how this depends on hydrodynamic forcing (Yang et al. 2009, Ysebaert et al. 2011). Moreover, seasonal biomass changes are highly relevant, especially in tidal salt marshes in the Temperate NE Atlantic where the aboveground plant biomass can be partly or completely lost during winter. This is really relevant due to the loss of ecosystem services. On the other hand, flume experiments have led to generalizations, by showing that wave damping by salt marshes is strongly affected by plant traits like rigidity, but also by vegetation characteristics, like vegetation density and standing biomass (e.g., Bouma et al., 2005a; 2010). Similarly, also for submerged aquatic vegetation, biomass is a dominant factor in explaining the vegetation wave attenuating capacity (e.g: Penning et al., 2009, for macrophyte species). In addition to this, a recent study on seagrass surrogates showed that imposing currents on top of the waves, strongly reduces the wave attenuating capacity of vegetation, and that the magnitude of this effect depends on shoot stiffness (Paul et al., 2012). However, vegetation structure, plant biomass and traits determining shoot stiffness differ strongly among coastal plant communities (pioneer zone, lower and upper salt marsh) so that wave attenuation is expected to vary between communities and plants dominating them (Bouma et al. 2005a, 2010).

Consequently, the role of vegetation structure in terms of wave attenuation remains relatively poorly understood, and modelers miss sufficient experimental data to validate their models across vegetation types. It seems essential to use real vegetation to get realistic results to enhance current understanding of ecological trade-offs associated to plant growth strategies. The use of mimics (based on plastic or flexible materials) or idealized vegetation (cylinders) is present in the literature (Augustin et al., 2009; Anderson and Smith, 2014), but far from providing realistic results. Although scaling laws to preserve plant mechanical conditions are used (Ghisalberti and Nepf, 2002), it is very difficult to find materials to represent both geometrical (shoot and leave structure) and mechanical (bending and stiffness) properties, in accordance with a hydraulic scaling. Open questions about the use of surrogates in laboratory experiments are arisen, such as geometrical representation of the plants (constant or variable height, width and thickness), spatial distribution of the plants (regular and/or random

arrangements) or plant fixing system to the bed (reproduction of the root characteristics: rigid or flexible). Moreover, the number of experiments using real vegetation under controlled flow conditions in a laboratory is low, mainly because of the difficulty of using and/or obtaining plants. Aspects such as collecting seed, growing or keeping plants alive and their properties during the experiments is not an easy task to solve.

The present contribution shows a methodology to perform eco-hydraulic modelling of salt marshes using real vegetation in order to determine the efficiency of plants to dissipate energy from waves and current. The novelty of the experimental work presented here is to study three dimensional wave and current interaction with real salt marshes, using both collinear and non-collinear waves and currents. Two different salt marshes species are considered due to their different biomechanical properties and standing biomass while they both can act as pioneer species in estuaries (Bouma et al. 2010): *Spartina anglica* and *Puccinellia maritima*. The methodology proposed here for conducting experiments with living plants in a basin, covers different steps from the collection and growing of the plants up to the way to perform the experiments. Although existing guides are already available in the literature, which point out the more important factors to be considered (e.g: Frostick at al., 2014), the present work shows also a case study where the methodology is successfully applied. The main objective is to provide a general methodology to address running experiments with living plants and considering both waves and current conditions, with the aim of extending both our understanding from an ecological and an engineering perspective.

The chapter is organized as follows. Section two is devoted to the identification of the experimental needs to perform experiments with real vegetation. Section three is focus on detailing the methodology, covering both practical and technical issues for the experiments presented here. The physical set-up, including the details about the flow conditions and the measurements, is introduced in section four. Section 5 presents a set of recommendations proposed based on the experience gained from the experiments. Finally, some conclusions are drawn in the last section.

4.2 General considerations for the use of real plants in wave basin experiments

When planning wave-basin experiments with living plants, a series of initial considerations have to be made in order to analyze the feasibility and the potential quality of the work to be carried out. In our work, the conceptual aim of the experiments was to analyze the wave damping and flow alterations due to wave and current interaction with salt marsh vegetation

patches/meadows considering the effect of different hydrodynamics, plant traits and meadows characteristics. Large-scale basin experiments using real vegetation was the preferred option in order to: 1) consider the collinear and non-collinear waves and currents; 2) avoid possible scale effects and 3) overcome the well-known limitations inherent to the use of mimics (Frostick et al. 2014). Addressing our overall objective via such basin experiment raises a series of important relevant questions regarding issues such as: the selection of the most appropriate species for the experiments; the source, amount and survivability of the selected plants; the geometric experimental set-up; how would plants be attached to the substrate to built a meadow; how would be the length of the experiments affect the conditions of the plants; what would be the water depths, waves and currents to be tested and how would plants response to them; what were the measurements to be made and the appropriate equipment and the last but not the least how would using real vegetation affect the logistics and operation of a large-scale experiment.

Although it is difficult to summarize all the different open questions presented during the experiments since different options may vary according to the species to be tested, the characteristics of the facility and the previous experience, a selected set of issues found to be the most relevant are addressed in this section. Whereas some of them have been treated in Frostick at al. (2014), in this chapter some general guidance is given providing the application to a real case.

4.2.1 Growing versus collection

For conducting flume experiments with real plants, once a given species has been selected, the question of whether plants should be grown on site or should be collected from nature is probably the first aspect to be answered (see sketch in Figure 4.1). Both possibilities carry advantages and disadvantages, and expenses should not be underestimated. Therefore, the choice for the planned experiment may vary from case to case. The questions below shall serve as orientation help:

- Do we know the ecology and phenology of the species?
- What is the quantity of plants needed for the experiments?
- Do we have the facilities and can we organize the logistics for growing?
- What is the availability of seeds? Can they be easily found and/or collected?
- What is the availability of plants? Can they be easily found and/or collected?

- Is it likely to obtain an official permission for collecting the seeds or plants?
- Can we provide the required working power during the planting and growing season?
- How long will the plants need to reach the required size and density?
- Is there any information about growing success?

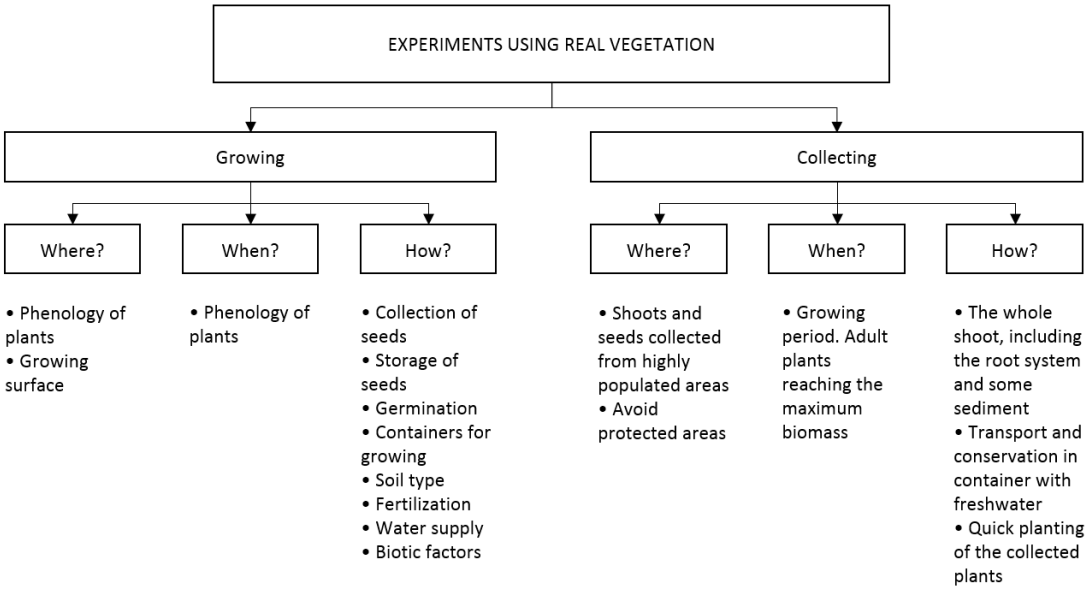

Figure 4.1 Flow chart: initial questions about collecting and planting strategies for using plants in lab experiments.

4.2.2 Growing

To develop a growing scheme a number of points have to be considered to determine the questions where, when and how to conduct the growing. A good knowledge of the ecology and phenology of the target plants is a fundamental need. It has to be decided whether to choose a growing area outdoor or a climate room based on the environmental restrictions of the species, the required quantity of plants and the available facilities. In addition, it has to be taken into account that most abiotic influences are two-sided; there will be not only a minimum, but also a maximum level of the factor that limits plant growth. Light intensity for example can be too low to assure a good growth. However, if light levels are too high, this may also damage the plants. Usage of a climate room allows growing a broader range of species and throughout the

year, but also restricts the amount of plants that can be grown, and may be more cost intensive. It is advisable to plan growing a higher number of plants than the actual number required for the experiments. It is advisable to check the onset and end of the vegetation growing period (temperature, day length, rainfall) before planning the time schedule of the experiment. Also, small-scale variation of climatic factors should be taken into account such as the proximity of buildings that can influence wind intensity, insolation or precipitation reaching the plantation area.

An important factor for time and finance planning is the availability of seeds. There are some plants for which it is possible to buy seeds, but in many cases, it will be required to collect seeds from the field. For doing so, it is necessary to check if an official permission is required due to environmental restrictions. Depending on species and quantity, collecting and preparing seeds can be a time intensive task. The seeds will have to be separated from remains of the inflorescence to prevent molding. The storage of the seeds in a dark and in most cases cool place is required to avoid germination impulses (e.g. light proof boxes in a fridge). In addition, irrigation frequency and amount should be determined. Sometimes it can be advisable to germinate seeds on petri dishes in a warm, moist and light room prior to planting. This can enhance germination success and plants can be spaced more evenly. In many cases germination impulses can enhance germination success. The type of germination impulse can vary between species, depending on their natural climatic conditions. Many species react positively when a considerable higher temperature is provided, e.g. some hours at 35° C.

The choice of the right container to grow the plants should be done attending to the rooting system depth of the selected species and the feasibility of transport and placing the plants into the experimental area. A good drainage system should be ensured, for example by making drainage holes in the containers and filling them with cotton wool to avoid soil loss. This avoids anoxic conditions in the soil which damage the plants, either by toxins, desiccation due to reduced water uptake by the roots or nutrient deficiency (Drew & Lynch, 1980).

Another important aspect is the selection of the soil to grow the plants. Choosing the right soil type is a question of the plant's requirements, availability and technical constraints in the flume or basin. Soil type, or in other word grain size distribution, does not only define rooting ability but also water holding capacity and retention of nutrients. Soil is important to be permeable and mixed with clay. A sandy soil will absorb water well, but will drain it as easy. More sand makes it easier for the roots to grow (faster), but also needs more fertilizer. That is, sand contains little nutrients and available nutrients are easily washed out, causing a low nutrient retention. Very clayey soils, in contrast, show a low infiltration rate but also a low drainage. The

water is held longer in the soil but is less available for plant roots due to high capillary forces in the soil pores. Silty loam shows the highest level of plant available water.

In most cases, fertilization will be advisable. Note that nutrients, while being necessary for plant growth in a certain concentration, can also be harmful at high concentrations (Hernandez-Soriano et al., 2012; Kronzucker et al., 2013). Using a slow-release fertilizer will lower the risk of over-fertilizing and assure a more continuous nutrient supply. Depending on the soil selection the nutrients addition to the soil will be higher or lower. In sandy soils nutrients are washed out faster and a higher additional supply will be needed. These nutrients can be added by fertilizers. Nutrient availability also depends on pH and organic matter content (Osman, 2013). Lack or excess of different nutrients can be recognized by certain changes in the plants' appearance (e.g., yellow leaves for N-shortage; purplish veins and stems for P-shortage). These signs can be checked in the respective specialized literature (e.g. Snowball & Robson, 1991).

An appropriate water supply is crucial for good plant growth, especially in the seedling phase when plants have very small roots. At that initial stage, a regular and well-distributed irrigation is very important. The use of sprinklers is also recommended to assure a good distribution of the water. To plan the irrigation times, the hazard of the plants being burnt while being wet during full sunshine should be considered. The loss of water due to temperature, wind and insolation has to be considered as well in order to preserve the best conditions for plant growing.

Additional to abiotic requirements of the plants like irrigation, nutrient supply and insolation, there are biotic factors that can influence plant growth. Competition by other species should be avoided by removing those (weed) plants. Pests in form of viruses, bacteria, fungi, insects, or slugs can cause considerable damage and should be taken into account when trying to identify the cause for a possible damage or reduced growth. Especially microbial pests are not easy to identify for the non-experienced, so consulting a professional can be a good solution. Some halophytic plants will grow better under application of saline water. If it is sprayed on the leaves it can also act as a (though weak) repellent against some pests. But be careful that spraying with salt water is not done when the sun is strongly shining, as this may cause osmotic-'burning' of the leaves.

The growing process could lead to failures in some cases and solutions must be found. One possibility is to transplant available plants from the field or areas with a high growing success. In order to permit resettlement of the plants after transplantation the root system should be damaged as little as possible. If for experimental or transport reasons the root systems have to be cleaned from soil, this can turn out to be difficult and time consuming and must be performed carefully. Plants with cleaned root systems can be stored for some time in water. Every act of

disturbance like collection from the field, cleaning of root systems, storage, transportation, and replanting is a stressor to the plant and can reduce their performance (in terms of re-rooting, growth and survival) after being transplanted. Therefore, it is advisable to keep every disturbance as small as possible. When transplanting vegetation from the field it should be considered that not all individuals might survive or continue growing in the long-term. Transplanting sufficient time ahead of the experiment will allow for root regrowth and stability of the plants but also carries some uncertainty about the survival.

Depending on the aim of the study, different sets of measurements of the vegetation will be required. To characterize the entire patch of vegetation, density, height and biomass can serve as good measures. Plant height can show a high variability and therefore it is recommendable to take sufficient replicates. Vegetation biomass is usually measured as dry mass / area. Density can also vary a lot from some places to others and a wide amount of measures should be considered in order to characterize the entire patch properly. Morphological traits like plant height, weight (dry or fresh) of the different plant organs (stem, leaves, roots), number, length, and onset of leaves, stiffness of stem and leaves can be used to characterize the plants behavior under hydrodynamic stress. These traits should always be measured on a representative subset, as there can be a noticeable intraspecific variation in a trait. Measurements should be taken at different stages of the growing period in order to monitor the plants growing. This rule applies for all biological measures.

4.2.3 Collecting

An alternative to growing plants from seeds is collecting them directly from the field. In most countries permission will be necessary to extract plants or collect seeds. If this will be easy or hard to obtain depends on the protection status of the target species and the protection status of the area it is growing in. In general, collecting plants is a considerably stronger disturbance of the ecosystem and thus it can be expected that permission is harder to obtain then for seed collection. Furthermore, apart from the question if a permission is required and likely to obtain, an own assessment of the impact of the disturbance on the ecosystem is advisable. There are also logistics constraints that should be considered when collecting a large amount of plants such as the availability of machines able to access the terrain or the store area.

The most recent example of a field collection strategy can be found in (Möller et al. 2014) where large-scale flume experiments were carried out using vegetated marsh blocks directly cut from a natural marsh.

4.2.4 Dismantling and disposal

The species selection can be performed attending to many different aspects such as biomechanical properties, growing time and success or attenuation capacity. This can lead to the selection of species which are not native from the area where the experiments are carried out. When no native species are used it has to be assured that no seeds, flowers, rhizomes or living plants leave the facility and thus have the chance on settling in nature. Special attention should be paid on the sediment that must be cleaned of any parts of clonal growth organs.

4.3 Plant growing and collection in the present experiments

Two different salt marsh species, both present in North European estuaries, were considered in the present experiments: *Puccinellia maritima* and *Spartina anglica*. They pioneer different habitat location in estuaries. *P. maritima* can be found in the middle and lower marshland, while *S. anglica* occurs in the lower marsh, i.e. pioneer zone (Bouma et al., 2010). Moreover, they are characterized by different biomechanical behavior. *P. maritima* can be considered a flexible plant with a high degree of bending, able to describe a waving behavior due to flow action. On the contrary, *S. anglica* is a stiff plant, with a limited degree of bending. This difference in stiffness yields a different species ability in trapping sediment or dissipating wave energy in natural environments as shown in Bouma et al. (2010). Plants morphologies are also different. The aforementioned features of the two selected species allow studying the influence of key plant traits in the attenuation capacity. Furthermore, the growing time of them is short, four months are enough to gain mature plants from seeds.

4.3.1 Growing

For both species seeds were collected at the Scheldt estuary (The Netherlands) to be later planted and grown at a laboratory area in Santander (northern Spain). Seeds of *S. anglica* were shipped in dormancy, protected from the light, in plastic containers with salty water. Containers were stored at 4ºC in dark conditions until germination. *P. maritima* seeds were also shipped in dormancy and protected from the light, in paper bags and dry conditions. Seeds storage was made at 4ºC.

The vegetated area needed to perform the experiments was a circle of 6 m of diameter, selected attending to the basin central pit dimensions (aspect described in detail in section four). The plants were grown in plastic boxes that later were used in the experimental setup. To fill the 6

m circle with the highest number of boxes, 92 big boxes (0.60 m long, 0.40m wide and 0.27 m high) and 18 small boxes (0.30 m x 0.40 m x 0.27 m) were required for each vegetation species. Nevertheless, to have available extra boxes 100 big and 25 small boxes were planted for each setup.

The number of seeds needed to obtain the required vegetated area depended on the species. The survival rate of *S. anglica* seeds was estimated on 5% and to cover the experimental area (28 m2) 6,000 seedlings were necessary (around 220 seedlings per square meter). Accordingly, 120,000 seeds were germinated. The germination was performed on petri dishes of 15 cm of diameter (70 seeds/dish), on permanently moist paper. To enhance the success, the germination was performed in a warm and moist room (±25-30 ºC) with natural light (left panel in Figure 4.2). The two germination batches of *S. anglica* were affected the fungus Periconia sp. which is known to be pathogenic to grasses. The estimated germination rate of the seeds of *P. maritima* was 100%. However, the roots of *P. maritima* seedlings are very fragile and transplanting in this stage might damage the plants. Consequently, the seeds of *P. maritima* were directly sown in the containers. To tackle possible eventualities, for the two species a higher number of seeds than required for the experiment were sown.

Boxes were placed outdoors in 5 double rows (right panel in Figure 4.2). For an easier subsequent transportation to the flume and to help drainage water to run below the planting area, boxes were placed over pallets. A major problem in this type of facility is the accumulation of water below the boxes, which may help algae and fungus to grow.

Figure 4.2 S. anglica seedlings in the climate room (left) and Outdoor plantation area (right).

To minimize the effect of box edges on the flow, which could induce additional and unrealistic roughness, boxes were filled to the top with sediment. The soil for growing was washed silica sand with a grain size of 200 µm (89 % sand, 9 % silt and 2 % clay) and 29m3 of sediment were used (1500 kg /m3). Two layers of slow-release fertilizer (4.5 g /dm3 of soil) were mixed with

the sand in the filling process (upper and bottom half). To prevent algae blooms no fertilizer was added to the top layer of sediment. Through the growing process additional foliar fertilizers were applied to plants limited by phosphorous (purple leaves) or nitrogen (yellow leaves). One reason for poor plant growth can be related to a change in soil pH due to fertilizer addition. Thus, the pH was constantly measured.

Although the two target species have a wide range of tolerance to salinity that allows them to colonize areas where other species cannot be established, their growth and photosynthetic capacity is enhanced by fresh water conditions. Accordingly, freshwater was used for irrigation. A drip irrigation system with 4 lines of pipes in big boxes and 3 lines in small ones was designed (Figure 4.3). The total hose length was about 900 m. The watering was set to start every 15 minutes, although it was adapted to the weather and stage of growing. Moreover, during hot days young plants were moistened by sprinklers early in the morning. To prevent the accumulation of water, two holes were made at the lower part of the boxes and filled with plastic pillow stuffing (synthetic cotton wool) for drainage. The presence of slugs and worms was avoided adding half strong salt water (17.5 g of salt /l) twice a week. Moreover, ecological pesticides were applied once a week after sunset to treat aphids (2 ml of piretrine and 1 ml of neem per litter of water) during three months.

Plants were grown outdoor from June to September, 2012. The growth rate is highly related with the air temperature. Based on the temperature range registered at Santander between 2006 and 2011 and on the time required for stems to achieve 30 – 40 cm of length (Bouma, 2012), four months were considered enough to achieve the required plants size.

Seedlings of *S. anglica* were planted individually in 10 cm depth holes (40 seedlings / big boxes; 20 seedlings/small boxes), once they reached 1.5 - 2 cm of height. The sowing of *P. maritima* was done with dry and wet seeds. Dry seeds were sown directly, while wet seeds were maintained in fresh water some days before sowing. It should be noted that none of the dry seeds germinated. Sowing density ranged from 1.5 g/m2 to 1.9 g/m2. Seeds were weighted, mixed with sand, scattered homogeneously on the boxes and covered with a thin layer of dry sand on the top. In the early germination stage, seedlings of *P. maritima* are extremely vulnerable to drought and light. Thus, to avoid plants to be burnt, seedlings were covered with a coconut net when bright sunlight. Additionally, a greenhouse-like coverage with mosquito net was built to protect the seedlings from birds.

The growth rate was monitored directly by measures and indirectly through pictures taken weekly (Figure 4.3). Growth was highly irregular and differences on the density and leaf length were observed for both species. Two weeks before the beginning of the experiments, the

average shoot length achieved within the small and big boxes was 28.4 ± 2.66 and 13 ± 1.89 cm, respectively. In most of the boxes neither the length (the expected length was 30 cm), nor the density was sufficient to perform the experiments. Consequently, one shipment with plants of *S. anglica* directly collected from the Scheldt estuary was planted in between the seedlings (see 3.2), which yielded the desired density (see 3.3). The differences observed in the boxes of *P. maritima* were highly related with the density of seeds sown. The boxes sown with a density of 1.9 g/m2 reached a maximum shoot height of 100 cm, grew extremely dense and some of them blossomed. Meanwhile, boxes sown with 1.5 g/m2 did not grow enough and they did not reach the required density. To homogenize the length and density of the boxes, some shoots from the dense boxes were transplanted into sparse boxes. Although, some of the roots broke when being taken out and replacing the plants the transplantation worked out well in achieving the desired density (see 4.3.3).

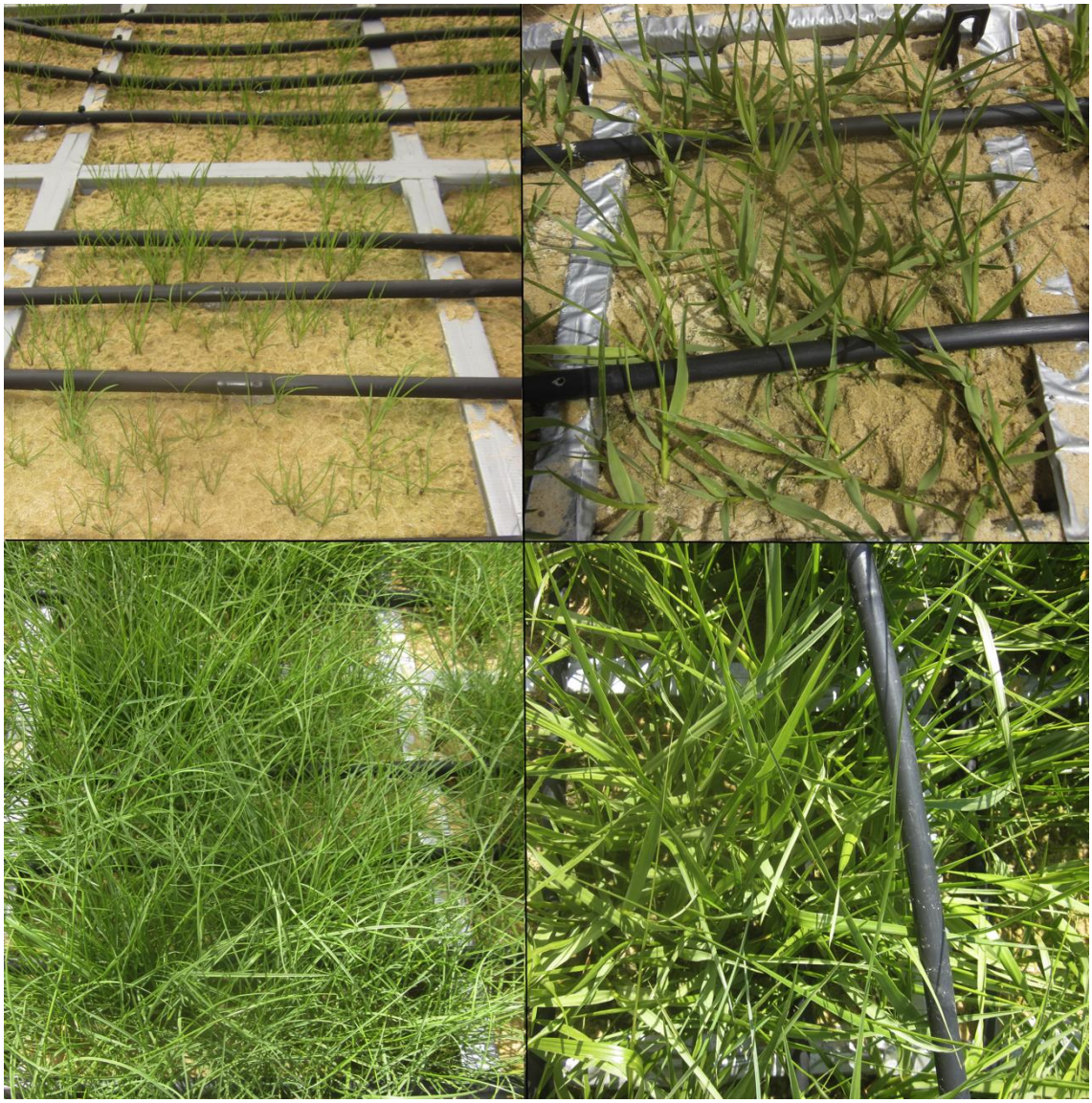

Figure 4.3 P. maritima (left) and S. anglica (right) growth. The start of the growing period is shown in the top panels and the end in the lower panels.

4.3.2 Collecting

The growing of *S. anglica* was not as successful as expected. The growth was scarce and the density lower than expected. Consequently, two weeks before starting the hydraulic experiments, around 6,000 plants were collected from the Eastern Scheldt estuary. To minimize the damage to above and below ground organs, plants were excavated with their root systems. For the transportation, root systems were cleaned from sediment, so that weight as well as

packing space was kept low and cleaned plants were stored in open plastic boxes with filtered seawater.

Plants were shipped two weeks before beginning the experiments and stored outdoor in open boxes with natural light, filtered seawater and fertilizer. Shoots were planted in the boxes 3 days before starting the tests. The length of the plants varied between 30 and 60 cm. To prevent loss of shoots with the water movement, plants were planted at 27 cm depth (bottom of the boxes) and the top of the sediment covered with pebbles. The number of shoots planted at each box depended on the initial density considering a desired final averaged density of about 700 shoots/m2.

4.3.3 Plant properties measurements

Density, standing biomass, plant traits and plant stiffness, including stem and leafs, were determined to characterize the plants. The average dry mass of the standing biomass (g DW m-2) and dry mass per shoot (both dried for 48h at 70ºC), were measured on representative subsamples at the end of the experiments. Subsamples for standing biomass were obtained by harvesting 15 boxes (10% of the total boxes). Dry mass per shoot was obtained by weighting 81 and 87 shoots of *S. anglica* and *P. maritima*, respectively, randomly selected and representative for the size distribution of the vegetation. Shoot density was obtained dividing standing biomass by the average shoot dry weight.

The finally used meadow density was 2436 shoots/m2 for *P. maritima* and 729 shoots/m2 for *S. anglica*. The meadow density was reduced in two sequential steps obtaining approximately the 66 and 33% of the original density for *P. maritima*, and only one for *S. anglica*, achieving 66% of the initial density in that case. With these density reductions, we targeted at having similar biomass levels for both species to be able to compare wave attenuation. As can be seen in Table 4.1, the biomass for the 66% of density for *P. maritima* is very similar to the one measured for the 100% of density for *S. anglica*. The same occurs for the 33% of density for *P. maritima* and the 66% of density for *S. anglica*. These density reductions were performed snorkeling over the meadow in order to avoid stepping on it and damage the plants. The density reduction of the whole meadow was performed in one day. Table 4.1 contains the target density obtained when the plant density was reduced by removing plants and the one achieved after the evaluation of the measurement existing in the meadow. Standing biomass was also determined for each configuration, as can be seen in Table 4.1.

Case	*Species*	*Target Density (shoots/m²)*	*Achieved Density (shoots/m²)*	**Biomass (g/m²)**
P100	*Puccinellia*	2436 (100%)		443
P66	*Puccinellia*	1608 (66%)	1389 (57%)	254
P33	*Puccinellia*	804 (33%)	877 (36%)	146
S100	*Spartina*	729 (100%)		290
S66	*Spartina*	481 (66%)	430 (59%)	171

Table 4.1 Vegetation conditions

Leaf traits were measured in subsamples of the 15 boxes selected for the monitoring (2 shoots/box of *P. maritima* and 3 shoots/box of *S. anglica*). Mean height, mean leaf width and mean number of leaves per shoot were evaluated by means of a statistical analysis carried out over the randomly chosen samples. Table 4.2 shows results obtained from the analysis for the mentioned properties and Figure 4.4 shows an example of one plant for the two species.

Species	*Average Height (cm)*	*Average leaf width (cm)*	*Average number of leaves per shoot*
Puccinellia maritima	47.29	0.30	5.5
Spartina anglica	28.40	0.60	5

Table 4.2 Mean plant dimensions for both species.

Figure 4.4 Mature P. maritima and S. anglica species.

Vegetation stiffness was measured by means of tensile strength test for both stems and leafs. Tests were performed in the Laboratorio de la División de Ciencia e Ingeniería de los Materiales (LADICIM) at the University of Cantabria, using plants, which correspond to the 100% density for both species (Figure 4.5). In order to preserve the biomechanical properties of the plants, tensile strength tests were carried out immediately upon harvesting plants from the nursery areas. Results for the Young's modulus of stem and leaf elasticity of both species are specified in Table 4.3. Although it is well known that biomechanical properties of the plants (stiffness and elasticity) are degraded along the time due to the plant stress during the performance of the experiments (Puijalon et al., 2005, 2008), it was minimized lowering the water level from the basin at the end of the day and keeping the plants exposed to natural light during the experiments. Although it was desirable to repeat tensile strength tests along the different stages of the experiments, it was not possible. In addition, the number of uprooted plants along the experiments was evaluated revealing quite stable mechanical properties.

Species	***Stem (MPa)***	***Leaf (MPa)***
Puccinellia	13	7.8
Spartina	164.2	77.6

Table 4.3 Young's modulus of elasticity for the stems and leaves of each vegetation species

Figure 4.5 Tensile strength test for S. anglica stem.

Plant measured properties were in agreement with the expected values considered when designing the experiments and these were representative of field conditions.

4.3.4 Dismantling

S. anglica is the result of chromosome doubling by *Spartina x townsendii* and the sterile hybrid between the cord-grass *Spartina maritima* and the introduced North American smooth cord-grass *Spartina alterniflora* (Nehring and Adsersen, 2006). This species has proven to be highly invasive in many parts of the world. Till now *S. anglica* is not cited in Spain, but *S. alterniflora* is catalogued as an invasive alien species (Sanz Elorza et al., 2004). Because of the high potential for natural dispersal of introduced aquatic species, precautionary measures were taken in the experimental setup dismantling. The main pathways of dispersal are whole plants, fragments of rhizomes or seeds to be introduced in the sanitation systems or leave the facility. To reduce the dispersal risk, plants were collected from the containers by hand and sediments were sieved. Plant remains were treated with herbicides, stored in dark conditions until dehydrate and calcined (500ºC, 24h). On the contrary, *P. maritima* is native from northern Spain and therefore, its disposing was less critical. However, the management of the plants and seeds was the same as for *S. anglica*.

4.4 Physical set-up

Experiments were performed in the CCOB (Coastal and Ocean Basin) laboratory at the Environmental and Hydraulic Institute "IH Cantabria" in Santander (Spain). The basin is 44 m wide, 30 m long and 4.75 m deep and it is capable to generate multidirectional waves and omnidirectional currents simultaneously, covering the objectives of the present work. Waves are generated using a segmented-type system formed by 64 independent wave paddles capable to generate multidirectional short and long crested waves. Although wave makers obey to both piston and flap-type motion, only piston-type was used in the experiments to better adept waves to shallow water conditions. Currents were created using 12 thrusters (900 mm in diameter) placed in a floor level below the basin bed. Water is pumped from the lower level, flowing up through a set of gates opened at the basin bottom level. Gates are disposed in two rows along the whole basin width, one close to the wave-makers and another one close by the opposite basin wall. Operating the thrusters accordingly, current is generated in the same or in opposite direction to waves (Figure 4.7). Although the wave generation device is equipped with an active absorption system, it was not used during the experiments. Wave-makers correction to absorb waves was not applied in order to ensure the same wave input signals to generate waves even when current was activated. In addition, several tests were performed to ensure that the energy dissipated by the passive absorbers (made of multi-layers of perforated screens), placed around the full basin perimeter was lower than 5%, and consequently did not affect to the measurements.

Vegetation was disposed taking advantage of a 6 m-diameter central pit located at the center of the wave basin, which can be lowered below the basin bottom up to 8 m. The pit is far enough from the gates allowing current to develop a uniform profile when reaching the meadow. Several tests were developed to confirm uniformity of profiles, by means of ADV measurements at different points in the water column before placing the vegetation in site. The level of the pit was adjusted down placing the boxes containing the plants inside, around 27 cm below the basin bottom. Groups of 4 plastic boxes containing plants were mounted over a pallet and they were moved with fork-lift inside the pit. The upper soil level of the boxes was set at the same level than the basin bottom. This allows saving time and efforts to ensure a smooth transition from the basin bottom to the vegetation patch. The other option to place the boxes in the basin is to build a transition slope long enough to ensure that velocity profiles affecting the vegetation respond to the target ones and they are uniform (Luhar and Nepf, 2011). Moreover, waves and currents were affected by a uniform bottom roughness across the test area corresponding to the basin concrete bed. In order to prevent washing up sediment from the boxes due to flow action, small gravel was disposed on the soil contained in the boxes filled up at the same level than the basin bed. Because the meadow was constructed using rectangular boxes and the pit

is circular, a platform made of wood was designed in order to cover the remaining space. Figure 4.6 shows the boxes set-up procedure and Figure 4.7 shows a detail about the boxes distribution. In order to keep the plants healthy, water level was lowered after the tests at the end of the day, keeping plants out of the water for almost 12 h per day. Although the basin is inside a building with a black roof, windows were kept open during the experiments in order to allow ensuring natural light reaching the plants, to preserve as close as possible natural conditions. Furthermore, the experimental timetable was fixed to work continuously in order to reduce the total number of days that plants were inside the basin.

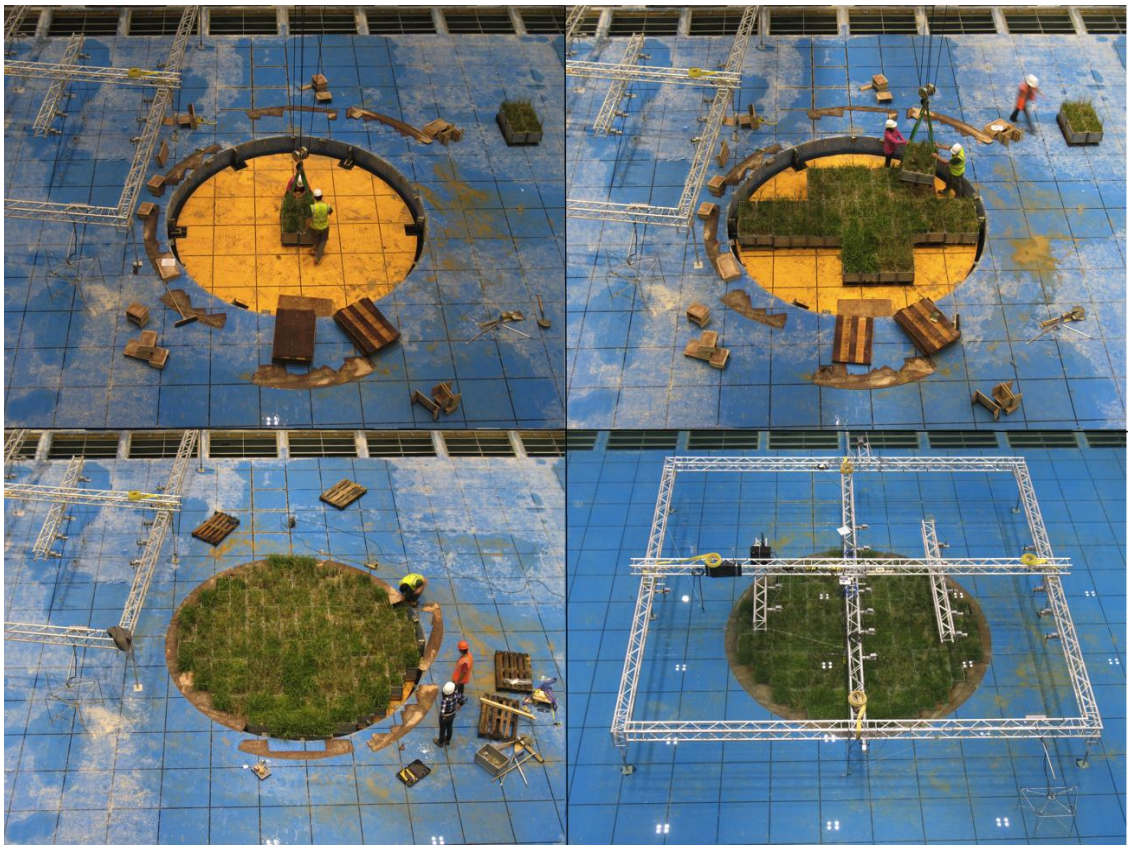

Figure 4.6 Boxes disposition in the lowered pit of the basin.

Free surface and flow velocities were measured during the experiments. Furthermore, a submerged camera was disposed to record plant movements and a top-side camera to record the tests. *P. maritima* tests were performed using 20 capacity free surface gauges and 3 ADVs to record the flow velocity. *S. anglica* tests were carried out using the same devices but including 8 extra free surface gauges (numbered in Figure 4.7 from 21 to 28). The position of the free surface gauges and the velocity ADVs is displayed in Figure 4.7. Crosses represent the location of free surface gauges. ADVs locations are plotted in the figure using triangles.

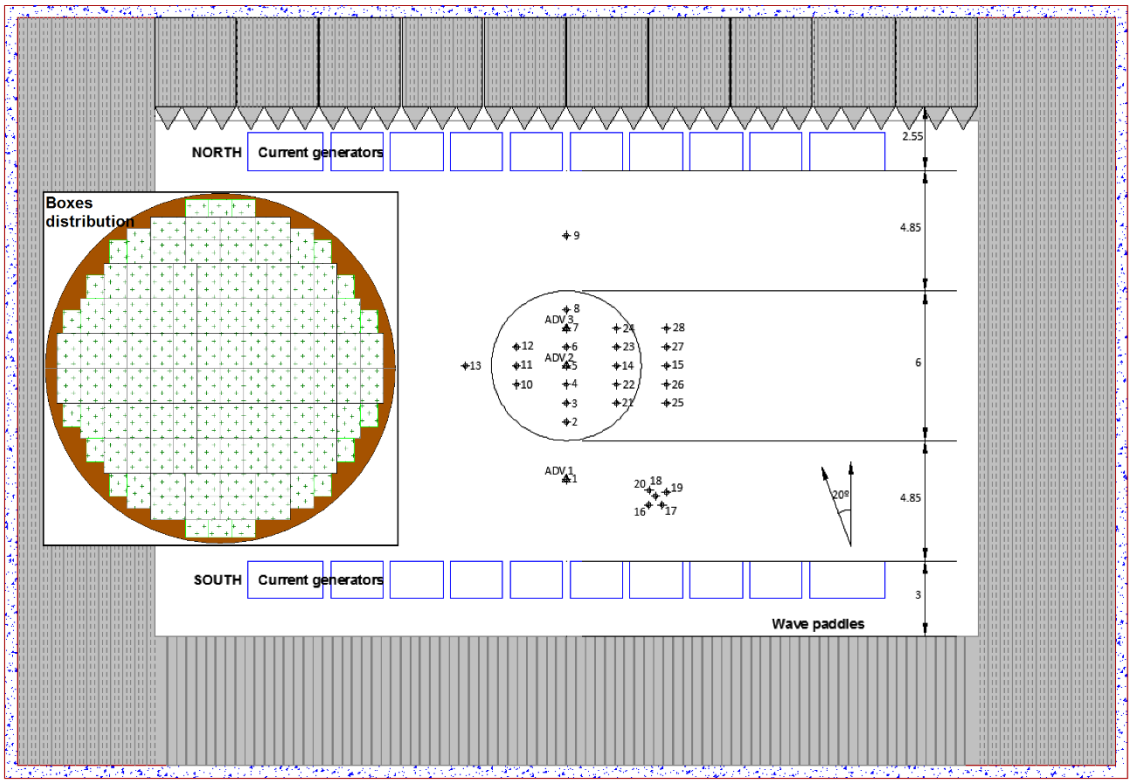

Figure 4.7 Free surface gauges and ADVs location sketch in the Cantabria Coastal and Ocean Basin. A detail of the distribution of the boxes in the pit is shown.

A group of five gauges was disposed close to the wave makers to calculate directional reflection (see gauges 16, 17, 18, 19 and 20 in Figure 4.7) using a Bayesian directional method. Two gauges were placed seaward (gauge 1) and leeward (gauge 9) the meadow in order to measure incident waves, from the wave-makers, and transmitted waves, from the meadow. The rest of the wave gauges were placed both inside (15 gauges) and outside (7 gauges) the meadow to record the spatial distribution of free surface. Gauges located inside were set following three alignments: along the diameter and at two lateral profiles in order to measure span wise free surface oscillations.

Velocity measurements were recorded using three 3-D Acoustic Doppler Velocimeter (ADV): two Vectrinos and one Nortek devices. The Nortek ADV was located seaward the meadow in order to evaluate incident flow conditions. The two Vectrinos were disposed inside the meadow, at the center of the pit and at halfway between the center and the leeward end. Velocity measurements were taken at a single elevation, 30 cm from the bed.

Synchronization of the measurements was performed using an external trigger to initialize both velocity and free surface measurements in order to easily relate free surface and velocity measurements. Both free surface and velocity were sampled at 120 Hz.

In order to prevent plant leaves entering the ADV measurement control volume, a special structure was designed (see Figure 4.8). It was made of plastic wires and installed at the ADV arm, protecting the ADV measuring sensor and keeping the measurement area free of plants. This system allows avoiding decreasing the number of shoots to be removed to create a clean area (cf. Luhar et al. 2010), minimizing the effect on the field density and consequently taking measurements under more realistic conditions.

Figure 4.8 Special structure built around the ADV

Wave Conditions	Type	H(m)|Hs(m)	T(s)|Tp(s)
R1	Regular	0.15	2
R2	Regular	0.20	2
R3	Regular	0.20	1.2
R4	Regular	0.20	1.7
R5	Regular	0.20	2.2
I	Irregular	0.12	1.7

Table 4.4 Wave conditions

P. maritima and *S. anglica* grow at the middle and upper tidal marshes and are permanently submerged only during flooding events. Since this research was focused on wave attenuation capacity of the plants during extreme events, four different water depths (h) were considered during the experiments, 0.40, 0.60, 0.80 and 1 m to be representative of flooding conditions. Five regular and one irregular wave cases were tested. Wave heights and wave periods were selected attending to wave conditions presented in estuarine zones and under extreme events. The location of *P. maritima* and *S. anglica* in the estuary corresponds to areas sheltered from large waves, consequently wave conditions are representative of average natural conditions at prototype scale. Details about wave characteristics are presented in Table 4.4. Regular wave conditions were generated using non-linear wave generation. Wave energy was distributed for irregular wave tests according to a JONSWAP-type spectrum with a 3.3-enhancement factor. Only one current velocity (Uc=0.3 m/s, depth averaged value) was considered, acting collinearly in the same and in opposite direction to wave propagation. The value of current velocity was selected according to the ones presented in Bouma et al. (2013) to reproduce conditions similar to natural environments. Additional tests were performed considering an obliqueness of 20º between waves and current.

For all the cases, 200 waves were measured. When waves and currents were tested simultaneously, waves were activated first to allow the wave train to develop. The current was activated next, leaving an extra time to allow the current to reach a steady stage before recording started.

As a summary, wave conditions specified in Table 4.4 were tested combined with the two current conditions, for the two species with the 100% of density and water depths 0.40 and 0.60 m. R1 and R3 wave conditions combined with currents were also tested for 0.80 and 1.00 m water depth. Vegetation with a lowered density was tested under R1, R3 and IR wave conditions combined with currents for 0.40 and 0.60 m water depth. Only R1 and R3 were considered for h = 0.80 and 1.00 m. R1, R3 and IR were tested with a 20º angle with respect to current direction for both current conditions and h = 0.40 and 0.60 m. The total number of experimental runs is 186 and they are summarized in Table 4.5.

Vegetation	*Wave conditions*	*Water depth (m)*	Current
P100, S100	R1 – R5, I	0.40, 0.60	+C, -C
P100, S100	R1, R3	0.80, 1.00	+C, -C
P66, P33, S66	R1, R3, I	0.40, 0.60	+C, -C
P66, P33, S66	R1, R3	0.80, 1.00	+C, -C
All	R1,R3,I θ=20º	0.40, 0.60	+C, -C

Table 4.5 Performed tests. +C means current in the same direction than wave propagation. –C means current in the opposite direction to waves.

Regarding the timetable to perform the experiments, one day was needed to introduce the boxes in the basin for each species and one day was spend for each meadow density change. Six days were used to perform the tests considering the 100% of density for both species and four days were needed to test the density reduction cases. This led to one month of experiments without interruption since the tests were performed continuously to diminish the total time plants were inside the basin in order to keep their properties unaltered.

4.5 Experimental operation and logistics: recommendations

Based on the experience gained from the unique set of experiments described in this work, a list of recommendations for each experimental step can be provided aiming at being helpful for future experimental efforts developed at the interface between engineering and ecology.

The first part of the experiments was the plant growing. During the four months spent to develop this part of the experiments, the next recommendations were learned:

- Germination is determinant and depends on many different factors that must be controlled to achieve the total number of seedlings needed for the experiments. In the experiments described here two germination batches of *S. anglica* seeds were carried out following the same procedure and using seeds collected in the same area, but in different years. The germination rate for the second batch was much lower than the one achieved for the first batch. So testing of seed batches for viability in terms of germination is highly important. Additional factors such as the emergence of fungus in the petri dishes or seeds, a change in

the room moisture percentage or temperature, affect the germination success. To prevent the presence of fungus, the use of gloves are advisable. Regarding the sowing of *P. maritima*, it was done with dry and wet seeds. Dry seeds were sown directly, while wet seeds were maintained in fresh water some days before planting. It was observed that none of the dry seeds grew up.

- Having a second (back-up) option to obtain plants is advisable, and the associated time and efforts should be considered. In our experiments the growing of *S. anglica* was not as successful as expected and 6000 plants were collected in the Eastern Scheldt estuary. In total the collection and cleaning of 6000 plants took about 100 working hours.

- Growing can be performed in a greenhouse. However, the construction and the associated costs should be taken into account. When it is most convenient to grow the plants close to the hydraulic experimental facility, some aspects should be considered. An area large enough to ensure adequate climatic conditions such as insolation hours or low wind intensity is needed. Furthermore, plants should be protected from birds, bugs and fungus. In our experiments, a greenhouse-like coverage with mosquito net was built and half strong salt water was added twice a week. Furthermore, ecological pesticides were applied once a week to treat aphids and fungus during three months. To avoid sunlight degradation it is advisable to apply pesticides after sunset.

- The water supply must be designed according to climatic conditions and the plants necessities. A drip irrigation system covering the plantation area is advisable to avoid wasting water. Our experience with salt marshes confirms that using fresh water to growth them is a good practice.

- Soil selection is a key factor and it depends on the species and their water needs. A common practice is to add fertilizers to the soil in order to enhance the plant growing. In our experiments, two layers of slow-release fertilizers were added and additional foliar fertilizers were added depending on the leaves colour. It is advisable to take into account this aspect since the colour of leaves is an indicator of the plants needs. For example, purple veins of the leaves may indicate they are limited by phosphorous while yellow leaves may point at nitrogen limitation. Moreover, plants dying can be related with pH changes because of the fertilizer added. Then, soil pH measurements are advisable.

- It is extremely important to avoid the introduction of an invasive species in the local environment when foreign species are used. Therefore, this aspect should be considered from the beginning. If an invasive species is (for good reasons) the topic of the study, precautionary measures must be taken. In our experiments, *S. anglica* is known to be an

invasive species. Hence, it was first of all ascertained that the growing area did not cause a risk of spreading. Moreoevr, at the end of the experiment, plants were collected by hand and sediments were sieved to treat them with herbicides, store the plant remains in dark conditions until dehydrate and calcine them.

The second part of the experiments were the set of tests developed in the basin. One month were spend to run the different tests with the different species and vegetation densities. The key aspects learn in this second part are highlighted here:

- The best option to place the vegetation inside the basin should be studied since that determines the time and effort needed and the influence on the generated flow conditions. In our case, the capability of lowering the tap of the basin pit was used to avoid building a platform and ensure a smooth transition from basin floor to the vegetated area. Plants were growing up in pallets, which were used later to lift the boxes and to introduce them in the basin.

- After placing the vegetation in the facility it is advisable to run a short wave train test to remove cut leaves or unconsolidated sediment from the facility and be ready to start the tests. Dust present on the plant leaves or in the soil contained in the boxes is preferable to be wash out in order to improve plant visualization specially when submerged video cameras are used. This washing out may to some extend be achieved by spraying the pans before bringing them into the facility.

- An aspect that should be considered when real vegetation is grown, is the uniformity of the meadow. When growing plants their characteristics may vary along the meadow. For that reason, the different elements that conforms the meadow should be disposed trying to minimize this effect. In our experiments, five different types of *S. anglica* boxes were identified regarding their plant characteristics. The different types where placed in the basin trying to obtain a uniform meadow and their location was mapped in order to relate it with possible developed flow patterns.

- The use of floating bodies can be useful in order to identify rapidly the developed flow patterns all along the basin and to select the best positions for the different sensors used to measure flow characteristics. In the present experiments, oranges were used as tracers in order to check flow patterns under wave and current conditions.

- Before running the tests, amount and sensors type to be used for monitoring the experiments should be selected. When flow characteristics are measured inside the meadow, some problems arise. Resistive free surface gauges are not a good option since the

interference of the plant leaves with the metallic sensor wires lead to wrong measurements. Therefore, capacitive gauges are more advisable and they were used in our experiments. Moreover, capacitive gauges are more stable than resistive ones and daily calibration is not needed saving time during the performance of the tests. Regarding velocity measurements, ADVs need for an area where plants are not interfering. One option is to remove shoots to create a clean area in the measurement control volume. However, in order to reduce the number of removed shoots in our experiments, a special structure was built using plastic wires able to keep the measurement area free of plants. Removal is itself a critical issue because an excessive remove of plants could alter locally meadow density.

- It is advisable to calibrate hydrodynamics conditions before starting the experiments specially when waves and currents are flowing simultaneously. It clearly depends on the relative magnitudes. In our tests waves were activated prior to current. Conversely, current velocity did not allow the waves to develop.

- When density cuts are desirable to reduce meadow density for additional tests, they should be done without damaging the plants. Depending on the size of the meadow this could be a challenging task. When plants cannot be reached from the meadow edge one option is to move the boxes, when it is possible, to have access to all of them. Another option is to build a walkway over the meadow to reach its center without moving the plants. The first is a very time consuming and risky action since soil and plant conditions can be altered significantly and test repeatability can be lost. The latter is demanding an external infrastructure special for each single test. In our experiments, cuttings were performed snorkeling with an amount of water enough to cover the plants. Two divers were able to cut the whole meadow without disturbing the plants. This practice was faster.

- It is important to maintain the plants characteristics along the experiments. Biomass measurements along the experiments is an advisable practice in order to check plants health and to qualify the stress due to flow action. It is directly related with attenuation capability. In our experiments, biomass was measured for both species at the beginning and at the end of the experiments. *S. anglica* biomass changed a 6 % from the beginning to the end of the tests. A loss of 11 % was qualify for *P. maritima*. These values were considered acceptable.

4.6 Conclusions

While working with real vegetation in physical experiments at large-scale facilities provides a unique way to get closer to reproducing the natural field environment under controlled

conditions, a successful application of this experimental approach is not exempted from complexity. Using real plants or other living organisms brings new challenges for conventional hydraulic facilities both in the planning, operation and overall logistics of the experiments that can only be faced under a cross-disciplinary approach at the interface between ecology and hydraulic engineering. While removal or collection of living plants in the field can have severe consequences to the environment and hence be limited by environmental restrictions, growing plants may require logistically and expertise-wise very demanding conditions limiting the number of facilities where such experiments can be carried out. Besides, the fact that plant conditions are highly sensitive to housing and experimental conditions and their variations with time, introduces new variables not usually acquainted in conventional hydraulic engineering, but are essential hurdles to take to progress current understanding.

While mimicking plants with different materials and similar stiffness at different scales has been the most extended approach to understand their hydrodynamics and transport processes, it is clear that scientific progress is linked to both increasing field work and controlled experiments with real vegetation without scaling.

Notwithstanding the important contributions made so far in the standardization of the current knowledge of physical modelling in ecohydraulics (Frostick et al., 2014), the experience in wave basins with real vegetation for coastal applications, especially at large scales is very limited. The present experience and recommendations may contribute to speed up the practice of using live vegetation in hydraulic engineering experiments.

"All water has a perfect memory and is forever trying to get back to where it was"

Toni Morrison

5

LARGE-SCALE 3-D EXPERIMENTS OF WAVE AND CURRENT INTERACTION WITH REAL VEGETATION

Summary

This chapter aims to assess the influence of different flow and vegetation parameters on the wave attenuation provided by two contrasting salt marsh species: *Puccinellia maritima* and *Spartina anglica*. Different water depths and wave parameters (height and period) are considered for both regular and irregular waves with and without an underlying uniform current coming from different directions. The study of the submergence ratio (h/h_v) influence shows that wave damping coefficient rapidly decreases as the plant submergence ratio increases. The high nonlinearities found in the wave-current interaction lead to different wave damping patterns in comparison to wave-only conditions. A smaller wave damping is found for waves and current acting in the same direction and an increase in the wave damping rate is obtained for

waves and current flowing in the opposite direction. These wave and current tests allow for the studying of the energy dissipation produced by the vegetation, increasing our knowledge about flow and plant interaction in estuarine conditions. The biomechanical properties of the two real salt marshes used in the experiments are also evaluated and related to wave damping revealing a higher attenuation for stiffer vegetation. Both, the vegetation density and the biomass strongly influence wave damping. Higher density and biomass values lead to higher attenuation rates for both species.

5.1 Introduction

In recent years, interest in how vegetation can help to attenuate energy from waves and currents has grown considerably, aiming at promoting natural-based solutions to address both adaptation and disaster risk reduction (Duarte et al. 2013; Temmerman et al. 2013; Möller et al. 2014). Coastal populations are exposed to a serious risk to human life and property since global climate change is increasingly exposing vulnerable areas to floods and coastal erosion (McGranahan et al. 2007; FitzGerald et al. 2008). Decades of research on how wetland vegetation can play a role in this aspect suggests that these low environmental impact structures have the capability of dissipating energy from waves and currents (Chapman VJ., 1974; Constanza et al., 1997; Gedan et al., 2010; Borsje et al., 2011). Protection provided by salt marsh vegetation in temperate regions has led to a growing number of physical experiments, both at the laboratory and field scale, to get a mechanistic understanding of how these species interact with hydrodynamics. Many complex physical processes are involved in the interaction of waves and currents with aquatic vegetation. Hydrodynamic parameters such as wave conditions (height and period), wave and current interaction or plant submergence ratio have been shown to be determinants in the flow energy dissipation provided by intertidal vegetation. Furthermore, plant ecological and morphological characteristics such as plant stiffness, vegetation density or biomass influence the degree of attenuation provided.

Field campaigns have been carried out to characterize the plant characteristics (e.g., Temmerman et al., 2003; Feagin et al., 2011) as well as their induced hydrodynamic attenuation (e.g., Ysebaert et al., 2011; Jadhav and Chen 2012). However, hydrodynamic conditions cannot be properly controlled in the field and additional issues related to natural seasonal variation of plants and the environment are also present. Accordingly, conclusions drawn from these studies have not led to generalizations and therefore, results are site and time specific. In spite of this, field studies provide measurements under realistic physical conditions.

Several laboratory experiments have also been performed to study the flow/vegetation interaction under better-controlled conditions. Most of these studies have been performed using vegetation mimics (e.g., Augustin et al., 2009; Anderson and Smith, 2014). Although the Cauchy number, which relates the plant elastic force and the inertia (Ghisalberti and Nepf, 2002), is used to design the mimics, the mechanical replication of plant characteristics has fundamental limitations. In addition, plant morphology is often simplified and not well reproduced. One factor, which emphasises these limitations, is the experiments' scale. The plant characteristics rescaling leads to simplifications and difficulties in preserving realistic plant mechanical behaviour. Despite all these limitations, only a few experiments have been performed using real vegetation (e.g., Bouma et al., 2005, 2010). Furthermore, the difficulties associated with the use of real plants (collection, growing, storage) have limited the scale of the experiments. The correct definition of hydrodynamic conditions is another important aspect in the experimental design. Many experiments have been performed considering either current conditions (e.g., Arbele and Järvelä, 2013; Bouma et al., 2013) or waves (e.g., Bouma et al., 2010; Yoon et al., 2011). However, the salt marshes habitat is located in the intertidal zone where both waves and currents interact with them. Despite this, only a few experiments considering both hydrodynamic forcings simultaneously can be found in the literature (Gaylord et al., 2003; Paul et al., 2012). These studies have indicated the strong influence that an underlying current may have on the wave attenuation capacity of the plants. However, none of these studies have considered currents flowing opposite to wave propagation and none of them have been performed using salt marsh vegetation.

This work is an analysis of a unique set of experiments performed with real vegetation and simultaneously combining waves and currents. A detailed description of the methodology followed to perform these experiments with living plants is presented in Chapter 4, whereas a detailed hydrodynamic analysis of the experimental data is carried out here. The experiments were performed using two salt marsh species (*Puccinellia maritima* and *Spartina anglica*; cf. Bouma et al. 2010) with contrasting biomechanical properties. The plants were grown in the laboratory for the present tests. The experiments were carried out in the Cantabria Coastal and Ocean Basin (CCOB) allowing a close to nature scale setup. This facility was also selected because of the possibility of studying the complex hydrodynamic processes developed in the waves and currents interaction with real vegetation, thereby addressing an important knowledge gap in the existing literature. Section 2 presents a summary of the experimental setup. The analysis of the influence that both flow and vegetation characteristics have on the wave damping provided by the plants is addressed in Section 3. Finally, some conclusions are drawn in Section 4.

5.2 Experimental set-up

A detailed description of the growing of the vegetation and the experimental setup is provided in Chapter 4. Hence only a brief description of the hydraulic facility and the flow and vegetation conditions considered in the experiments is presented here. Experiments are carried out in the 30 m long, 44 m wide and 4.75 m deep Cantabria Coastal and Ocean Basin (CCOB). This facility allows for the testing of different combinations of water depths and the combined effect of waves and currents at large-scale. Experiments were conducted under wave and current flow conditions for different submergence ratios using real vegetation in order to overcome the well-known limitations inherent to the use of mimics (Frostick et al. 2014). A sketch of this facility is displayed in Figure 5.1 where the location of the wave paddles and the current generators is shown.

In order to analyze the role played by vegetation characteristics on flow damping, two contrasting vegetation species have been selected: *Puccinellia maritima* and *Spartina anglica* (cf. Bouma et al. 2010). *Puccinellia maritima* is a flexible species that can occur in the middle and lower marsh. Its biomechanical properties confers it with a high degree of bending and a waving motion under wave action (Bouma et al. 2010). *Spartina anglica* is a pioneer species that grows on the low marsh. *S. anglica* is stiffer than *P. maritima* and describes a cantilever motion under wave action (Paul et al., 2012). To keep these properties unaltered during the experiments the basin was drained each day for at least 12 hours and the plants were permanently illuminated with natural light.

The vegetation is arrayed in the center of the basin where a 6 m diameter circular pit is located. The vegetation is placed over the pit tap, which is then lowered to dispose vegetation at the basin floor level. This placement provides a smooth transition from the basin bottom to the vegetation field thus avoiding the need for the construction of a false bottom.

Free surface and velocity measurements are taken. *P. maritima* tests were carried out using 20 capacity free surface gauges and 3 ADVs to record the flow velocity whereas *S. anglica* tests included 8 additional free surface gauges. The location of the free surface gauges and the velocity ADVs is shown in Figure 5.1.

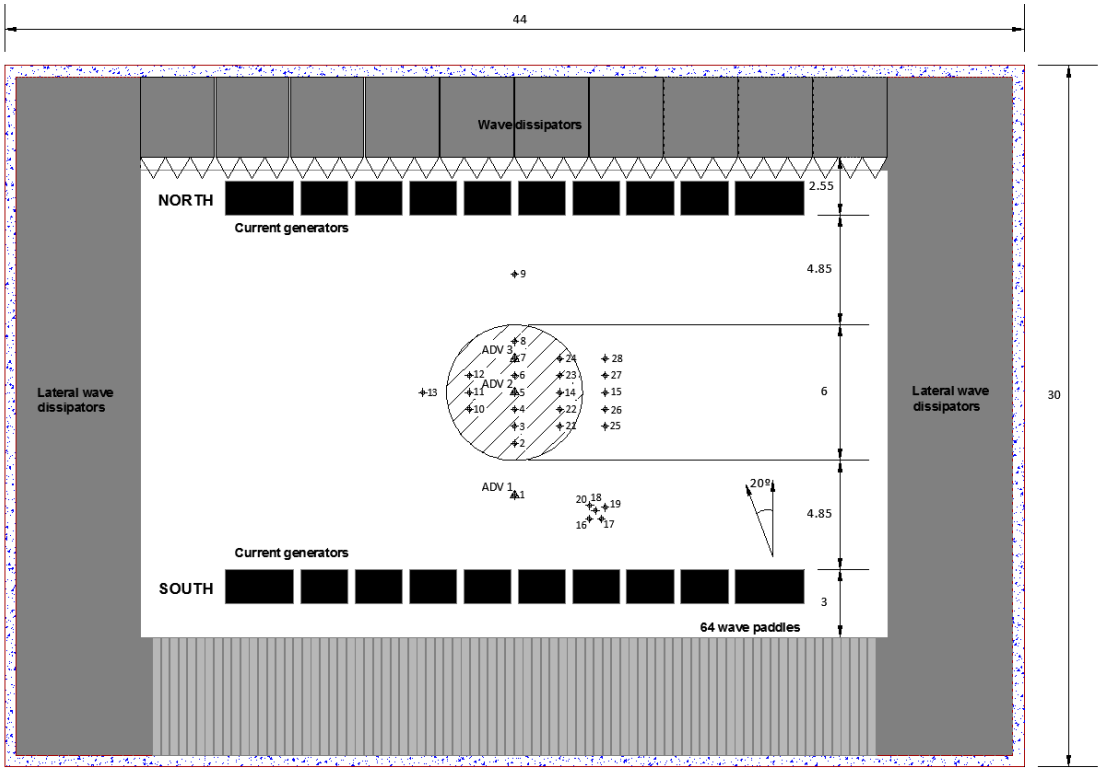

Figure 5.1 Cantabria Coastal and Ocean Basin. Free surface gauges and ADVs location.

5.2.1 Flow conditions

The influence of the relative water depth (hr), defined as the ratio between water depth and vegetation height (hr = h / hvegetation) has been examined using four different water depths: h = 0.40 m, 0.60 m, 0.80 m and 1 m. These values correspond to water depths during flooding events (e.g., Bouma et al. 2005b). The influence of wave parameters is also considered by testing 6 different wave conditions, as shown in Table 5.1, where H is the wave height and T the wave period for regular waves and Hs and Tp, significant wave height and peak period for irregular waves respectively. Wave conditions were selected attending to field conditions under average storm events.

Wave Conditions	Type	H(m)|Hs(m)	T(s)|Tp(s)
R1	Regular	0.15	2
R2	Regular	0.20	2
R3	Regular	0.20	1.2
R4	Regular	0.20	1.7
R5	Regular	0.20	2.2
IR	Irregular	0.12	1.7

Table 5.1 Wave conditions

A minimum of 200 waves was recorded for each of the 6 test cases. Wave and current conditions were generated by combining the test cases in Table 5.1 with following and opposing underlying currents as shown in Table 5.2. Current velocities were chosen based on Bouma et al. (2005b). After allowing a warming period in order to reach a uniform current profile, a minimum of 200 waves were recorded.

Current Conditions	Velocity (m/s)
+C	0.3 (South-North)
-C	0.3 (North-South)

Table 5.2 Current conditions

The influence of wave incidence on wave and current interaction with vegetation, was tested considering three of the wave conditions presented in Table 5.1 (R1, R3 and IR) but generating them with a wave angle (θ) with respect to the current direction equal to 20º.

5.2.2 Vegetation conditions

Two vegetation species with contrasting geometry and biomechanical properties were chosen in order to analyze the effects of stiffness and plant morphology. Additionally, different vegetation densities were tested by cutting randomly selected shoots from the meadow in order to avoid changing the size distribution. The *P. maritima* meadow was thinned in two sequential steps obtaining approximately 66% and 33% of the original density. *S. anglica* was cut only once, resulting in two tested densities, 100% and 66% of the original density. The 100% densities are representative of field conditions whereas the lower densities are used to study the relative importance of this parameter in energy attenuation. Table 5.3 summarizes the tested vegetation densities.

Case	Species	Target Density (shoots/m2)	Achieved Density (shoots/m2)
P100	P. maritima	2436 (100%)	
P66	P. maritima	1608 (66%)	1389 (57%)
P33	P. maritima	804 (33%)	877 (36%)
S100	S. anglica	729 (100%)	
S66	S. anglica	481 (66%)	430 (59%)

Table 5.3 Vegetation conditions

Plant dimensions were also measured for both species. Mean height and width of the leaves as well as the mean number of leaves per shoot are shown in in Table 5.4.

Species	Mean Height (cm)	Mean leaf width (cm)	Mean number of leaves per shoot
P. maritima	47.29	0.30	5.5
S. anglica	28.40	0.60	5

Table 5.4 Mean plant dimensions for both species.

The vegetation stiffness was measured in the Material Science and Engineering Division Lab (LADICIM) of the University of Cantabria where tensile strength tests for vegetation, leaves and stems are performed. The Young modulus of *S. anglica* was approx. 10 fold higher than that of *P. maritima*, regardless whether we compared leaves or the stem (Table 5.5).

Species	Stem (MPa)	Leaf (MPa)
P. maritima	13	7.8
S. anglica	164.2	77.6

Table 5.5 Young modulus for the stems and leaves of each vegetation species

Finally, the standing biomass for each density of both species was obtained. These values are obtained by measuring the dry mass per shoot of representative samples. The dry mass was evaluated by weighing the samples after placing them in a muffle oven for 48 hours at 70ºC. The density reductions were performed targeting at having similar biomass levels for both species to be able to compare wave attenuation. Table 5.6 shows that the biomass for the 66% of density for *P. maritima* is very similar to the one measured for the 100% of density for *S. anglica*. The same occurs for the 33% of density for *P. maritima* and the 66% of density for *S. anglica*. Therefore, similar biomass levels were obtained for both species.

Case	Biomass (g/m2)
P100	443
P66	254
P33	146
S100	290
S66	171

Table 5.6 Biomass for each cut and both species, P. maritima (P) and S. anglica (S), the accompanying number code corresponds to the meadow density percentage

The plant characteristics previously described can explain the plants behavior under flow action (waves and current) and therefore, their attenuation capacity. Standing biomass and stiffness play an important role when dissipating energy. Whereas *P. maritima* is very flexible and bends to the ground, *S. anglica* stays erect (see Figure 5.2).

Figure 5.2 P. maritima (left) and S. anglica (right) disposal in the basin.

5.2.3 Test program

A total of 276 tests were performed over 30 days. For P100 and S100 and h= 0.40 m and 0.60 m, all the wave conditions displayed in Table 5.1 were tested, combined with both current conditions specified in Table 5.2. For h = 0.80 m and 1.00 m only R1 and R3 wave conditions were tested. Vegetation with a lowered density was tested under R1, R3 and IR wave conditions combined with currents for h= 0.40 m and 0.60 m. Again only R1 and R3 were considered for h = 0.80 m and 1.00 m. Finally, R1, R3 and IR were tested with a 20º angle with respect to the current direction for both current conditions and h = 0.40 m and 0.60 m. All these combinations are specified in Table 5.7.

Vegetation	Wave conditions	Wave angle (θ)	Current	Water depth (h)
P100 and S100	R1 – R5, IR	0	+C, -C	0.40 m
P100 and S100	R1 – R5, IR	0	+C, -C	0.60 m
P100 and S100	R1 and R3	0	+C, -C	0.80 m
P100 and S100	R1 and R3	0	+C, -C	1.00 m
P100 and S100	R1, R3 and IR	20º	+C, -C	0.40 m
P100 and S100	R1, R3 and IR	20º	+C, -C	0.60 m
P66, P33 and S66	R1, R3 and IR	0	+C, -C	0.40 m
P66, P33 and S66	R1, R3 and IR	0	+C, -C	0.60 m
P66, P33 and S66	R1 and R3	0	+C, -C	0.80 m
P66, P33 and S66	R1 and R3	0	+C, -C	1.00 m
P66, P33 and S66	R1, R3 and IR	20º	+C, -C	0.40 m
P66, P33 and S66	R1, R3 and IR	20º	+C, -C	0.60 m

Table 5.7 Performed tests

5.3 Experimental results and discussion

The set of runs performed in the CCOB allows for the studying of the influence of water depth, the combined effect of waves and currents considering normal and oblique incidence and the wave and vegetation characteristics effect on the energy dissipation produced by the vegetation meadow. As in previous studies (e.g.: Koftis et al., 2013; Ozeren et al., 2013; Anderson et al., 2014), the analysis is based on the energy conservation equation. The wave height damping formulation presented by Dalrymple et al. (1984) is used for regular wave conditions. This formula assumes linear wave theory and considers that energy dissipation is only due to the drag force produced by the vegetation and a damping coefficient constant over depth. The wave decay is expressed as:

$$\frac{H}{H_0} = \frac{1}{1 + \beta x} \tag{1}$$

where *H* is the wave height and β the damping coefficient for regular wave trains. The subscript *0* refers to the incident wave height and *x* is the longitudinal distance along the meadow. Mendez and Losada (2004) extended this formulation for nonbreaking random waves over

constant depth assuming a Rayleigh distribution and deriving the wave height evolution as a function of the root-mean-square wave height as:

$$\frac{H_{rms}}{H_{rms,0}} = \frac{1}{1+\beta' x} \tag{2}$$

where *Hrms* is the root-mean-square wave height and β' is the damping coefficient for random waves. This formula is used for the random wave cases. Wave decay was obtained for the tests which includes both waves and currents considering the same mathematical model presented in equations (1) and (2). Damping coefficients, β in the following, are calibrated to best fit to the experimental data.

5.3.1 Water depth

The importance of the relationship between water depth and vegetation height on wave energy dissipation produced by submerged vegetation has been reported by several authors both, for field (e.g.: Ysebaert et al., 2011) and laboratory studies (e.g.: Augustin et al., 2009). Wave decay recorded for water depth (0.40 m, 0.60 m, 0.80 m and 1.00 m) values is analyzed and the associated damping coefficients are obtained. Results for *P. maritima* with 100% density and R1 wave conditions are shown in Figure 5.3.

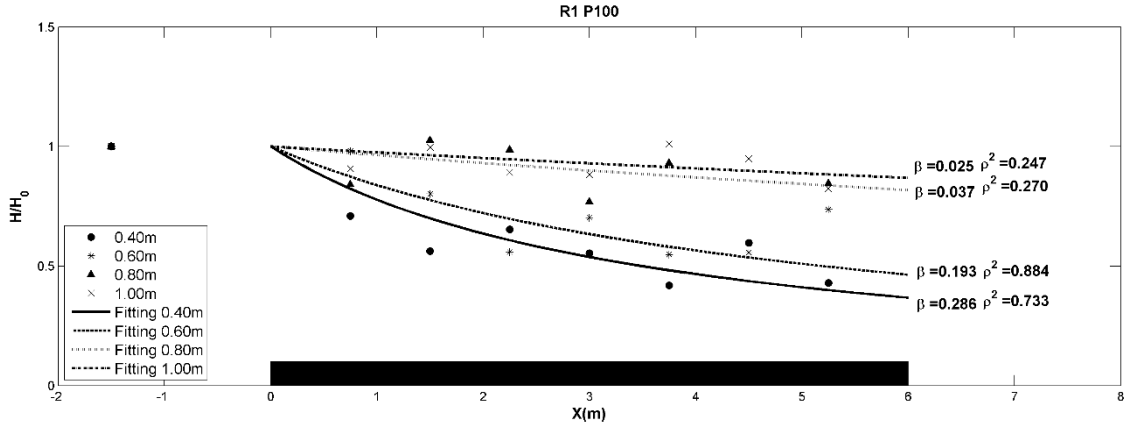

Figure 5.3 Wave height evolution along the P. maritima field (black square) for R1 and P100 and water depths, h = 0.40 m, 0.60 m, 0.80 m and 1.00 m.

A higher wave damping is observed for smaller water depths. This is directly related to the relative water depth (hr = h / hvegetation). Therefore, a smaller value of this variable implies a higher water column fraction affected by vegetation considering a relative water depth equal to 1 when vegetation is affecting the entire water column. There is a significant difference between

the results obtained with the lowest and highest water depths. Results for h = 0.80 m and 1 m fit lower values of the damping coefficient and show low correlation. This is related to the low damping rate achieved for these water depths due to the weak interaction between flow and vegetation. However, the vegetation strongly influences the wave evolution for the 0.40 m and 0.60 m depths, showing an attenuation of the incident wave height of up to 50%. For 0.40 m the full water column is affected by vegetation since the *P. maritima* average height is 47.29 cm, which means a relative water depth equal to 1. Additionally, the standing biomass associated to the 47.29 cm of height of this flexible vegetation is concentrated along the 0.40 m water depth due to its low stiffness and its floatability. For 0.60 m, although vegetation is not affecting to the entire water column, a large fraction is also occupied by the plants, leading to a high wave damping rate.

In order to extend this analysis, tests performed considering R1 conditions and all vegetation densities for both species are examined for the four water depths. Previous studies have found a logarithmic relationship between wave attenuation and water depth (e.g.: Ysebaert et al., 2011). As shown in Figure 5.4, the damping coefficient can be related to the water depth for all different vegetation conditions using a logarithmic law.

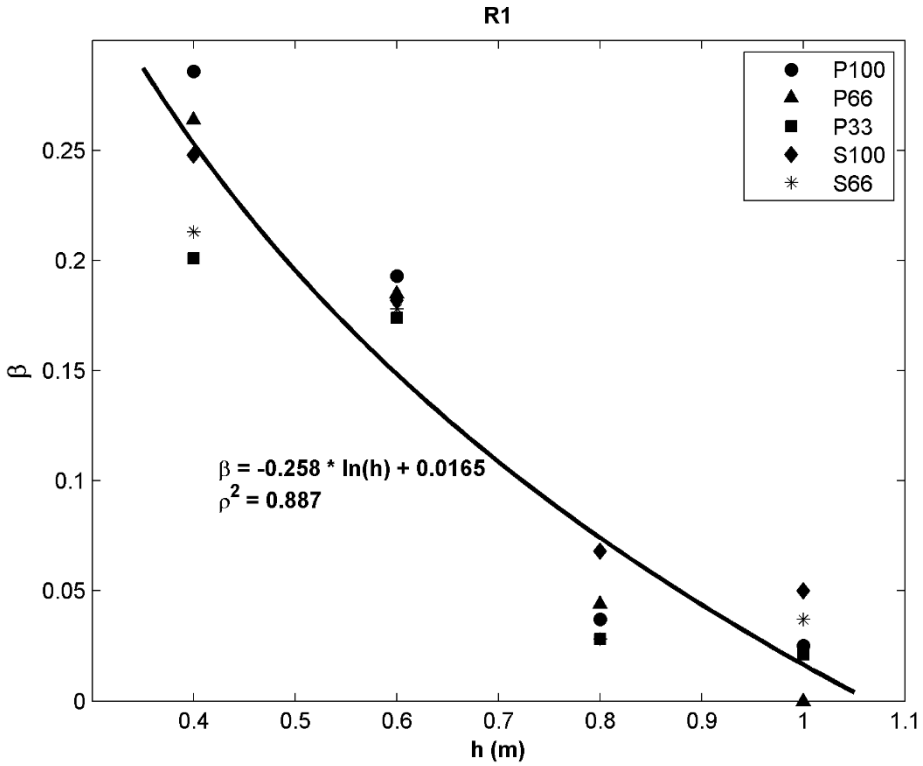

Figure 5.4 Damping coefficient for all the vegetation densities and species under R1 wave conditions.

A decay of the wave damping coefficient with increasing water depth is clearly visible. Results for the five vegetation conditions fit well with the presented equation revealing a consistent behavior of the different species and densities in terms of water depth influence. The higher dispersion of the points associated with different vegetation conditions is observed for h=0.40 m, meaning that vegetation density and species biomechanical properties have a higher influence in shallower depths where the interaction between flow and vegetation is stronger. The influence of these vegetation parameters will be discussed later in detail.

Other authors have studied the influence of water depth in terms of the relative water depth (e.g.: Yang et al., 2012). Since two different species with different plant heights are considered in this study, the relative water depths associated with them are different. In Figure 5.5, damping coefficients are represented in terms of the corresponding relative depths.

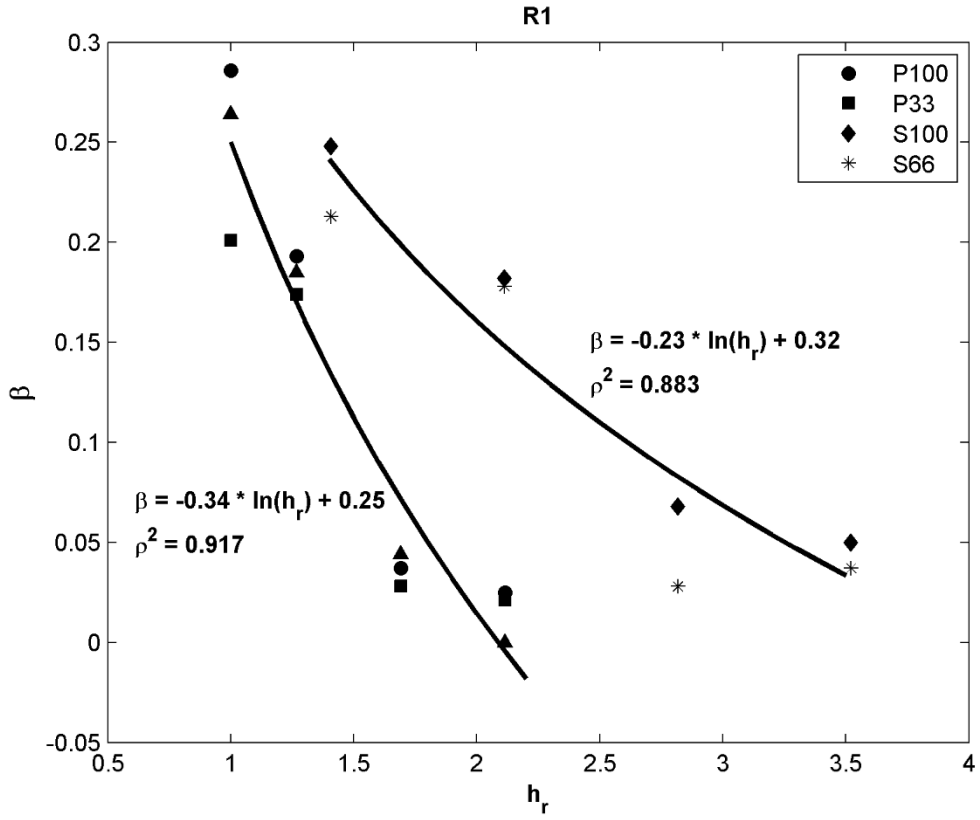

Figure 5.5 Damping coefficient for all vegetation densities and species as a function of the relative water depth under R1 wave conditions

Results show a different relationship for each of the vegetation species. The larger plant height measured for *P. maritima* leads to a smaller range in the relative water depth, whereas *S. anglica* records extend in a wider relative depth range. For the same relative water depth, the damping

coefficient associated to *S. anglica* is higher than the one for *P. maritima*. This is related to the biomechanical characteristics of the vegetation revealing a higher attenuation for rigid plants. Flexible vegetation strongly attenuates wave energy when the water depth is totally occupied by vegetation (hr ~ 1). However, the wave damping coefficient rapidly decreases as the plant submergence ratio increases. The decay associated with the rigid vegetation is, instead, smoother. Furthermore, wave damping is strongly influenced by the vegetation density for each species and for the same relative water depth. This aspect is discussed in detail in the following sections. Under identical conditions, for any relative water depth, vegetation density and stiffness influence the damping process.

5.3.2 Wave height and period

Several authors have reported the influence of both wave period and wave height on wave damping. However, contradictory results have been presented so far. Cavallaro et al. (2010) reported higher wave attenuation for larger wave heights whereas Manca et al. (2012) presented a decreasing attenuation for larger waves for the same seagrass species. Different results are also found depending on wave period. Infantes et al. (2012) presents field measurement with higher attenuations for longer wave periods whereas results presented by Anderson et al. (2014) suggest the opposite. Dubi and Torum (1996) presented an equation to relate the damping coefficient to the wave period reporting wave damping increase or decrease depending on the wave period range.

Five different regular wave conditions were tested in the present experiments to evaluate the influence of wave height and period. A comparison of the damping coefficients associated with each of the 5 considered wave conditions is presented in Figure 5.6 for P100 and S100 vegetation (100% density in both cases, see Table 5.6). Results correspond to h=0.40 m water depth.

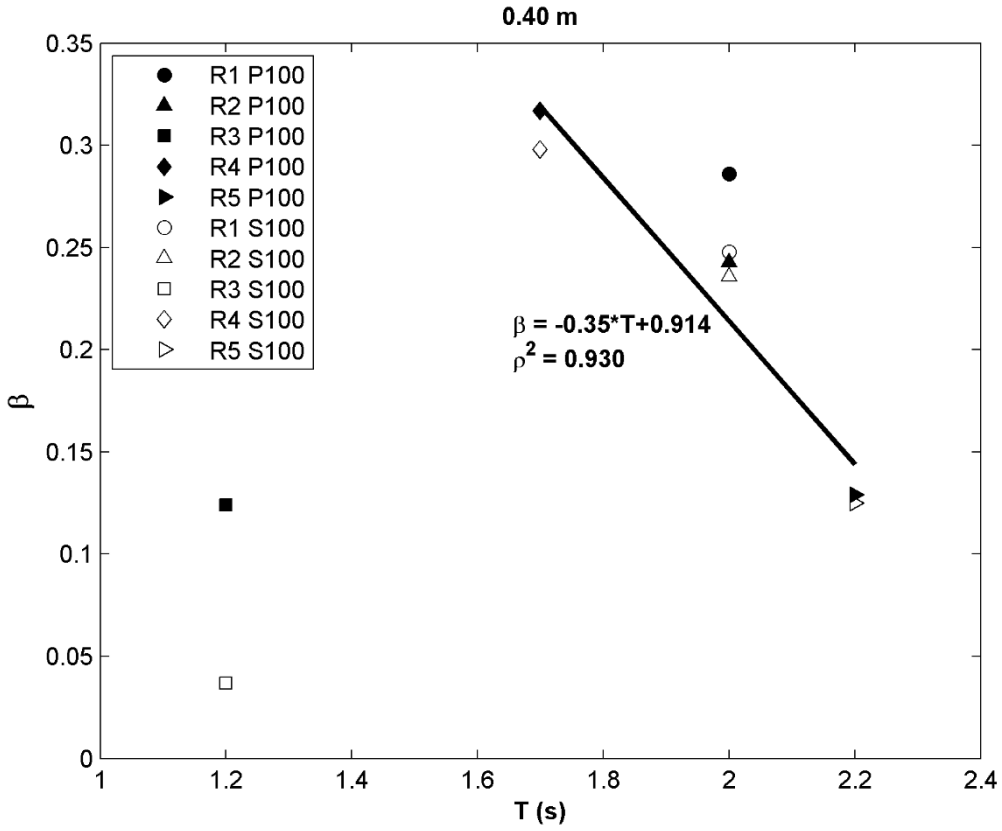

Figure 5.6 Damping coefficient for R1-R5 wave conditions, h=40cm and P100 and S100 vegetation characteristics.

For both species, a higher damping coefficient is associated with shorter wave periods, except for R3 (Figure 5.6). A similar behavior is presented by Dubi and Torum (1996) who reported increased wave damping for small wave periods whereas longer periods result in a decreased wave damping. However, the formula proposed by Dubi and Torum (1996) does not fit the present results. This is not surprising since that formulation was obtained for different flow conditions and macro algae species. The results presented here for the same wave height (H = 0.20 m) fit to a linear relationship considering periods between 1.7 and 2.2 s. However, a general trend is not observed when all regular wave trains are considered. Particularly, the R3 wave train shows the smallest damping rate for the smallest wave period converse to the trend observed for the results obtained for higher periods.

Wave height results for R1 reveals a higher wave damping than for case R2 suggesting a higher attenuation for smaller wave heights. This is in agreement with results presented in Bradley and Houser (2009) linking this correlation to plant flexibility. Flexible vegetation tends to extend in the direction of the flow and becomes streamlined, leading to reduced drag. This effect is

enhanced for higher wave heights due to the associated higher velocities and bending forces. Manca et al. (2012) also reported the same relationship between wave height and damping for stiffer vegetation (*Posidonia oceanica* mimics with Young modulus equal to 0.9 GPa). Therefore, their results are in agreement with the ones presented in Figure 5.6 for *P. maritima* and *S. anglica*.

Figure 5.6 shows similar damping coefficients for both species under R2 and R5 wave conditions. These more energetic waves are attenuated in a similar way for both vegetation types whereas waves with a smaller wave period (R3) or a smaller wave height (R1) show higher differences in the degree of attenuation. Thus, for the less energetic conditions, vegetation stiffness and standing biomass are more important for energy dissipation.

5.3.3 Combined waves and currents

Previous studies have reported the influence of a current on wave attenuation for kelp (Gaylord et al., 2003) or seagrasses (Paul et al., 2012). These studies reported a decreasing canopy wave attenuation capacity for an underlying current, especially when it follows the waves. Neither of them presented results for currents opposing waves. In this work, tests are carried out considering both following and opposing currents normally to the wave crests in order to analyze the effect of these underlying currents on wave damping produced by real salt marsh vegetation.

Figure 5.7 presents results for waves only, waves and currents following (Waves+Current) and waves and opposing currents (Waves-Current) for three different wave conditions (R1, R3 and IR). Results correspond to h=0.40m and 0.60 m and one single vegetation species, *P. maritima* with 100% density, P100.

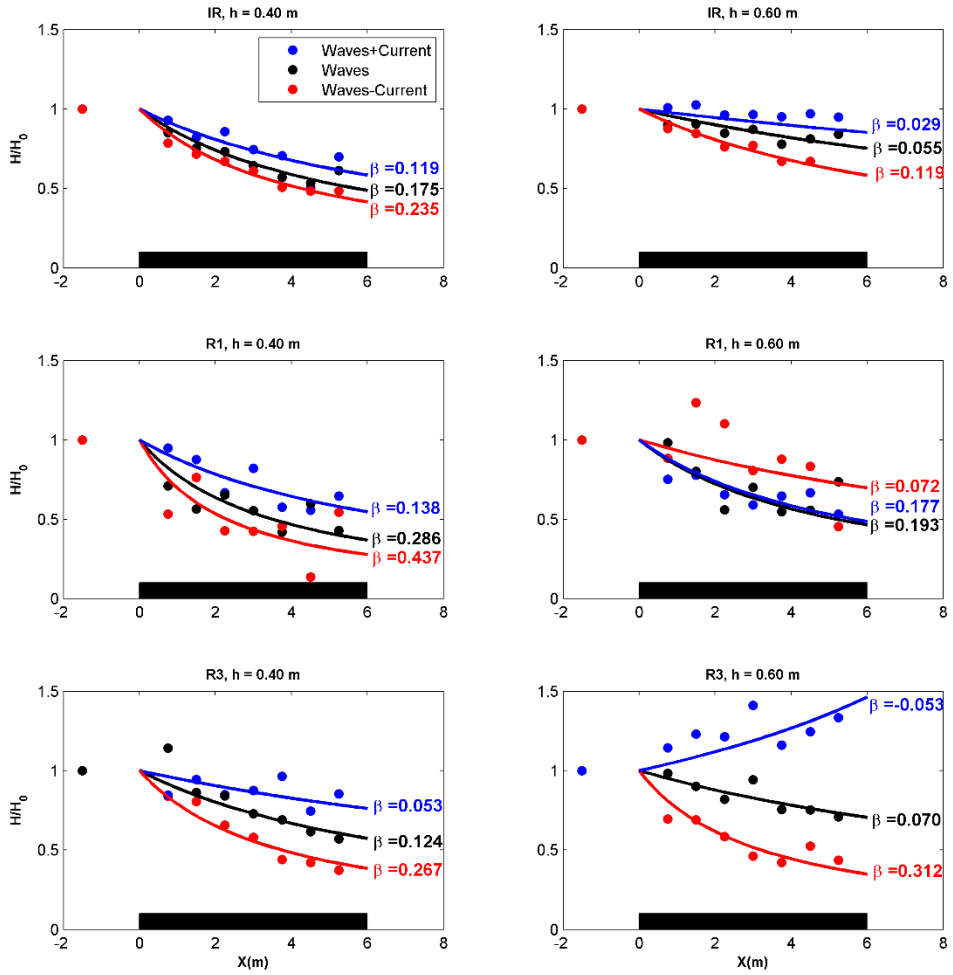

Figure 5.7 Wave damping for P100 recorded for waves (black), waves and following current (blue) and waves and opposing current (red). Wave conditions: IR, R1 and R3. h=0.40 m and 0.60m.

As can be seen in the figure, results are highly dependent on water depth and flow conditions. Irregular waves present very consistent results with water depth being the primary parameter controlling the overall damping induced by wave vegetation. It can be seen that the highest damping is achieved for the shallowest water depth, independently of flow conditions. Please note that the same damping coefficient, $\beta = 0.119$ is reached for the h=0.40 m case under waves and following currents as for the h=0.60 m case under wave and opposing currents. It indicates the smaller damping rate achieved for higher water depths and the influence that current direction has on wave damping.

When it comes to comparing the different flow conditions for given water depths, the highest damping is achieved for waves and an opposing current. Conversely, the lowest damping is

achieved with waves and a following current. The latter is in agreement with results presented by Paul et al. (2012) and Gaylord et al. (2003) for seagrasses and kelps, respectively. It can thus be concluded that the presence of currents either following or opposing waves modifies the resulting damping for waves only.

The two regular wave conditions displayed in the figure exhibit a singular behavior for h = 0.60 m. Wave damping obtained for R1 and current opposing wave propagation is smaller than the one for waves. There is a wave height enhancement along the meadow for R3 and waves and current moving in the same direction. These singularities are observed for all vegetation conditions tested in the experiments. Figure 5.8 contains the damping coefficients for all the vegetation conditions tested during the experiments for the combined action of waves and currents. Results are presented only for h = 0.40 m and 0.60 m.

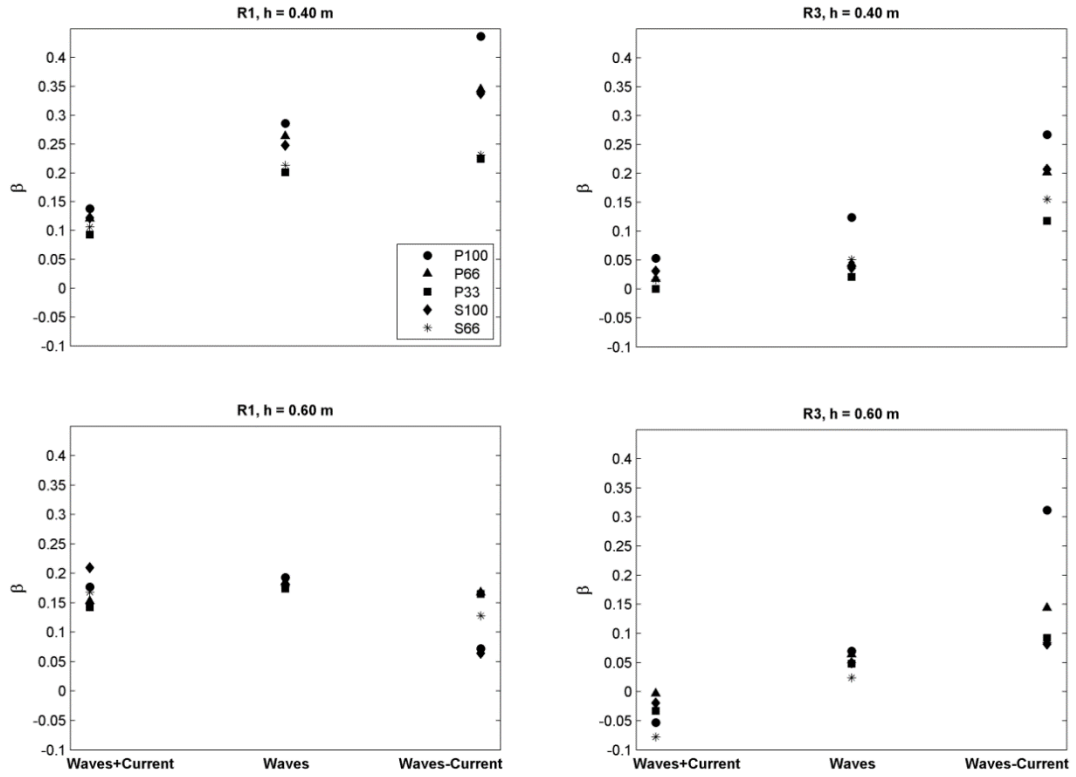

Figure 5.8 Damping coefficient for all vegetation conditions and R1 and R3 over 0.60 m of water depth.

Figure 5.8 shows larger wave damping for current opposing to waves when water depth is 0.40 m (upper panels). Results shown in the lower panels corresponding to 0.60 m water depth exhibit a different trend. Case R1 (lower left panel) shows slightly lower β values for current

opposing to waves. The difference is much higher for cases with a higher vegetation density (P100 in dots and S100 in diamonds). Moreover, R3 results (lower right panel) lead to negative damping coefficients resulting in increasing wave heights along the vegetation meadow. These features could be due to the strong effect that current velocity has on the less energetic wave trains for h = 0.60 m due to the current flow blocking produced by the meadow. The flow patterns developed in the basin around the meadow when waves and currents are tested together are different depending on the water depth. For h=0.40 m the entire water column is occupied by vegetation for *P. maritima* and for more than 70% for *S. anglica* with the result that almost all the current flow is diverted by the vegetation patch. Consequently, the current velocity inside the meadow is almost zero. This effect is enhanced with higher vegetation densities since the current blocking by the meadow is larger. However, for h=0.60 m vegetation takes only 50% of the water column and the generated uniform current flows on the top of the meadow. A sketch of these two different patterns is shown in Figure 5.9.

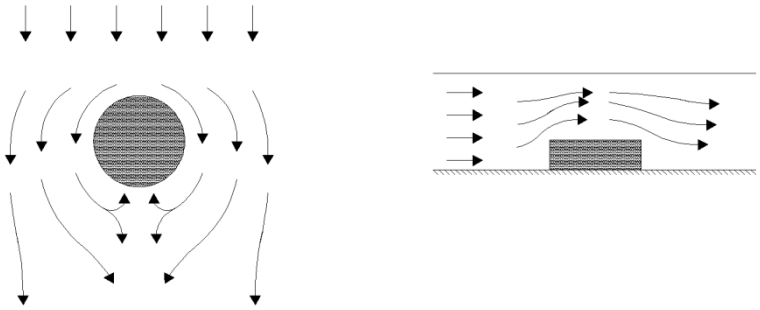

Figure 5.9 Current pattern for 0.40 m, top view (left) and 0.60 m (right) of water depth, side view.

Supporting this explanation, velocity records measured by three ADVs located 25 cm from the bottom (see Figure 5.1 for ADV location in the experimental setup) are displayed in Figure 5.10. The three velocity components are shown for two cases run with P100 and currents following and opposing waves for h = 0.40 m.

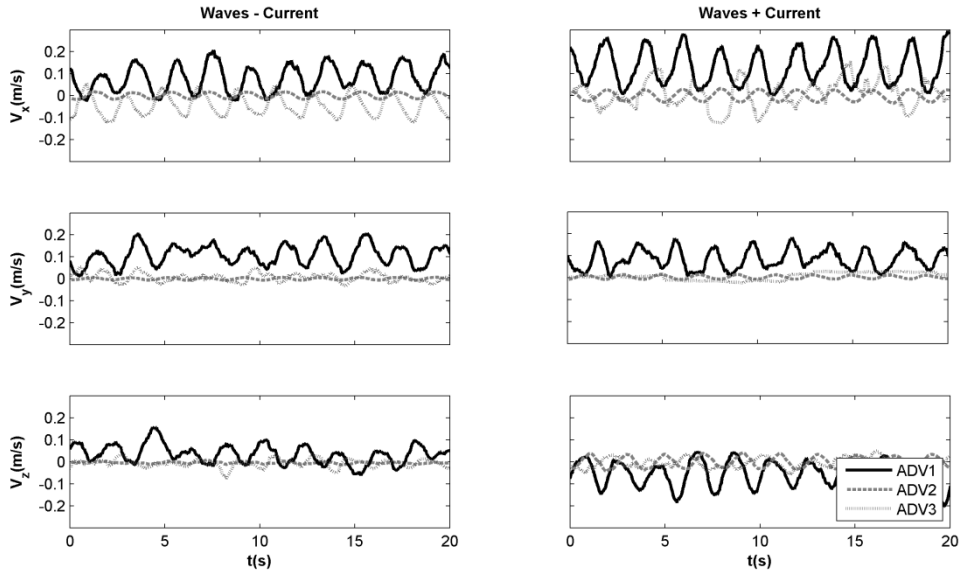

Figure 5.10 Velocity measurements for the three ADVs, P100, h = 0.40 m and current opposing (left) and following (right) waves.

The ADV located at the center of the meadow (ADV2) shows small velocity values in all components, yielding a close to zero time average value. This means that the velocity magnitude measured inside the meadow is due to wave action and not to the current. This effect is observed for both current directions. In addition, the horizontal velocity component measured by ADV1 has a positive mean value for both current directions. This is due to the recirculation pattern produced for an opposing current in the smallest water depth (left panel in Figure 5.9). ADV3 records are higher than the ones obtained for ADV2 for both current directions. This is due to the combined effect of the recirculation patterns developed around the meadow and the velocity penetration into the field, which is higher for ADV3 because it is closer to the meadow edge.

Whereas there is no strong interaction between waves and currents in the meadow area for h=0.40 m, it is enhanced for h = 0.60 m since current velocity is mainly passing over the plants and a total current blocking is not developed. To better understand this nonlinear interaction, velocity measurements taken at a location 0.40 m from the bottom in 0.60 m of water depth are analyzed. ADV3 measurements in cases R1 and R3 are displayed in Figure 5.11 corresponding to waves only and waves and current in opposite direction. Figure 5.12 shows the ADV2 measurements for the same wave conditions and currents acting in the same direction.

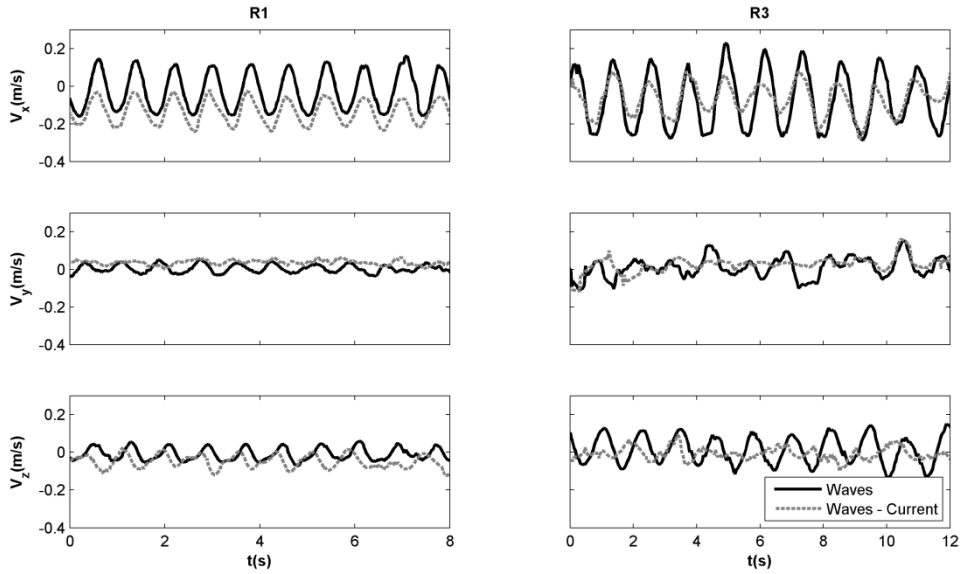

Figure 5.11 ADV3 velocities at 0.40 m from the bottom for h=0.60 m and R1 (left) and R3 (right) wave conditions (black solid line) and both acting joint to an underlying current in the opposite direction (grey dashed line).

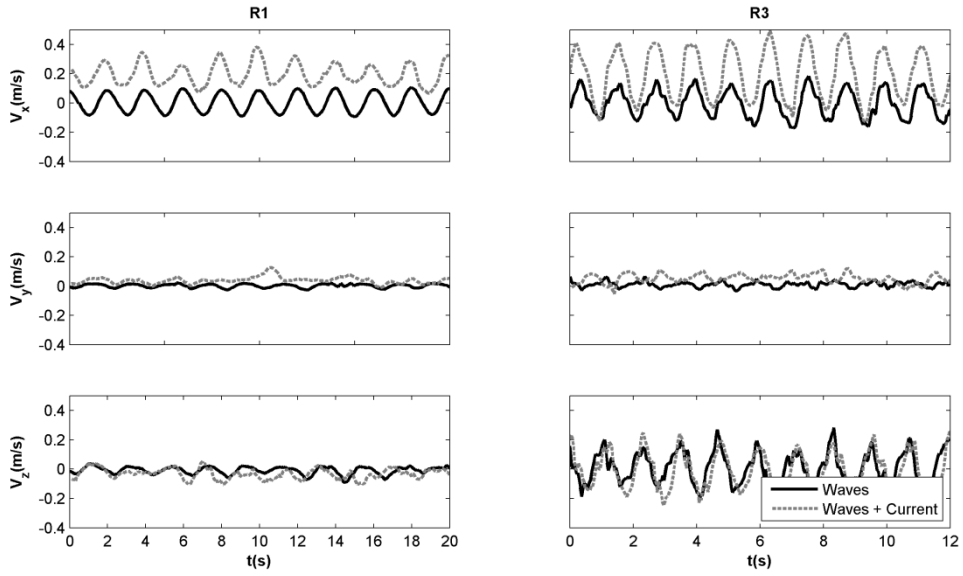

Figure 5.12 ADV2 velocities at 0.40 m from the bottom for 0.60 m of water depth and R1 (left) and R3 (right) wave conditions (black solid line) and both acting joint to an underlying current in the same direction (grey dashed line).

A displacement of the horizontal time averaged velocity when current is activated is shown for R1 conditions (left column in Figure 5.11), revealing the strong influence of the current in this

case. This effect is not observed for R3 (right column) where the velocity record shows a zero time averaged horizontal velocity showing almost only wave influence. Consequently, the small wave height in case R1 is strongly modified by the opposing current leading to a decrease in wave damping and a predominant effect of current on wave propagation.

Figure 5.12 shows instead the effect of the current acting in the same direction as the waves. R1 shows again a displacement of the mean horizontal velocity according to current direction and the velocity amplitude of the waves is almost the same as the one recorded for waves only. However, R3 exhibits a different pattern. Again, the time averaged velocity value is displayed but in this case the velocity amplitude is increased significantly. Observed higher velocities can be explained by a wave height enhancement along the meadow by current, as observed in Figure 5.7.

Authors such as Longuet-Higgins and Stewart (1960) or Baddour and Song (1990) have reported Wave and current interaction in terms of the ratio between the wave and current velocity in order to determine which effect is predominant. The relationship between the damping coefficient and the ratio between the current velocity (U0) and the characteristic wave velocity (Uw) is shown in Figure 5.13. Wave velocity is evaluated at the top of the beginning of the meadow following previous studies on wave-vegetation interaction (e.g.: Asano et al., 1988; Mendez et al, 1999).

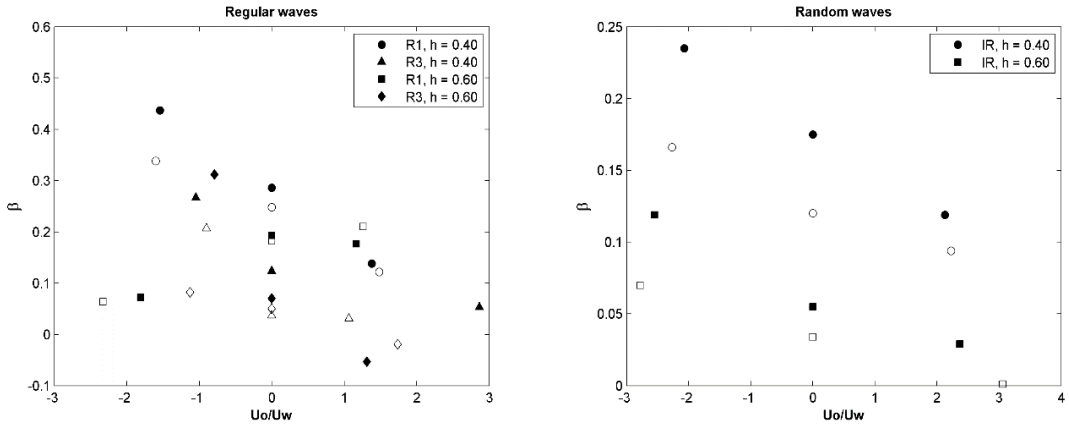

Figure 5.13 Relationship between the damping coefficient and the velocity ratio for P100 (solid black points) and S100 (black points).

As can be seen in the right panel of Figure 5.13, wave damping decreases with positive velocity ratio (waves and current acting in the same direction) for random waves. Conversely, wave damping increases for negative velocity ratios (current opposite to waves). This behavior is also observed for regular wave conditions and h = 0.40 m, as can be observed in the left panel.

Therefore, the obtained general trend is that wave damping decreases when the velocity ratio increases. Results for R1 and R3, and h = 0.60 m appear to behave differently according to the high influence of the current pattern produced by the meadow.

5.3.4 Oblique waves and currents

In order to extend the study on waves and current interaction, non-collinear waves and currents are tested. Wave height evolution along the meadow obtained for three wave conditions (R1, R3 and IR) is shown in Figure 5.14. Waves and current are generated with a 20º angle. Cases correspond to h = 0.40 m. In order to better understand the role played by wave obliqueness to current, results corresponding to collinear cases are also included in the plots.

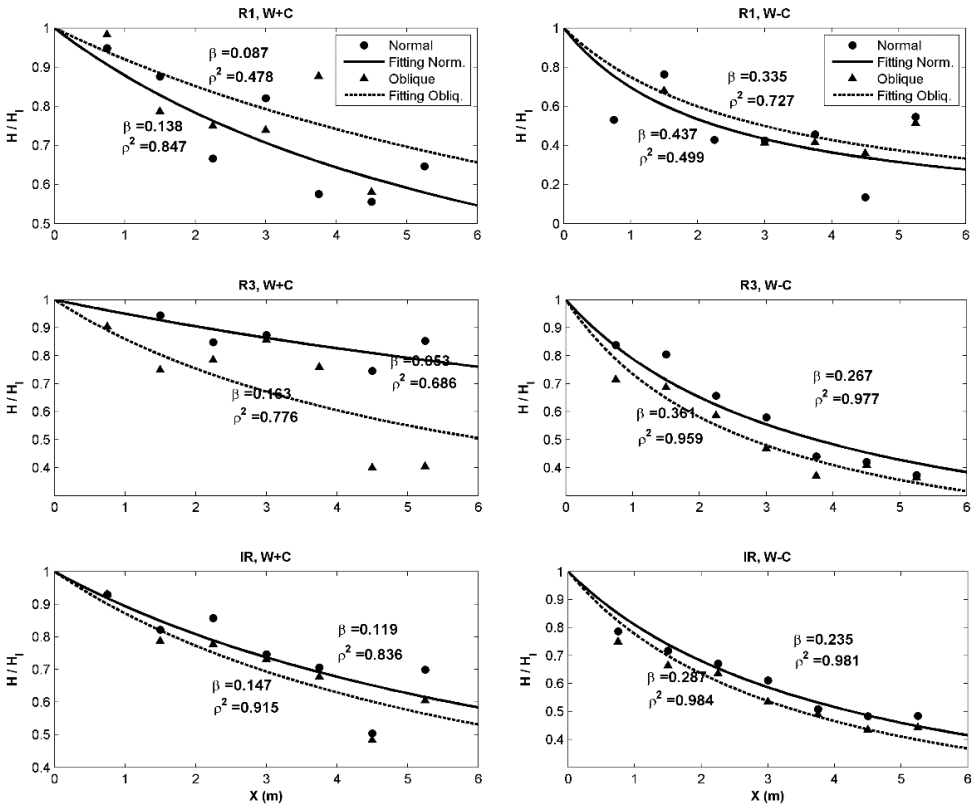

Figure 5.14 Wave height evolution for R1, R3 and I, ϑ=20º and current following (left) and opposing waves (right).

Figure 5.14 shows a different behavior between R1 and the other two cases. While results for R3 and IR show an increase in wave height attenuation for oblique waves with respect to collinear wave and current, a reduction is observed for R1. These results highlight the different

interaction produced between waves and current, which attend to their specific characteristics, as was shown in the previous section.

Attending to the local wave records along the meadow, R3 and IR show an amplification of wave damping for oblique waves. In both cases, measurements for oblique conditions appear below the ones obtained for collinear waves. However, this feature is not detected for R1. Wave characteristics for this case are less energetic and consequently the influence of current on the waves is stronger, yielding to a less clear influence of obliqueness on damping. Nonetheless, the general observed trend is that oblique incidence between waves and currents induce higher damping rates.

5.3.5 Vegetation density

Several authors (e.g.: Bouma et al., 2010; Anderson et al., 2014) have reported the importance of vegetation density on wave energy attenuation. In the present experiments, three different densities are tested for *P. maritima* and two for *S. anglica*. Wave height evolution for R1 and IR are presented in Figure 5.15 together with the associated damping coefficient for the different densities considered. Cases correspond to h=0.40 m.

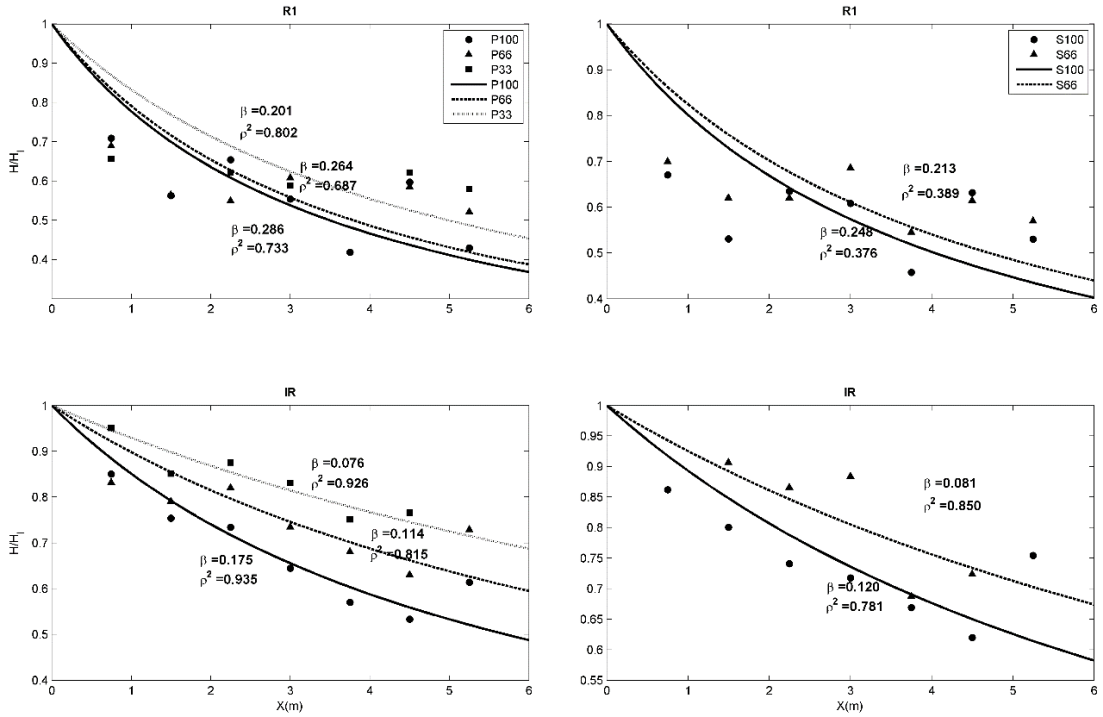

Figure 5.15 Wave height evolution and damping coefficient for R1 and IR, h= 0.40 m and for both species, P. maritima and S. anglica.

Results for both species reveal a strong relationship between wave damping and vegetation density. Lower vegetation density implies a decrease in wave damping for both species. This is consistent with previous work and is detected for all wave conditions in the present experiments.

Paul et al. (2012) introduced a new concept to account for different densities and vegetation lengths, the so-called one-side leaf area index (LAI = leaf length*leaf width*density). This parameter is used here to analyze the influence of vegetation density on wave damping. The damping coefficients are presented as a function of the LAI in Figure 5.16.

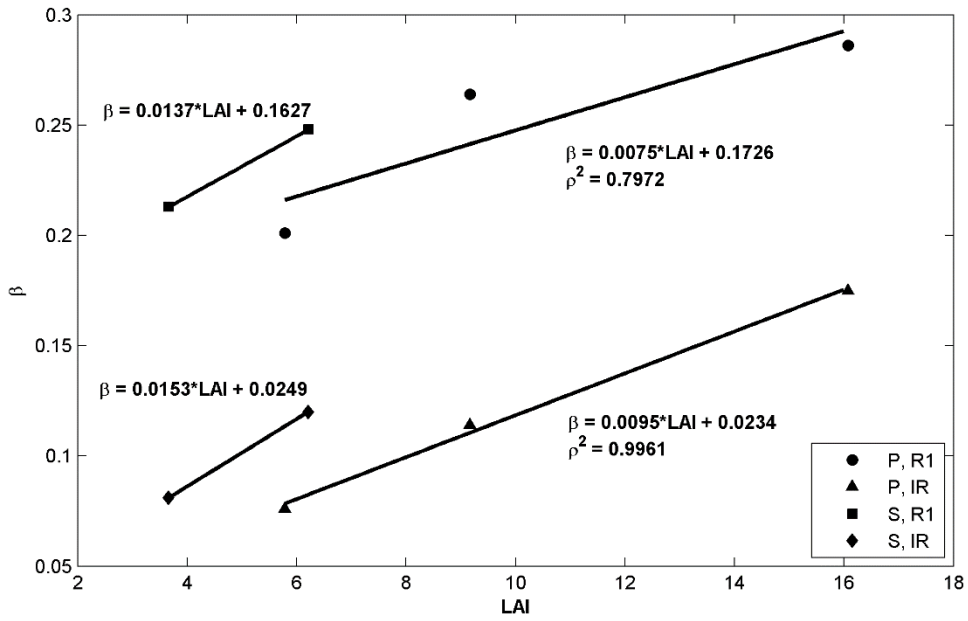

Figure 5.16 Relationship between the damping coefficient and the LAI for the different densities of both species (P and S) and two wave conditions (R1 and IR).

The results obtained in Figure 5.16 show a linear trend for each species and for all wave conditions. Although more points would be necessary to perform the adjustment, as a first analysis the fittings in Figure 5.16 shows a higher slope for *S. anglica*. This is in agreement with results presented by Paul et al. (2012) where a higher slope is obtained for stiffer material. That study pointed out the importance of the plant motion, distinguishing two types (cantilever and whip-like) and argued that a flexible material requires around a 4 times larger LAI value than a stiff material to produce the same attenuation. Bouma et al. (2010) found that smaller *S. anglica* densities are as effective as higher densities for *P. maritima* in dissipating wave energy. Results presented in Figure 5.16 are in agreement with both studies. *P. maritima*, which exhibits a whip-

like motion, requires around twice the *S. anglica* density, which moves like a cantilever, to produce the same wave damping.

5.3.6 Vegetation standing biomass

Vegetation standing biomass is related to its capacity to dissipate energy. The use of this parameter allows introducing variables such as vegetation density, area or even stiffness in an indirect way. Bouma et al. (2010) reported similar wave attenuation for *P. maritima* and *S. anglica* species when expressed in terms of standing biomass. Damping coefficients found in the experiments are represented as a function of standing biomass for different wave conditions in Figure 5.17. Cases for h = 0.4 m are presented. In order to extend the analysis, results for wave and current conditions are also plotted in the same figure.

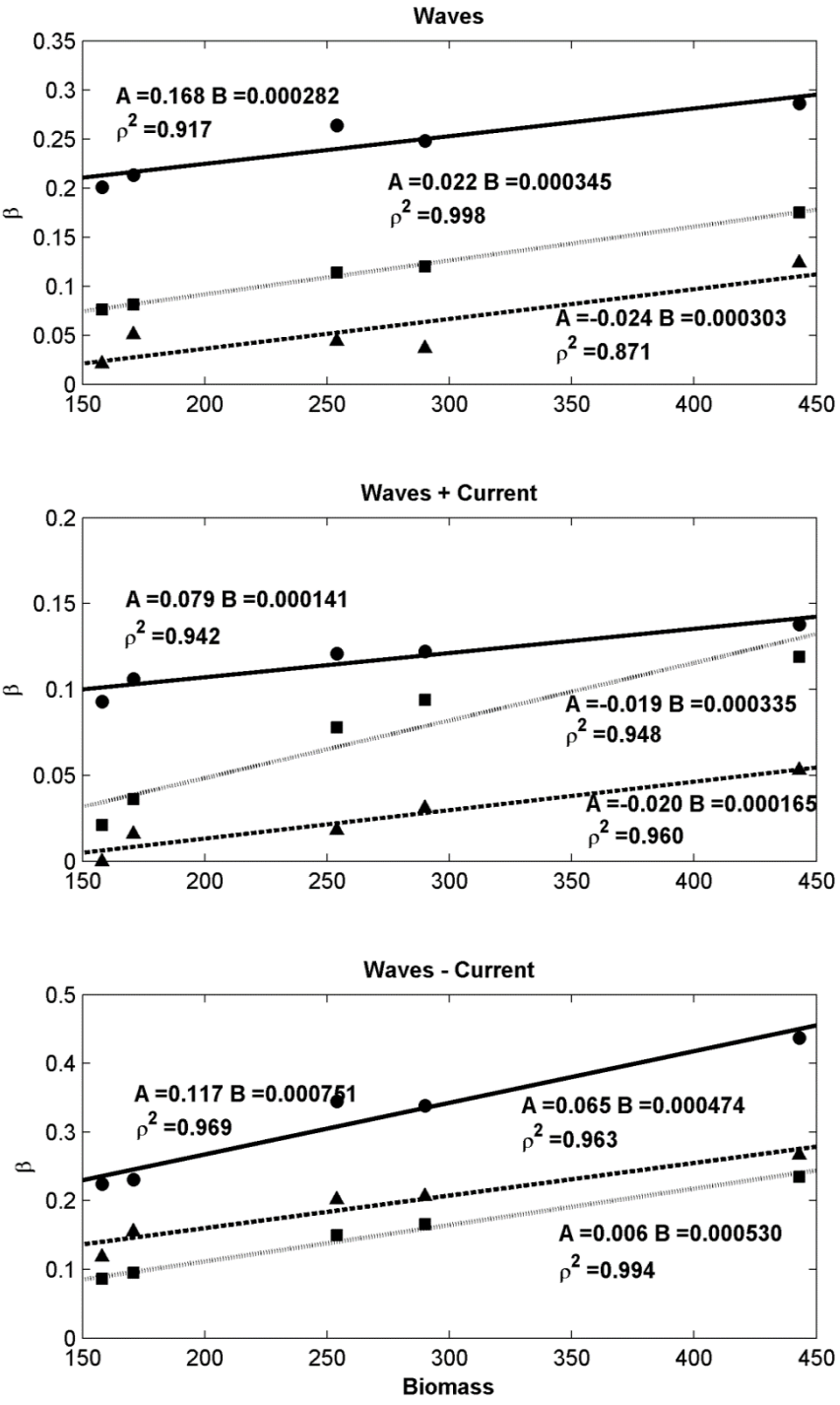

Figure 5.17 Damping coefficient for different standing biomass values. R1 (circles and solid line), R3 (triangles and dashed line) and IR (squares and dotted line) for waves only and waves and following and opposing current.

The relationship between the damping coefficient and vegetation standing biomass has been found to be linear (Bouma et al., 2010). Therefore, the formula $\beta = A + B * Biomass$ is applied for each wave condition. High correlation coefficients are obtained when fitting, supporting the existence of a linear relationship. In addition, a very interesting result is achieved. A very similar slope value (B) disregarding wave conditions is obtained from the fitting in the top panel. This indicates that changes in standing biomass modified the wave damping achieved for different wave conditions at a similar rate. This is not experienced for waves and currents together where different slopes are obtained for each wave condition. This highlights the nonlinear interaction between waves and currents.

The linear relationship found for both species in the present analysis suggests that standing biomass has a strong influence on wave damping, even larger than vegetation stiffness. Although Young's modulus for *S. anglica* is much larger than the one for *P. maritima*, standing biomass for both species fit linearly with β, with a high degree of correlation.

This analysis is extended next to evaluate the influence of water depth on wave damping also using a linear fitting for case R1. Results are plotted together in Figure 5.18 for the four water depths considered in the experiments.

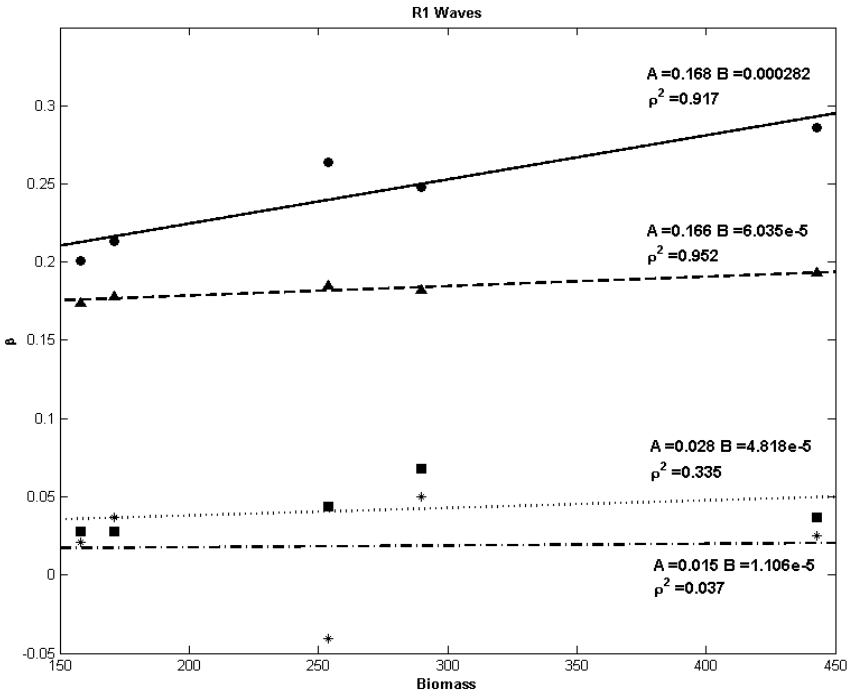

Figure 5.18 Damping coefficient for different biomass values and water depth. h= =0.40 m (Circles and solid line), h=0.60 m (triangles and dashed line), h=0.80 m (squares and dotted line) and h= 1.0 m (stars and dotted-dashed line).

Fittings show higher slopes for smaller water depths revealing a stronger influence of vegetation standing biomass for higher relative depths. Standing biomass influence can also be noticed attending to the values obtained for the correlation coefficients for the different water depths. Low correlation is obtained for high water depths where vegetation influence is smaller, as was pointed out in previous sections in this chapter.

5.4 Conclusions

An extensive analysis to assess the influence of waves and current and vegetation parameters on the energy attenuation provided by vegetation of two contrasting salt marsh species (*Puccinellia maritima* and *Spartina anglica*) has been presented. Different water depths and wave parameters (height and period) are considered for both regular and irregular waves with and without an underlying uniform current coming from different directions. Experiments have been developed in the Cantabria Coastal and Ocean Basin (CCOB) to study vegetation at a real scale and under controlled conditions. The study has been performed in terms of wave damping by analyzing the wave decay obtained for each test.

The analysis of the experimental data has shown a high correlation between the wave damping coefficients and water depth. A logarithmic fitting law was found to explain the variation of wave damping with water depth in both vegetation species. Wave damping estimation for the different wave conditions has allowed for the studying of the influence of wave height and wave period. As a general trend, higher wave damping has been obtained for shorter wave periods and smaller wave heights.

Tests run with currents following and opposing wave propagation direction have allowed for the evaluation of the influence of collinear current direction on wave damping. Wave damping decreases for waves and current acting in the same direction whereas it increases when current opposes wave propagation. This general trend is affected by the flow patterns developed around the vegetation meadow for different water depths. Current has been observed to diverge around the meadow due to the blocking induced by vegetation for small water depths. Therefore, flow velocities within the meadow are only due to waves. When the standing plant is not fully occupying the entire water depth, blocking is less effective. Observed patterns influence the wave and current interaction, especially for the less energetic wave conditions, and therefore, the damping rate. Velocity records at three different locations and for different water depths support the existence of these patterns and their influence on wave conditions. When waves are generated obliquely to current, wave damping increases.

Attending to vegetation characteristics, meadow density strongly influences wave damping rates. It has been shown that wave damping increases consistently with increasing vegetation density for both species. The difference in the biomechanical properties of both species has been also highlighted in the different results obtained in terms of the LAI. It has been found that *P. maritima* (flexible species) requires around twice the *S. anglica* (stiff species) density to deliver the same wave damping. Finally a study of the standing biomass influence has been performed. A linear relationship has been found between the vegetation standing biomass and the damping coefficients for the different densities in both species. It suggests that standing biomass has a strong influence on wave damping, even larger than vegetation stiffness. Furthermore, the fits obtained for different wave conditions exhibit almost the same slope. This indicates that changes in standing biomass modified the achieved wave damping for different wave conditions at a similar rate. This is not experienced for waves and current tests yielding different rates, highlighting the nonlinear interaction between waves and currents. The influence of the standing biomass is enhanced for smaller water depths where flow-vegetation interaction is stronger.

"when I meet God, I am going to ask him two questions: why relativity? And why turbulence? I really believe he will have an answer for the first"

Albert Einstein

6

A NEW FORMULATION FOR VEGETATION-INDUCED DAMPING UNDER COMBINED WAVES AND CURRENTS

Summary

This chapter presents a new formulation for vegetation-induced damping under the action of combined waves and currents. The new formulation accounts for the energy loss produced due to the mechanical work carried out on the vegetation and the produced wave damping when waves and currents are acting simultaneously. It is derived for current flowing in the same and in opposite direction to wave propagation. First, the formulation is obtained for regular waves and later extended for random wave trains considering Rayleigh wave height distribution. These formulations are then applied to laboratory data in order to obtain the associated drag coefficients. This allows obtaining a new formulation for the drag coefficient for wave and current conditions.

6.1 Introduction

Coastal vegetation, such as salt marshes or seagrasses, serves as buffer areas against flooding and erosion (e.g.: McGranahan et al. 2007; FitzGerald et al. 2008, Duarte et al. 2013). These habitats develop in areas commonly affected by tidal currents or wave-induced currents flowing simultaneously to wind or swell waves (e.g.: Ysebaert et al., 2011). Therefore, they are subject to the combined effect of both waves and currents. To date, the vast majority of studies focusing on energy dissipation induced by coastal vegetation have studied current flows (e.g.: Fonseca et al., 1992; Ghisalberti and Nepf, 2002; Bouma et al., 2013) or wave conditions (e.g.: Kobayashi et al., 1993; Mendez et al., 1999) separately.

The effects of a following (propagating in the same direction) or opposing uniform current on the propagation of surface gravity waves have been studied by several authors. Longuet-Higgins and Stewart (1960, 1961) first introduced the wave and current interaction in the energy flux equation by means of the radiation stress. A first order velocity potential for an irrotational wave-current field over a horizontal bottom was proposed by Peregrine (1976) and then adopted by several authors such us Baddour and Song (1990). They developed fourth order equations for the determination of wavelength and height and the energy flux density expressed to the second order in wave amplitude. Later, Jonsson et al. (1995) extended these equations to higher-order Stokes waves. Many analytical expressions can be found in the literature to describe the wave-current interaction but the complexity of this nonlinear interaction has lead to the use of numerical tools to be able to overcome complex configurations and higher order effects. Recently, numerical models have been developed to accomplish the high nonlinear effects present in the wave-current interaction. Approaches based on the mild-slope wave equation (Chen et al., 2005) or Boussinesq equations (Zou et al., 2013) have been used to model the nearshore wave-current interaction. More sophisticated models based on RANS equations (Zhang et al., 2014) have been presented in the last years.

Besides the aforementioned wave and current interaction studies, the momentum damping produced by aquatic vegetation under wave and current conditions has been poorly characterized. Based on the conservation of energy equation, Dalrymple et al. (1984) was the first to formulate a semiempirical expression to consider the energy loss for regular waves propagating through vegetation. Dalrymple et al. (1984) formulation was later extended by Mendez and Losada (2004) for random waves. Ota et al. (2004) extended the wave decay model presented by Kobayashi et al. (1993) for wave and current conditions considering a linear combination of the wave and current wave decay. Later, Li and Yan (2007) presented a three-dimensional model based on RANS equations, in which advection, diffusion and pressure terms are solved separately and vegetation is modeled as a sink of momentum. They concluded that

current flowing in the same direction as wave propagation increases wave decay based on computed vertical velocity profiles. These results contradict the laboratory measurements presented by Paul et al. (2012) which conducted flume experiments using vegetation flexible mimics to study the effect of a waves combined with a following current.. They found that tidal currents reduce wave energy dissipation. Recently, Hu et al. (2014) proposed a new empirical relationship between the drag coefficient and a new Reynolds number based on laboratory data. This formulation was obtained for a non-predictable Reynolds number based on a mean velocity measured inside the canopies field. Tests were performed using rigid cylinders and currents in the same direction as wave propagation. The analysis of different current velocity values reveals different effects on wave damping. Small current velocities lead to smaller wave damping in comparison to pure wave conditions and the opposite occurs for higher currents. However, tests performed for different current velocity were performed changing the generated wave height and therefore they are not directly comparable. Furthermore, the proposed analytical model for current-wave flows presents some limitations since it is obtained for shallow water conditions considering the linear superposition of waves and currents velocities without considering the interaction between them.

Following the energy conservation approach presented by previous authors (e.g.: Dalrymple et al., 1984; Mendez and Losada, 2004), this work aims to obtain the relationship between the energy loss produced due to the mechanical work carried out on the vegetation and the induced wave damping when waves and currents are acting in the same and in opposite direction considering the interaction between both flow conditions. The analytical model proposed here is based on the experimental results of experiments conducted in the Cantabria Coastal and Ocean Basin (CCOB) large basin at real scale and using two real vegetation species. The experimental set-up is presented in Section 2. The new model for the wave damping under wave-current-vegetation interaction is presented in Section 3. In Section 4, the new formulation is used to fit experimental data and found new expressions for the drag coefficient under pure waves and wave and current conditions. Finally, some conclusions are presented in Section 5.

6.2 Experimental set-up

Experiments were conducted in the Cantabria Coastal and Ocean Basin (CCOB) large-scale facility under waves combined with following and opposing currents. Two saltmarshes species were grown up from seeds to test real vegetation under different flow conditions. The flow and vegetation characteristics are specified in the following sections. A more detailed description of the experimental setup can be found in Chapters 4 and 5 of this thesis.

6.2.1 Flow conditions

The energy dissipation induced by real vegetation is studied for different flow conditions. Five different regular and one random wave trains (Table 6.1) are tested under three different flow conditions (pure waves, waves and current in the same direction and waves and current in the opposite direction). Two different water depths are considered: 0.40 and 0.60 m.

Wave Conditions	Type	H(m)|Hs(m)	T(s)|Tp(s)
R1	Regular	0.15	2
R2	Regular	0.20	2
R3	Regular	0.20	1.2
R4	Regular	0.20	1.7
R5	Regular	0.20	2.2
I	Irregular	0.12	1.7

Table 6.1 Wave conditions

The six wave conditions were tested considering wave trains including 200 waves, allowing a statistical representative number of waves. For regular waves, more than 150 waves are recorded with uniform characteristics at the generation boundary composed of 64 independent wave makers. All cases in Table 1 were tested in combination with a 0.30 m/s current acting in both directions. Measurements began for 200 waves after a uniform current profile was reached. Consequently, a total number of 18 different flow conditions were tested.

6.2.2 Vegetation conditions

Tests were conducted to analyze flow interaction with two real salt marsh vegetation species, namely, *Spartina anglica* and *Puccinellia maritima*. These two species develop in the pioneer zone and the lower marsh of the marsh zone, respectively. They were selected to provide information on sensitivity to different biomechanical properties, namely differences in flexibility of both species as well as geometry and biomass. The Young modulus, geometric dimensions and dry weight were measured for both species and are summarized in Table 6.2.

Species	Esteam (MPa)	ELeaf (MPa)	Plant length (m)	Leaf length (m)	Number of leaves/shoot	Leaf width (m)	Dry weight shoot (gr/shoot)
Spartina	164.2	77.6	0.284	0.178	5	0.006	0.460
Puccinellia	13	7.8	0.473	0.230	5.5	0.003	0.184

Table 6.2 Biomechanical plant properties for both species

Energy dissipation induced by the drag force acting on the vegetation is dependent on the plant length. Bending observed for flexible vegetation results in a reduced drag-forming area of the canopy. Consequently, the actual vegetation length affected by the flow depends on the plant behavior under different flow conditions (waves and currents) and will be a function of plant geometry, flexibility and buoyancy (Luhar and Nepf, 2011). Plant motion influences the energy dissipation induced by plants.

The two species considered in this study behave differently under identical flow conditions due to their different biophysical properties. *S. anglica* responds to flow like a cantilever whereas *P. maritima* exhibits a whip-like motion. For *P. maritima* the effect of current velocity is a strong bending due to its high flexibility. Figure 6.1 shows a schematic representation of the motions experienced by both species under pure wave conditions and under combined waves and currents, extracted from visual observations during the experiments.

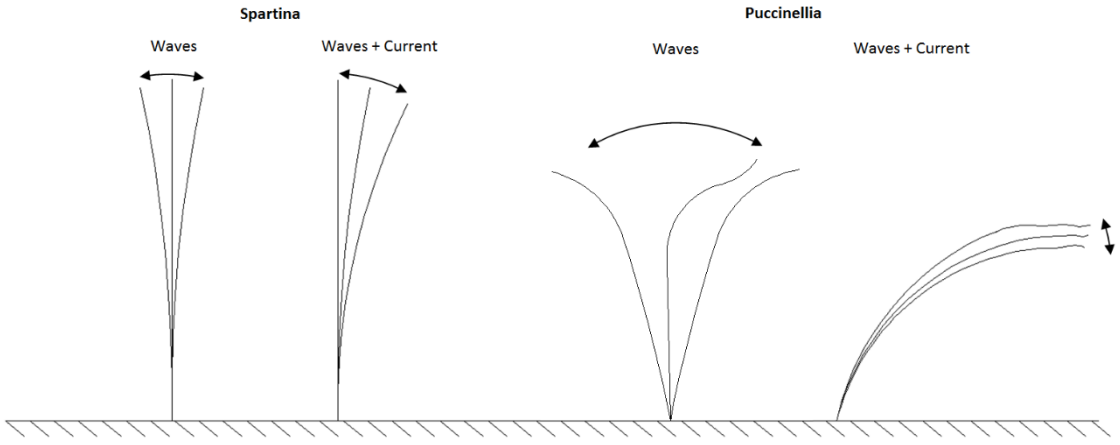

Figure 6.1 Schematic representation of plant movement. The stiff species (Spartina) moves lika a cantilever under waves (left) and waves+current (right). The flexible species (Puccinellia) moves in a whip-like motion under waves (left) and waves+current (right).

Based on the above it can be concluded that including the influence of the deflected plant length on the estimation of the dissipation produced by flexible vegetation is very important. Not considering the reduced drag-forming area due to bending may lead to an overestimation of energy dissipation. Luhar and Nepf (2011) proposed a new formulation to calculate the nondimensional deflected length of a plant based on its bending angle (θ). An estimation of the bending angle was obtained for different flow conditions by means of video recording during the experiments. The observed mean bending angle for *S. anglica* was almost zero, whereas *P. maritima* bended according to flow velocities especially when current was acting combined with waves. A mean vertical angle between 30 and 40º was estimated for pure wave conditions. This value was observed to increase strongly when current was acting, yielding values between 45 and 55º. Luhar and Nepf (2011) formulation presented in equation (1) is used to calculate the relationship between the deflected length and the plant length (l).

$$\frac{l_D}{l} = \int_0^l cos\theta dz \tag{1}$$

For *P. maritima* and considering waves only, $\frac{l_D}{l}$ ratio is 80%, whereas under the combined effect of waves and currents this ratio is reduced to 60%. Therefore, the combined effect of waves and currents contributes reducing the drag-forming area.

Another aspect that influences energy dissipation is vegetation density. In this work three different plant densities (numbers of shoots per square meter) were considered for *P. maritima* and two for *S. anglica* in the experimental setup. Densities tested are summarized in Table 6.3.

Case	Species	Density (shoots/m2)
P100	P. maritima	2436
P66	P. maritima	1389
P33	P. maritima	877
S100	S. anglica	729
S66	S. anglica	430

Table 6.3 Vegetation conditions

High densities, P100 and S100, are representative of field conditions whereas the lower densities (P66, P33 and S66) are used to carry out a sensitivity analysis of different vegetation conditions on drag imposed by vegetation. Lower densities may be representative of vegetation seasonality or different health conditions. P100 and S100 were tested under all wave conditions. However, only R1, R3 and I wave conditions are considered for the lowered densities. In total 276 tests were carried out as a combination of two different species and varying densities, water depths, wave heights and periods and pure, following and opposing currents. A detailed analysis of the resulting data set can be found in Chapter 5 of this thesis.

6.3 Analytical damping formulation for waves and currents conditions

6.3.1 Regular waves

Waves and currents propagating though a vegetation meadow lose energy due to dissipation produced by vegetation on the flow. Dalrymple et al. (1984) described a model for regular waves by relating the wave energy flux gradient produced along the vegetation field to the dissipation induced by the plant canopies. Following the same approach, a new analytical formulation is presented in this section for regular wave conditions acting together with an underlying current. This formulation is based on the following assumptions:

1. Current is uniform over the water depth and alongshore the meadow.
2. Current and waves propagates normally.
3. Linear wave theory is assumed.
4. An irrotational and uniform wave-current field is considered.
5. Doppler Effect is considered in the wave velocity field.
6. Plant motion is neglected and it is consider that the drag coefficient value covers the ignorance of plant motion. Therefore, the dissipation is considered to be only due to drag force.
7. Drag force horizontal component is the dominant one.
8. Drag coefficient is a depth-averaged coefficient.

9. Constant depth and horizontal bottom is assumed.

10. Dense vegetation conditions are considered.

Based on the above assumptions, the conservation of energy equation for waves and current conditions is expressed as:

$$\frac{\partial E_{wc} c_{g_{wc}}}{\partial x} = -\varepsilon_{D_{wc}} \tag{2}$$

where E_{wc} is the energy density associated to waves and current conditions, $c_{g_{wc}}$ the group velocity for the same flow conditions, x is the along vegetation coordinate and $\varepsilon_{D_{wc}}$ the time average rate of energy dissipation per unit horizontal area induced by the vegetation.

Considering the velocity potential of the irrotational and uniform wave-current field (assumptions 1 - 5), to first order in wave elevation (Peregrine, 1976), the group velocity associated to this flow conditions is expressed as:

$$c_{g_{wc}} = \frac{\partial \sigma_{wc}}{\partial k} = U_0 + \frac{1}{2}\left(1 + \frac{2kh}{sinh2kh}\right)\left(\frac{g}{k} tanhkh\right)^{1/2} \tag{3}$$

where σ_{wc} is the wave-current angular frequency ($\sigma_{wc} = \sigma - U_0 k$), k is the wave number, U_0 is the uniform current velocity, σ is the wave angular frequency, h is the water depth and g is the gravitational acceleration. Again considering an irrotational and uniform wave-current field the depth-integrated and time-averaged energy flux density of wave-current field can be expressed to the second order in the wave height, H, as follows (Baddour & Song, 1990):

$$E_{wc} = \frac{\rho}{16} g \left(1 + \frac{2kh}{sinh2kh}\right)\left(\frac{g}{k} tanhkh\right)^{1/2} H^2 + \frac{\rho}{16} g U_0 \left(3 + \frac{4kh}{sinh2kh}\right) H^2 + \frac{3\rho}{16} k U_0^2 \left(\frac{g}{k} cothkh\right)^{1/2} H^2 + \frac{\rho}{2} h U_0^3 \tag{4}$$

where the first term represents the bodily transport of energy by the wave group velocity (wave mean energy density times the group velocity). The second term corresponds to the transport of that bodily energy performed by the current velocity and accounts for the work done by the current against the radiation stress of the waves. The third and fourth term represent the kinetic energy transport performed by the current. They account for the mean current energy density transport conducted by the relative wave drift velocity, the mean wave action energy density transport carried by the current velocity and the mean current energy density transport performed by the current. Therefore, the first term corresponds to the wave energy component,

the last one to the current energy component and the second and the third to the energy due to the non-linear interaction between waves and currents.

The depth-integrated and time-averaged energy dissipation per unit horizontal area considering the horizontal direction as the predominant flow direction and the horizontal bottom at $z = -h$, is given by:

$$\varepsilon_{D_{wc}} = \overline{\int_{-h}^{-h+l_D} F_{wc} u_{wc} dz} \tag{5}$$

where l_D is the deflected plant length defined in previous section. This length gets very important in the estimation of the energy dissipation induced by flexible vegetation since the energy lose area is reduced due to plant bending. For rigid plant conditions l_D gets equal to l, the plant length. F_{wc} is the force acting on the vegetation per unit volume. According to several authors (Dalrymple et al., 1984; Kobayashi et al., 1993; Mendez and Losada, 2004) plant swaying and inertial force are neglected and this force is considered to be equal to the horizontal drag force (assumptions 6, 7 and 8) given by:

$$F_{wc} = \frac{1}{2}\rho C_{D_{wc}} a N u_{wc} |u_{wc}| \tag{6}$$

where $C_{D_{wc}}$ is the depth-average drag coefficient, N is the number of vegetation stands per unit horizontal area and a is the plant area per unit height of each vegetation stand normal to u_{wc} which is the horizontal velocity given by:

$$u_{wc} = U_0 + \frac{gk}{2\sigma_{wc}} H \frac{coshk(h+z)}{coshkh} sin(kx - \sigma t) \tag{7}$$

The vegetation density strongly influences the macroscale flow patterns and the penetration flow within the vegetation meadow. Luhar et al. (2010) highlighted the higher incanopy velocities associated to wave conditions in agreement with the experimental results presented by Lowe et al. (2005) who stated that oscillatory flow increases water motion inside a canopy in comparison to the results obtained with unidirectional flow. Zong and Nepf (2010) experimental results shown an almost zero incanopy velocity for a dense patches and a fully developed region within the vegetation where the current velocity remains constant along the patch length (assumption 1). Also, Nepf (2012) reported that for dense canopies and almost zero current velocity is registered inside the canopy. Belcher et al. (2003) predicted that dense canopy regimes occurs at $\frac{t}{\Delta S^2} l > 0.1$ where t is the vegetation thickness and ΔS is the averaged plant spacing. This parameter is calculated for all tested conditions yielding values much greater than

0.1. Therefore, all tested vegetation conditions in the CCOB experiments are considered as dense canopies (assumption 10).

Furthermore, experimental observations reveal no penetration of the current velocity inside the vegetation meadow and current flow patterns that flow around and over the meadow depending on the submergence ratio. This aspect is discussed in next section (see also Figure 6.3). These observations are supported by the velocity measurements taken inside the meadow which reveal an almost zero current component and a predominant oscillatory one (Chapter 5). Therefore, the contribution of the current velocity to the drag force is neglected for dense vegetation conditions. This assumption is in agreement with the main physical basis of the conservation of energy equation which considers that the change in the energy flow is only produced by the dissipation induced by vegetation. Due to the Doppler effect, wave period is modified by current affecting to the wave celerity and therefore, the velocity considered to estimate the energy dissipation is expressed as:

$$u_{wc} = \frac{gk}{2\sigma_{wc}} H \frac{coshk(h+z)}{coshkh} sin(kx - \sigma t) \tag{8}$$

This Doppler effect is not considered in Hu et al. (2014). Their model do not considered the change in the wave period induced by the underlying current. Besides that, the wave velocity formulation in that study is particularized for shallow water conditions. Considering the velocity of equation (8) the energy dissipation is expressed as:

$$\varepsilon_{D_{wc}} = \overline{\int_{-h}^{-h+l_D} \frac{1}{2} \rho C_{D_{wc}} aN \left(\frac{gk}{2(\sigma - U_0 k)} H \frac{coshk(h+z)}{coshkh} sın(kx - \sigma t) \right)^2}$$

$$\overline{\left| \frac{gk}{2(\sigma - U_0 k)} H \frac{coshk(h+z)}{coshkh} sın(kx - \sigma t) \right|} dz \tag{9}$$

Phase averaging and solving the vertical integration, the energy dissipation rate is given by:

$$\varepsilon_{D_{wc}} = -\frac{2}{3\pi} \rho C_{D_{wc}} aN \left(\frac{gk}{2(\sigma - U_0 k)} \right)^3 \frac{sinh^3 kl_D + 3sinhkl_D}{3kcosh^3 kh} H^3 \tag{10}$$

This formulation differs to the energy dissipation proposed by Dalrymple et al. (1984) for regular waves since first, it considers the drag coefficient for waves and current conditions, second the wave angular frequency is modify due to Doppler effect and third the deflected plant length is considered.

The conservation of energy equation have been used by previous authors to obtain an expression for the wave decay produced along the meadow. Dalrymple et al. (1984) was the first to present an expression for regular waves where the wave damping is a function of a damping coefficient:

$$H = \frac{H_0}{1 + \beta x} \tag{11}$$

where β is the damping coefficient for regular waves. Analogously, solving the differential equation (2) and assuming a constant depth and horizontal bottom (assumption 9), the wave decay for wave and current conditions can be obtained as:

$$H = \frac{H_0}{1 + \beta_{wc} x} \tag{12}$$

where β_{wc} is the damping coefficient for waves and current conditions expressed as:

$$\beta_{wc} = \frac{A_0 H_0}{B} \tag{13}$$

$$A_0 = \frac{2}{3\pi} \rho C_{D_{wc}} a N \left(\frac{gk}{2(\sigma - U_0 k)} \right)^3 \frac{sinh^3 kl_D + 3sinhkl_D}{3kcosh^3 kh} \tag{14}$$

$$B = \left[\frac{\rho g}{8} \left(1 + \frac{2kh}{sinh2kh} \right) \left(\frac{g}{k} tanhkh \right)^{\frac{1}{2}} + \frac{\rho g}{8} U_0 \left(3 + \frac{4kh}{sinh2kh} \right) + \frac{3\rho k}{8} U_0^2 \left(\frac{g}{k} cothkh \right)^{\frac{1}{2}} \right] \left[U_0 + \frac{1}{2} \left(1 + \frac{2kh}{sinh2kh} \right) \left(\frac{g}{k} tanhkh \right)^{\frac{1}{2}} \right] \tag{15}$$

This new expression of the damping coefficient for wave and current conditions can be used to obtain the associated drag coefficient in a predictable way in contrary to Hu et al. (2014) where the mean velocity along the field is considered in the estimation of this coefficient. Many authors have based their studies on this coefficient (Kobatashi et al., 1993; Mendez et al., 1999). Dalrymple et al. (1984) formulation allows estimating the drag coefficient for regular wave conditions as:

$$C_D = \frac{9\pi}{4aNH_0 k} \frac{(sinh2kh + 2kh) sinhkh}{sinh^3 kl_D + 3sinhkl_D} \beta \tag{16}$$

The formulations presented in this study allows estimating the drag coefficient for wave and current conditions as:

$$C_{Dwc} = \frac{3\pi}{2aN\left(\frac{gk}{2(\sigma - U_0 k)}\right)^3 H_0} \frac{3k cosh^3 kh}{sinh^3 kl_D + 3sinhkl_D} \left[\frac{g}{8}\left(1 + \frac{2kh}{sinh2kh}\right)\left(\frac{g}{k} tanhkh\right)^{\frac{1}{2}} + \frac{g}{8} U_0 \left(3 + \frac{4kh}{sinh2kh}\right) + \frac{3k}{8} U_0^2 \left(\frac{g}{k} cothkh\right)^{\frac{1}{2}}\right]$$

$$\left[U_0 + \frac{1}{2}\left(1 + \frac{2kh}{sinh2kh}\right)\left(\frac{g}{k} tanhkh\right)^{\frac{1}{2}}\right] \beta_{wc} \quad (17)$$

This coefficient accounts for the energy flux gradient produced along the meadow for wave and currents flowing normally in both, the same and in the opposite direction.

6.3.2 Extension for random waves

Mendez and Losada (2004) extended Dalrymple et al. (1984) formulation for random waves. The wave decay for this conditions was expressed as:

$$H_{rms} = \frac{H_{rms,0}}{1 + \beta' x} \quad (18)$$

where β' is the damping coefficient for random waves. Mendez and Losada (2004) presented the drag coefficient associated to this formulation as:

$$C'_D = \frac{3\sqrt{\pi}}{aNH_{rms,0}k} \frac{(sinh2kh + 2kh)sinhkh}{sinh^3 kl_D + 3sinhkl_D} \beta' \quad (19)$$

Assuming a Rayleigh distribution as in Mendez and Losada (2004) a characterization of the random variation in wave height can be achieved satisfactory. The Rayleigh probability density function is a function of the root-mean-square wave height, *Hrms*, according to:

$$p(H) = \frac{2H}{H_{rms}^2} exp\left[-\left(\frac{H}{H_{rms}}\right)^2\right] \quad (20)$$

where

$$H_{rms}^2 = \int_0^\infty H^2 p(H)\, dH \quad (21)$$

Since the energy dissipation is a function of the cubit mean wave height, the relationship between that height and the root-mean-square wave height is obtained:

$$\int_0^\infty H^3 p(H)\, dH = \frac{3\sqrt{\pi}}{4} H_{rms}^3 \tag{22}$$

Considering this relationship and assuming constant depth and horizontal bottom the wave decay for random waves and currents is expressed as:

$$H_{rms} = \frac{H_{rms,0}}{1 + \beta'_{wc} x} \tag{23}$$

where β'_{wc} is the damping coefficient and is obtained as:

$$\beta'_{wc} = \frac{A'_0 H_{rms,0}}{B} \tag{24}$$

$$A_0 = \frac{1}{2\sqrt{\pi}} \rho C_{D_{wc}} aN \left(\frac{gk}{2(\sigma - U_0 k)}\right)^3 \frac{sinh^3 kl + 3sinhkl}{3kcosh^3 kh} \tag{25}$$

The wave parameters considered in previous equations are the ones obtained considering the peak wave period and the root-mean-square wave height. Again, the drag coefficient associated to these conditions can be obtained as:

$$C'_{Dwc} = \frac{2\sqrt{\pi}}{aN\left(\frac{gk}{2(\sigma - U_0 k)}\right)^3 H_{rms,0}} \frac{3kcosh^3 kh}{sinh^3 kl_D + 3sinhkl_D} \left[\frac{g}{8}\left(1 + \frac{2kh}{sinh2kh}\right)\left(\frac{g}{k} tanhkh\right)^{\frac{1}{2}} + \frac{g}{8} U_0 \left(3 + \frac{4kh}{sinh2kh}\right) + \frac{3k}{8} U_0^2 \left(\frac{g}{k} cothkh\right)^{\frac{1}{2}}\right]$$

$$\left[U_0 + \frac{1}{2}\left(1 + \frac{2kh}{sinh2kh}\right)\left(\frac{g}{k} tanhkh\right)^{\frac{1}{2}}\right] \beta'_{wc} \tag{26}$$

This coefficient accounts for the dissipation produced along the meadow for random waves and currents flowing in the same and in opposite direction to wave propagation.

6.4 Drag coefficients calculation

6.4.1 Wave height damping analysis

Energy dissipation induced by a vegetation meadow can be estimated in terms of the wave height decay along the vegetation field. Formulations presented by Dalrymple et al. (1984) and

Mendez and Losada (2004) for regular and random waves respectively, determine the wave damping as a function of a damping coefficient (Equations 11 and 18 in this chapter). These formulas have been used in previous studies (e.g.: Koftis et al., 2013; Ozeren et al., 2013; Anderson et al., 2014) to calibrate the damping coefficient by fitting experimental results. The same approach is followed in the present study where previous formulations are used to estimate the wave decay under pure wave conditions. Equation (12) is used to fit results for regular waves and currents and equation (23) for random waves and currents. An example of the fittings obtained is shown in Figure 6.2 where the damping coefficients for four different wave conditions and h=0.40 and 0.60 m are displayed. For simplicity, all damping coefficients are expressed as β.

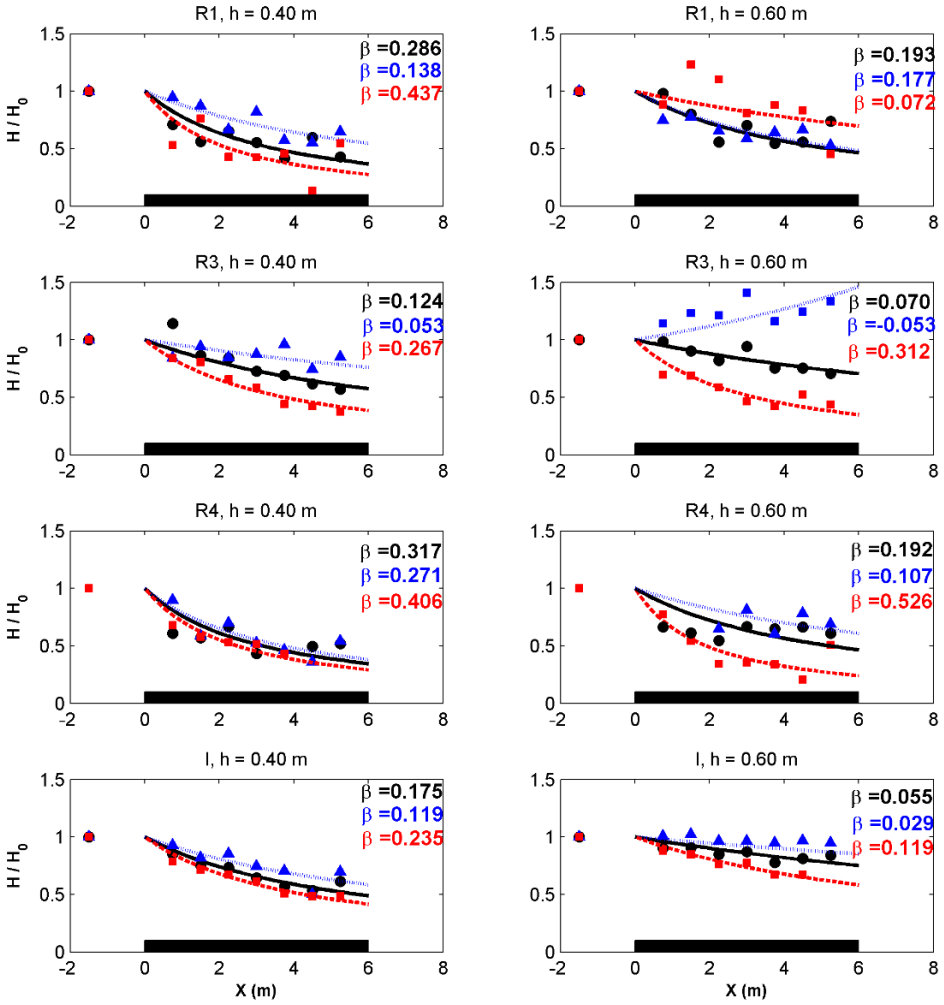

Figure 6.2 Wave damping decay fitting for four different pure wave conditions (black), acting simultaneously to a current following wave propagation (blue) and in the opposite direction (red). Results for h = 0.40 m (left) and 0.60 m (right). The damping coefficient and the correlation coefficient for each case are displayed.

Results for h = 0.40 m (left column) reveal a smaller wave attenuation when waves and current flows in the same direction (blue) in comparison to pure wave conditions (black) in agreement with Paul et al. (2012). Hu et al. (2014) discusses the effect of a following current in terms of the ratio between current velocity and waves velocity ($\alpha = \frac{U_0}{U_w}$). They exposed that for small values of α ($\alpha < 0.65 - 1.25$ depending on the test) currents flowing in the same direction as wave propagation reduces the wave attenuation produced by vegetation. That analysis is performed based on Dalrymple et al. (1984) formulation for regular waves apply to both, pure waves and waves and current conditions without considering the modification of Dalrymple et al. (1984) formulation when currents are flowing with waves (as shown in previous section). This joint to the α values of the presented experiments that ranges from 0.50 to 1.4 leads to consider that the obtained reduction in wave attenuation produced when current in flowing in the same direction as waves is in agreement with previous studies.

Conversely, when the current is flowing opposing waves (red) wave damping increases. This behavior is observed for all wave conditions and h=0.40 m. Therefore, it can be stated that for this water depth following currents tends to reduce wave attenuation while an opposing current increases wave damping.

Results for h = 0.60 m show the same general trend although some different behaviors are observed. They correspond to wave conditions with the smallest wave height and period that are strongly influenced by wave-current interaction. At h=0.60 m the current flow pattern differs from the one developed for h = 0.40 m where plants are emerged or nearly emerged. A sketch of both conditions is displayed in Figure 6.3.

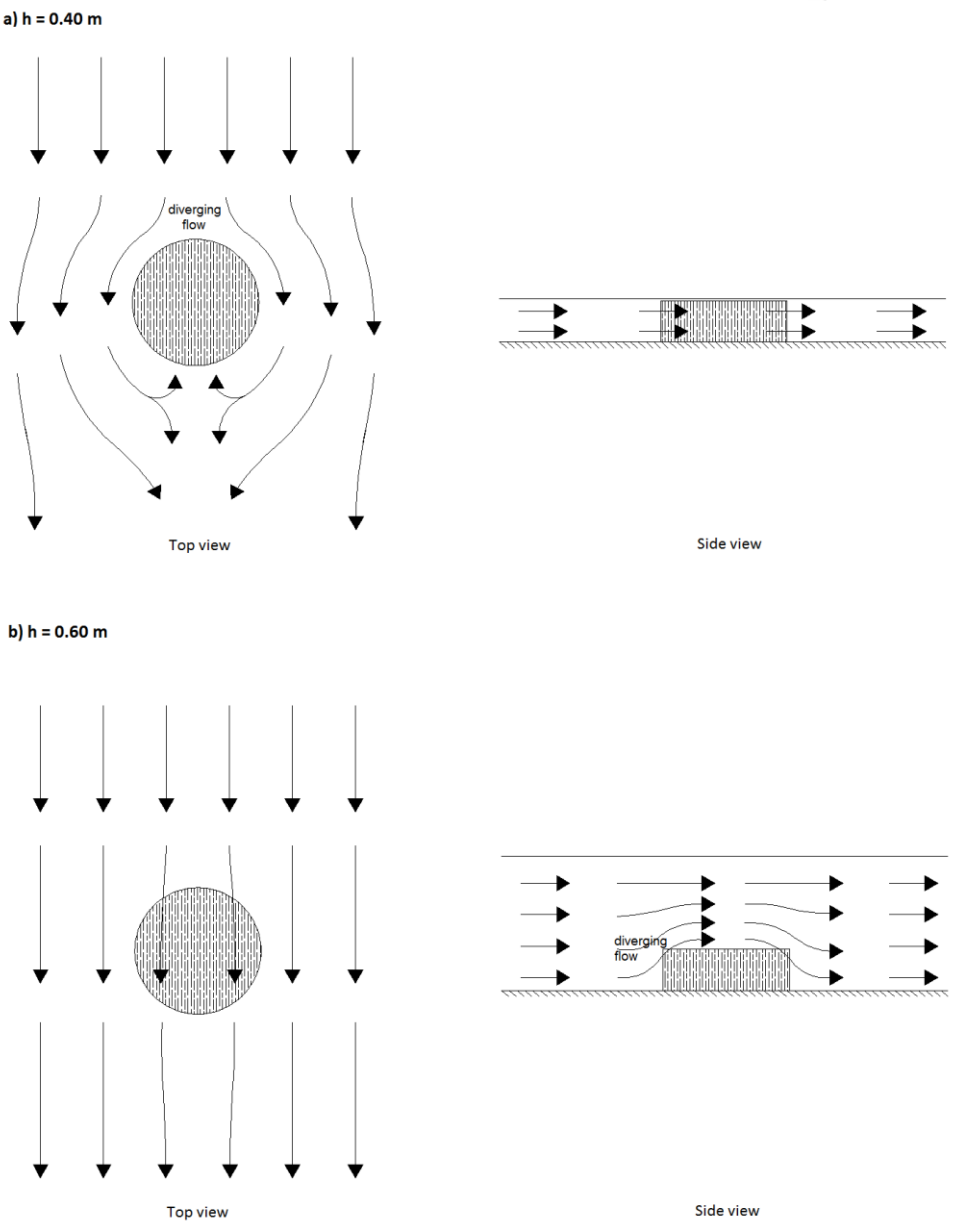

Figure 6.3 Current flow patterns for a) h = 0.40 m and b) h = 0.60 m. Black circle and square represent the vegetation meadow.

For h = 0.40 m current patterns show a strong diverging flow at the leading edge of the vegetation field. The current flow is diverted toward the non-vegetated area decelerating at that location and the velocity in the transverse direction increases leading to a small penetration of the current velocity in the meadow. This pattern is in agreement with Zong and Nepf (2010) experiments performed with artificial vegetation with similar densities as the ones presented in this study.

The current flow pattern for the submerged condition (h = 0.60 m; right column in Figure 6.2) presents instead a diverging flow in the vertical direction. The resistance presented by the vegetation leads to the blockage of the current velocity in that area and diverting the flow toward the free flow above the vegetation field. This effect enhances the shear layer formed at the interface between the vegetation patch and the free flow. Both the current flow focusing over the vegetation field and the developed shear layer at that area yield to a strong interaction between the current and the waves. Less energetic waves are highly modified under these conditions. The wave train with the smallest wave period (R3) is strongly influenced by currents in the same direction. Wave height remains almost constant or even increases inducing damping coefficients close to zero or even negative values. Also the wave train with the smallest wave height (R1) presents a different behavior, in this case for currents in the opposite direction. Where for the other tests a negative current increases wave damping for this particular small amplitude waves, the damping is reduced. Table 6.4 shows the damping coefficients obtained for all laboratory experiments.

Vegetation	Case	H (m) | Hs (m)	T (s) | Tp (s)	h (m)	N (stems/m2)	β Waves	β Waves + Current	β Waves - Current
P100	**R1**	0.15	2	0,4	2436	0,286	0,138	0,437
	R2	0.20	2	0,4	2436	0,243	0,198	0,353
	R3	0.20	1,2	0,4	2436	0,124	0,053	0,267
	R4	0.20	1,7	0,4	2436	0,317	0,271	0,406
	R5	0.20	2,2	0,4	2436	0,129	0,013	0,208
	I	0.12	1.7	0,4	2436	0.175	0.119	0.235
	R1	0.15	2	0,6	2436	0,193	0,177	0,072
	R2	0.20	2	0,6	2436	0,17	0,11	0,247
	R3	0.20	1,2	0,6	2436	0,07	-0,053	0,312
	R4	0.20	1,7	0,6	2436	0.192	0,107	0,526

	R5	0.20	2,2	0,6	2436	0,026	0,091	0,072
	I	0.12	1.7	0,6	2436	0.055	0.029	0.119
P66	**R1**	0.15	2	0,4	1389	0,264	0,121	0,345
	R3	0.20	1,2	0,4	1389	0,044	0,018	0,202
	I	0.12	1.7	0,4	1389	0.114	0.078	0.15
	R1	0.15	2	0,6	1389	0,185	0,153	0,168
	R3	0.20	1,2	0,6	1389	0,064	-0,003	0,144
	I	0.12	1.7	0,6	1389	0.04	0.032	0.099
P33	**R1**	0.15	2	0,4	877	0,201	0,093	0,224
	R3	0.20	1,2	0,4	877	0,021	0	0,118
	I	0.12	1.7	0,4	877	0.076	0.021	0.086
	R1	0.15	2	0,6	877	0,174	0,142	0,165
	R3	0.20	1,2	0,6	877	0,048	-0,033	0,092
	I	0.12	1.7	0,6	877	0.033	0.018	0.048
S100	**R1**	0.15	2	0,4	729	0,248	0,122	0,338
	R2	0.20	2	0,4	729	0,236	0,22	0,274
	R3	0.20	1,2	0,4	729	0,037	0,031	0,207
	R4	0.20	1,7	0,4	729	0,298	0,145	0,133
	R5	0.20	2,2	0,4	729	0,125	-0,03	0,163
	I	0.12	1.7	0,4	729	0.12	0.094	0.166
	R1	0.15	2	0,6	729	0,182	0,21	0,064

	R2	0.20	2	0,6	729	0,166	0,15	0,169
	R3	0.20	1,2	0,6	729	0,05	-0,019	0,082
	R4	0.20	1,7	0,6	729	0,140	0,149	0,394
	R5	0.20	2,2	0,6	729	0,056	0,11	0,017
	I	0.12	1.7	0,6	729	0.034	0.001	0.07
S66	**R1**	0.15	2	0,4	430	0,213	0,106	0,231
	R3	0.20	1,2	0,4	430	0,051	0,016	0,155
	I	0.12	1.7	0,4	430	0.081	0.036	0.095
	R1	0.15	2	0,6	430	0,178	0,168	0,128
	R3	0.20	1,2	0,6	430	0,024	-0,078	0,084
	I	0.12	1.7	0,6	430	0.029	0.017	0.075

Table 6.4 Damping coefficients obtained for each test.

These damping coefficients are directly related to the drag coefficient and they are used to evaluate the drag coefficient for each test.

6.4.2 Drag coefficients for regular waves

The drag coefficients associated to pure regular wave conditions are obtained using Dalrymple et al. (1984) formulation (Equation 16 in this chapter). Drag coefficients are obtained considering the damping coefficients fitted to experimental results as shown in section 4.1 and for $l_D = 0.80 * l$ for *P. maritima*, as explained in section 2.2. In the coming figures, results are represented as a function of the Reynolds number calculated, following previous studies (e.g.: Kobayashi et al., 1993 or Mendez et al., 1999), using the characteristic velocity (V_c) defined as the maximum horizontal velocity at the top of the first plant of the meadow. This location is evaluated considering the deflected plant length. Then, the Reynolds number is expressed as follows,

$$Re = \frac{aV_c}{\nu} \tag{27}$$

where v is the kinematic viscosity. Although Hu et al. (2014) presented a better correlation between CD and Re for a new Reynolds number defined in terms of a mean in-canopy velocity, it is not considered here since that approach is not useful for predictive applications requiring mean in-canopy velocity to be measured. Results are shown in Figure 6.4 jointly with results from formulation presented by Mendez et al. (1999) for non-swaying conditions.

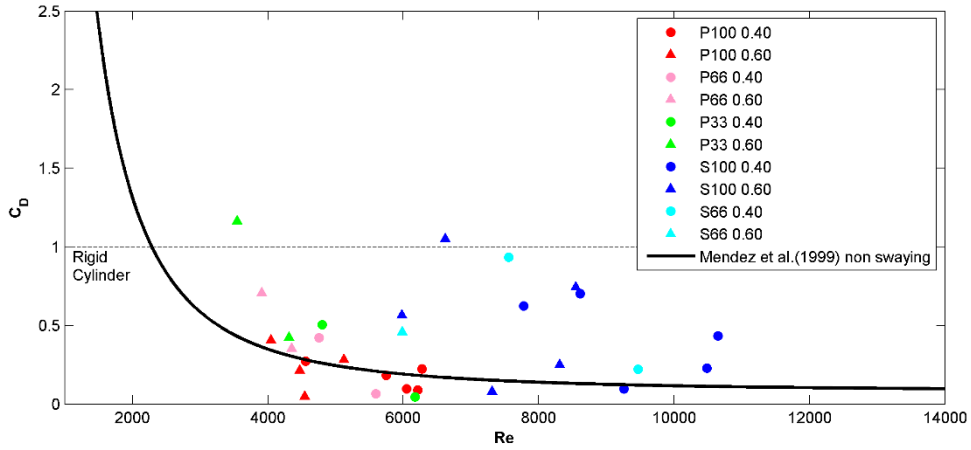

Figure 6.4 Drag coefficient for regular wave tests. Mendez et al. (1999) formulation for no swaying conditions is displayed.

Despite the scattering observed in Figure 6.4, the drag coefficients obtained using Dalrymple et al. (1984) formulation are in the same range as estimated by Mendez et al. (1999) empirical relationship. Drag coefficients for h = 0.40 m fits better to Mendez et al. (1999) formulation than results for h = 0.60 m. For h=0.60 m Mendez et al. (1999) formulation provides a worse fit because the vegetation effect is smaller for this water depth. Since both species behaves differently under flow conditions the associated Reynolds number are also different. *P. maritima* bends under flow action leading to a smaller characteristic velocity than the one obtained for *S. anglica*. Thus, the results for both species range at different Re values and drag coefficients for *P. maritima* fits better to Mendez et al. (1999) formulation.

The drag coefficient for combined waves and current is obtained following equation (17). Drag coefficients are represented as a function of the Reynolds number obtained considering the absolute value of the wave-current velocity (u_{wc}). Previous studies such as Hu et al. (2014) considers the linear summation of pure waves velocity and current velocity. In this study, the wave velocity affected by the currents following equation (8) is considered. In order to calculate this velocity for currents following waves, the wave velocity associated to the wave crest is considered whereas the maximum negative wave velocity (associated to the wave through) is taken for currents in the opposite direction to wave propagation.

$$Re_{wc} = \frac{a|u_{wc}|}{\nu} \tag{28}$$

The damping coefficients obtained from the fitting of the experimental results of waves and currents are used in this case. Figure 6.5 shows the results obtained for current following (top panel) and opposing (lower panel) wave propagation.

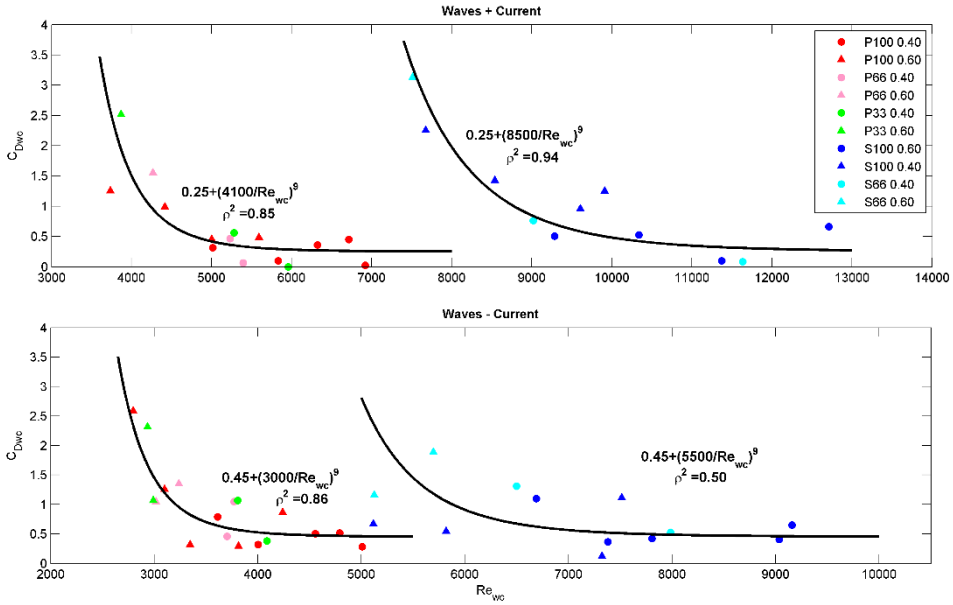

Figure 6.5 Drag coefficients for waves and current at the same direction (top panel) and waves and current in the opposite direction (lower panel).

Drag coefficients for both species are clearly different in both panels in Figure 6.5. Reynolds numbers associated to both species diverge under the effect of a current due to the differences in deflected plant lengths. As has been shown in section 6.2.2, *P. maritima* bends under combined wave and current to about a 40% of its plant length whereas *S. anglica* remains almost upright due to its stiffness. Although two clusters are observed, a similar trend is followed in both cases. The range of the Re for combined waves and current in the same direction is inherently higher than the one for pure waves because of the current effect in the wave frequency that leads to a higher velocity. The opposite occurs for waves and current flowing in opposite direction.

The range of the Re for combined waves and current tests is higher than the ones obtained for pure waves. This is due to the higher velocity considered in the Re calculus.

Figure 6.4 and Figure 6.5 show different Re ranges for both vegetation species. The different vegetation characteristics used to calculate the Re leads to this difference. Although the deflected length has been considered to determine the location where the characteristic velocity is obtained, the biomechanical properties of the different species are not included in the Re calculation. These properties can be introduced indirectly by the consideration of the deflected plant length as the characteristic dimension in the Reynolds number. Then, a new Reynolds number including the effect of plant deflection is defined as,

$$Re_{wc}^{D} = \frac{l_D |u_{wc}|}{\nu} \tag{29}$$

This definition of the Re is similar to the one used for flow over submerged steps or flow around a channel-bottom cavity (Rodi et al., 2013). Using this new definition for the Reynolds number, drag coefficients for combined wave and current acting in both directions are presented in Figure 6.6 for both species. Results for the different vegetation are plotted with different colors while circles and triangles represent drag coefficients for h= 0.40 m and h = 0.60 m, respectively.

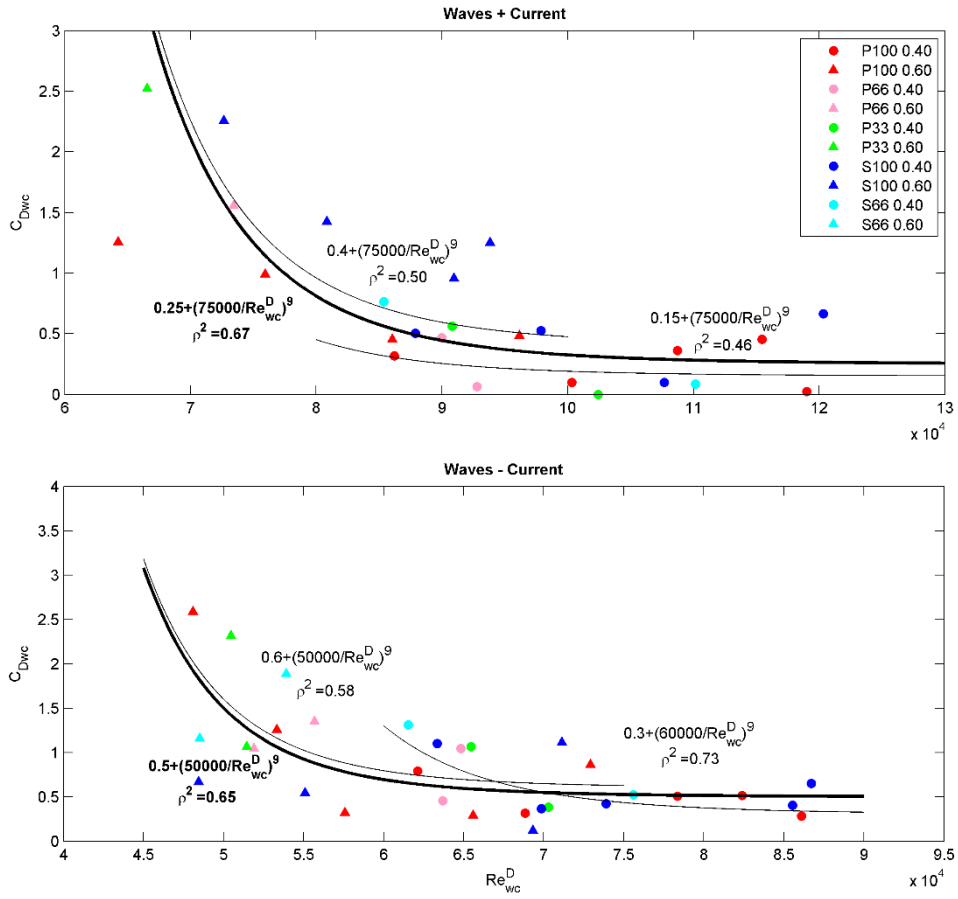

Figure 6.6 Drag coefficients for waves and current at the same direction (top panel) and waves and current in the opposite direction (lower panel) as a function of Re_{wc}^{D}.

The relationship found between the drag coefficients and the deflected Reynolds numbers is very similar for both species. In fact, results for both species are in the same range. This allows obtaining a common fitting for both *P. maritima* and *S. anglica* drag coefficients. Attending to water depth, a different fitting has been obtained for the two water depths (thin lines in Figure 6.6). These two different fittings respond to the diverse current flow patterns developed for each water depth (Figure 6.3) as has been explained in Section 6.4.1. However, the influence of these flow patterns in the wave damping is reflected in the drag coefficient values since a single fitting for both water depths can be found for each of the current directions (thick lines in Figure 6.6). Therefore, the submergence ratio hardly affects the C_D pattern, submerged cases present lower Re values, thus higher C_D.

The Reynolds numbers for these cases in which the deflected plant length is considered are higher since this value is much higher than the plant width. As for the classical Re, the deflected Reynolds number range is different depending on the current direction since the wave-current angular frequency used to calculate u_{wc} depends on current direction. Then a different fitting is obtained for each current direction (top and low panel in Figure 6.6).

Fitting found in Figure 6.6 shows that the deflected Reynolds number can be used in order to obtain a common fitting for *P. maritima* and *S. anglica* drag coefficients. Then, drag coefficients obtained for pure wave conditions are displayed in Figure 6.7 as a function of the deflected Reynolds number for regular waves ($Re^D = \frac{l_D V_c}{\nu}$).

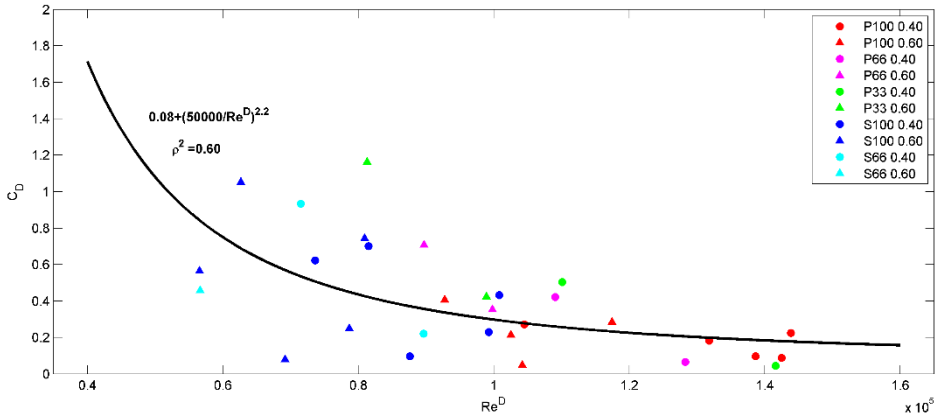

Figure 6.7 Drag coefficients for waves as a function of Re^D.

A new fitting to establish the relationship between the drag coefficient and the Re^D is obtained based on Mendez et al. (1999) formulation for non-swaying conditions changing the coefficient that is divided by the new Reynold number. Figure 6.7 shows this fitting. It can be observed that results for h = 0.40 m fits better to the new formulation whereas C_D for h = 0.60 m present a higher dispersion. This is related to the higher vegetation influence for the smallest water depth.

The fittings obtained in Figure 6.6 and Figure 6.7 lead to a different drag formulation in terms of the Reynolds number including deflection for each flow condition: pure waves, waves and currents in the same direction and waves and currents in the opposite direction. These fittings are expressed as,

$$C_D = 0.08 + \left(\frac{50000}{Re^D}\right)^{2.2} \qquad regular\ waves \qquad (30)$$

$$C_{Dwc+} = 0.25 + \left(\frac{75000}{Re_{wc}^{D}}\right)^{9} \quad regular\ waves + currents \quad (31)$$

$$C_{Dwc-} = 0.50 + \left(\frac{50000}{Re_{wc}^{D}}\right)^{9} \quad regular\ waves - currents \quad (32)$$

Previous formulations allow obtaining the drag coefficient for two vegetation species with very different biomechanical properties that do not fit to the same law when the deflected length is not considered in the Reynolds number calculation. Therefore, this new definition of the Reynolds number can be used for different vegetation species including their properties in the drag force calculation. This way the drag force used in the damping analysis not only includes the meadow density and the vegetation width but also the vegetation length that actually is affecting the water column by means of the drag coefficient.

6.4.3 Drag coefficients for random waves

Mendez and Losada (2004) formulation for random waves is used to evaluate the drag coefficient for pure random waves. The drag coefficient derived from that formulation is presented in equation (19). Again the calibrated damping coefficients for these conditions (β') are used to obtain the associated drag coefficient. Results as a function of the classical Re are shown in Figure 6.8.

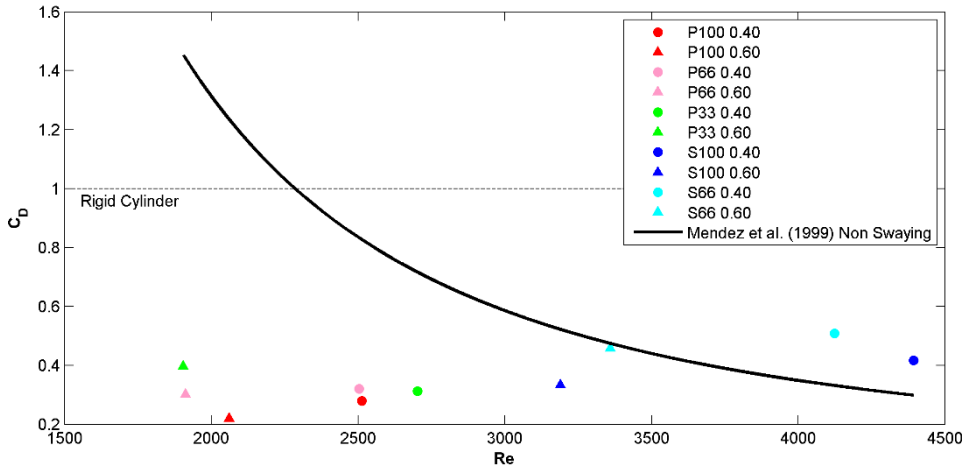

Figure 6.8 Drag coefficients for random waves.

Mendez et al. (1999) formulation gives a better fit to *S. anglica* but overestimates coefficients for *P. maritima* perhaps due to the whip-like behavior far from the mechanical characteristics of

the plants used in their assumptions. Results for *S. anglica* and *P. maritima* are clearly different as seen for regular waves.

The drag coefficients associated to wave and current conditions are also calculated. The analytical formulation presented in previous section for random waves is used to evaluate the drag coefficient according to the calibrated damping coefficients. Then, the drag coefficient is calculated using equation (26).

As has been explained in previous section, results for both species converge to the same trend when the deflected Reynolds number is used instead the Re used in previous studies. For this reason, the drag coefficients obtained for pure waves and waves and current conditions are represented in terms of the Re^D. This Reynolds number is calculated in this case considering the significant wave height and the peak period. Figure 6.9 shows the drag coefficients obtained for pure random waves in the top panel, for random waves and current acting in the same direction in the middle panel and for current opposing waves in the bottom panel.

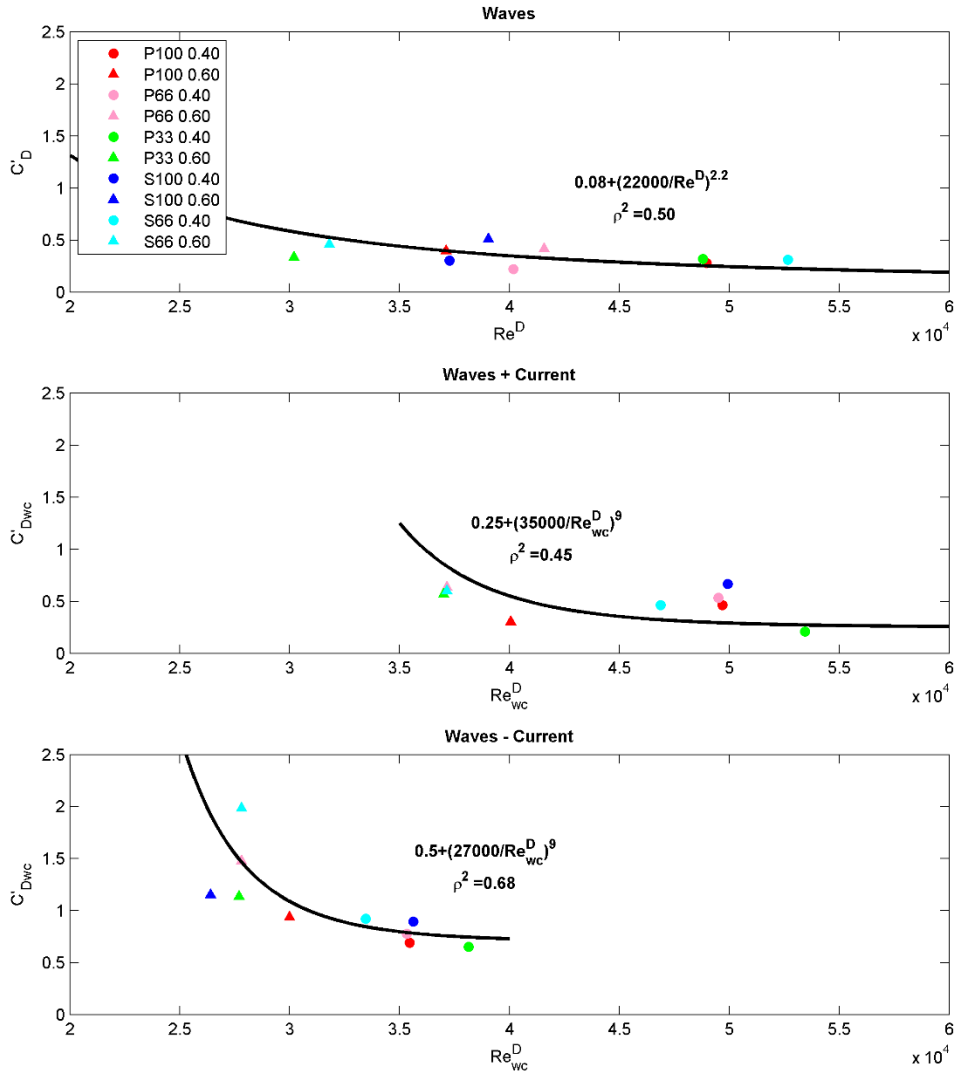

Figure 6.9 Drag coefficients for pure random waves (top panel), random waves and current in the same direction (middle panel) and waves and current in the opposite direction (bottom panel) with respect to the deflected Reynolds number.

Figure 6.9 shows a different fitting for each flow condition. Although the Reynolds number range is not very large and the correlation coefficients found for these fittings are not higher enough to state general conclusions, fittings for random waves respond to the same behavior found in regular waves. Depending on the current direction and the deflected Reynolds number value the drag coefficient is changed with respect to pure wave conditions. Thus, for Re_{wc}^{D} higher than 40000 the highest drag coefficient is found for waves and current in opposite directions. The same was observed for regular waves for Re_{wc}^{D} higher than 90000. These values of the deflected Reynolds number respond to values of the classical Reynolds number higher than 3000 which means turbulent flow conditions. For that range drag coefficients for pure waves and waves

flowing in the same direction as an underlying current are very similar in agreement with results presented by Hu et al. (2014).

Although a large range of the Reynolds numbers and a higher number of experimental tests would be necessary to extend the fittings presented in Figure 6.9, as a preliminary estimation, the drag formulations for pure random waves and random waves flowing with currents are expressed as:

$$C'_D = 0.08 + \left(\frac{22000}{Re'^D}\right)^{2.2} \qquad random\ waves \qquad (33)$$

$$C'_{Dwc+} = 0.25 + \left(\frac{35000}{Re'^D_{wc}}\right)^{9} \qquad random\ waves + currents \quad (34)$$

$$C'_{Dwc-} = 0.50 + \left(\frac{27000}{Re'^D_{wc}}\right)^{9} \qquad random\ waves - currents \quad (35)$$

Although the same type of formulas are presented for regular and random waves the drag coefficient formulations found for both types of waves are different. This is due to the different wave characteristics considered in both cases. Regular trains allow us studying the behavior of a specific wave frequency and height. These non-realistic conditions are commonly used in laboratory and numerical experiments and enable to understand the wave-current-vegetation interaction in simplified terms. On the other hand, random wave trains respond to an energy spectrum that includes a set of wave frequencies with their corresponding wave heights. These trains better represent real conditions and allow us studying the evolution of this energy spectrum when interacting with currents and vegetation. Furthermore, the frequency spread and the interaction between the different frequencies that conforms the spectrum is considered when generating these random trains. These aspects yield to the differences found between the results for regular and random waves.

6.5 Conclusions

Following an energy conservation approach, a new formulation for the energy loss produced due to the mechanical work carried out on the vegetation and the produced wave damping when waves and currents are acting simultaneously has been presented. The new formulation has been derived for currents flowing in the same and in opposite direction to wave propagation. It is also extended for random wave trains considering Rayleigh wave height distribution. A new formulation for the drag coefficient is also obtained from the energy balance for both, regular

and random waves. These new formulation allows obtaining the drag coefficient as a function of the damping coefficient calibrated from the wave height decay produced along a vegetation meadow.

An important aspect pointed out in this study is the plant length considered in the energy analysis for flexible vegetation. It is very important to consider the deflected length in the analysis of the induced energy dissipation when working with flexible vegetation since this is the actual length that is affecting the flow in terms of drag force. This length is a function of the deflected plant angle and it depends on vegetation characteristics (stiffness and buoyancy) and hydrodynamic forcing (waves and currents). Then, two values have been presented in this study for *P. maritima* distinguishing between pure waves and combining waves and current. The deflected length has been also considered in the calculation of a new Reynolds number. The deflected Reynolds number is calculated considering the deflected plant length as the representative length following an analogy to flow over submerged steeps attending to the observed flow behavior. This allows introducing in this characteristic non-dimensional number the vegetation bending.

Laboratory data from the experiments performed in the CCOB using real vegetation and pure waves and waves and current conditions interacting in both directions have been used to apply the proposed formulations to a real case. The different proposed wave decay relationships for the different flow conditions allow fitting experimental data and obtain the damping coefficient associated to each test. Results found for this damping coefficient reveal a higher energy damping for waves and current flowing in the opposite direction than for pure wave conditions. The opposite occurs when the current is acting in the same direction as wave propagation.

Finally, the drag coefficient associated to each experiment has been also calculated using the formulations that relate this coefficient with the damping coefficient. The representation of these drag coefficients with respect to the deflected Reynolds number enables obtaining new formulations for the drag coefficient as a function of the Reynolds number. A new formulation for each flow conditions has been presented.

"Water is the driving force of all nature"

Leonardo da Vinci

7

THREE DIMENSIONAL MODEL FOR TSUNAMI WAVE INTERACTION WITH MANGROVE FOREST

Summary

A three dimensional numerical approach based on IHFOAM to study the interaction of tsunami waves with mangrove forest is presented is this chapter. As a first approximation, the problem is modelled by means of solitary waves impinging on emergent rigid cylinders. Two different conceptual approaches are implemented into IHFOAM. Solving the URANS equations provides a direct simulation of the flow field considering the actual geometry of the array of cylinders. A modified version of the volume-average URANS equations by introducing a drag force to model the momentum damping created by the cylinders is used in the second approach. Both the direct and macroscopic simulations are validated against laboratory experiments for wave damping with very high agreement. A large set of numerical experiments to analyse flow parameters and uniform and random cylinder array distributions are analysed and use to compare pros and cons of the different approaches. Large differences are found in the forces exerted on the vegetation for uniform and random distributions. Generalizations obtained from uniform arrangements

could lead to underestimation of wave-exerted forces, especially for low dense configurations. Wave forces calculated with the macroscopic approach by means of the drag coefficient yields clear underestimations.

7.1 Introduction

Different authors have pointed out that mangrove forests provide coastal protection. Shuto (1987) quantitatively estimated the effectiveness of coastal pine forests in Japan against tsunami by statistically analysing the physical damage suffered by the trees. After the December 2004 tsunami, Kandasamy and Narayanasamy (2005) performed a study in 18 coastal hamlets along the southeast coast of India highlighting the importance of mangrove forests in coastal area protection. Following with this idea several authors (e.g. Mazda et al., 2006; Tanaka et al., 2007; Vo-Luong and Massel, 2008) reported the human and economic damage reduction produced at places where dense mangrove forests were present in comparison with bare sand areas.

Since mangrove capacity attenuating tsunami waves has been proven, many authors have focused on assessing tsunami wave attenuation and flow patterns around the plants. Due to the complexity of the problem, physical models have been frequently used to determine dissipation capacity of mangroves. Many of these studies have been carried out using simplified vegetation models, such us cylinders, disposed in uniform and organized arrangements. Huang et al. (2011) performed a set of runs to study wave evolution along three different cylinder arrangements and different field widths. Also Irtem et al. (2009) tested cylindrical timber sticks to study tsunami run-up reduction. The same runs where performed considering artificial trees. Authors pointed out the necessity of future studies where different types of trees are considered for random horizontal distributions. In the last years, different authors have used more sophisticated plant models. Ismail et al. (2012) tested prototype Rhizophora mangrove forests formed by three different parts: canopy, trunk and root. They showed the strong influence of forest density and width on wave damping. Strusinska et al. (2013) also reproduced Rhizophora species developing a novel tree parameterization, which accounts for both biomechanical and structural tree properties. Both solitary waves and tsunami bores were tested and similar wave damping was recorded for both flow conditions. They also pointed out that the highest forces were always measured at the first trees row and their magnitude was independent of the forest length. Another aspect studied was the importance of wave incident characteristics in their propagation along the vegetation patch. All these experimental studies reported the capacity of mangrove forests on attenuating wave energy and the complex processes produced in the interaction of tsunami waves with vegetation fields, such as the wave height enhancement at

the seaward edge of the mangrove forest or the nonlinear wave damping behaviour. Moreover, such studies also pointed out different limitations and gaps, such as scale effects, vegetation parameterization, flow conditions modelling, plants horizontal distribution or constraints in physical space that must be considered and covered in future studies.

In recent years, numerical approaches have been also developed to predict and to reproduce the effect that mangrove forests have on tsunami wave propagation. Most of these numerical models are based on shallow water two-dimensional vertical averaged equations. Teh et al. (2009) introduced the Morison equation in a model based on the Boussinesq equations considering the drag and the inertia coefficients as calibration parameters. They used the formulas proposed by Harada and Imamura (2003) for these coefficients, which were based upon data collected on coastal pine forest in Japan. Formulations were quantified as a function of the volume of trees under the water surface within a chosen control volume. More recently, Suzuki et al. (2011) implemented Mendez et al. (2004) formulation in the SWAN model to reproduce wave dissipation over vegetation fields. They included a vertical layer schematization for vegetation with variable vertical area such as mangroves. However, Mendez et al. (2004) was determined for submerged seaweed, far from the biomechanics properties of rigid mangrove forest. These models allow obtaining an estimation of wave damping produced by mangrove forests but they are based on empirical coefficients, which need to be calibrated to achieve realistic results. In addition they are not able to solve the vertical distribution of the velocity field or to deal with high turbulence flows. Another important limitation is the prediction of the pressure field, which is far from a hydrostatic behaviour, especially for bore-type tsunami waves. These aspects can be critical in the estimation of the protection provided by a mangrove forest.

More recently, the use of the Navier-Stokes (NS) equations has been applied with the main motivation of getting a better flow representation to improve the understanding of dissipation mechanisms induced by vegetation (Chapter 3). Models based on NS equations allow simulating flow vertical components and the flow between individual elements considering appropriate turbulence effects. As a first approximation, Mei et al. (2013) presented a semi-analytical theory of wave propagation through vegetated water based on a linearized version of the NS equations. The model extended the solution presented for long waves in Mei et al. (2011) to consider waves of intermediate period and length. Both works present a model able to simulate the micro-scale flow modelling around idealized rigid vegetation formed by cylinders, to determine macro-scale properties. One of the limitations of that approach is that the solution can cover only linear solutions although reasonable results are also found out of the range of applicability for waves of intermediate length. With the same spirit, the use of a numerical model based on the complete NS equations is used in this work. The combination of two approaches is presented, the first is based on a microscopic simulation of the flow around the vegetation whereas the

second takes advantages of a macroscopic definition of the flow by means of the wave damping parameterization. The modelling presented here increases the range of applicability of Mei et al. (2013) approach considering the complete version of the NS equations. The limitations in the flow modelling derived from the use of a simplified macroscopic approach will be investigated.

The work is organized as follows. First, the mathematical description of the model is presented for both approaches, macro- and microscopic modelling. Model validation is carried out next, using laboratory experiments. Next section includes additional simulations carried out aiming at studying the influence of solitary wave steepness, vegetation density and vegetation arrangement on the tsunami wave attenuation and the forces exerted on the plants. A discussion on the differences in the flow induced forces and wave damping is included.

7.2 Mathematical model

Two different approaches have been followed to simulate tsunami wave interaction with mangrove forest. First, direct simulation of the wave induced flow field around the vegetation is carried out using the Unsteady Reynolds-Averaged Navier-Stokes (URANS) equations. The flow within the mangrove forest is resolved considering the individual cylinder actual geometry. A standard $\kappa - \omega$ SST model is included as the turbulence closure, due to its ability to deal with reverse pressure gradients that are developed around rigid cylinders (Menter, 1994). This approach could be understood as a direct simulation considering that the flow is resolved at the space between cylinders. The second mathematical approach is focused on a macroscopic representation of the flow field within the vegetation. A simplification of a standard Volume-Averaged URANS (VARANS) set of equations presented in del Jesus et al. (2012) and Higuera et al. (2014) is used. The model first presented in Chapter 3 of this thesis neglects the role played by the porosity of the field resolving the flow as a combination of a drag force, to represent wave damping, and a modified $\kappa - \varepsilon$ turbulence model, used to consider enhanced turbulence by vegetation. Comparisons of flow velocities within the vegetation field shown in Chapter 3 demonstrate the accuracy of this approach to reproduce flow characteristics for high-density vegetation fields.

7.2.1 Numerical model description

IHFOAM model (Higuera et al., 2013a) is used in the first approach for direct simulation of the wave induced flow field around the vegetation. IHFOAM is a three-dimensional Navier-Stokes (NS) solver built on the OpenFOAM platform. The model uses a modified version of the

OpenFOAM standard “interFoam” solver. IHFOAM allows simulating gravity waves (Higuera et al, 2013a, 2013b) and porous media flows (Higuera et al, 2014a, 2014b). It also incorporates a set of algorithms to generate and absorb waves at the boundaries without the use of relaxation zones, speeding-up the simulations and ensuring a correct representation of the wave-induced hydrodynamics in the numerical domain.

The aforementioned NS equations, which include continuity (Eq. (1)) and momentum conservation (Eq. (2)) equations, are the governing mathematical formulations for free surface flows, linking fluid pressure and fluid velocity. The assumption of incompressible fluids applies for most coastal engineering problems.

$$\frac{\partial \bar{u}_i}{\partial x_i} = 0 \tag{1}$$

$$\frac{\partial \rho \bar{u}_i}{\partial t} + \bar{u}_j \frac{\partial \rho \bar{u}_i}{\partial x_j} - \frac{\partial}{\partial x_j}\left(\mu_{eff} \frac{\partial \bar{u}_i}{\partial x_j}\right) = \frac{\partial p^*}{\partial x_i} - g_i x_j \frac{\partial \rho}{\partial x_j} \tag{2}$$

In equations (1) and (2) ρ is density calculated as $\rho = \alpha \rho_{water} + (1-\alpha)\rho_{air}$ where α is the single phase function according to equation (3) and ρ_{water} and ρ_{air} are the water and air densities; p^* is the pseudo-dynamic pressure; x_i is the Cartesian position vector with respect to the reference frame (x_1, x_2, x_3); $\bar{u}_i$ are the fluid velocity components $(\bar{u}_1, \bar{u}_2, \bar{u}_3)$ regarding the Cartesian system of coordinates; g_i is the acceleration of gravity which is acting along the vertical axis ($g_1 = 0$, $g_2 = 0$, $g_3 = g$) and μeff is the efficient dynamic viscosity, which takes into account the molecular dynamic viscosity plus the turbulent effects: $\mu_{eff} = \mu + \rho \nu_t$. The newly introduced vturb is the turbulent kinetic viscosity, obtained from the turbulence modelling. This solver supports several turbulence models (e.g. κ − ε, κ − ω SST, and LES), however only κ − ω SST is considered in this work.

An additional equation (Eq. (3)) must also be taken into account to describe the movement of the air and water phases. IHFOAM solver considers only a single phase function (α), defined as the quantity of water per unit of volume at each cell. This means that if $\alpha = 1$ the cell is full of water, if $\alpha = 0$ the cell is full of air, and in any other case it belongs to the interface. Phase movement is described by the following equation:

$$\frac{\partial \alpha}{\partial t} + \frac{\partial \bar{u}_i \alpha}{\partial x_i} - \frac{\partial \bar{u}_{c,i} \alpha (1-\alpha)}{\partial x_i} = 0 \tag{3}$$

in which $\bar{u}_{c,i}$ is an artificial compression term used to preserve a sharp interface between air and water calculated as $\bar{u}_{c,i} = min(C_\alpha |\bar{u}_i| \; at \; x_i, max(|\bar{u}_i|) \; \forall \; x_i at \; free \; surface)$ where C_α is a

factor specified by the user (by default equal to 1). This term is evaluated individually for each volume. The first term is calculated considering the velocity at each individual finite volume and the second term considers the maximum of the velocity in every volume in the domain being part of the free surface ($\alpha < 1$). This term has been widely used (e.g.: Weller et al., 1998; Rusche, 2002; Higuera et al. 2013a) and it is standard in the two-phase flow solver available in OpenFOAM.

In order to study the tsunami wave interaction with mangrove forests using a macroscopic approach, IHFOAM needs some modifications. A second approach is proposed here by volume averaging the URANS equations presented in (1) and (2). It relies on obtaining a mean behavior of the flow within the vegetation by averaging its properties over control volumes. Volume averaging NS equations allows representing the vegetated area as a continuous medium, defined by its macroscopic properties only and considering the coupling of the velocity and pressure fields, inside and outside the vegetation. Hence, it allows eliminating the need of a detailed description of its complex geometry, as in the first approach and a speed-up of the calculations, because coarser grids can be used. This simplification, however, introduces new terms in the equations (del Jesus et al., 2012 and Higuera et al., 2014) that need to be modeled, such as the drag and the inertia forces. In the present work a simplification has been followed due to the specific characteristics of vegetation, which exhibit high porosity values. Equations presented for porous media flow by del Jesus et al. (2012) and Higuera et al. (2014) are adapted neglecting the role played by porosity on fluid acceleration (both local and convective). This approach is not new and has been successfully applied to flow interacting with vegetation using both a RANS turbulence approach (Hiraoka et al., 2006 for steam flow and Chapter 3 of this thesis for wave flow) or Dupont et al. (2010) for air flow by means of LES modelling of the turbulent flow. Equations (1) and (2) are then modified by considering the volume averaged as follows:

$$\frac{\partial \langle \bar{u}_i \rangle}{\partial x_i} = 0 \tag{4}$$

$$\frac{\partial \rho \langle \bar{u}_i \rangle}{\partial t} + \langle \bar{u}_j \rangle \frac{\partial \rho \langle \bar{u}_i \rangle}{\partial x_j} - \frac{\partial}{\partial x_j}\left(\langle \mu_{eff} \rangle \frac{\partial \langle \bar{u}_i \rangle}{\partial x_j} \right) = \frac{\partial \langle p^* \rangle}{\partial x_i} - g_i x_j \frac{\partial \langle \rho \rangle}{\partial x_j} - \overline{F_{D,\,i}} - \overline{F_{I,\,i}} \tag{5}$$

where $\langle \bar{u}_i \rangle$ is the volume average velocity, $\langle \mu_{eff} \rangle$ is the volume averaged efficient viscosity, $\langle p^* \rangle$ is the volume averaged pseudo-dynamic pressure, $\langle \rho \rangle$ is the volume averaged density, $\overline{F_{D,\,i}}$ is the drag force and $\overline{F_{I,\,i}}$ is the inertia force. The drag force and the inertia force, which account for loss of momentum induced by the plants are modelled as follows:

$$\overline{F_{D,\,i}} = \frac{1}{2}\langle\rho\rangle C_D a N \langle\bar{u}_i\rangle|\langle\bar{u}_i\rangle| \tag{6}$$

$$\overline{F_{I,\,i}} = \langle\rho\rangle C_M \frac{\pi a^2}{4} N \frac{\partial\langle\bar{u}_i\rangle}{\partial t} \tag{7}$$

where a is the width of the vegetation element, C_D is the drag coefficient, N is the number of plants per unit area and C_M is the inertia coefficient which is equal to $C_M = C_m + 1$ where C_m is considered equal to 1 (Sumer and Fredsoe, 2006). In this approach, the flow field between the vegetation elements is not resolved. Turbulence modelling is carried out by means of a modified k-ε model for wave flow (Chapter 3). The presence of vegetation is considered by adding a source energy production term, k_w, and sink energy dissipation term, ε_w, in the traditional κ − ε turbulence model. These terms take into account the turbulence enhancement by vegetation. These two additional terms are included in the turbulence model as:

$$\frac{\partial k}{\partial t} + \langle\bar{u}_j\rangle\frac{\partial k}{\partial x_j} = \frac{\partial}{\partial x_j}\left[\langle\nu_{eff}\rangle\frac{\partial k}{\partial x_j}\right] + \langle\nu_t\rangle\frac{\partial\langle\bar{u}_i\rangle}{\partial x_j}\left(\frac{\partial\langle\bar{u}_i\rangle}{\partial x_j} + \frac{\partial\langle\bar{u}_j\rangle}{\partial x_i}\right) - \varepsilon + \underbrace{C_{kp}C_D a N\sqrt{\langle\bar{u}_j\rangle\langle\bar{u}_j\rangle}k}_{k_w} \tag{8}$$

$$\frac{\partial\varepsilon}{\partial t} + \langle\bar{u}_j\rangle\frac{\partial\varepsilon}{\partial x_j} = \frac{\partial}{\partial x_j}\left[\left(\frac{\langle\nu_t\rangle}{\sigma_\varepsilon} + \langle\nu\rangle\right)\frac{\partial\varepsilon}{\partial x_j}\right] + C_{\varepsilon1}\frac{\varepsilon}{k}\langle\nu_t\rangle\frac{\partial\langle\bar{u}_i\rangle}{\partial x_j}\left(\frac{\partial\langle\bar{u}_i\rangle}{\partial x_j} + \frac{\partial\langle\bar{u}_j\rangle}{\partial x_i}\right) - C_{\varepsilon2}\frac{\varepsilon^2}{k} + \underbrace{C_{\varepsilon p}C_D a N\sqrt{\langle\bar{u}_j\rangle\langle\bar{u}_j\rangle}\varepsilon}_{\varepsilon_w} \tag{9}$$

where k is the turbulent kinetic energy, ε the turbulent dissipation rate, $\langle\nu_{eff}\rangle = \langle\nu\rangle + \langle\nu_t\rangle$ and $\langle\nu_t\rangle = C_\mu\frac{k^2}{\varepsilon}$. C_μ , $C_{\varepsilon1}$, $C_{\varepsilon2}$ and σ_ε are closure coefficients with values 0.09, 1.44, 1.92 and 1.3 respectively. Values given by Hiraoka et al. (2006) for the new empirical constants C_{kp} and $C_{\varepsilon p}$ are used ($C_{kp} = 1$ and $C_{\varepsilon p} = 3.5$). These coefficients are kept constant for all the simulations in this work.

Inflow boundary conditions have been established following Higuera et al. (2013), which takes into account the generation at the inflow boundaries and the wave absorption at the outflow boundaries by means of Dirichlet boundary conditions, instead relaxation zones. Velocity field is defined attending to the solitary wave characteristics tested in Huang et al. (2011). Non-slip boundary condition is considered at the bottom, at side boundaries and at the cylinder surface. A log-law is considered as a boundary condition for the k- ε turbulence model for solid walls (cylinder, bottom and flume sides). Values for the k-ω SST turbulence model used in the first approach are set, according to Menter (1992). Initial values for turbulence in both approaches

are defined according to Wilcox (2006). The upper boundary is considered open to air where an atmospheric pressure value is set.

7.3 Validation

IHFOAM has been validated for both the direct simulation and the macroscopic approaches. Laboratory tests performed by Huang et al. (2011) have been found suitable because they present solitary wave evolution along an idealized mangrove forest built with emergent vertical cylinders. Experimental information on flow characteristics or wave-induced forces on the array of cylinders is unfortunately lacking, and only free surface evolution is used to show model performance.

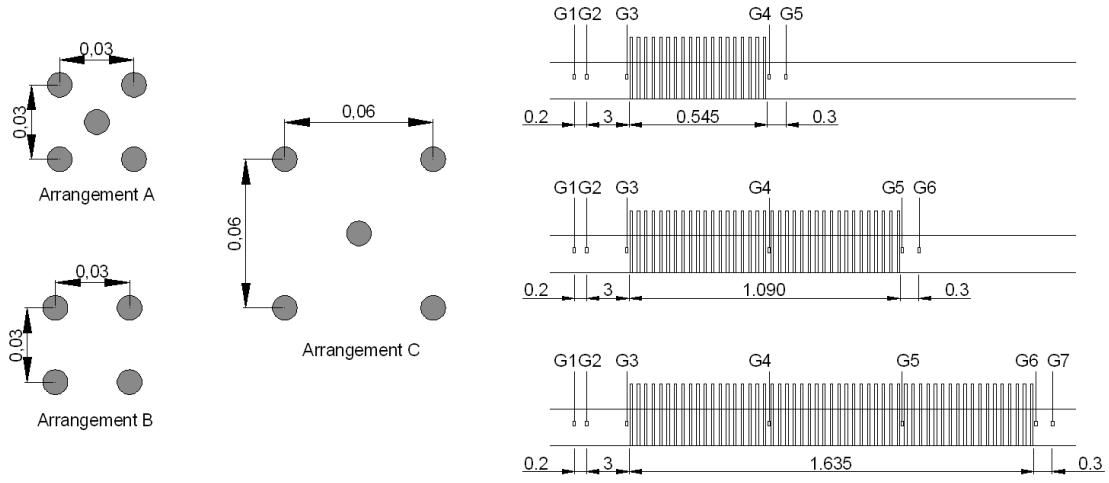

Figure 7.1 Cylinders arrangements (left) and field length (right).

Huang et al. (2011) present different tests in a 32 m long and 0.55 m wide wave flume using emergent 0.01m-cylinders made of Perspex. They were arranged following three different configurations, A, B and C, with densities equal to N = 2228, 1108 and 560 cylinders/m2, respectively (Figure 7.1). Three field lengths l = 0.545, 1.090 and 1.635m were considered, as can be seen in Figure 7.1. All tests were run considering a water depth equal to h = 0.15m. Solitary wave height was varied from H = 0.02 to 0.06m during the experiments.

Validation for the macro-scale modelling has been focused on the determination of the drag coefficient value, CD. A fitting procedure is conducted to find the best CD for modelling the wave induced damping. Both the wave height evolution and the free surface profiles along the vegetation are considered to best represent the quality of the experiments.

Validation for the direct simulation approach is carried out with a detailed simulation of the complete array of cylinders. Each individual cylinder has been considered in the numerical domain. In this case, no empirical coefficients have been used to reproduce experimental measurements. Only standard coefficients from the $\kappa - \omega$ SST are used that remain unchanged for all simulations. The advantage of the second approach is the absence of calibration of the empirical parameters to reproduce the physical processes. However, the computational cost increases, as it will be discussed later.

7.3.1 Macroscopic approach

The computational domain is defined considering the same geometrical characteristics of the physical wave flume. A non-constant grid-sized and three-dimensional mesh is considered. The discretization is 0.02m in both horizontal directions and 0.006m in the vertical direction. The mesh is refined near the mean water level in order to improve free surface resolution. Values of 0.01m in the horizontal and 0.003m in the vertical directions are considered. Sensitivity to grid size has been tested (not shown here) with negligible differences observed within values close to the ones selected.

Wave generation in the model has been targeted to obtain the same solitary wave in the first free surface gauge as the one measured by Huang et al. (2011) to ensure the same incident wave conditions to model wave damping by vegetation. Wave absorption is set at the onshore boundary in order to absorb outgoing waves. Numerical simulations are carried out attending to the different vegetation arrangements and vegetation densities considered during the experiments, in order to determine the drag force (see Eq. (5)). Drag coefficient, CD, is the only calibration parameter varied to adjust wave damping in the numerical simulations to measurements.

The first simulation is performed considering the longest vegetation field (l = 1.635m) with the lowest vegetation density (N = 560cylinders/m2). Figure 7.2 shows both numerical model results and laboratory measurements for an incident wave height of 0.05m. In this case, the best-fitting drag coefficient is 1.52, the same as presented by Huang et al. (2011) (see Table 1). In this work, the best-fit values for drag coefficients are such that the difference between the maximum free surface elevation of the experimental and numerical data at the gauge located leeward the cylinder field is a minimum. That value is lower than 5% in all cases analysed. As can be observed in the figure, the model reproduces very well the wave height transformation along the vegetation field.

Previous studies such as Mendez and Losada (2004) and Ma et al. (2013) have neglected the inertia force in this approach. In order to analyse this hypothesis Figure 7.2 shows the numerical free surface evolution with and without considering the inertia force contribution.

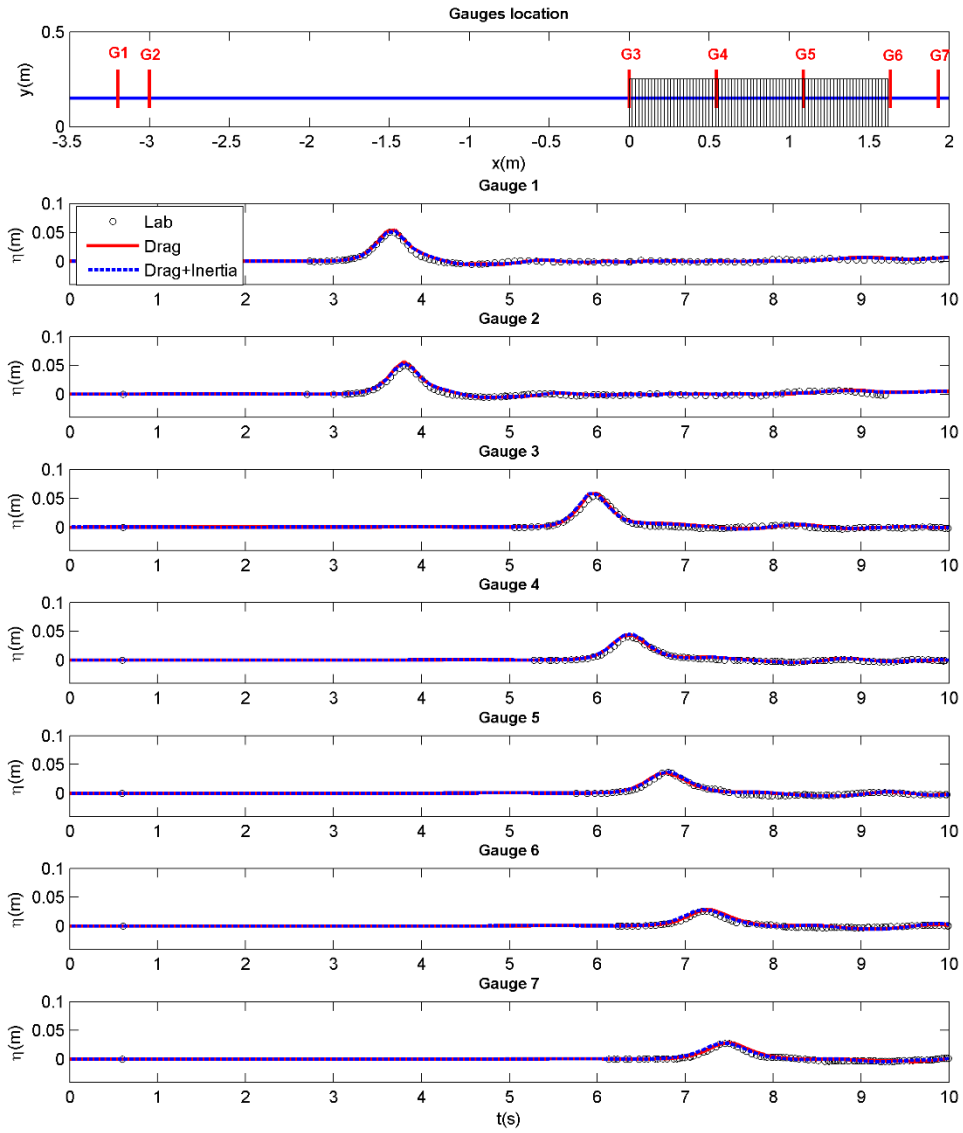

Figure 7.2 Comparison between numerical and laboratory free surface evolution for arrangement C and vegetation length 1.635m for an incident wave height equal to 0.05m. Numerical results considering drag and inertia forces (dashed blue line) and only drag force (red).

As can be seen results show that, for this case, both numerical results are almost identical, what can be interpreted as an almost negligible contribution from the inertia component. In order to find an explanation the Keulegan-Carpenter number of the flow is calculated considering a

solitary wave length equal to $2.12h/\sqrt{H/2h}$ (Dean and Dalrymple, 1991) and its corresponding wave period. For all cases considered in these experiments KC numbers vary between 88 and 106, that is within the range where drag force is dominant (Chakrabarti, 1987). Based on the numerical experiment and the evaluation of the KC range, the inertia force contribution in the rest of the simulations considering the macroscopic approach can be neglected. Please, not that this assumption may not be valid under different flow conditions.

The second simulation is performed considering arrangement A (see Figure 7.1), using a 0.545m long vegetation field. A 0.0417m incident solitary wave height is simulated, according to the free surface recorded at gauge 1. Figure 7.3 shows the comparison between the numerical and experimental results for two free surface gauges located offshore and onshore the vegetation field (G1 and G5 in Figure 7.1 for the 0.545m-long field). An additional simulation is carried out considering a lower vegetation density (arrangement B) and a longer vegetation field (l = 1.090m). Again results for the free surface gauges offshore and onshore of the meadow (G1 and G5) are presented in Figure 7.4 for an incident wave height equal to 0.03m. Drag coefficient is set searching for the best fitting between numerical and laboratory data. The obtained drag coefficient corresponds to 2.45 for arrangement A and 1.45 for arrangement B. These values are in agreement with the ones obtained by Huang et al. (2011), as is shown in Table 1, following a numerical approach based on Boussinesq equations.

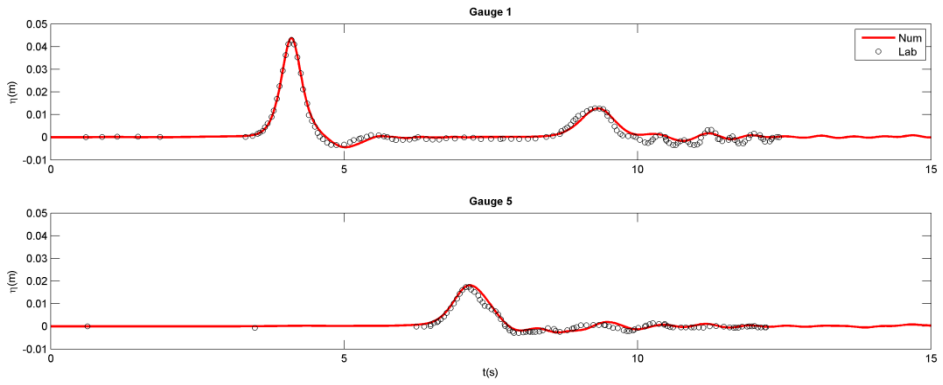

Figure 7.3 Free surface elevations for arrangement A and cylinder field length 0.545m and an incident wave height of 0.0417m.

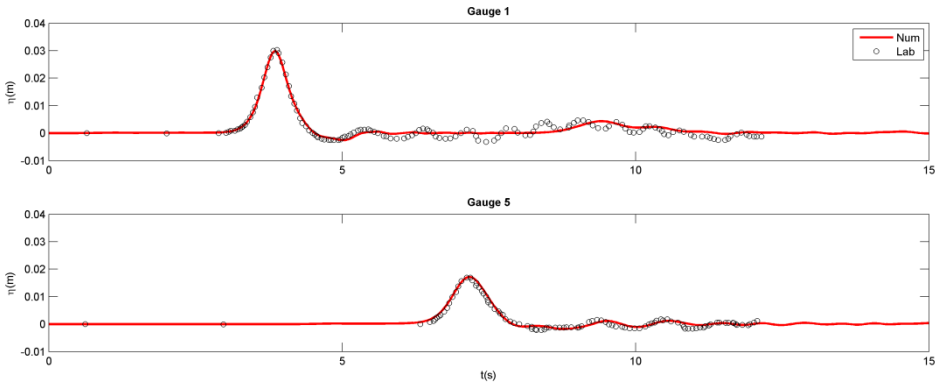

Figure 7.4 Free surface elevations for arrangement B and cylinder field length 1.090m and an incident wave height of 0.03m.

As can be observed in Figure 7.3 and Figure 7.4 the model is able to reproduce the solitary wave attenuation produced by vegetation. Moreover, the reflected wave by the cylinder field is simulated with a high degree of accuracy, as can be clearly observed at the upper panel in Figure 7.3 at t= 9s. Almost a 30% of the incident wave height is reflected in this case. This effect is not so strong in Figure 7.4 due to a lower field density. The model does not reproduce small amplitude radiated waves by the individual cylinders, as can be observed in both upper panels in Figure 7.3 and Figure 7.4. Since geometry of the cylinders is not reproduced in this approach radiation cannot be solved numerically.

Arrangement	***Numerical fitting***	***Huang et al. (2011)***
A	2.45	2.45
B	1.45	1.41
C	1.52	1.52

Table 7.1 Comparison between obtained C_D coefficients and values given by Huang et al. (2011)

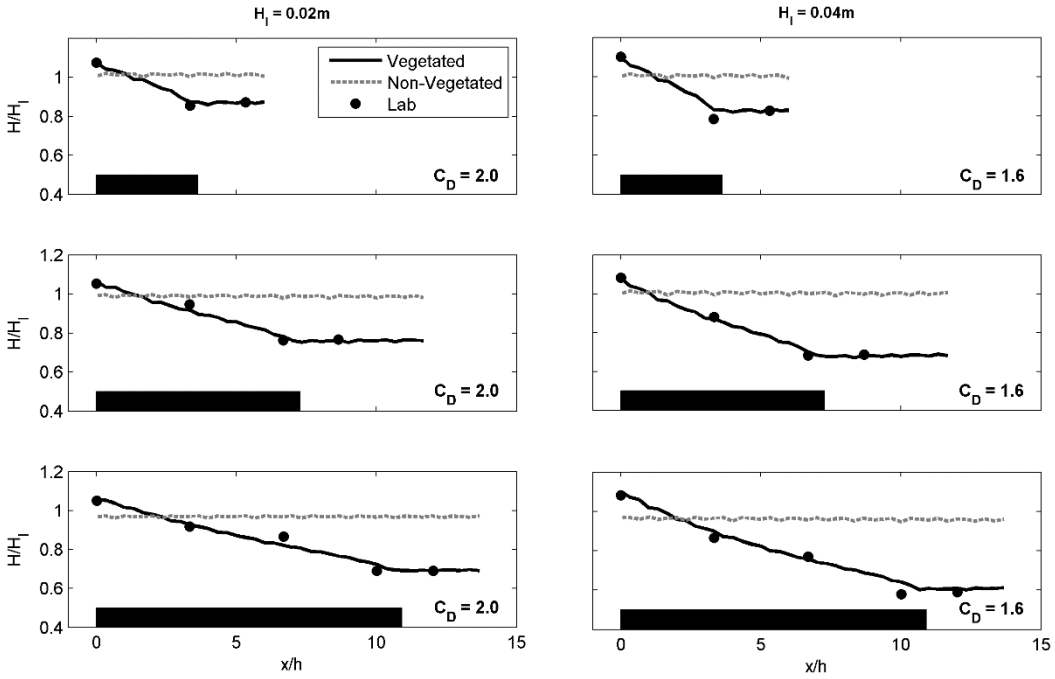

Figure 7.5 Wave height evolution for arrangement C and the three vegetation lengths, (0.545, 1.090 and 1.635m) and two wave heights, 0.02m (left) and 0.04m (right). Black boxes represent the cylinder field. Results without vegetation are shown in dashed line.

To extend model validation, wave height evolutions for arrangement C are compared with experimental data for three vegetation lengths, (l = 0.545, 1.090, 1.635m) and two different incident wave heights (Hi = 0.02 and 0.04m). Figure 7.5 shows the evolution of wave height along the numerical domain for cases with vegetation (black solid line) and without vegetation (grey dashed line). Differences point out the role played by the cylinders field in dissipating wave energy, with almost negligible wave damping in the non-vegetated cases. Best-fit drag coefficients obtained when reproducing the experiments are displayed in the figure. Wave height attenuation along the vegetation field is well reproduced by the model for all the cases. The obtained dissipation is solely produced by drag since no breaking occurs in any of the cases considered. The drag coefficient is constant for a given wave height independently of the length of the field. For identical conditions higher waves lead to higher damping rates, obtaining up to a 40% of wave height reduction for the longest cylinder field.

7.3.2 Direct simulation approach

Huang et al. (2011) experiments are also used to validate the direct simulation approach using Eq. (1) and (2). In this case the N-S equations are solved considering individual rigid cylinders

introduced in the domain mimicking the exact setup used in the experiments. Since the flow has to be solved between the cylinders, a finer grid is needed yielding a higher computational cost. In order to reach a balance between the computational effort and the accuracy of the results, a mesh sensitivity analysis is carried out first considering arrangement C. The analysis is focused on the numerical representation of the free surface and the solitary wave forces exerted on the cylinders according to different spatial resolutions. Figure 7.6 shows a zoom of the three meshes considered in the analysis.

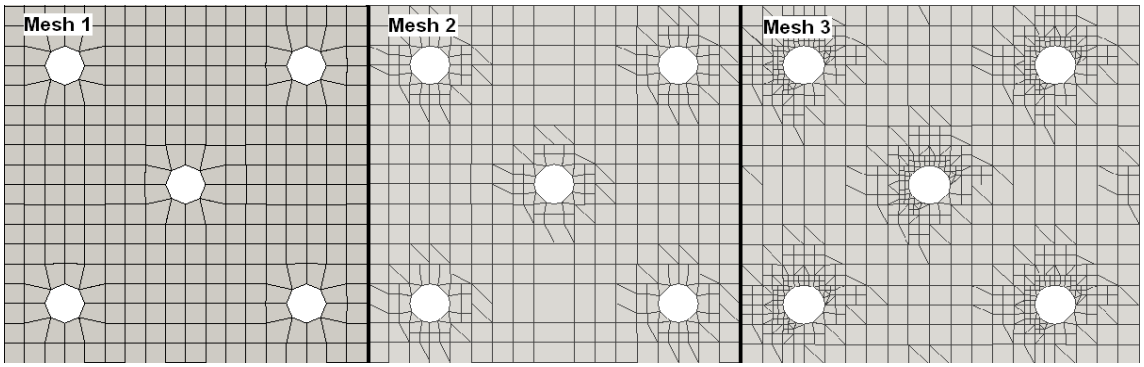

Figure 7.6 Mesh sensitivity analysis. Increasing resolution from left to right.

Mesh 1 corresponds to the coarser mesh and Mesh 3 is the one with the smaller cells. As can be seen in the figure, the difference between meshes lies on the refinement introduced around the cylinders in order to get a better flow representation of the small scale flow features. The three meshes share the same initial discretization, that is a uniform 0.005m in the horizontal and 0.003m in the vertical cell size. The refinement used in Mesh 2 yields to a cell size of 0.0025m in the horizontal direction and 0.0015m in the vertical. Mesh 3 has a 0.00125m cell size around the cylinders. The sensitivity analysis is carried out using arrangement C and a vegetation patch length of 0.545 m that means a total number of elements equal to 13.228.840 for Mesh 1, 14.444.400 for Mesh 2 and 18.649.780 for Mesh 3. The computational time associated to Mesh 1 is 4 days in 16 processors using a HPC machine (2.6 GHz) to simulate 10s. Computational cost for Mesh 2 and Mesh 3 is increased by a factor of 2 and 4, respectively.

Sensitivity analysis results are presented in Figure 7.7. Wave height evolution (left panel) and the maximum forces exerted on the cylinders located along the central line of the meadow (right panel) are presented for the three meshes. Wave height is normalized by the target incident wave height (HI). Forces are divided by ρg(h+HI)Aw, where, ρ is the water density, g is the gravitational Aw is the cylinder wet y-sectional area (a*(h+HI)).

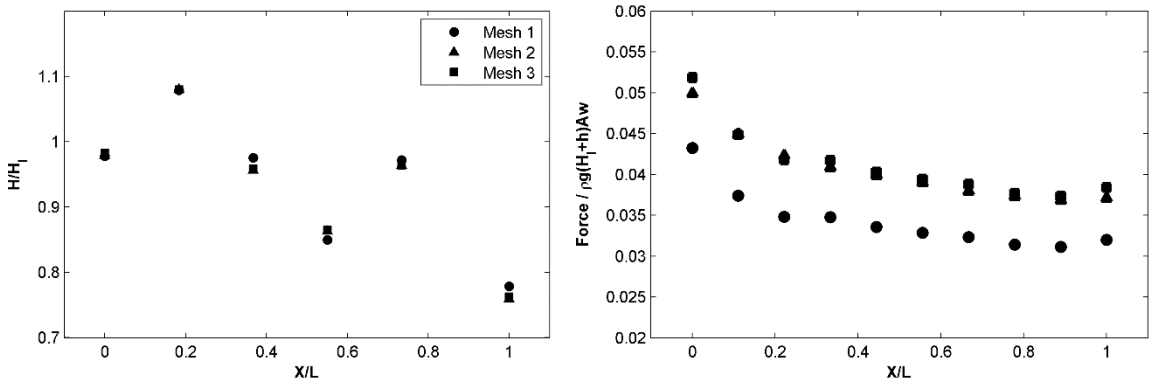

Figure 7.7 Comparison of wave height evolution and forces for the three different meshes. Left: Wave height evolution. Right: force exerted on the cylinders along the central line.

As can be observed in Figure 7.7, wave height evolution is very similar for the three meshes although higher discrepancies are found for the coarser mesh, i.e. Mesh 1. However, the differences found analysing the maximum forces exerted on the cylinders are more relevant. There is a significant discrepancy in the calculation of the maximum wave-induced forces, revealing a high resolution dependency. Mesh 1 exhibits an underestimation of the forces, due to the poor spatial resolution around the cylinders. However, no relevant differences are observed between forces calculated using Mesh 2 and 3. A maximum error smaller than 4% is found between the results obtained for the first cylinder for both meshes. In this comparison, results for the first cylinder are used because maximum forces are located there. Based on previous results Mesh 2 is selected to perform the present study.

In order to validate the numerical ability to represent the solitary wave induced flow around the individual cylinders forming the field, a simulation considering arrangement C with l = 1.635m is carried out. The $\kappa - \omega$ SST turbulent model is used. Numerical predictions of the free surface time history are compared with laboratory measurements presented by Huang et al. (2011) and presented in Figure 7.8.

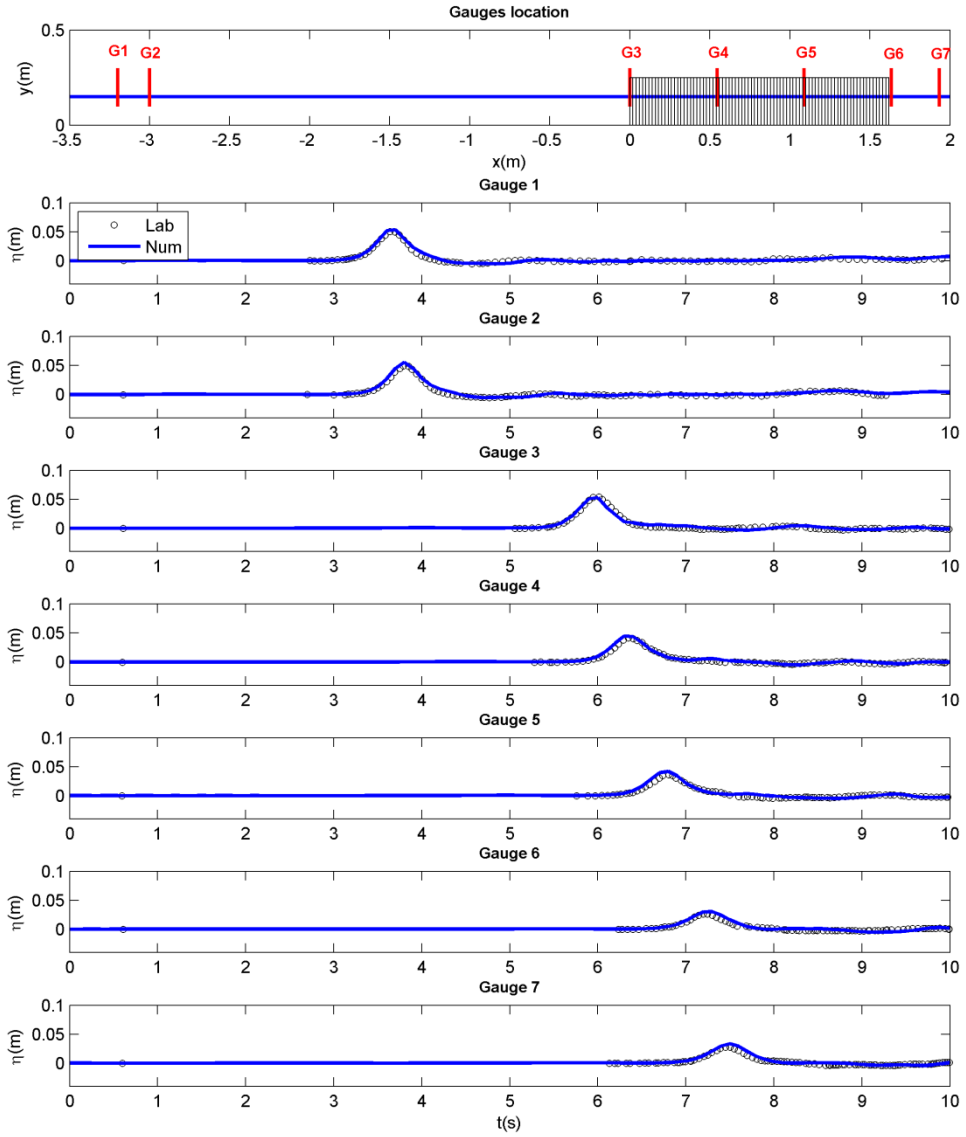

Figure 7.8 Comparison between numerical and laboratory free surface evolution for arrangement C and vegetation width 1.635m for an incident wave height equal to 0.05m.

Figure 7.8 shows a good agreement between experimental measurements and numerical results with differences in the maximum wave height smaller than 15% (gauge 7, t = 7.5s). Similar agreements have been found for all the simulated cases. Therefore, the model allows reproducing with high agreement the free surface evolution along the cylinders field considering the set of individual cylinders without the need of calibration parameters.

7.3.3 Comparison between both approaches

The macroscopic approach offers the advantage of a reduced computation cost. Besides the damping induced by vegetation using a drag coefficient is extensively used in combination with other wave equations. Consequently, a comparative analysis of the two-presented approaches is carried out in this section in order to gain more knowledge about pros and cons of each approach. Numerical results are compared with laboratory experiments and shown in Figure 7.9.

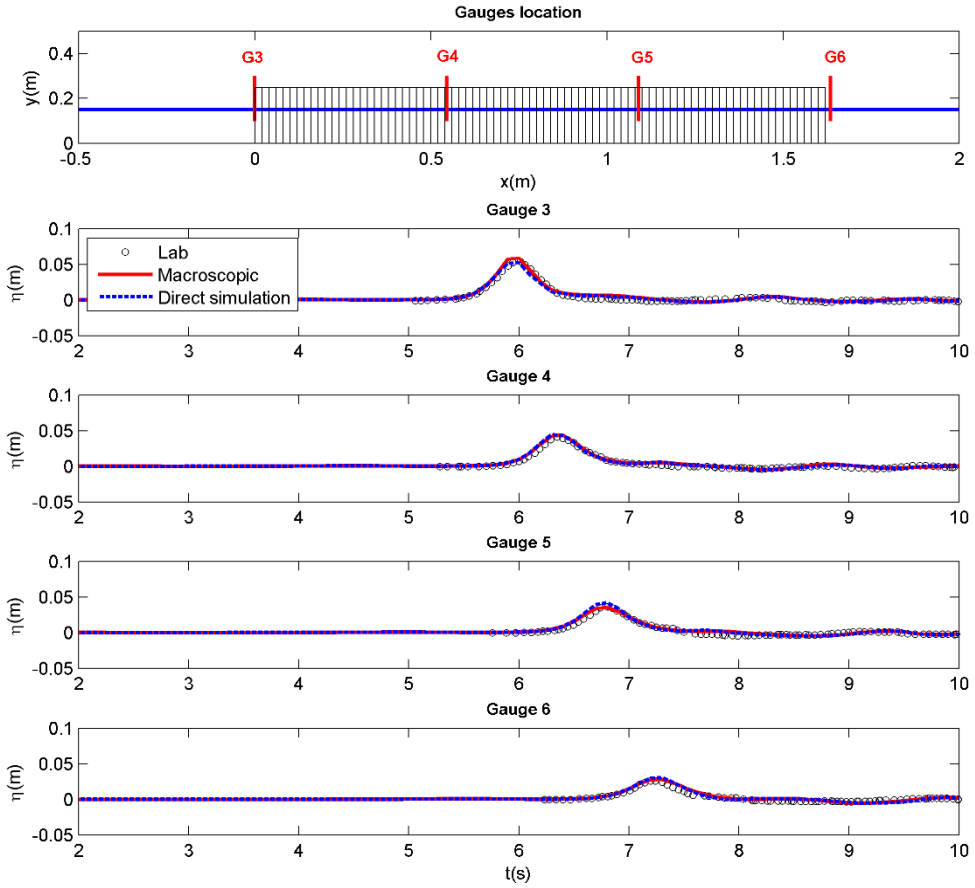

Figure 7.9 Free surface evolution for arrangement C and vegetation width 1.635m for an incident wave height equal to 0.05m. Numerical results considering the macroscopic approach (red solid line) and the direct simulation approach (blue dashed line) are shown.

Figure 7.9 shows almost no differences between the free surface results obtained with both approaches. The highest differences are found in gauges 3 and 5 where the macroscopic approach overestimates and underestimates the wave height, respectively, but differences are

smaller than 10%. In gauge 3 the strong discontinuity at the beginning of the cylinders array is better reproduced when the cylinders are included in the simulations. The macroscopic approach seems not to be able to represent the edge effects at the beginning of the array so accurately. It can be seen in gauge 5 that the macroscopic flow representation produces a higher dissipation at the first half of the field. However, it can be concluded that overall, the differences between both approaches are small when modelling wave evolution along the patch.

The main difference lies on the computational cost. Mesh discretization in both approaches is very different since the introduction of each individual cylinder demands very small cells. The horizontal cell size for the macroscopic approach is 0.01m. However, this value is reduced to 0.0025m around the cylinders. This reduction at the cell size increases significantly the number of elements of the mesh, from 1.252.496 to 19.432.400 involving a huge increase in the computational cost, from 14 hours in 4 processors to 2 days and 16 hours in 64 processors, using a HPC machine (2.6 GHz) to simulate 10s.

Despite of the increase in the computational cost, the direct numerical approach is very useful because it is free of flow parameterizations such as the ones presented in the macroscopic approach by means of the drag coefficient. It is also able to provide very useful information, not available from the macroscopic approach, such as the forces on the cylinders or detailed flow characteristics inside the vegetation patch. An example of the horizontal flow velocity and turbulent intensity ($U_I = \sqrt{2k}$, where k is the turbulent kinetic energy from the κ – ω SST model) inside the field obtained with the direct simulation is displayed in Figure 7.10.

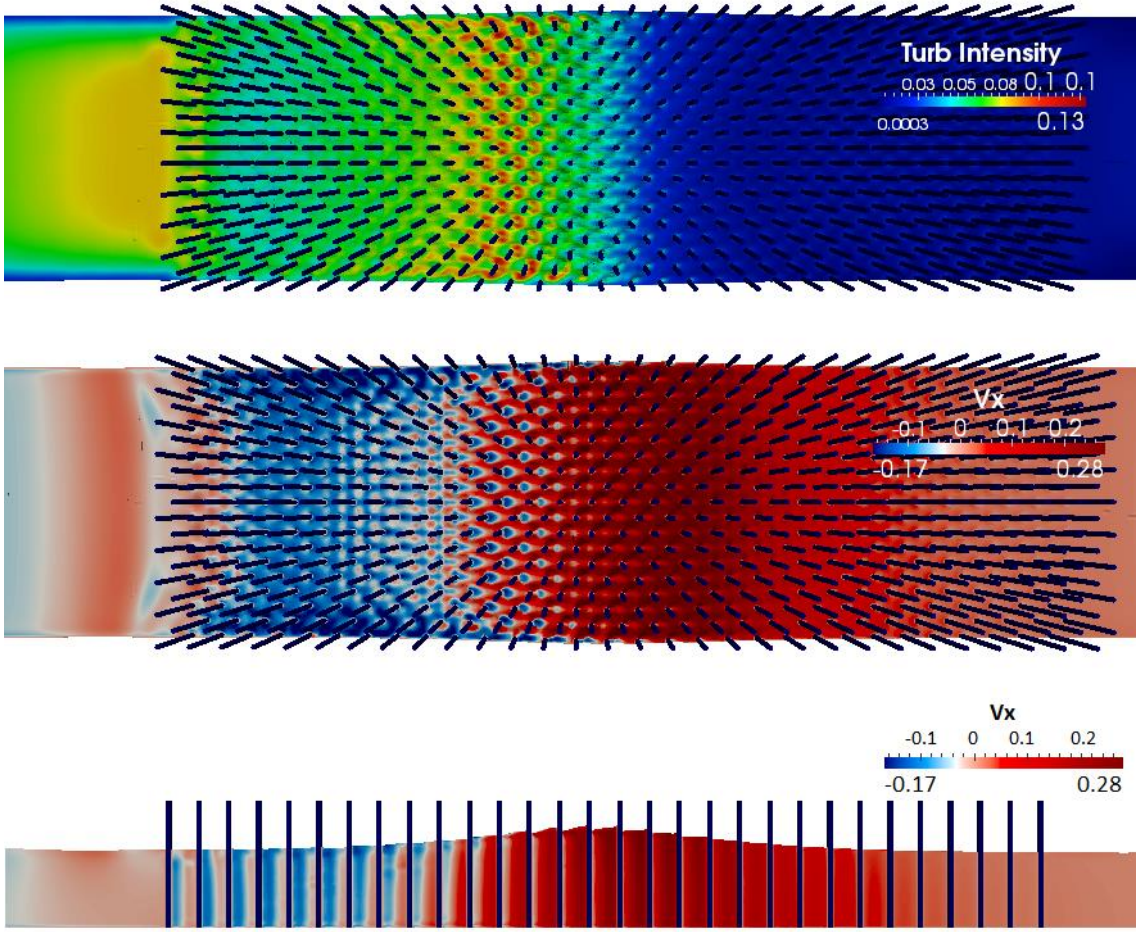

Figure 7.10 Turbulent intensity and horizontal flow velocity inside the cylinders field for arrangement C and wave height equal to 0.05m.

The figure shows a snapshot of the solitary wave passing along the cylinders array, when the wave crest is at the center of the field. It can be observed how flow separation around the cylinders is developed after the crest passes. According to both the horizontal velocity and the turbulent intensity fields, the shape of the wake vortices is symmetric in the middle of the numerical wave flume, as expected. However, non-symmetric vortices are visible at the lateral boundaries, which represent the laboratory flume walls. It is noticeable that the maximum forces were obtained when the crest is reaching the cylinders, but not when the wake is developed.

7.4 Flow analysis based on direct simulation

Once the numerical model has been demonstrated to be able to reproduce wave induced damping with a high degree of accuracy when the geometry of the cylinders is resolved, it is used in this section to explore the detailed hydrodynamics of the flow. Simulations are performed considering the geometry of the cylinders in the numerical domain with different arrangements. This approach is free of numerical parameterizations and the drag force does not need to be parameterized. Only turbulence is modelled in the simulations by means of the $\kappa - \omega$ SST turbulent model, which uses standard coefficients.

A set of direct numerical simulations is carried out with the aim of studying the influence of several parameters on wave damping: solitary relative wave height, vegetation density and vegetation arrangement. Wave heights of H = 0.025, 0.5 and 0.15m are studied with the following associated relative wave heights H/h = 0.17, 0.33 and 0.67, respectively. Field density is taken into account by means of the use of the three densities used by Huang et al. (2011), 2228, 1108 and 560 cylinders/m2, respectively. Finally, vegetation arrangement is included in the analysis considering Huang et al. (2011) uniform arrangements (A, B and C, presented in previous section) and additional random arrangements. All simulations are run for h = 0.15 m and l = 0.545 m. Table 2 summarizes the parameters covered.

Arrangement	*Wave height (m)*	*Relative wave height (H/h)*	*Distribution*
A	0.025 / 0.05 / 0.10	0.17 / 0.33 / 0.67	Uniform / Random
B	0.025 / 0.05 / 0.10	0.17 / 0.33 / 0.67	Uniform / Random
C	0.025 / 0.05 / 0.10	0.17 / 0.33 / 0.67	Uniform / Random

Table 7.2 Relevant parameters considered in the direct numerical simulations.

The numerical domain is 4.60 m long, 0.55 m wide and 0.28 m high. A solitary wave is generated at one side of the numerical domain and active wave absorption is considered onshore allowing outgoing waves leave the domain. Mesh 2 is used following the results obtained for the sensitivity analysis presented in previous section. A sketch of the mesh discretization used for the three different arrangements (A, B and C) is shown in Figure 7.11 including a zoom of the mesh resolution around the cylinders. The total number of volumes in the numerical mesh is 17.684.448, 15.583.200 and 14.444.400 for arrangements A, B and C, respectively.

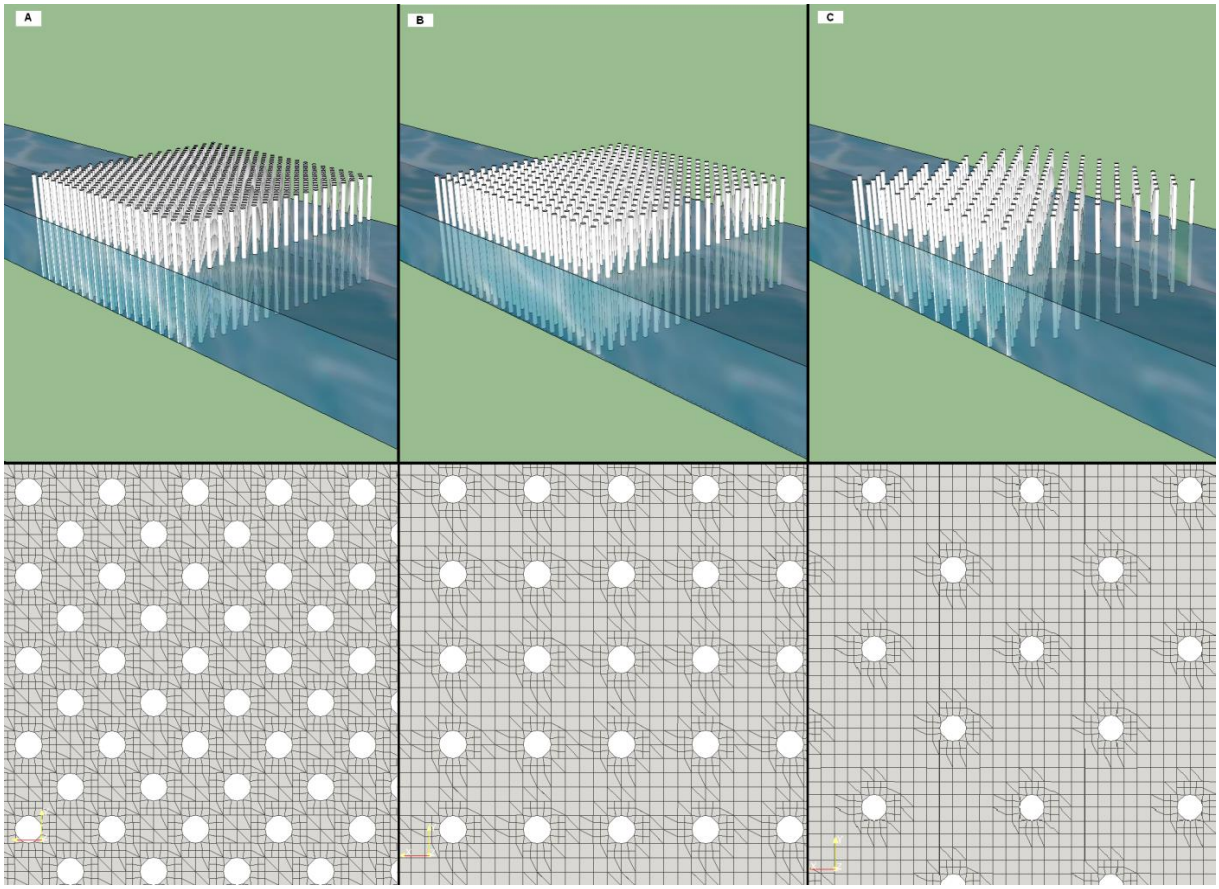

Figure 7.11 Cylinders introduced in the domain (first row) and top view of the considered meshes (second row) for each arrangement (A, B and C).

Free surface information is obtained from the model at different locations in order to calculate wave damping. Wave height is evaluated at three locations offshore of the meadow (X/L = -3.67, -0.92 and -0.14) and at two locations onshore (X/L = 1.10 and 1.30) for the three arrangements. Additional information is also obtained inside the meadow along the cylinders central line in all cases. Different locations are chosen depending on the arrangement. For the sake of clarity, these locations are represented in Figure 7.12 where the central cylinders line of the field is coloured in black. A detailed top view shows the exact location of the point, in red, where the free surface is calculated numerically. Cylinders plotted in black are the ones used to evaluate wave-induced forces, as it will be shown later.

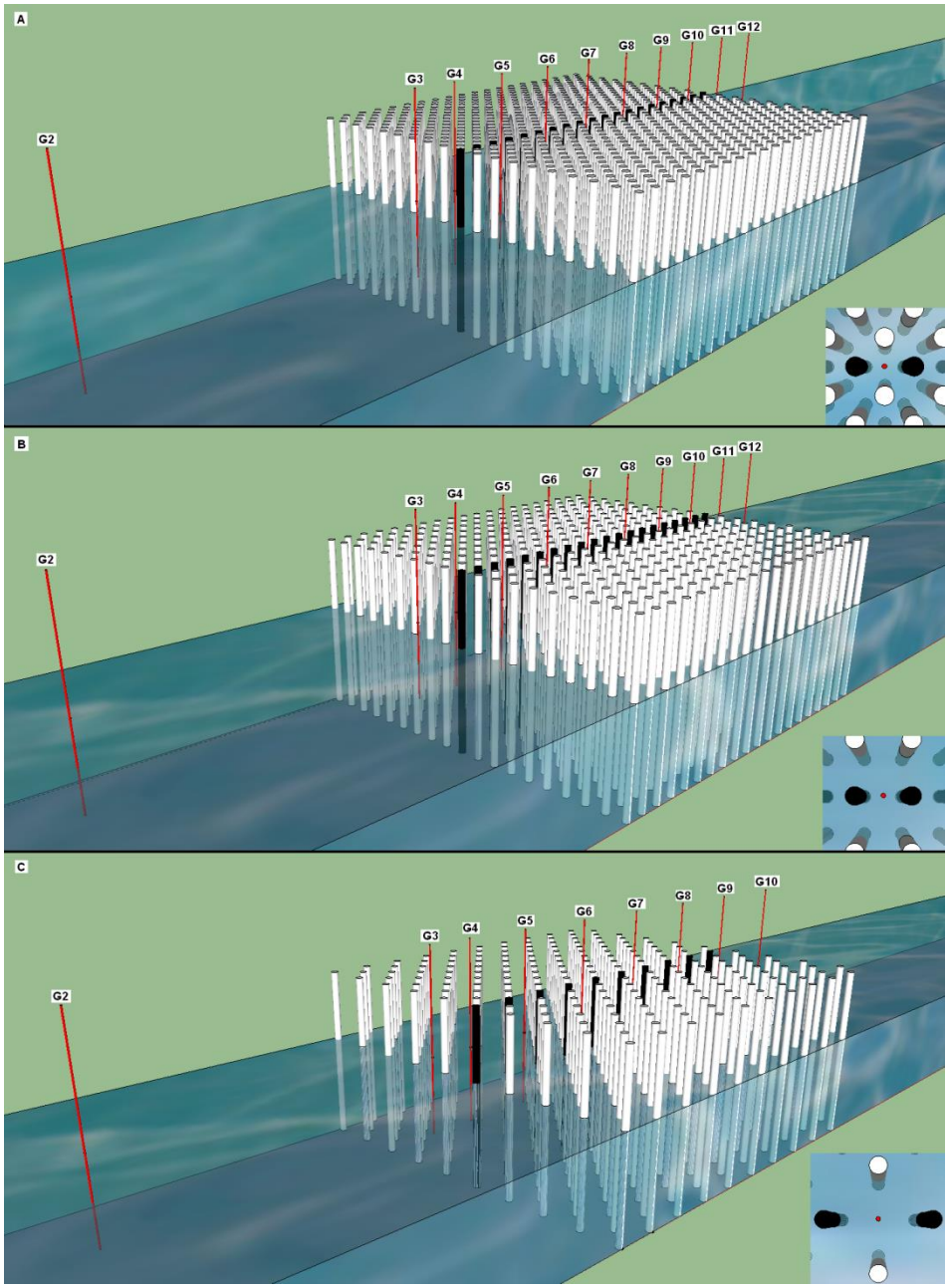

Figure 7.12 Gauges location (in red) for the three arrangements (A, B and C) and l = 0.545m. Top view of the location of one gauge is shown for each arrangement at the bottom right corner.

7.4.1 Analysis of solitary wave non-linearity

The influence of relative wave height is analysed first. The three selected wave heights (0.025, 0.5 and 0.15m) are simulated considering arrangements A, B and C with a uniform cylinder

distribution. Free surface evolution along the field is studied for the different conditions. Four representative free surface gauges are selected for each arrangement, one offshore the vegetation patch (X/L = -0.92), two inside the vegetation patch (X/L = 0.30 and 0.80) and one leeward the patch (X/L = 1.30). Figure 7.13 shows the free surface time history at each location for the three wave heights and the three arrangements. Free surface is normalized by the incident wave height at X/L = -0.92. Solitary waves are plotted at the same time instant to visualize changes in wave celerity when traveling along the patch.

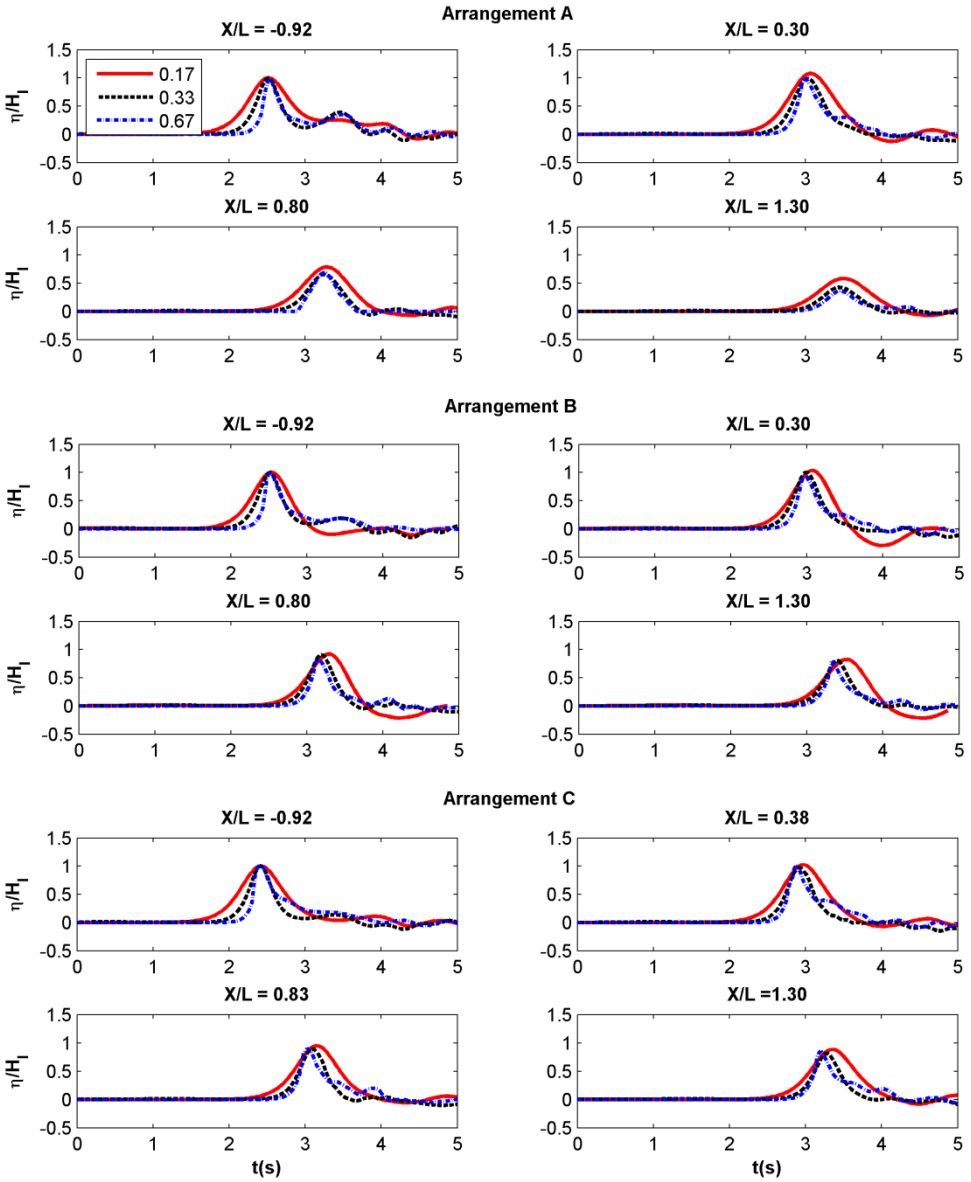

Figure 7.13 Free surface evolution along the cylinders field for arrangement A, B and C and H = 0.025m (red solid line), 0.05m (black dashed line) and 0.10m (blue dash-dotted line) at four locations.

The highest wave shows the largest asymmetry, with a front almost vertical and a longer tail in all the cases. Furthermore, the wave evolution along the field does not change linearly with the relative wave height. It can be observed that for the three arrangements, the smallest relative wave height (H/h = 0.17) has a different behaviour than waves with H/h = 0.33 and 0.67.

Free surface measurement in front of the field reveals a strong reflection for the densest arrangement (A) while this effect is weak for arrangements B and C. This reflection is smaller for the smallest wave and almost the same for the other two simulated waves. Free surface leeward the field shows higher wave attenuation when increasing wave nonlinearity. Although generated solitary waves travel at different speed according to their different wave height, smaller differences are found for the denser cylinders configuration (arrangement A). Momentum damping appears as an effective mechanism to reduce wave celerity and vegetation arrangement seems to play also a relevant role.

Regarding wave height evolution along the patch, the asymmetry of the highest wave is reduced for the densest arrangement where more energy is attenuated. However, for the other two arrangements, wave profile remains non symmetric along the patch, especially for the sparsest one.

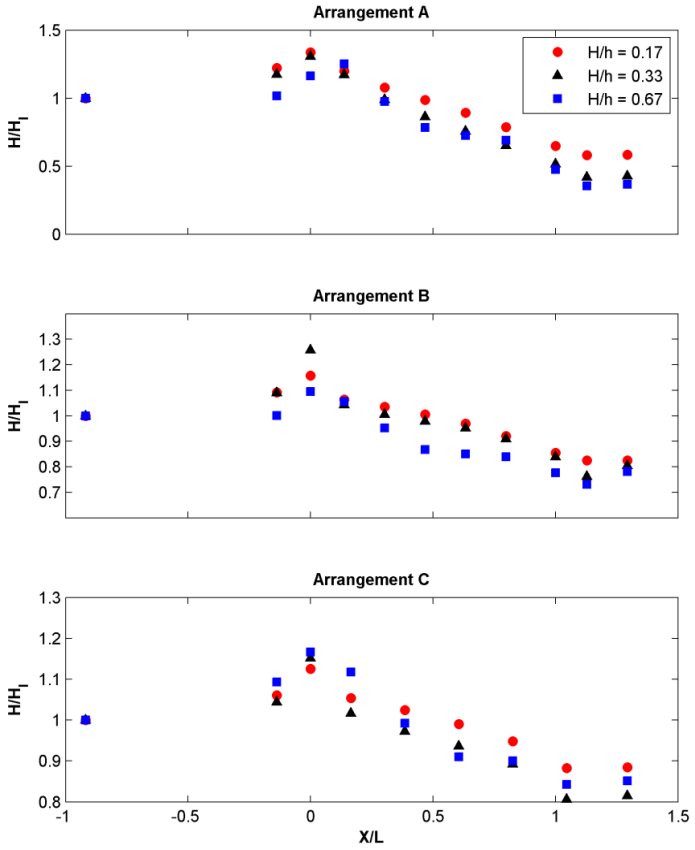

Figure 7.14 Wave height evolution for the three arrangements and H = 0.025m (red circle), 0.05m (black triangle) and 0.10m (blue square).

In order to evaluate wave damping produced for the three arrangements, solitary wave height evolution along the patch is presented in Figure 7.14. All the simulated cases present a common feature at the seaward edge of the patch: increasing wave height varying with field density. Larger values are obtained for the densest configuration (arrangement A) as a result of a local effect due to the increase of flow resistance induced by the cylinders. Wave height enhancement factors of 1.3 are calculated in that case. Arrangements B and C show values around 1.2, as a consequence of a lower flow resistance. This effect is very relevant in the characterization of the flow behaviour at the seaward edge of the patch, as it will be discussed later. Wave height rapidly decreases with increasing relative wave height. Arrangement A shows the largest dissipation rates due to its denser configuration.

Wave induced forces at the cylinders are calculated by means of the flow and pressure fields at each individual cylinder. The central row (in black colour, in Figure 7.12) is chosen to be

representative of the force distribution along the patch. Solitary wave induced force is obtained considering both, pressure and viscous forces on each cylinder as follow:

$$F_{max} = max\left(\int_0^{\eta}\left(p + \mu_{eff}\frac{\partial \bar{u}_i}{\partial x_i}\right)dA\right) \tag{10}$$

where η is the location of the free surface, p is the total pressure field, μ_{eff} is the efficient kinematic viscosity which includes the laminar and the turbulent contribution to shear stresses, $\bar{u}_i$ is the velocity field and dA the area differential along the cylinder. The maximum force exerted on the central line cylinders is obtained and represented in Figure 7.15 for different wave heights. The maximum forces are normalized by $\rho g(h + H_I)A_w$.

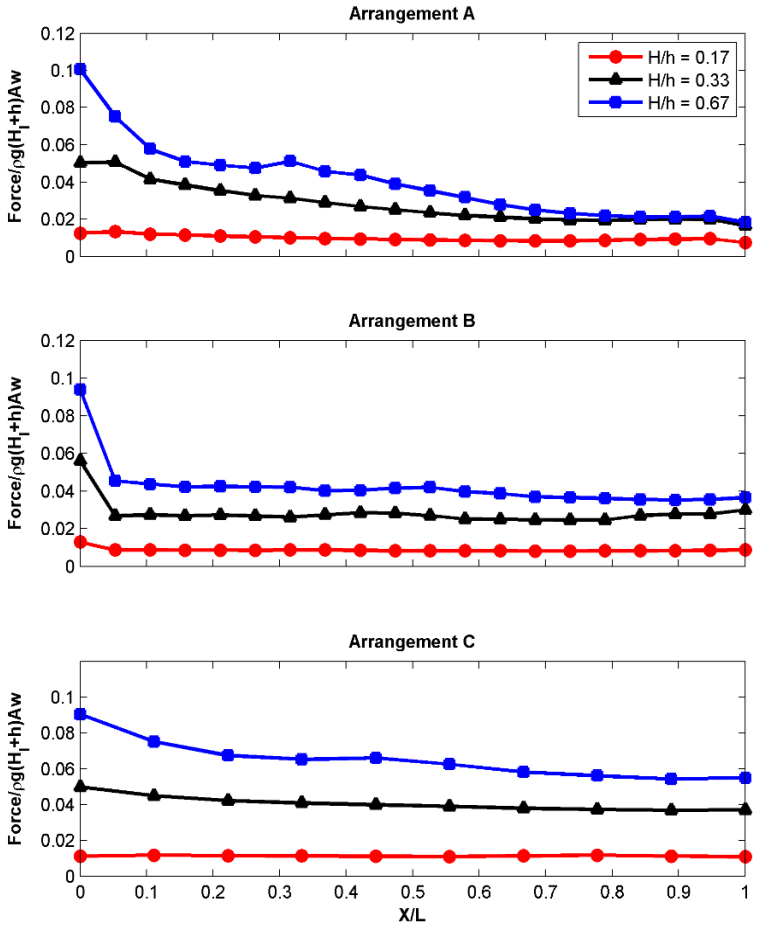

Figure 7.15 Forces at the cylinders of the central line for the three arrangements and H = 0.025m (red circle), 0.05m (black triangle) and 0.10m (blue square).

The wave height increase observed previously at the seaside edge induces a visible increase in the maximum force in all the cases. This feature is very relevant especially when the density of

the cylinders increases, as shown for arrangement A. This effect could have a clear influence on the survival of the plants exposed to waves located at the seaside part of the field. Another important aspect derived from the results is that the maximum force increases with relative wave height if no breaking takes place. The smallest wave height shows an almost constant value of the maximum force along the three arrangements. Maximum forces slightly decrease along the patch for the other two studied wave conditions, being more relevant in the densest cylinder configuration (arrangement A). Therefore, the force reduction rate is higher for nonlinear waves.

7.4.2 Arrangement influence

Previous results have shown a strong dependency of the cylinder arrangement on wave evolution along the vegetation patch and wave induced forces. Characteristics such as the patch density or the cylinders arrangement are studied more in detail in this section. First, arrangements A, B and C, defined according to Huang at el. (2011) experiments, are studied to determine the influence of a regular spatial distribution on flow patterns. Due to the motivation found in real mangrove forest, which follow a random distribution in space, additional simulations are performed. Three new arrangements are designed considering the densities of the uniform arrangements, but randomly distributed. Wave damping and wave-exerted forces are analysed in all the cases.

7.4.2.1 Uniform distribution

Solitary wave height evolution and forces exerted on the cylinders are represented in Figure 7.16 for the three uniform arrangements A, B and C. The same three wave conditions used in the previous section are considered here.

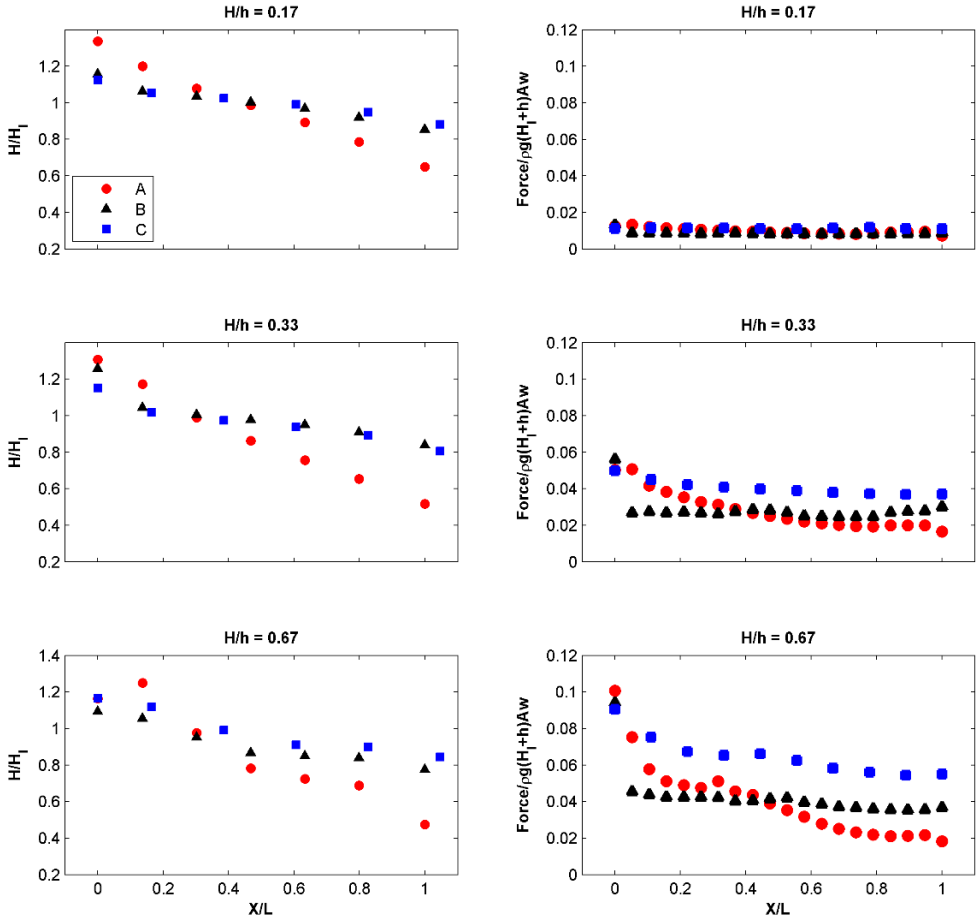

Figure 7.16 Wave height evolution (left column) and forces exerted on the cylinders (right column) for the three wave heights (in vertical) and the three cylinders arrangements (A, B and C).

Numerical results presented in Figure 7.16 show a strong dependency on the cylinders arrangement of wave height evolution. This pattern is related to the density associated to each configuration, namely N = 2228, 1108 and 560 cylinders/m2 for arrangement A, B and C, respectively. Arrangement A, with the highest density, produces a higher flow blocking at the seaward edge of the patch yielding a higher increase in wave height. Wave attenuation appears stronger for the denser arrangement at inner locations in the patch showing the highest wave attenuation at the end (X/L=1). A similar behaviour for solitary wave evolution along the field is found for arrangement B and C. That feature is due to the low density in arrangement C and the existence of preference flow channels in arrangement B, as it will be discussed later, which makes the flow through the field easier, developing low dissipation rates.

Figure 7.16 also shows the strong influence of plant arrangement on the maximum force acting on the cylinders. Arrangements A and C follow a five cylinder stencil configuration whereas arrangement B considers cylinders forming a uniform square grid. As can be observed, the maximum force on the first cylinder is almost the same for all arrangements, as expected. The first row of cylinders is directly exposed to wave action. However, force evolution differs along the field for each arrangement. A rapid and large reduction in the maximum force is observed for arrangement A, showing the lowest force values at the end of the patch. Cylinders damp most of the wave energy due to the higher density and the smaller spacing between cylinders. Therefore, this densest arrangement produces the highest reduction of forces acting on the cylinders in accordance to the wave height damping. Maximum force is less attenuated in arrangement C due to the low density and the larger spacing between cylinders. Finally, arrangement B shows a different behaviour with an almost constant maximum force along the patch, except for the first cylinder. The uniform squared configuration produces clearly different preference flow channels due to the large spacing between cylinders. Flow is developed along the gaps, which are oriented in the wave propagation direction. This effect can be seen in Figure 7.17, which presents a top view of three snapshots of the horizontal velocity field magnitude at the free surface for the three arrangements. As can be seen for arrangement B (middle row), wave induced flow is channelled along the oriented uniform gaps as the solitary wave is passing along the field. Cylinders are not directly exposed to flow and they are shadowing each other. For that reason almost constant maximum forces along the vegetation are found. This effect is not seen for arrangement A, with a higher density, smaller cylinders spacing and non-staggered configuration. Although arrangement C also corresponds to a non-staggered configuration, the large cylinders spacing produce the existence of clear developed preference flow channels.

It is also interesting to note the change in wave celerity seen for the three arrangements. Free surface elevation snapshots at time step 6.2 s show that the wave crest is located at different positions for the three arrangements. The higher the density of the field the higher the celerity reduction. For the same time step the wave reflected from the meadow can be observed. Reflection is also directly related to the cylinders density.

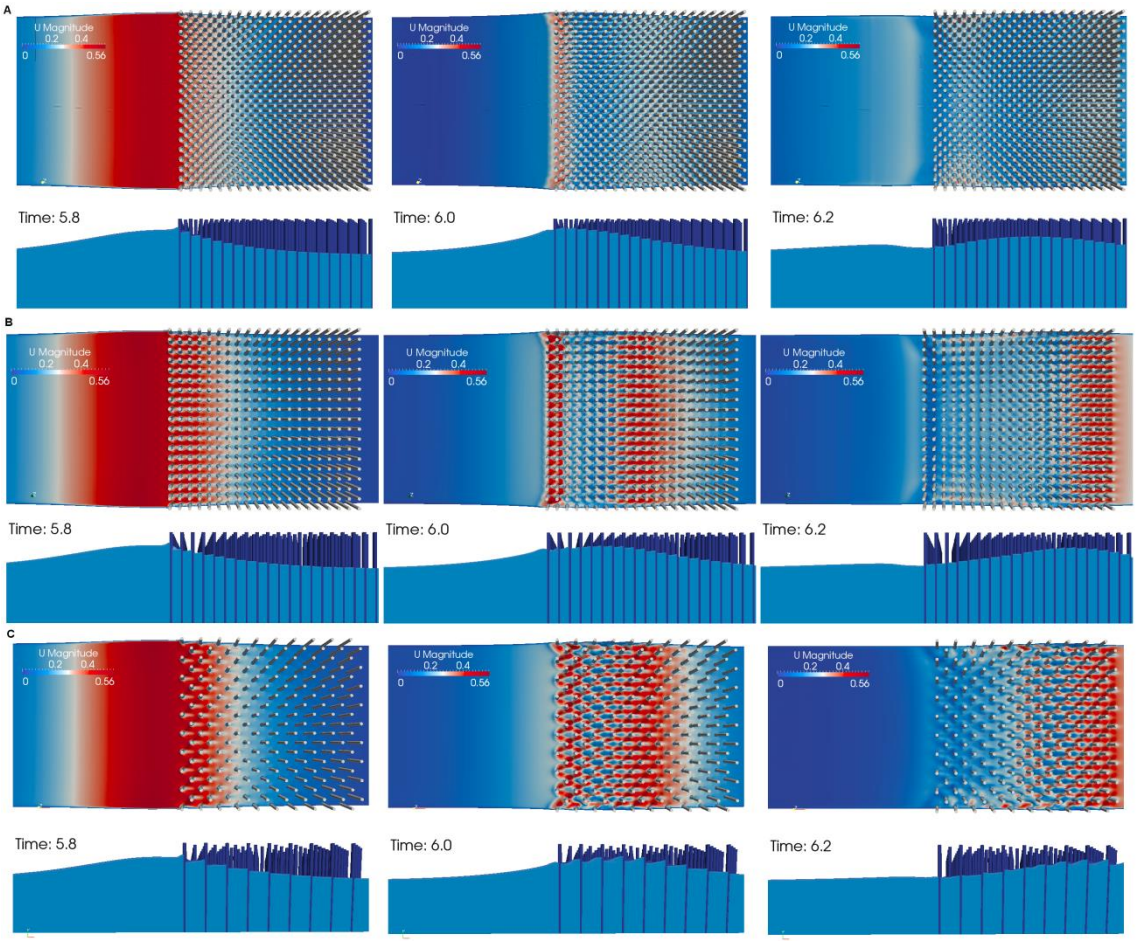

Figure 7.17 Flow velocity and free surface elevation for three time steps in the three arrangements A (upper row), B (middle row) and C (lower row).

As a conclusion, it is noted that the wave induced forces and the wave attenuation due to the rigid vegetation is clearly influenced by the cylinders arrangement. Wave damping rates are sensitive to relative location, density and spacing between cylinders. Flow patterns developed under arrangement B perhaps do not represent realistic scenarios found in nature and could lead to wrong conclusions due to a very uniform and unrealistic arrangement.

7.4.2.2 Random distribution

Although the influence of random vegetation distribution in flow patterns under uniform currents has been investigated (i.e.: Koch and Ladd, 1997; Nepf, 1999; Tanino and Nepf, 2009), only few studies have considered wave flow (e.g.: Anderson, 2010). In order to overcome the limitations found for a uniform arrangement and to study more realistic configurations, three new simulations are performed considering a random distribution of cylinders.

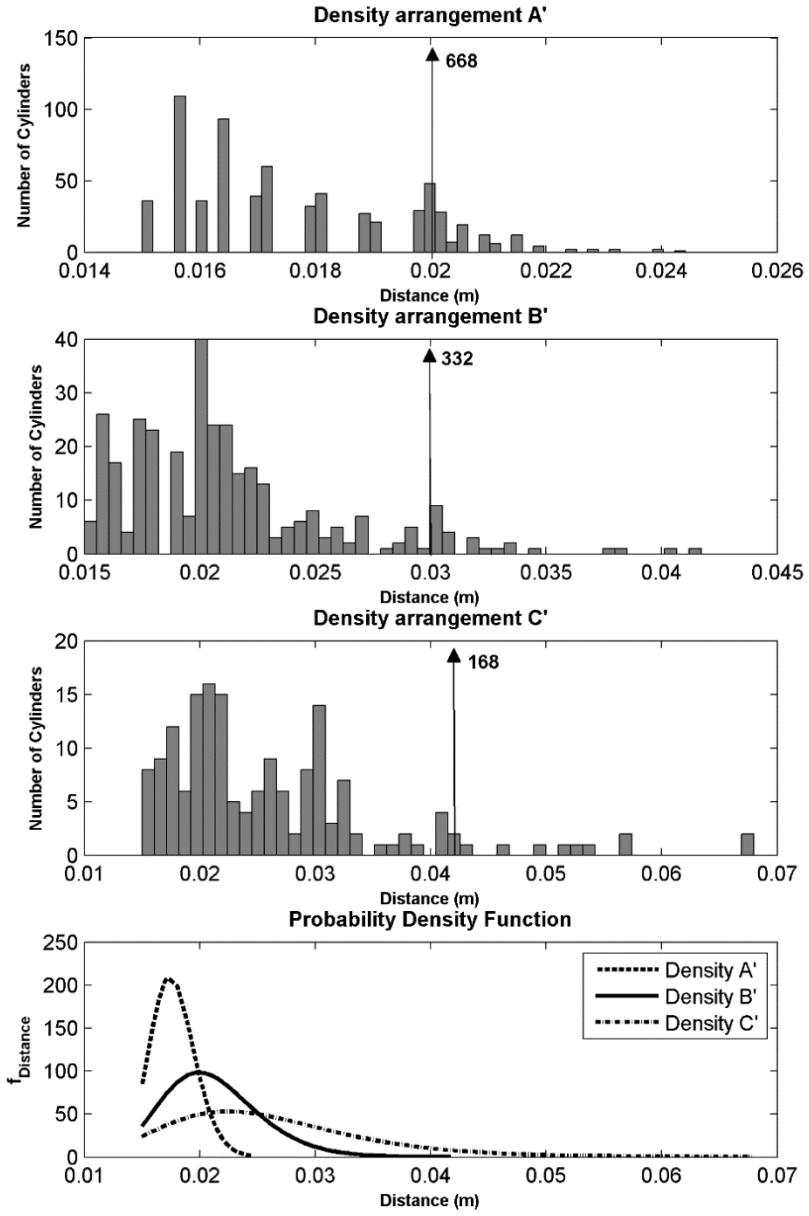

Figure 7.18 Cylinders distance histogram for densities of arrangements A', B' and C'. Arrows represent the values for uniform arrangements. Last image shows the probability density function for the three random configurations.

New configurations (A', B' and C') are calculated considering the cylinders density for arrangements A, B and C (N = 2228, 1108, 560cylinders/m2, respectively) for the same vegetation patch length, i.e.: 0.545m. In order to obtain random distributions, the total number of cylinders associated with each density is disposed randomly, with a minimum distance between cylinders, equal to half of the cylinder diameter. Figure 7.18 shows the cylinders

spacing histogram associated to each density. The total number of cylinders for each uniform arrangement is included in the figure. The corresponding distance of uniform distributions is presented in each panel by means of an arrow. The lower panel shows the cylinders spacing lognormal probability density function for each random configuration.

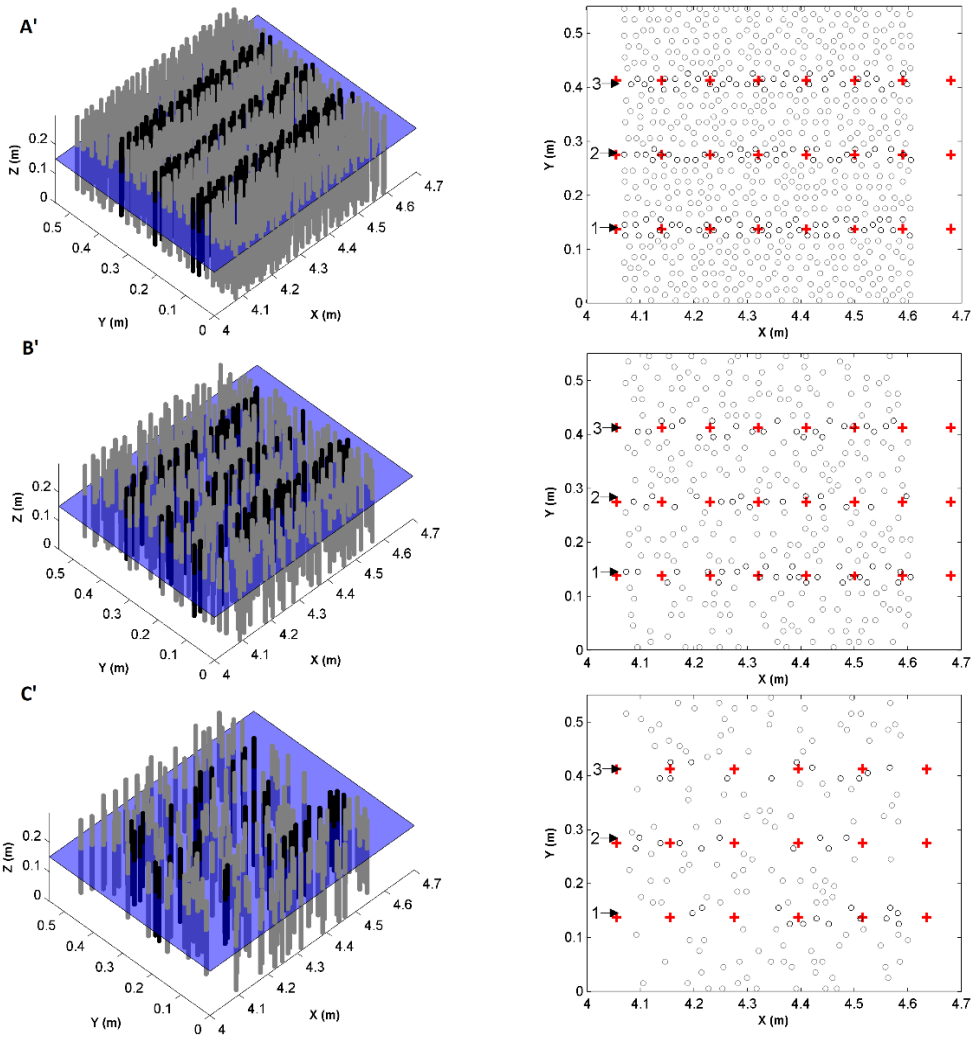

Figure 7.19 Random cylinders distributions for density of arrangements A', B' and C'. Black cylinders are located in the three control sections.

Figure 7.19 shows the three configurations used in this study for the cylinders random distributions. A top view is shown at the right panels for each arrangement. In order to study wave height evolution and the forces exerted on the cylinders, three longitudinal transects along the field, shown in the figure, are considered in order to get representative results. Relative wave height is evaluated at the same locations as the ones used for the uniform arrangements,

represented with red crosses in Figure 7.19. Forces are evaluated in the cylinders plotted in black in the three panels.

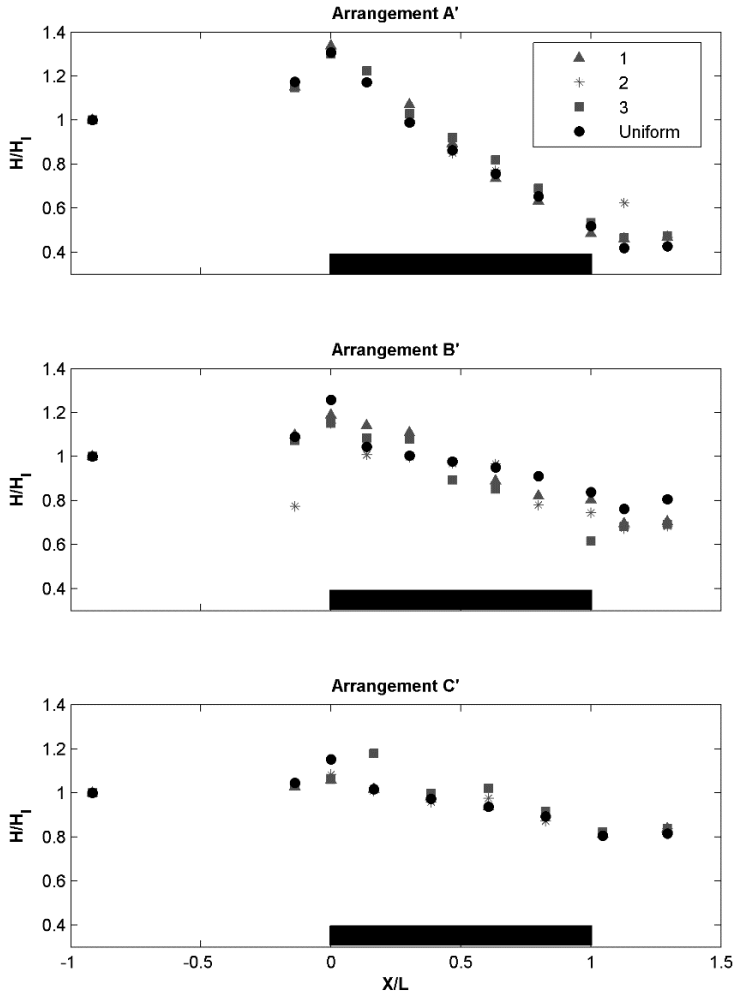

Figure 7.20 Relative wave height evolution along the cylinder field for random and uniform arrangements A', B' and C'. Results for control sections 1 (triangles), 2 (stars) and 3 (squares) are represented for random configurations.

Figure 7.20 shows wave height evolution along the vegetation patch for the three random arrangements, along the three transects shown in Figure 7.19. Results corresponding to the uniform configuration are also included in the plots. As can be observed in the figure, wave height evolution is very similar for random control sections and uniform arrangements. The highest differences are found for arrangement B' where wave damping produced for the random distributions is larger than the one obtained for the uniform patch, revealing the strong influence of the preference channels in the flow pattern. Additionally some local effects can also be observed from the numerical results. Wave height increase at the seaward edge of the patch

is almost negligible for arrangement C' (lower panel) probably due to the fact that the number of cylinders at the beginning of the field is lower in the random configuration. The wave increase effect is located farther inside the field for results in transect 3.

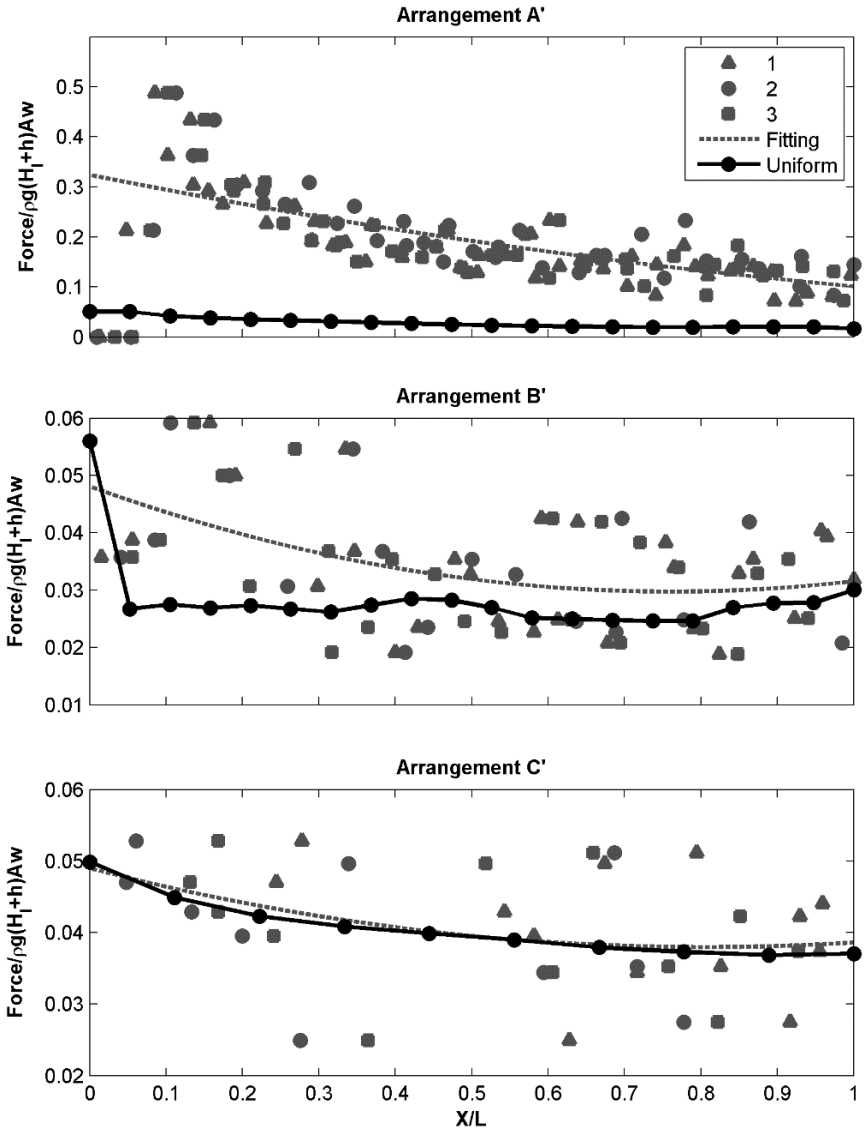

Figure 7.21 Forces exerted on the cylinders of the three control sections of the random configuration and the cylinders of the central line of the uniform distribution.

Consequently, in terms of wave damping and neglecting very local effects, overall density, field length and relative water depth are more relevant than plants distribution within the field. Differences increase with decreasing plants distribution but for cases considered, they remain in a ±10 - 20% of the uniform distribution damping results. It can be concluded that based on

these results dynamics triggered by wave height differences are only anticipated at the edges of the field.

Forces are calculated according to Eq. (10). The evolutions of the maximum forces along the patch are plotted in Figure 7.21. Results correspond to cylinders included in the three transects. They are plotted together with a quadratic fitting law in order to estimate averaged values along the patch. Results obtained for uniform distributions are also included in the plot. One common aspect observed in the figure is the large dispersion of the maximum force obtained for the random arrangements. This is mostly due to local effects in the velocity flow field linked to the relative location of the cylinders. However, a decaying trend is observed in the maximum force along the patch in the individual force values, also confirmed by the fitting curve. Another important aspect obtained from the simulations is that for the uniform arrangement the maximum force is lower along the patch. Random distributions turn in decreasing stems alignment and increasing grouping. This lowers the probability of wake sheltering on individual downstream cylinders. This effect is higher for larger density values. Thus, for the densest arrangement the force obtained with a uniform configuration is less than half the one estimated for the random case. The shadowing effect between cylinders is less effective in a random distribution, increasing the wave-exerted force. This feature is also visible when wave induced flow is analysed.

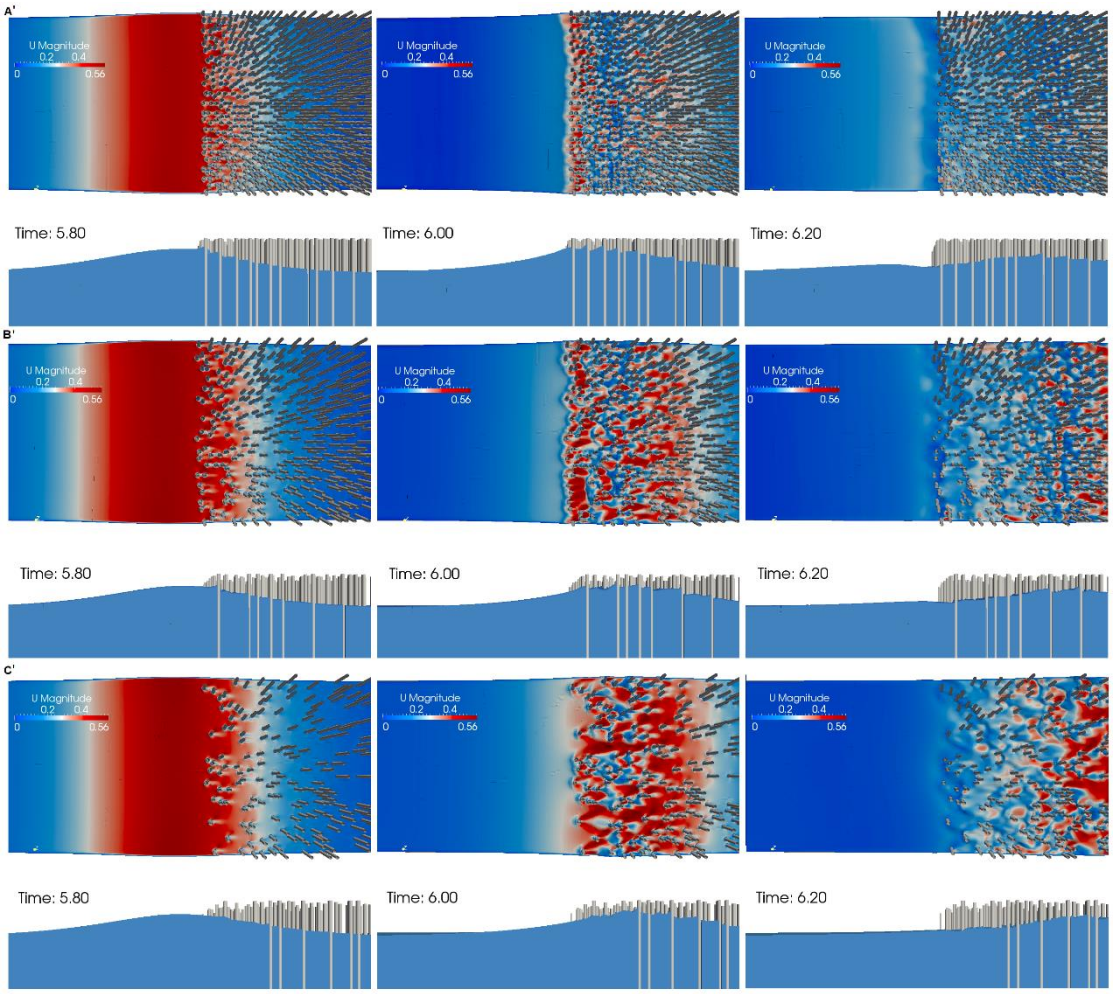

Figure 7.22 Flow velocity and free surface elevation for three time steps in the three random arrangements.

Figure 7.22 shows snapshots of the horizontal velocity fields at the free surface developed between the cylinders for the three random configurations. Three different time steps are presented when the solitary wave is travelling along the field. A side view of the free surface is also plotted in the lower panels. Results show irregular flow patterns in comparison to the regular velocity fields observed for uniform cylinder arrangement (Figure 7.17). Both wakes, created behind the cylinders, and flow accelerations, formed at the constrictions by the random paths created around the cylinders, are clearly observed. Moreover, isolated cylinders can be observed in the less dense configurations (two lower panels) as a result of the random arrangements, responsible for the larger forces induced by waves.

As a summary, it is very important to point out that the idealized arrangements that are usually tested in laboratory experiments or simulated numerically give reasonable good results in terms

of overall wave damping. However, large differences are found in the forces exerted on the vegetation for uniform and random distributions. Generalizations obtained from uniform arrangements could lead to underestimation of wave-exerted forces, especially for high dense configurations and the ones that could be found in nature, which follow random arrangements.

7.4.3 Discussion on the numerical approach

So far, it has been demonstrated that both numerical approaches provide an accurate wave height evolution along the cylinders array but with different computational costs. Regarding the estimation of the forces exerted on the individual elements, the first approach allows obtaining these forces directly since individual cylinders are introduced in the domain. However, the evaluation of forces using the macro-scale approach is only possible considering the drag force formulation presented in Eq. (6).

In this section the differences between the two approaches in force calculation is examined. Drag coefficients obtained in the model validation in Section 3 are used to calculate maximum forces on the cylinders for the macroscopic approach. The characteristics of these cases as well as the calibrated drag coefficient for each case are specified in Table 3. The Reynolds number associated to each wave condition is also shown in the table. This number is defined as $Re = \frac{aV_c}{\upsilon}\mathrm{Re} = \frac{\mathrm{aV_c}}{\upsilon}$, where a is the cylinder diameter, Vc the maximum solitary wave celerity ($\sqrt{g(h+H_i)}$) and v the dynamic viscosity.

Run	*Arrangement*	*Width (m)*	H_i *(m)*	*Re*	C_D
V1	A	0.545	0.041	13.688	2.45
V2	B	1.090	0.03	13.288	1.45
V3	C	1.635	0.05	14.007	1.52

Table 7.3 Validated cases characteristics and calibrated drag coefficients

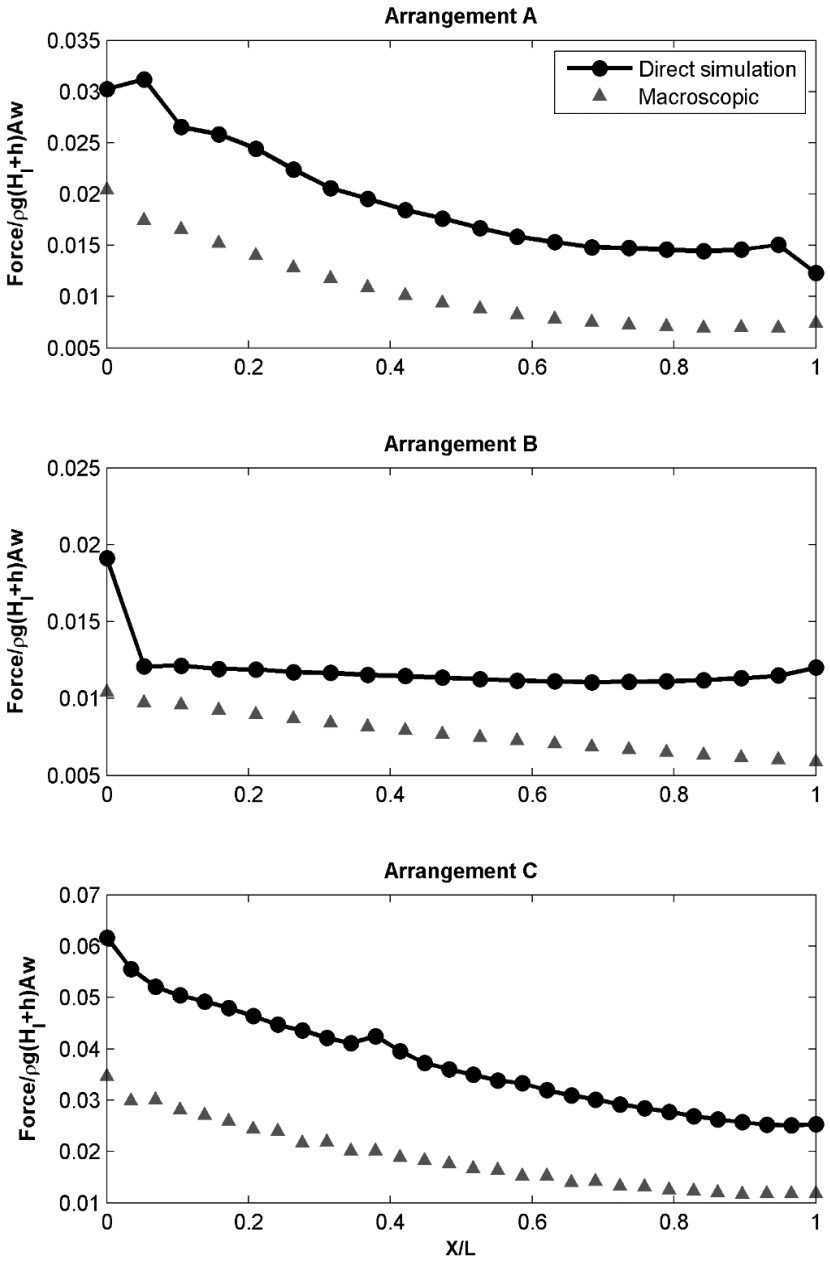

Figure 7.23 Forces on the cylinders of the central line (black dots) and at those locations for the drag approach (grey triangles).

Maximum forces on the cylinders are presented in Figure 7.23 for the three uniform arrangements. Although the velocity field obtained with the macroscopic approach is not representing a real velocity field inside the cylinder array, it was demonstrated in Chapter 3 that a very accurate reproduction of the flow inside the vegetation is achieved. In that study, ADV measurements obtained inside a flexible vegetation patch were compared with numerical

results obtained using the same approach showing a high degree of agreement. Following the same procedure used in experimental analysis (i.e.: Mazda et al, 1997, Strusinska-Correia et al., 2013), wave forces are characterized here using the velocity field. Figure 7.23 shows a clear mismatch between values from both approaches. Maximum force is underestimated if using the macroscopic modelling. The trend observed for the force is the same for both approaches, decreasing along the patch. Results for arrangement B do not obey to that trend in the direct simulation pointing out again the influence of the flow patterns along the preference flow channels created along the direction of wave propagation. The macroscopic approach is not able to catch this feature and keeps a monotonic damping along the field.

In order to study more in detail the differences found between both approaches a new set of simulations is performed. The numerical model is used as a numerical laboratory, and the simulations, which consider the individual cylinders, are used as a reference to determine the drag coefficient value for the macroscopic approach. Nine simulations are performed considering arrangements A, B and C and three wave heights (0.025, 0.05 and 0.10m). The drag coefficient for each simulation is set to obtain the same wave damping as in the simulations run considering the individual cylinders. Following this procedure, the obtained drag coefficient values as well as the run characteristics are shown in Table 4.

Run	***Arrangement***	***Width (m)***	H_i ***(m)***	***Re***	C_D
1	A	0.545	0.025	13.102	3.45
2	A	0.545	0.05	14.007	2.35
3	A	0.545	0.10	15.660	1.55
4	B	0.545	0.025	13.102	1.5
5	B	0.545	0.05	14.007	0.7
6	B	0.545	0.10	15.660	0.6
7	C	0.545	0.025	13.102	2
8	C	0.545	0.05	14.007	1.52
9	C	0.545	0.10	15.660	1

Table 7.4 Calibrated drag coefficient

The obtained drag coefficients vary consistently with wave height and Re. The wave height evolution obtained with these drag coefficients is compared with the results obtained with the direct simulation approach for the uniform arrangements in Figure 7.24.

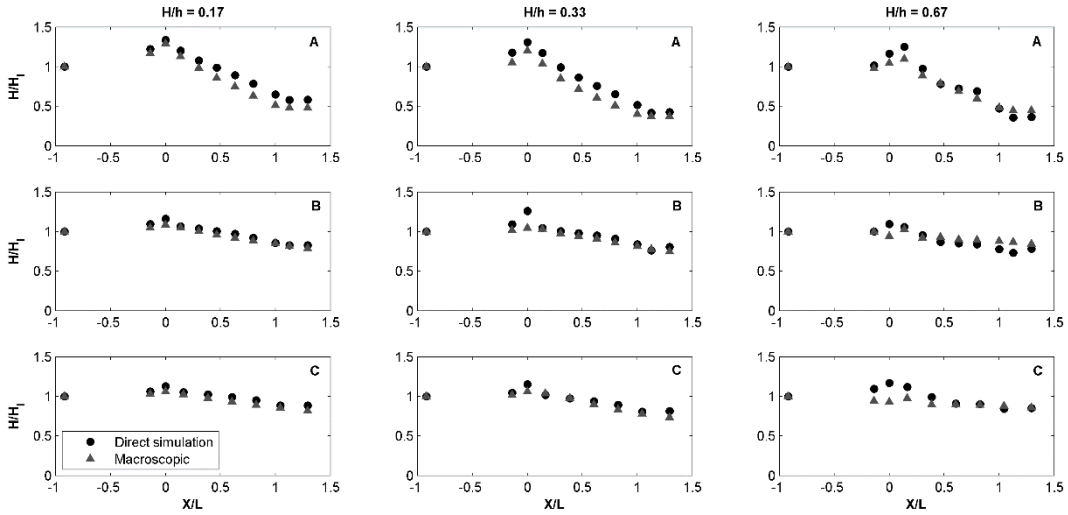

Figure 7.24 Wave height evolution comparison between both approaches.

As can be observed in Figure 7.24, wave height evolution is very well reproduced by the macroscopic approach. Minor discrepancies are observed at the edges of the meadow where the local effects produced in the cylinders field are not reproduced precisely using the macroscopic approach, especially for arrangement B. Therefore, although there is a good agreement between both approaches attending to the general wave height evolution, the local effects at the edge are not captured so well. These effects are more important when the nonlinearity of the wave increases as can be observed for cases with H/h = 0.33 and 0.67.

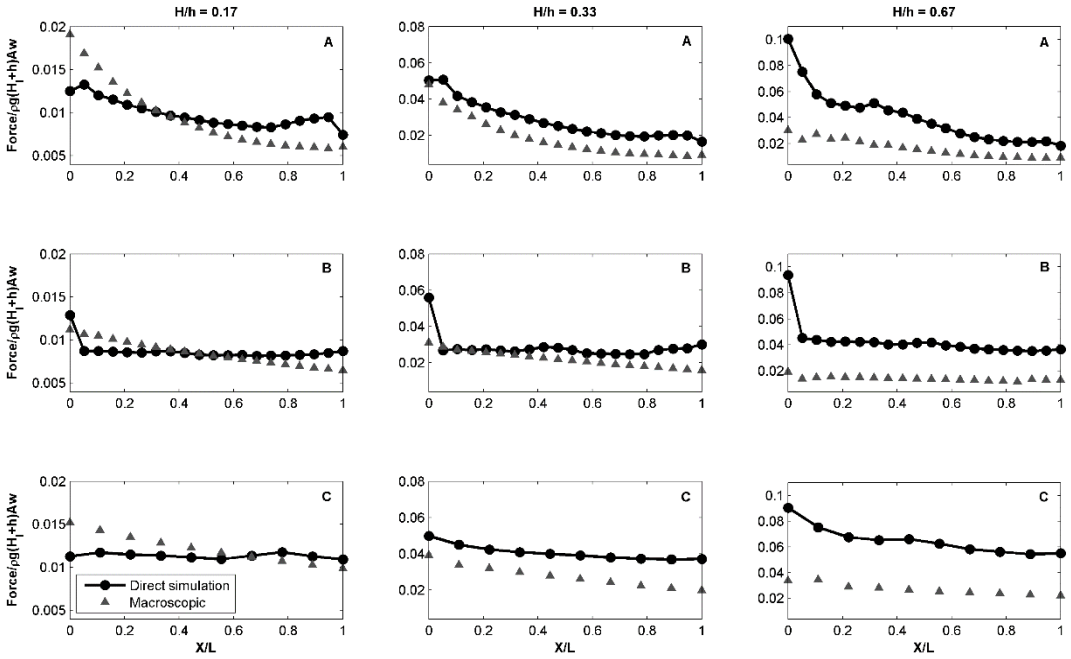

Figure 7.25 Forces at the cylinders of the central line (black dots) and at those locations for the drag approach (grey triangles) for the nine simulations considering the three arrangements and three different wave heights.

The drag force associated to these new simulations is also evaluated. Figure 7.25 shows the comparison between both approaches. Important discrepancies are obtained when forces are estimated using both approaches, not only in the values but also in the trend followed by the force along the patch. It can be observed that for the cases with the smallest wave height there is a force overestimation around the first half of the meadow that turns into an underestimation in the second half for the three arrangements for the macroscopic approach. This effect is higher for the arrangements with higher density. However, when the wave nonlinearity increases, forces obtained with the drag approach are smaller than the ones recorded simulating the individual elements. This effect is stronger if the wave nonlinearity increases. The forces obtained with the macroscopic approach for the location of the first cylinder are three times smaller than the ones recorded simulating the individual elements. Therefore, maximum forces obtained from the macroscopic approach are underestimated significantly for higher nonlinear waves.

The weakest point of the use of the macroscopic approach is the determination of the drag coefficient which has been varied according to the flow characteristics and cannot be predicted beforehand. Although several formulations can be found in the literature to estimate the drag coefficient for waves damped by vegetation (e.g.: Kobayashi et al., 1993; Mendez et al., 1999)

and more recently, waves and current attenuation (Hu et al., 2014), none of them are especially fitted for solitary waves. Tanino and Nepf (2008) proposed an empirical formulation for the mean drag coefficient for random cylinders arrays:

$$C_D = 2\left(\frac{\alpha_0}{Re} + \alpha_1\right) \tag{11}$$

where α_0 and α_1 are two empirical parameters that depend on the solid volume fraction (ϕ = volume of cylinders/total volume): $\alpha_1 = (0.46 \pm 0.11) + (3.8 \pm 0.5)\phi$ and $0 \leq \alpha_0 \leq 0.85$. The formulation for unidirectional flow and emerged vegetation presented by Cheng and Nguyen (2011) is also considered:

$$C_D = \frac{50}{Rv^{0.43}} + 0.7\left[1 - exp\left(-\frac{Rv}{15000}\right)\right] \tag{12}$$

where $Rv = \frac{\mathrm{r_v V_c}}{\nu}$ with $r_v = \frac{\pi}{4}\frac{1-\lambda}{\lambda}a$ and λ is the fraction of cylinder-occupied bed area. The drag coefficients obtained from the best fitting are plotted in Figure 7.26 and compared with existing formulas as a function of the Reynolds number. In this chapter, $\mathrm{V_c}$ has been defined as the maximum solitary wave celerity. The three arrangements are presented separately to better compare with both formulations.

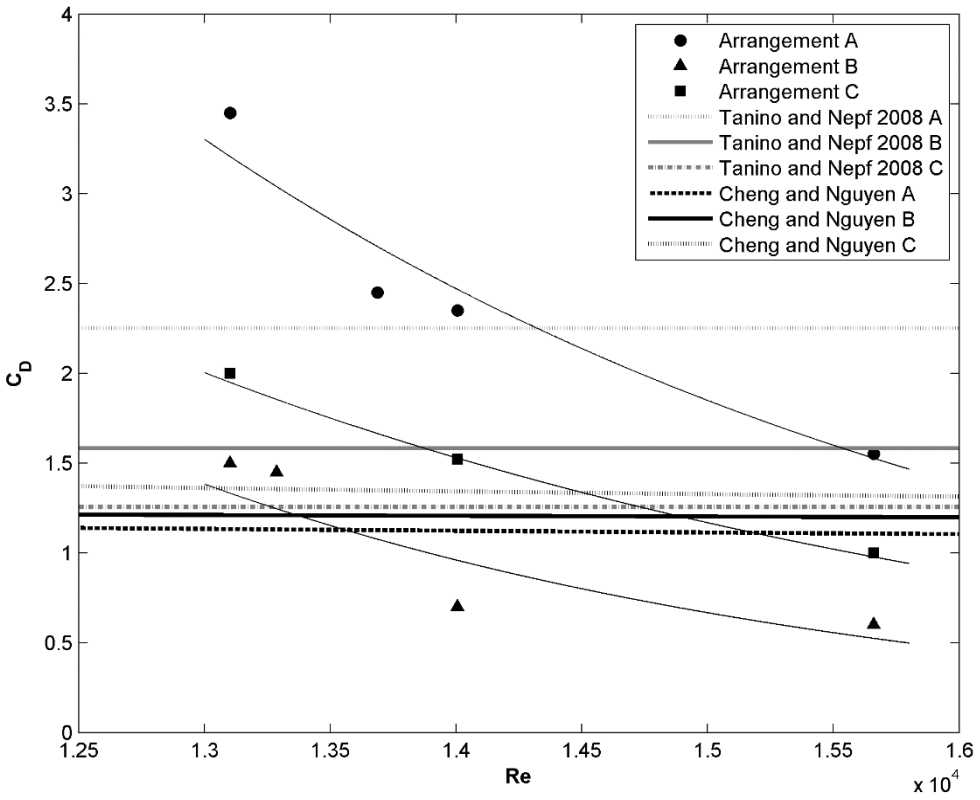

Figure 7.26 Calibrated drag coefficients and formulas from literature.

As can be observed existing formulations do not correspond with the calibrated drag coefficients obtained numerically. Neither the formula presented by Tanino and Nepf (2008) nor the one proposed by Cheng and Nguyen (2011) are able to capture the change produced in the drag coefficient for the simulated Reynolds number range. Therefore, it seems necessary to perform new studies to obtain an appropriate formulation for this type of conditions where the hydrodynamic forcing is a solitary wave and the rigid elements are emerged. Also the meadow characteristics should be included. Fittings obtained for the different arrangements shown in Figure 7.26 reveal clear differences in the values of CD for the same Re depending on the arrangement, revealing the important role played by the vegetation density on the drag coefficient. Furthermore, it is interesting to note that drag coefficient values for arrangement B are smaller than the ones obtained for arrangement C which has a small density. This is due to the cylinders arrangement and the preferable flow channels produced in arrangement B, perhaps not representative of a real mangrove forest.

7.5 Conclusions

The numerical modelling of the interaction of tsunami waves with mangrove forests is addressed in this study as a first approach by means of solitary waves impinging on emergent rigid cylinders. Two different numerical approaches are followed: a direct simulation of the flow field considering the actual geometry of the cylinders array and a macroscopic modelling of the flow within the forest, which introduces a drag force to model the momentum damping created by the plants.

To our knowledge, this is the first time that a three-dimensional model is presented to model wave damping by vegetation including an adapted turbulence model for macroscopic flow modelling around vegetation. The model is validated for both approaches using laboratory data with a very good agreement with laboratory measurements for free surface evolution along the mangrove forest. While macroscopic modelling needs the calibration of the drag coefficient, direct simulation approach is free of parameterizations. Direct simulation has proven to have a high potential to be used to study local effects and more realistic scenarios. The main drawback brings the high computational cost.

The model is used as a numerical laboratory to get very valuable information about the flow field and the wave exerted forces on the vegetation by means of a very refined resolution around the cylinders. Additional simulations are carried out with the aim of studying the influence of solitary relative wave height, vegetation density and vegetation arrangement on the tsunami wave attenuation and the forces exerted on the plants. Not only uniform but also random arrangements are considered in order to determine close to nature scenarios.

It is seen from the simulations that the wave induced forces and the wave attenuation due to the rigid vegetation is clearly influenced by the arrangement. Wave damping rates are affected by the relative location of the cylinders, the solid fraction of the patch and the cylinders spacing. It is found that uniform arrangements that are usually tested in laboratory experiments or simulated numerically give reasonable good results according to wave damping. However, large differences are found in the forces exerted on the vegetation for uniform and random distributions. Generalizations obtained from uniform arrangements could lead to underestimation of wave-exerted forces, especially for low dense configurations and the ones found in nature, which follow random arrangements.

The macroscopic approach is able to produce satisfactory results for the prediction of wave height evolution along the patch and the momentum damped by vegetation if the appropriate CD is found. However, maximum wave-exerted forces on the cylinders are not well reproduced.

The differences observed in the numerical results suggest the necessity of using the exact geometry of the plants to correctly address the forces exerted by the flow on the plants. Deviations increase for increasing Reynolds number and wave non-linearity.

Following the macroscopic approach to reduce computational costs requires new CD formulations. Current formulations were obtained for periodic waves and submerged plants providing results far from the values obtained numerically in this work. It is also detected the strong influence of the vegetation density and the plant arrangement on wave exerted forces on the cylinders. New studies to find appropriate formulations for tsunami waves, which better address the parameterization of the tsunami wave damping by rigid vegetation as mangrove forest need to include the influence of plant arrangements, plant geometry or Reynolds number. Direct simulations with IHFOAM may contribute to better parameterize drag forces in wave models aiming to simulate damping at large scales.

"Wealth is like sea-water; the more we drink, the thirstier we become"

Arthur Schopenhauer

8

EXPERIMENTAL AND NUMERICAL ANALYSIS OF WAVE ATTENUATION BY VEGETATION PATCHES

Summary

An experimental study conducted in the Directional Wave Basin at the University of Cantabria is presented to analyse the influence of flow and cylinder parameters on wave attenuation considering three setups of vegetation patches. Regular, random and solitary waves were run considering different wave characteristics. The cylinder configurations formed by one, eight and four patches were tested under emergent, near emergent and submerged conditions. These configurations are parameterized by means of a new parameter, the equivalent field length (Le), which is used to relate cylinders' distribution with their wave attenuation capacity. This new parameter allows comparing results for the three patches configurations. Results are analysed considering the influence of wave height and period, revealing larger attenuation rates for

higher wave heights and shorter wave periods. The influence of water depth is also considered by means of the submergence ratio (SR) in order to account for the percentage of water column affected by vegetation. Higher attenuation rates are obtained for emergent conditions. A meaningful relationship is found between wave attenuation and a new parameter, the depth wave number ($kLe * SR$), that accounts for submergence conditions and field characteristics. Finally, wave attenuation is also related to Keulegan-Carpenter and Reynolds numbers showing a high scatter of the data. This scatter is reduced by the consideration of a new Reynolds number (Re_s^{Le}) that is calculated considering the field vegetation dimensions affecting the flow.

8.1 Introduction

Coastal protection provided by vegetation has long been a topic of interest. The interaction of flow with vegetation fields influences coastal protection (Costanza et al., 1997; Borsje et al., 2011; Temmerman et al., 2013; Hashim et al., 2013, Duarte et al. 2013) and also affects many ecological processes, such as sediment transport (Chen et al., 2007; Bouma et al., 2007) or supply of dissolved nutrients (Cornelisen and Thomas, 2004) among others. Sea level rise (Menendez and Woodworth, 2010) and the increase in frequency and intensity of extreme events associated with waves (Izaguirre et al., 2013) related with climate change, increase the risk of erosion and flooding in the coastal area. The integration of natural systems in the portfolio of coastal defences is an interesting option from an ecological, social and economic point of view (Barbier et al., 2008; 2011). For that reason, many experimental and numerical studies have been developed to characterize and quantify that protection. Most of them are focused on wave attenuation produced by a vegetation field under controlled flow conditions, especially laboratory experiments. Although many of them have been performed considering different wave conditions: regular waves (Liu et al., 2014), random wave trains (Lowe et al., 2007; Koftis et al., 2013) or solitary waves (Huang et al., 2011; Strusinska-Correia et al., 2013) there is still no agreement on the influence of wave parameters on wave attenuation. Regarding wave height, both increase (Tschirky et al., 2000; Cavallaro et al., 2010) and decrease (Bradley and Houser, 2009; Manca et al., 2012) in wave attenuation have been found in previous studies with increasing wave heights. Likewise, higher attenuation has been reported for both, shorter (Anderson and Smith, 2014) and longer waves (Infantes et al., 2012). Therefore, more effort is still needed in the study of the influence of wave parameters on wave attenuation. Another important parameter in wave attenuation is the submergence ratio. The relationship between vegetation height and water depth strongly influences wave attenuation. Previous studies such as Nepf (1999) or Augustin et al. (2009) have pointed out the different flow patterns developed

under different submergence ratios. Therefore, this parameter should be considered in wave attenuation evaluation since it can be essential to control wave energy damping

Not only flow conditions influence wave attenuation. Vegetation field properties strongly determine the ecosystem wave attenuation capacity. A wide range of vegetation species can be found in coastal areas with completely different characteristics. Several studies have been performed attending to individual plant characteristics like flexibility (Luhar and Nepf, 2011; Paul et al., 2012; Ozeren et al., 2013). Important attention has also been paid to vegetation density (number of shoots per square meter) and its role on wave attenuation (Luhar et al., 2008; Bouma et al., 2010). Recently, some studies have been performed to analyse the influence of shoots distribution in the interaction of flow and vegetation (Tanino and Nepf, 2008). However, only very few studies have been focused on studying vegetation patchiness. Vegetation fields in nature are neither uniform nor continuous. Many intertidal ecosystems present flow channels between vegetation patches or non-uniform fields due to changes in substratum or human action among others. Therefore, there is a need to extend the analysis on the influence of vegetation patchiness on wave attenuation. Most of the literature available has been based on the analysis of experimental data obtained at small-scale experiments conducted using seagrasses under uniform flow conditions (Fonseca at al., 1983; Fonseca and Koehl, 2006; Folkard, 2005). These studies are focused on characterizing mean and turbulent flow patterns. Flow patterns developed inside and around a finite patch formed by cylinders have been also studied (Zong and Nepf, 2010) in order to characterize the flow and its implications in sediment and nutrients deposition. Recently, Irish et al. (2014) carried out laboratory experiments to evaluate the tsunami run-up reduction by vegetation patches. However, the influence of patchiness on wave attenuation remains unstudied.

The present work presents a series of experiments conducted to study the influence of different wave conditions and water depths interacting with three configurations including a different number of patches composed of vertical rigid cylinders. Regular, random and solitary waves are tested for three different water depths. The effect of vegetation patchiness is studied one, four and eight patches. Results for this unique set of experiments are analysed and discussed in terms of wave parameters, submergence ratio and field geometric characteristics. The experimental set-up and tests are described in section 2. Section 3 is devoted to present and discuss the attenuation results obtained for the different tests and conclusions are drawn in section 4.

8.2 Experimental set-up

Experiments were conducted in the Directional Wave Basin at the University of Cantabria. The wave basin is 8.6 m wide, 1 m deep and has an effective length of 24.1 m as shown in Figure 8.1. The lateral boundaries are vertical walls. The left end is equipped with a piston-type wavemaker composed of 10 paddles that can move independently. The wavemaker stroke is 90 cm. At the right end a gravel beach is built to dissipate waves. Three different geometric configurations are tested in the experiments with their centre located at 12.3 m from the wave paddles mean position in the x direction and centred in the transversal direction (Figure 8.1).

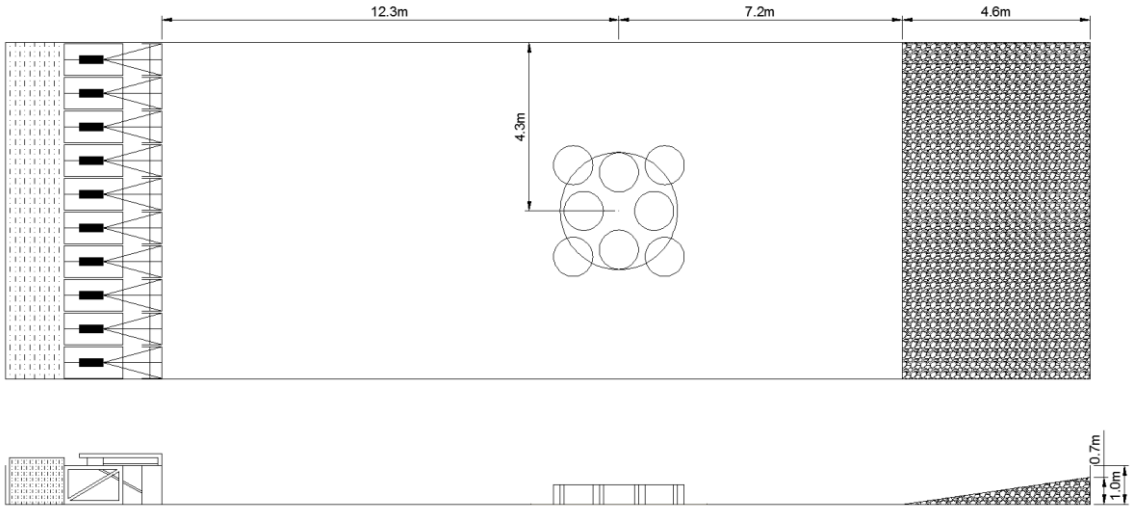

Figure 8.1 Wave basin and location of the three geometric configurations.

The three geometric configurations considered in the experiments are built using wood rigid cylinders. A platform is fixed to the basin bottom with a sufficient number of holes to screw the cylinders to conform the three configurations saving time when setting up different configurations during the experiments. Cylinders are 3 cm in diameter; 50 cm tall and they are uniformly distributed with a separation of 9 cm between centres. For the first configuration, 880 cylinders are disposed in a single 3 m diameter circular shape. The second configuration is composed by 8 circular cylinder patches of 1 m diameter. Each patch is composed of 112 cylinders that leads to a total number of cylinders equal to 896. The four inner patches of the second configuration form the third configuration. Figure 8.2 shows the cylinders distribution for the three configurations.

These three configurations are selected in order to study the influence of having vegetation patches instead of a continuous field. Configuration 2 is built with almost the same number of cylinders as Configuration 1 but they are distributed forming eight individual patches. The

location of these patches is selected looking for covering the available drilled area with a minimum distance between patches to allow developing flow preference channels. The third configuration was selected based on the second one looking for a configuration formed by half of the cylinders with different preference channels.

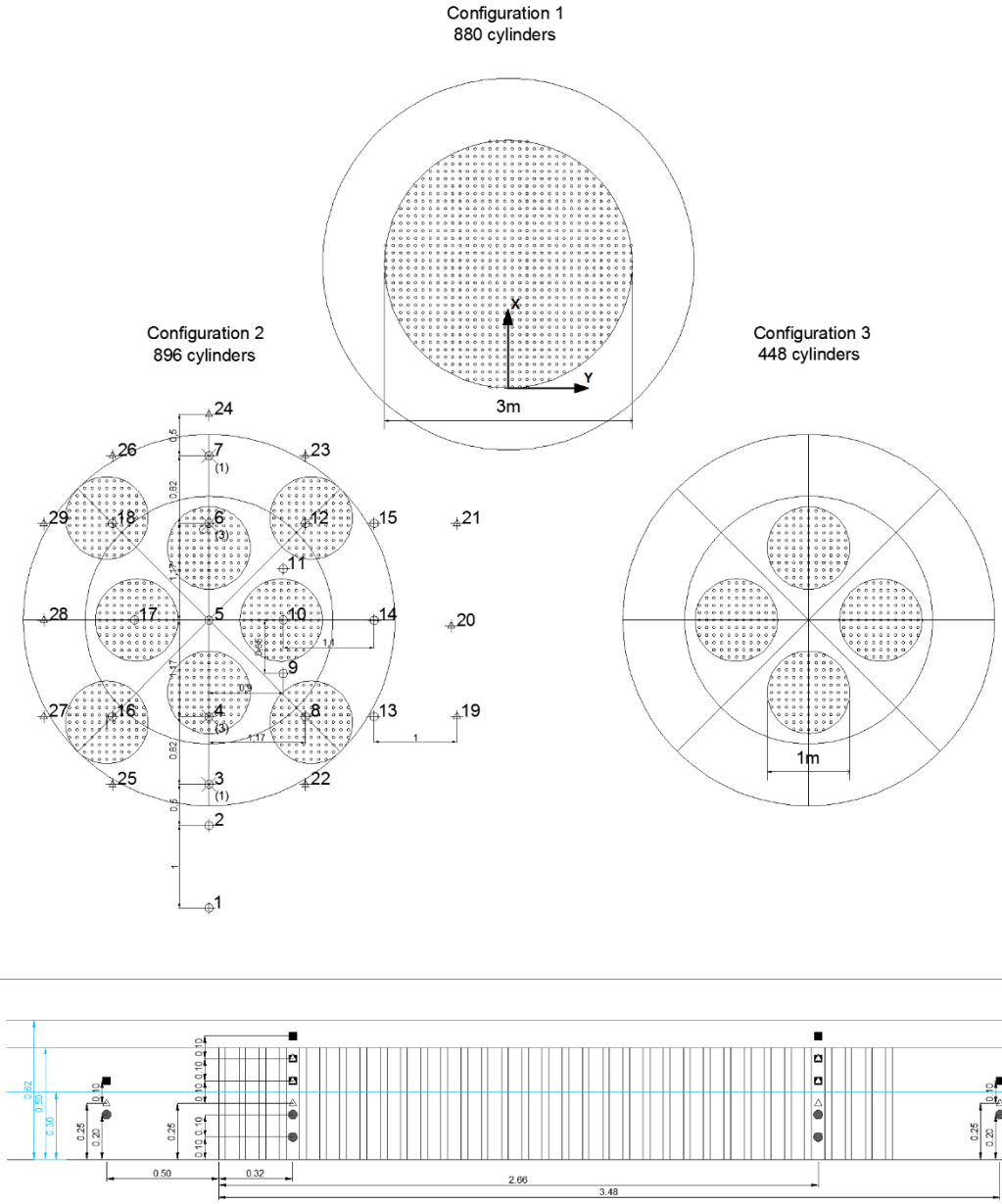

Figure 8.2 Configurations tested in the experiments. Top panel: resistance gauges (circles), acoustic gauges (triangles) and ADVs (crosses specifying the number of devices at each location between brackets) are displayed in Configuration 2. Bottom panel: ADVs location for the three water depths: h = 0.30 m (circles), h = 0.50 m (triangles) and h = 0.62 m (squares).

Three water depths are considered for the three configurations in order to analyze the influence of submergence ratio, defined as the ratio between vegetation height and water depth. Emergent, near-emergent and submerged conditions are tested considering h = 0.30, 0.50 and 0.62 m respectively.

In order to compare wave interaction with the three configurations the same instrumental setup is considered in all the cases. This allows comparing measurements taken at the same location for the three configurations. 29 wave gauges (18 resistive and 11 ultrasonic, Table 8.1) sampling at 50 Hz are distributed around and inside the different patches, as shown in Figure 8.2 and Figure 8.3.

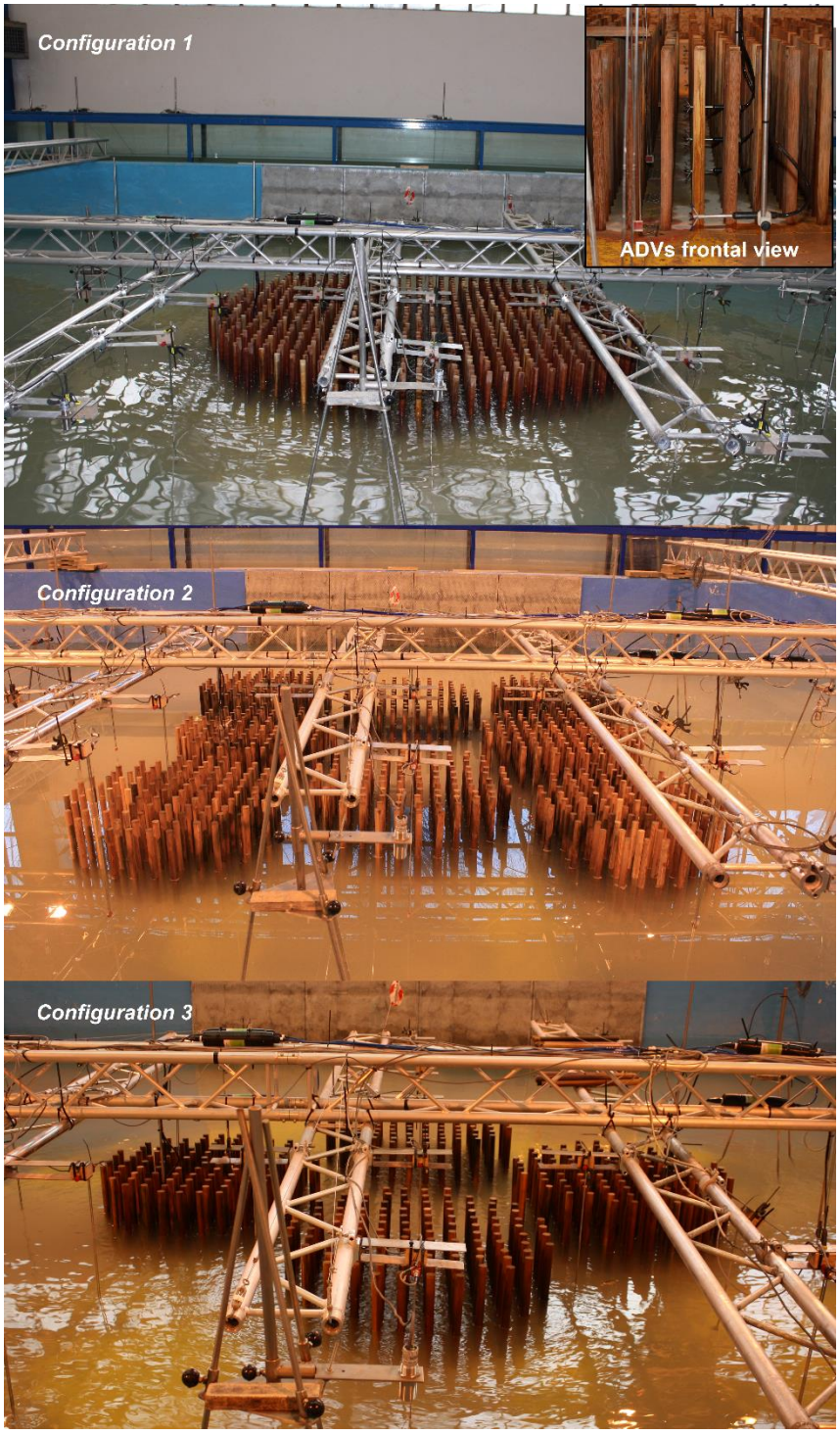

Figure 8.3 Side view of the three geometric configurations in the experiments. A detailed frontal view of ADVs is shown in the upper right corner.

Velocity is also measured using 8 ADVs located at the same position for the three configurations but at different heights for the different water depths tested. The first ADV is located offshore the patches measuring the incident velocity whereas a second one is used to measure the same height onshore the patches (lower panel in Figure 8.2). Two arrays of 3 ADVs each are disposed inside the patches at three vertical positions as shown in the lower panel of Figure 8.2 and upper right corner of Figure 8.3.The exact positions of each ADV for the different water depths are specified Table 8.2. ADVs sampling rate is 50 Hz and they are synchronized with the wave gauges. The top panel of Figure 8.2 shows the location of the ADVs (crosses) and the number of ADVs at each position whereas the lower panel shows their vertical position with a different symbol for each water depth. The ADVs positions for the three water depths are specified in Table 8.2 establishing the origin of the vertical coordinate at the free surface. The ADVs are located at Y = 0 for all cases.

Wave gauge	X (m)	Y (m)
WG1	-2	0
WG2	-1	0
WG3	-0,5	0
WG4	0,32	0
WG5	1,49	0
WG6	2,66	0
WG7	3,48	0
WG8	0,32	1,17
WG9	0,84	0,9
WG10	1,49	0,9
WG11	2,14	0,9
WG12	2,66	1,17

WG13	0,32	2
WG14	1,49	2
WG15	2,66	2
WG16	0,32	-1,17
WG17	1,49	-0,9
WG18	2,66	-1,17
WG19	0,32	3
WG20	1,49	3
WG21	2,66	3
WG22	-0,5	1,17
WG23	3,48	1,17
WG24	3,98	0
WG25	-0,5	-1,17
WG26	3,48	-1,17
WG27	0,32	-2
WG28	1,49	-2
WG29	2,66	-2

Table 8.1 Wave gauges location

ADV	X (m)	Z (m)
ADV1	-0,5	-0,10 (h = 0,30)
		-0,25 (h = 0,50)

		-0,27 (h = 0,62)
ADV2	0,32	-0,20 (h = 0,30)
		-0,25 (h = 0,50)
		-0,27 (h = 0,62)
ADV3	0,32	-0,10 (h = 0,30)
		-0,15 (h = 0,50)
		-0,17 (h = 0,62)
ADV4	0,32	-
		-0,05 (h = 0,50)
		-0,07 (h = 0,62)
ADV5	2,66	-0,20 (h = 0,30)
		-0,25 (h = 0,50)
		-0,27 (h = 0,62)
ADV6	2,66	-0,10 (h = 0,30)
		-0,15 (h = 0,50)
		-0,17 (h = 0,62)
ADV7	2,66	-
		-0,05 (h = 0,50)
		-0,07 (h = 0,62)
ADV8	3,48	-0,10 (h = 0,30)
		-0,25 (h = 0,50)

	-0,27 (h = 0,62)

Table 8.2 ADVs position

In order to analyse the influence of different wave parameters on wave attenuation, regular conditions are tested first. To extend the study to more realistic conditions random wave trains are also considered. Finally, a set of experiments is run considering solitary waves to extend the knowledge about the interaction of solitary waves with vegetation patches. Regular waves are tested covering a wave height range between 0.05 and 0.15 m and periods from 1.5 to 3.0 s. 100 waves are tested for each regular wave condition. The Reynolds number associated to each flow condition for the three different water depths is calculated as $Re = dV_c/\upsilon$ where d is the cylinders diameter, V_c the characteristic velocity defined as the maximum horizontal velocity at the top of the first cylinder of the patch and υ is the kinematic viscosity. The Re ranges from 3053 to 14136. The characteristics of the 29 regular trains tested in the experiments are specified in Table 8.3.

Test	h (m)	H (m)	T (s)	L (m)	Re
R1_1	0,3	0,05	1,5	2,34	4712
R1_2	0,3	0,05	2	3,26	4517
R1_3	0,3	0,05	2,5	4,15	4432
R1_4	0,3	0,05	3	5	4387
R2_1	0,3	0,1	1,5	2,34	9424
R2_2	0,3	0,1	2	3,26	9034
R3_1	0,3	0,15	1,5	2,34	14136
R3_2	0,3	0,15	2	3,26	13551
R4_1	0,5	0,05	1,5	2,83	3905
R4_2	0,5	0,05	2	4,06	3628
R4_3	0,5	0,05	2,5	5,24	3511

R4_4	0,5	0,05	3	6,4	3451
R5_1	0,5	0,1	1,5	2,83	7810
R5_2	0,5	0,1	2	4,06	7255
R5_3	0,5	0,1	2,5	5,24	7022
R5_4	0,5	0,1	3	6,4	6902
R6_1	0,5	0,15	1,5	2,83	11715
R6_2	0,5	0,15	2	4,06	10883
R6_3	0,5	0,15	2,5	5,24	10534
R6_4	0,5	0,15	3	6,4	10353
R7_1	0,62	0,05	1,5	2,99	3107
R7_2	0,62	0,05	2	4,36	3068
R7_3	0,62	0,05	2,5	5,67	3053
R8_1	0,62	0,1	1,5	2,99	6214
R8_2	0,62	0,1	2	4,36	6136
R8_3	0,62	0,1	2,5	5,67	6106
R9_1	0,62	0,15	1,5	2,99	9321
R9_2	0,62	0,15	2	4,36	9204
R9_3	0,62	0,15	2,5	5,67	9159

Table 8.3 Regular wave tests

Additionally, 31 random wave trains are tested. The significant wave height ranges from 0.05 to 0.15 m and the peak wave period varies from 1.5 to 3.6 s. The Reynolds number calculated considering the significant wave height and peak period to evaluate V_c, ranges from 3046 to 10883. Tests characteristics, including wave length and peak period are detailed in Table 8.4.

Test	*h (m)*	*Hs (m)*	*Tp (s)*	*Lp (m)*	*Re*
I1_1	0,3	0,05	1,5	2,34	4712
I1_2	0,3	0,05	2	3,26	4517
I1_3	0,3	0,05	2,5	4,15	4432
I1_4	0,3	0,05	3	5	4387
I2_1	0,3	0,07	2	3,26	6324
I2_2	0,3	0,07	2,5	4,15	6205
I3_1	0,3	0,1	2	3,26	9034
I3_2	0,3	0,1	2,5	4,15	8864
I4_1	0,5	0,05	2	4,06	3628
I4_2	0,5	0,05	2,5	5,24	3511
I4_3	0,5	0,05	3	6,4	3451
I5_1	0,5	0,07	2	4,06	5079
I5_2	0,5	0,07	2,5	5,24	4916
I5_3	0,5	0,07	3	6,4	4831
I5_4	0,5	0,07	3,6	7,77	4775
I6_1	0,5	0,1	2	4,06	7255
I6_2	0,5	0,1	2,5	5,24	7022
I6_3	0,5	0,1	3	6,4	6902
I6_4	0,5	0,1	3,6	7,77	6821
I7_1	0,5	0,15	2	4,06	10883

I7_2	0,5	0,15	2,5	5,24	10534
I7_3	0,5	0,15	3	6,4	10353
I8_1	0,62	0,05	2	4,36	3068
I8_2	0,62	0,05	2,5	5,67	3053
I8_3	0,62	0,05	3	6,95	3046
I9_1	0,62	0,07	2	4,362	4295
I9_2	0,62	0,07	2,5	5,67	4274
I9_3	0,62	0,07	3	6,95	4264
I10_1	0,62	0,1	2	4,36	6136
I10_2	0,62	0,1	2,5	5,67	6106
I10_3	0,62	0,1	3	6,95	6092

Table 8.4 Random wave tests

Finally, 11 solitary waves are considered with a Reynolds number ranging from 55589 to 81374. This Reynolds number is calculated as $Re_{solitary} = d * c/\upsilon$ where c is the solitary maximum wave celerity defined as $c = \sqrt{g(h+H)}$ where H is the incident wave height. The solitary wavelength is approximated following Dean and Dalrymple (1991) formulation: $L_{solitary} = 2\frac{2.12h}{\sqrt{H/h}}$. The characteristics of the tested solitary waves are displayed in Table 8.5.

Test	h (m)	H (m)	L(m)	Re
S1	0,3	0,05	3.34	55589
S2	0,3	0,075	2,68	57540
S3	0,3	0,1	2,34	59427
S4	0,5	0,05	6,78	69685
S5	0,5	0,1	3,92	72783
S6	0,5	0,15	3,61	75755
S7	0,5	0,18	9,02	77484
S8	0,62	0,05	7,31	75755
S9	0,62	0,075	6,29	77198
S10	0,62	0,1	5,16	78615
S11	0,62	0,15	4,77	81374

Table 8.5 Solitary wave tests

The 71 wave conditions specified in Table 8.3, Table 8.4 and Table 8.5 are tested for the three geometric configurations given a total of 213 tests.

8.3 Experimental results and discussion

Free surface measurements recorded by the different wave gauges used in the experiments can be used to analyze the differences found between cylinders configurations. These measurements are also used to check the experiments quality. The symmetry of the three configurations allows checking the absence of a transversal wave by comparing measurements taken at both sides of the central line. This aspect was checked during the experiments with satisfactory results.

The different wave evolution patterns developed along the three geometries can be analysed by comparing the free surface time series recorded by the gauges located at different positions.

Figure 8.4 and Figure 8.5 show these free surface time series for solitary waves S3 (H = 0.10 m and h = 0.30 m) and the three configurations. Measurements of the free surface gauges are presented for those located at the central line, Figure 8.4, and to the right of the central line in Figure 8.5.

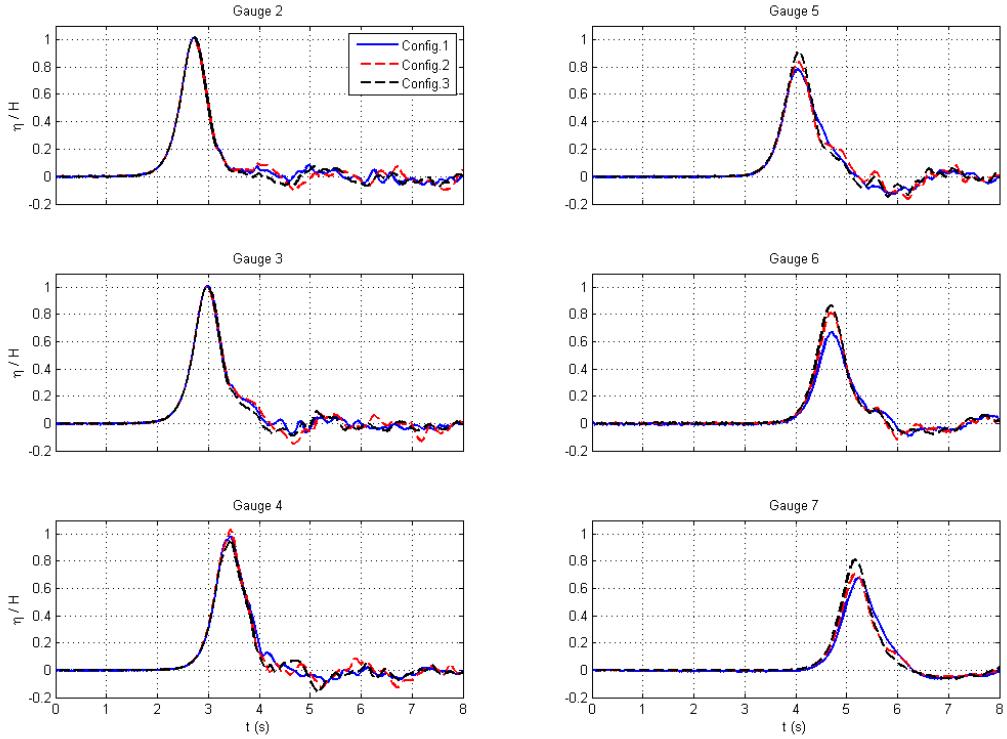

Figure 8.4 Free surface time series for solitary wave S3 and the three cylinders configurations measured at the central line of the field.

Results for Gauge 2 presented in Figure 8.4 shows the same incident wave for the three configurations but a different reflection pattern behind the wave crest. That effect is also observed in Gauge 3 where the wave reflected from the cylinders reaches the free surface gauge first. Gauge 4 is inside the cylinders field at the front of the three configurations showing almost the same result in all three. However, Gauge 5 presents higher differences. The highest wave height reduction is obtained for Configuration 1. Results for Configurations 2 and 3 reveal a smaller wave attenuation, which is in agreement with the absence of cylinders at that location for both configurations. Wave attenuation is higher for Configuration 2 than for Configuration 3 due to the higher number of patches present in the second one. Gauge 6 results follow the same trend as the ones measured by Gauge 5. The time series recorded onshore the field by Gauge 7 shows again the highest attenuation for Configuration 1. However, it can be observed that wave heights measured for Configuration 1 and 2 are very similar. In order to analyse this aspect more

in detail the free surface time series recorded by gauges located at the right of the central line are presented in Figure 8.5.

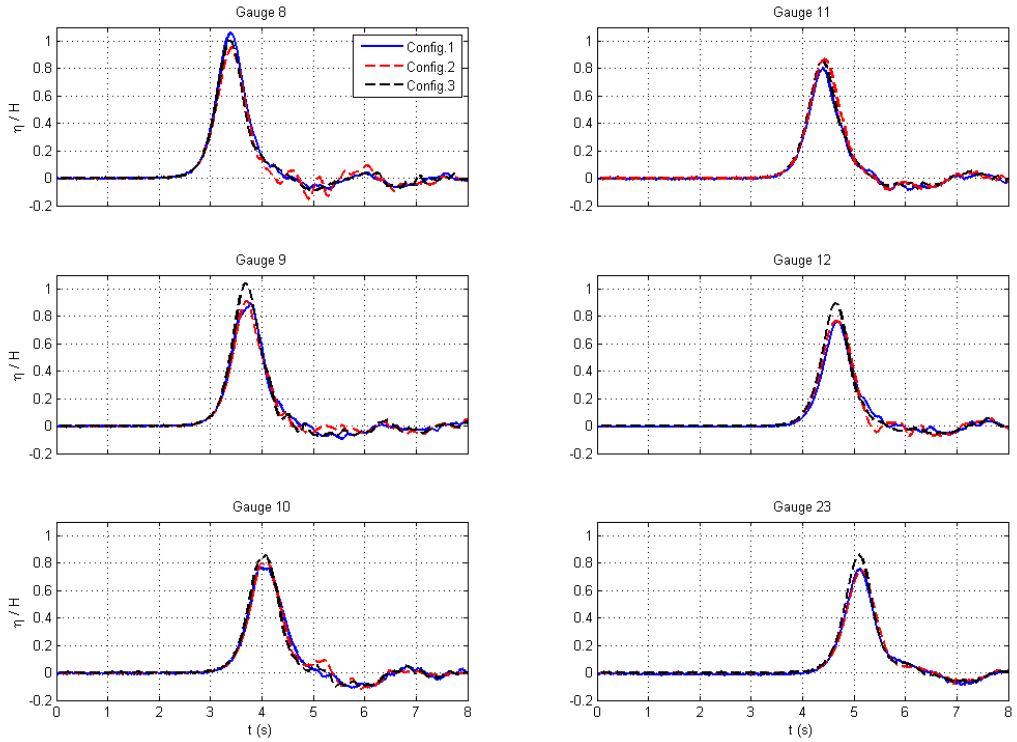

Figure 8.5 Free surface time series for solitary wave S3 and the three cylinders configurations measured to the right of the central line.

Results measured for Configuration 2 by Gauge 8 present wave attenuation and transformation produced by the cylinders patch located at that position for this configuration. Results for Gauge 9 show almost the same wave height for Configurations 1 and 2. The wave attenuation produced by the first right patch in Configuration 2 is almost the same as the one induced by the cylinders disposed offshore gauge 9 in Configuration 1. Wave height for Configuration 3 is not jet affected by the cylinders. Gauge 10 is located inside the cylinders for the three configurations, which is reflected in the clearly visible wave height attenuation. Results for Configuration 1 present the smallest wave height in Gauge 11 since the other two configurations do not have cylinders at that location. Results for Gauge 12 shows the smallest attenuation produced by Configuration 3 whereas Configurations 1 and 2 have almost the same wave height and the same is observed in Gauge 23.

The results presented in Figure 8.4 and Figure 8.5 highlight the local differences in wave evolution found between the different configurations, which are a consequence of cylinders location. These effects are interesting regarding aspects such as sediments transport or wave

exerted forces on the vegetation elements. However, those are not the aims of this paper, which is focus on the analysis of wave attenuation produced by different vegetation spatial distributions considering patches. Therefore, a higher scale analysis that considers the entire field is carried out in the present study, searching for a new parametrization that can relate the vegetation patchiness with wave attenuation.

In order to include the presence of vegetation patches in the analysis of wave attenuation produced by a cylinders field a new parametrization is needed. The presence of vegetation patches is considered by means of a spatial redistribution of the cylinders that conform each configuration and the area occupied by them in each case. This spatial redistribution will lead to an equivalent field length that varies depending on the number of patches that conforms the original field and their locations. This equivalent field length is obtained first considering a benchmark case consisting of a continuous and homogeneous field. The benchmark configuration is created by considering a unit area of 1 m2 completely covered by cylinders. These cylinders are separated a distance equal to the mean spacing between the cylinders that conform the different patches, s_0. In the present experiments, this mean spacing is 9 cm for all patches. The porosity of this benchmark field, n_0, is calculated as $1 - \frac{A_C}{A_0}$ where A_C is the area occupied by the cylinders and A_0 is the area of the field (1 m2). This porosity will be related to the porosity obtained for each configuration in order to include the amount of patches present in each case. The porosity for each configuration, n, is calculated considering the area of the square that surrounds the different patches (solid line in Figure 8.6). Then, this porosity is calculated as $1 - \frac{A_C}{A_E}$ where A_E is the area of the envelope square and A_C stands again for the area of the total number of cylinders, N_C, for each configuration. Thus, the equivalent field length, L_e, is obtained by distributing uniformly according to the base spacing the total number of cylinders for each configuration and including the cylinders distribution by means of the porosity as,

$$L_e = s_0 \sqrt{N_C} \frac{n_0}{n} \tag{1}$$

Figure 8.6 shows the equivalent square for each configuration, in dashed line, and the corresponding value of the respective equivalent field length.

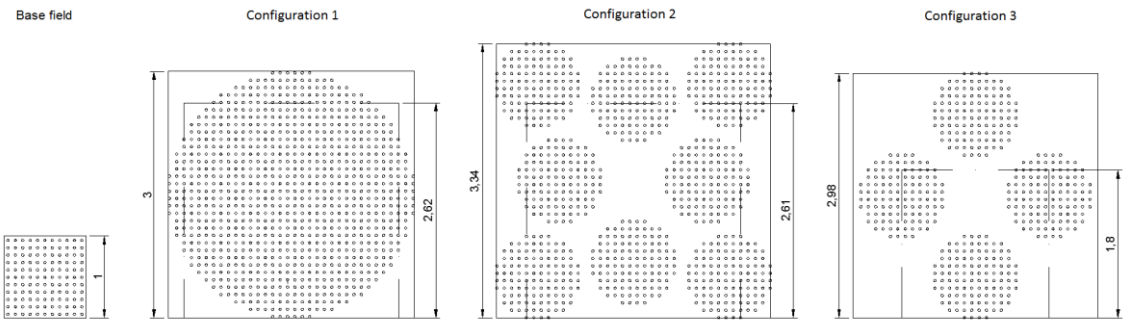

Figure 8.6 Benchmark field for the equivalent field length evaluation and the obtained equivalent field length for each configuration represented by the dashed square.

Figure 8.6 shows a similar value of the equivalent field length for configurations 1 and 2 (2.62 and 2.61 m) although the number of cylinders for both configurations is not the same and they are distributed differently. The smallest L_e is obtained for configuration 3 (1.8 m) which contains the smallest number of cylinders distributed in patches.

Different wave conditions are tested in the experiments. A different analysis is carried out attending to the wave type (regular, random and solitary waves). These analysis are described in the following subsections where the influence of wave height, wave period and water depth is analysed. The last one is studied by means of a nondimensional parameter, the submergence ratio defined as:

$$SR = \frac{h_v}{h} \tag{2}$$

where h_v is the vegetation height and h the water depth. This parameter has been widely used (e.g.: Strusinska-Correia et al., 2014; Anderson and Smith, 2014) and it is very relevant when evaluating the influence of the water depth since it represents the percentage of the water column occupied by vegetation. A submergence ratio greater than 1.0 indicates an emergent vegetation.

8.3.1 Regular wave analysis

Wave attenuation for regular waves is obtained based on the wave height damping formulation presented by Dalrymple et al. (1984). The formulation considers that energy dissipation is only due to the drag force produced by vegetation assuming linear wave theory. Wave decay is expressed as a function of an attenuation coefficient, which is taken to be constant over the depth. The wave decay is expressed as:

$$\frac{H}{H_i} = \frac{1}{1 + \beta x} \tag{3}$$

where H is the wave height and β the attenuation coefficient for regular waves. The subscript i refers to the incident wave height and x is the longitudinal distance along the meadow. This formulation has been widely used in previous studies such as Koftis et al. (2013), Ozeren et al. (2013) or Anderson et al. (2014). Wave attenuation is measured for the three configurations at the centerl line. These measurements are taken since the global attenuation produced by each configuration will be related to the parametrization described in the previous section, the effective length, that defines each configuration from a macro scale perspective including the existence of patches.

The incident wave height, H_i, is measured at free surface gauge 3, 0.5 m offshore the field and measurements of gauges 4, 5 and 6 are considered to fit the wave decay formulation as is shown in Figure 8.7. The free surface recorded at gauge 7 is not considered since that location is strongly influenced by 3D effects. After a sensitivity analysis, 40 waves are considered to evaluate the wave height at each location. The reflection coefficient is analyzed using measurements from gauges 1, 2 and 3. This coefficient is below 0.25 for all cases with most than 50% of the tests with a value below 0.15.

The influence of wave height, wave period and water depth on wave attenuation is analysed for the three configurations and the influence of patchiness is also introduced in the analysis. Velocity measurements are also compared.

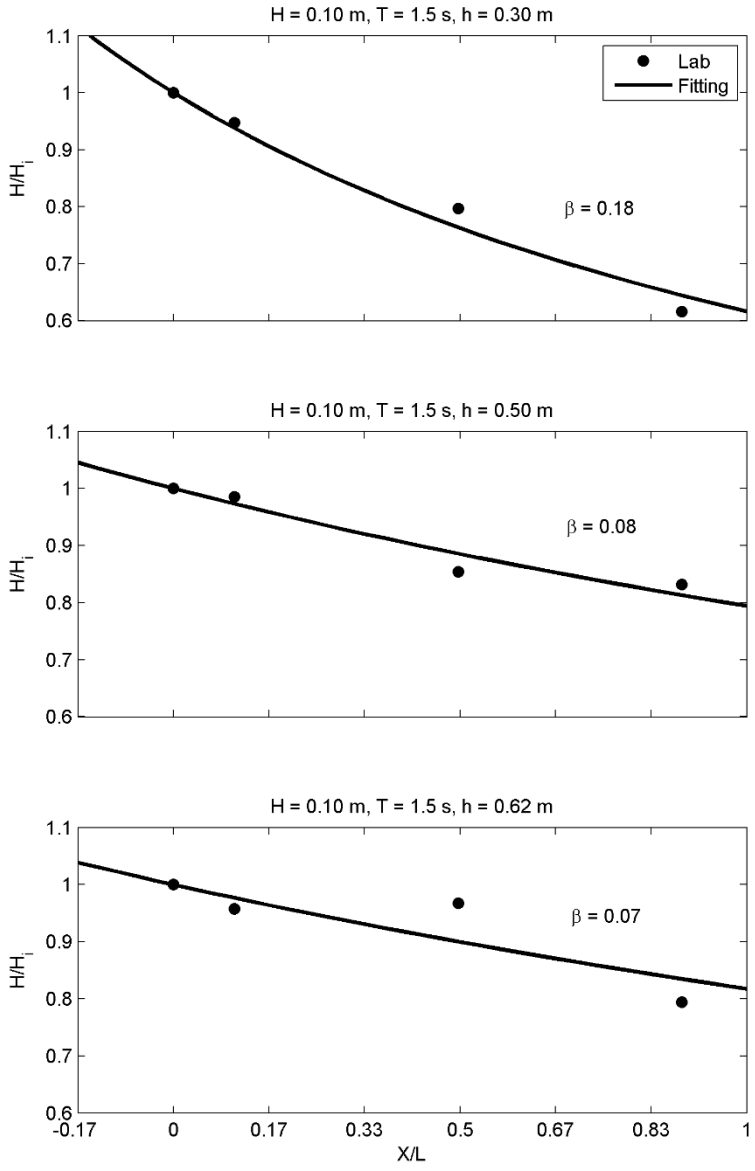

Figure 8.7 Wave decay fitting for regular waves with H = 0.10 m and T = 1.5 s and the three water depths. Damping coefficient is shown for each case.

For the three configurations and water depths, Figure 8.8 shows the wave attenuation coefficient as a function of the incident relative wave height (Hi/h) and the different wave periods.

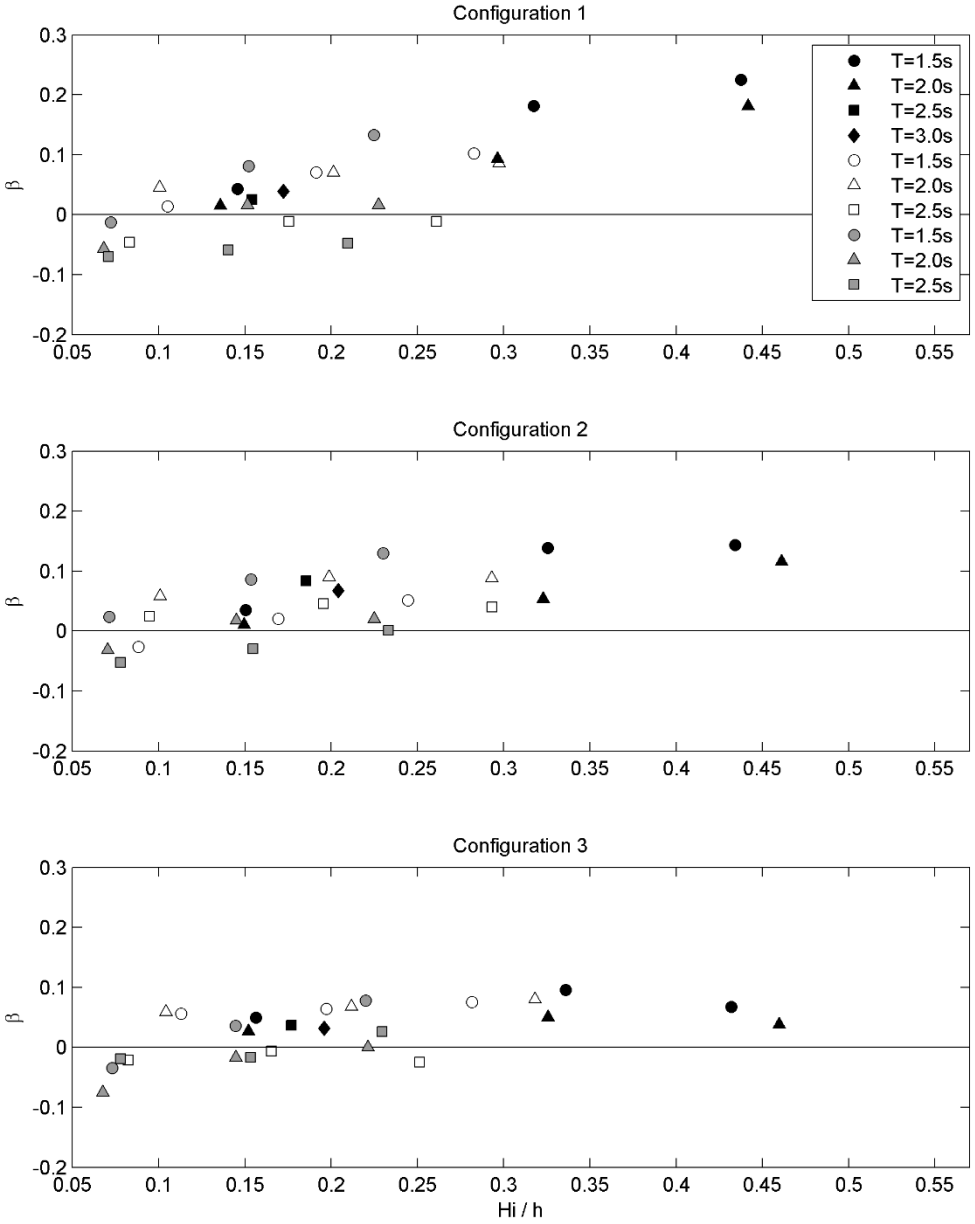

Figure 8.8 Wave attenuation as a function of relative wave height. Results for the three configurations and water depths: 0.30m (black solid symbols), 0.50m (black symbols) and 0.62m (grey solid symbols).

Relative wave height is directly related to wave attenuation. Higher wave height values result in higher wave attenuation. This is in agreement with previous studies such as Cavallaro et al. (2010) or Anderson and Smith (2014). Results for the emergent case (solid black symbols) show the highest attenuation values whereas a negative attenuation is observed for many submerged cases (grey solid symbols). Therefore, for submerged cases with a small relative wave height

there is a wave height enhancement along the field. This is because these small waves propagate over the field increasing wave height.

Wave attenuation is also influenced by wave period. The relationship between the wave attenuation coefficient and the relative wave number (kh) accounting for wave period and water depth is plotted in Figure 8.9.

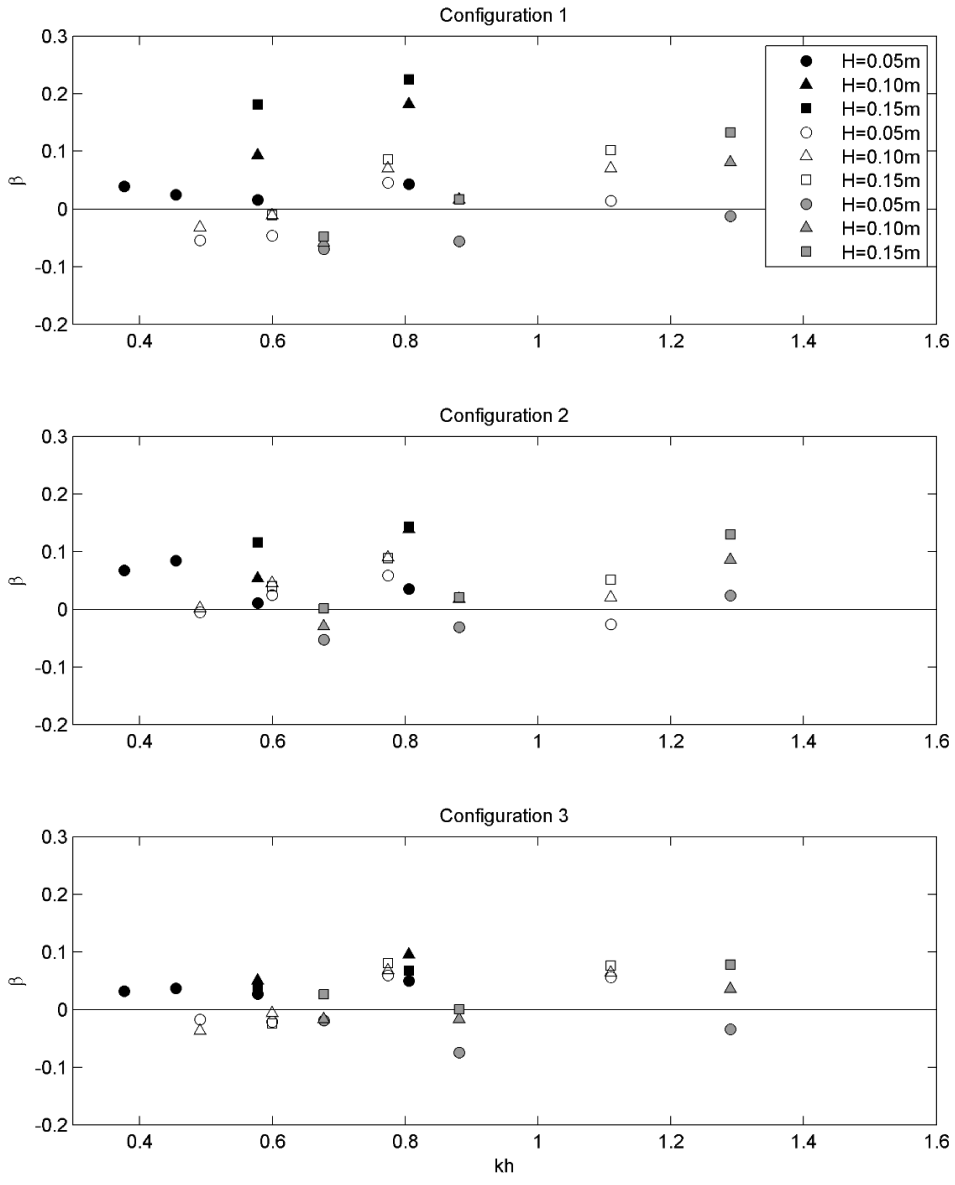

Figure 8.9 Wave attenuation as a function of the relative wave number. Results for the three configurations and water depths: 0.30m (black solid symbols), 0.50m (black symbols) and 0.62m (grey solid symbols).

A general trend for the three water depths is observed: a decrease in wave attenuation with the relative wave number is found. Therefore, higher attenuation values are obtained for shorter wave periods. This trend is also reported by Anderson and Smith (2014) and in Chapter 5. However, results for the three water depths are clearly different. Emergent cases (black solid symbols) have the smallest relative wave numbers and the highest attenuation rates. Conversely, the highest relative wave numbers are obtained for submerged cases (grey solid symbols) presenting the smallest wave attenuation. This relationship between the relative wave number and the attenuation for different water depths can be reorganized by considering also the submergence ratio which has a strong influence on wave dissipation. This parameter accounts for the column of water affected by the vegetation. Therefore, a new relative wave number can be defined when flow is affected by vegetation by multiplying kh by SR. This depth wave number ($kh * SR$) includes the percentage of water column affected by vegetation and therefore, introduces the vegetation height in the calculation. Figure 8.10 shows the attenuation results as a function of this new parameter.

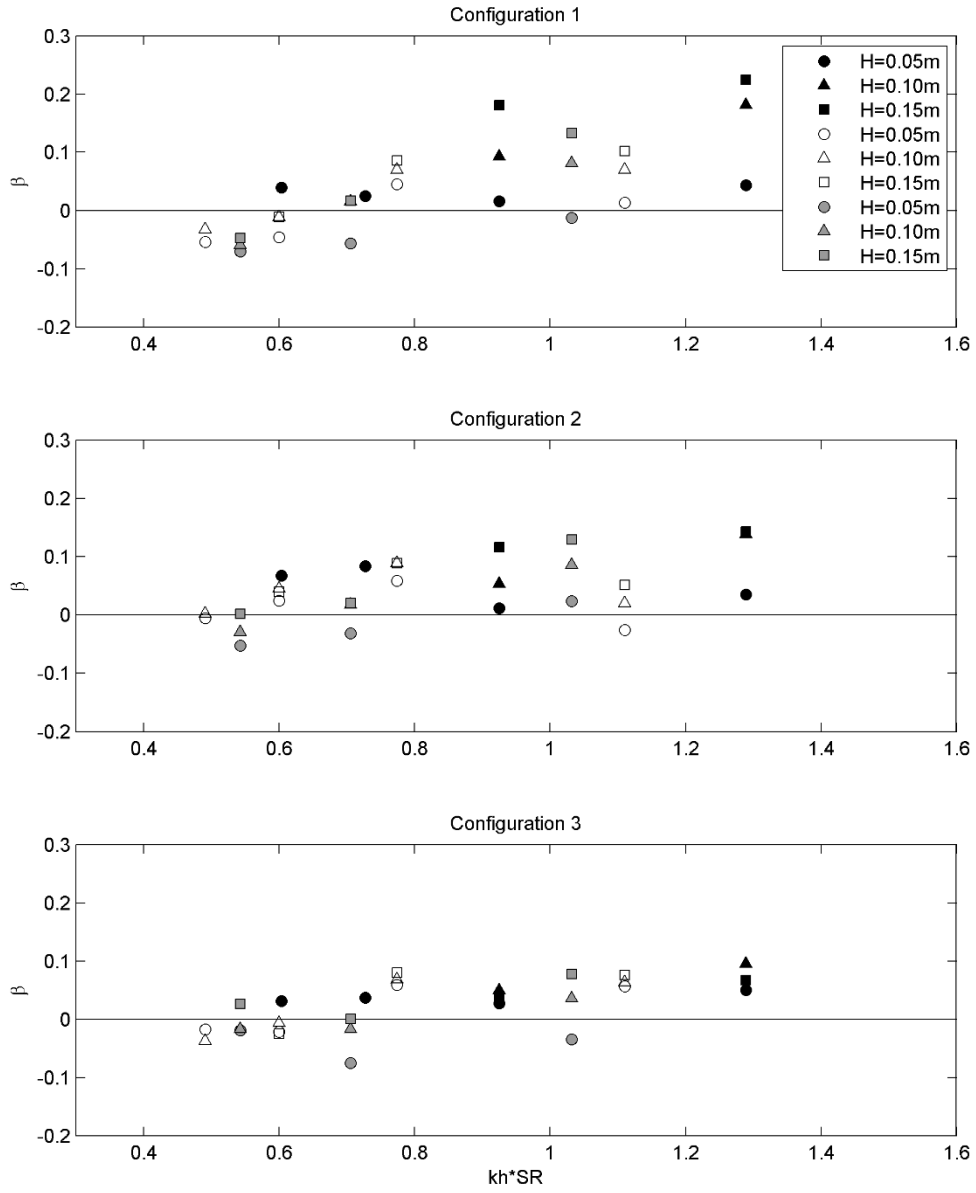

Figure 8.10 Wave attenuation as a function of the relative wave number times the submergence ratio. Results for the three configurations and water depths: 0.30m (black solid symbols), 0.50m (black symbols) and 0.62m (grey solid symbols).

Figure 8.10 shows higher attenuation values for higher $kh * SR$. The depth wave number increases according to the amount of the water column affected by vegetation. Higher depth wave numbers imply shorter waves which correspond to higher kh. Therefore, this new parameter includes both effects in the attenuation analysis.

Figure 8.8 shows different wave attenuation values for the same relative wave height and different configurations. Also, a different wave attenuation for each configuration and the same

relative wave number is displayed in Figure 8.9 and Figure 8.10, highlighting the influence of the number of cylinders and their spatial distribution on the wave attenuation induced by the field. The parameterization presented in the previous section defines the equivalente field length in order to account for these field characteristics. Therefore, this parameter is considered to define a new nondimensional number named the field wave number, kL_eSR. The kL_eSR allows relating the longitudinal and vertical characteristic lengths of the waves and the vegetation field. It firstly relates the wave length ($k = 2\pi/L$) with the equivalent field length and secondly, the field height with the water depth by the SR. The attenuation coefficients are displayed as a function of this parameter in Figure 8.11.

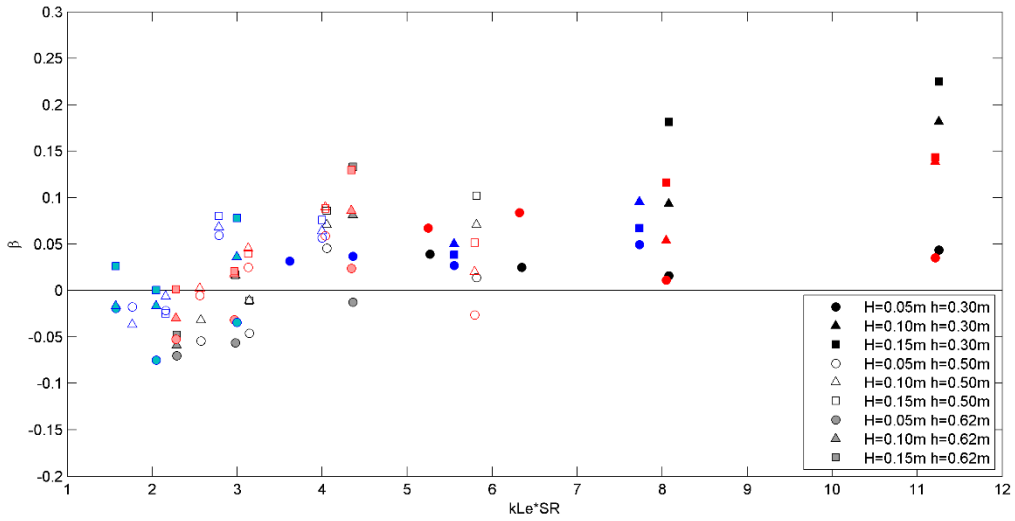

Figure 8.11 Wave attenuation as a function of the wave number times the submergence ratio and the equivalent field length for Configuration 1 (black), Configuration 2 (red) and Configuration 3 (blue). Different wave heights (symbols) and water depths (color intensity) are displayed.

Results for Configuration 3 (in blue), exhibiting a smaller attenuation capacity, are displayed for $kL_eSR < 8$ in Figure 8.11 whereas Configurations 1 and 2 are associated to higher field wave number values. Figure 8.11 shows negative damping coefficients for $kL_eSR < 3$, which reveals a wave height enhancement for these cases. As a general trend, Figure 8.11 shows higher damping rates for larger kL_eSR values. Large kL_eSR values are associated to long and high fields with respect to the wave length and water depth, respectively. Therefore, longer and higher fields with respect to flow characteristics induced larger attenuation rates.

Many studies relate wave attenuation with nondimensional numbers such as Keulegan-Carpenter ($KC = U_c T/d$) and Reynolds (Re) numbers. The relationship between the damping coefficients obtained for all regular cases and these two numbers is displayed in Figure 8.12.

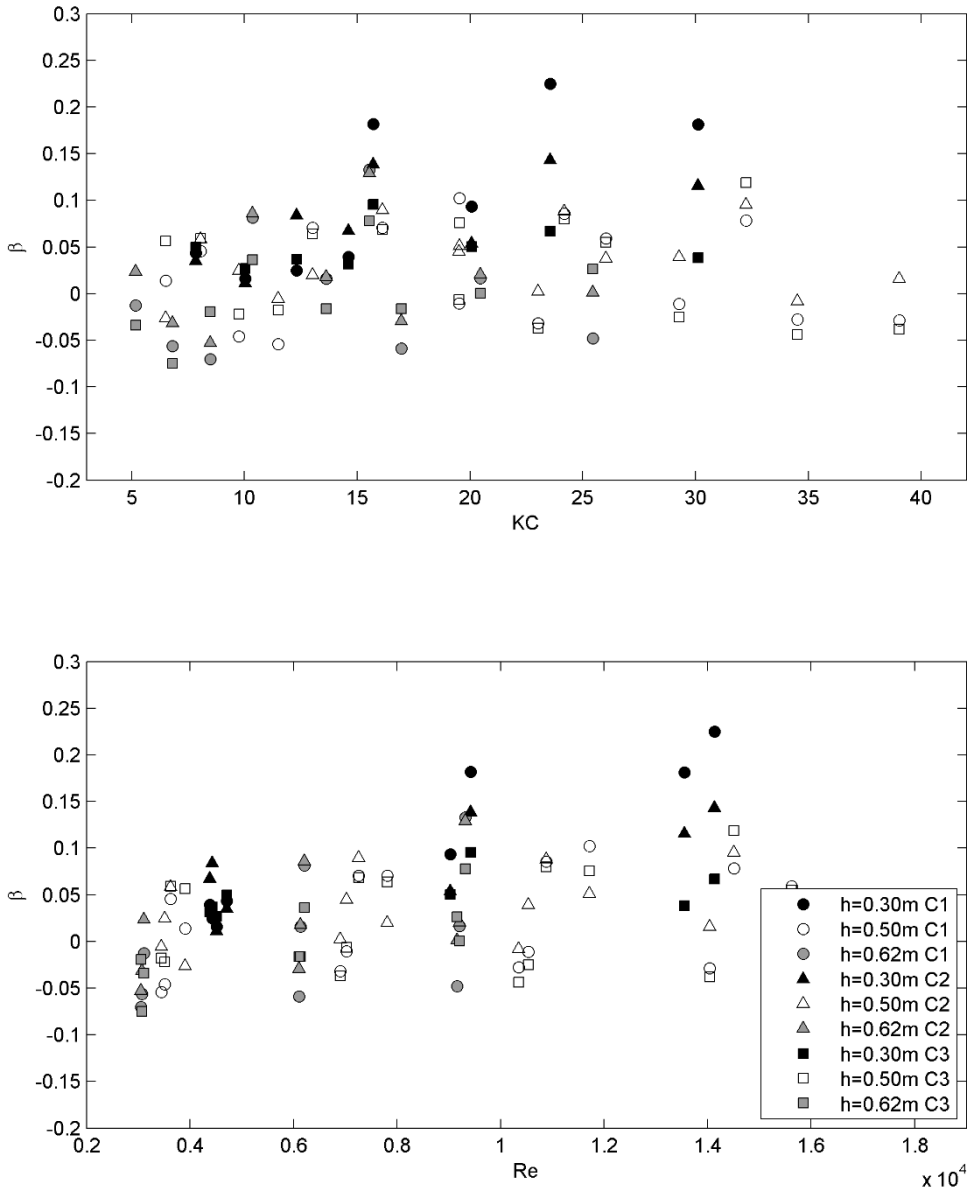

Figure 8.12 Wave attenuation as a function of the Keulegan-Carpenter number (top panel) and the Reynolds number (lower panel).

The KC describes the relative importance of the drag forces over the inertia forces. For KC values smaller than 10, inertia forces progressively dominate. For this range, the upper panel of Figure 8.12 shows a high number of cases characterized by negative damping coefficient. From this

value up to KC=20 both inertia and drag force components are significant and for KC > 20, the drag force progressively dominates. Considering positive damping coefficient values, since damping formulation is set for cases in which wave attenuation is significant, and the KC range in which drag force component is significant, the general trend shows a higher attenuation for higher KC. This is in agreement with previous studies such as Jadhav et al. (2013).

The Re number is defined as the ratio of the inertia to the viscous forces. The lower panel of Figure 8.12 shows a higher attenuation for higher Re. This is related to the wave height and submergence ratio since higher H and SR involve higher V_c and therefore higher Re. A high dispersion of the data is observed. Different attenuation values are found for the same Re number according to the submergence ratio and the configuration with higher values, corresponding Configuration 1 and $SR = 1$. A new Reynolds number can be defined considering a characteristic length scale that accounts for the field properties. This length scale can be defined as the effective area affecting the flow per longitudinal length ($L^* = Le\frac{h_v}{h} = LeSR$). Then, the new Reynolds number, named field Reynolds number is defined as:

$$Re_s^{Le} = \frac{L^* V_c}{\upsilon} \tag{4}$$

Figure 8.13 shows the damping coefficient values as a function of this new nondimensional field number.

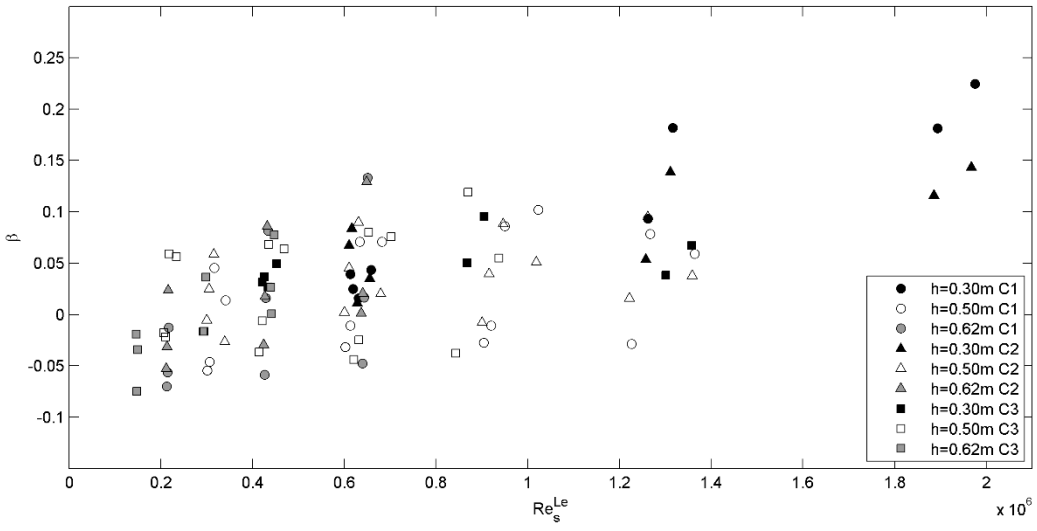

Figure 8.13 Attenuation coefficients for all regular wave tests as a function of the field Reynolds number.

Data presented in Figure 8.13 is less scattered compared to that in Figure 8.12. Damping coefficients are reorganized according to their submergence conditions with larger Re_s^{Le} values for emergent cases and according to their equivalent field length with again larger Re_s^{Le} values for longer fields.

Velocity measurements are also analysed. 6 ADVs are used for tests run with h = 0.30 m and two additional devices are installed for h = 0.50 and 0.62 m. The location of each ADV is displayed in Figure 8.2 and Table 8.2. Figure 8.14 shows the maximum horizontal velocity recorded in the flow propagation direction (X-direction) by each ADV for the three configurations and water depths for H = 0.10 m and T = 2 s. These values are obtained as the mean of the maximum X-velocity amplitude recorded for 40 waves.

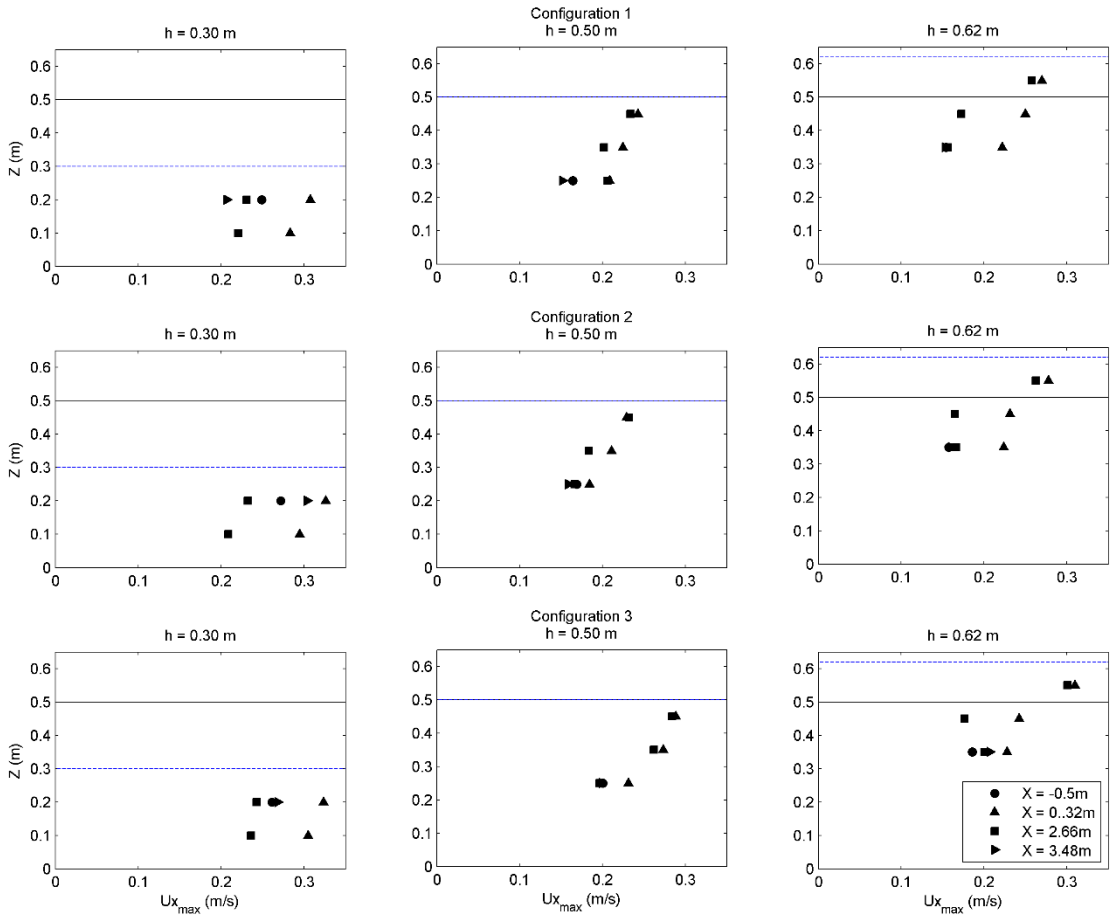

Figure 8.14 Maximum velocity recorded by the ADVs for the three configurations and water depths (blue dashed line) for H = 0.10 m and T = 2 s. Black solid line represents the cylinders height.

Velocities recorded for h = 0.30 m show an increase at the beginning of the field (X = 0.32 m) and a decrease in the velocity values along it (X = 2.66 m) with respect to the incident conditions (X = -0.5 m). The velocity measured onshore the meadow (X = 3.48 m) is smaller than the one recorded at the most offshore location (X = -0.50 m) for configuration 1. However, for configurations 2 and 3 the onshore velocity is almost equal or even larger than the offshore one. This is due to the three dimensional flow patterns produced around the individual patches that lead to this velocity enhancement at the end of the field. A higher reduction in the maximum velocity amplitude is recorded for Configurations 1 and 2 in comparison to Configuration 3 inside the field. This is in agreement with the obtained wave height attenuation values. Measurements for h = 0.50 m reveal a small attenuation especially close to the surface since the still water level is equal to the cylinders height. At Z=0.45 m measurement at the beginning and at the end of the field are almost equal whereas at lower Z values there is a stronger decrease of the velocity. Results for the submerged case (h = 0.62 m) show the skimming flow developed over the cylinders. There is a velocity increase above the field due to the strong developed shear layer. Velocity measurements inside the cylinders show an increment in the velocity at the beginning of the field which is reduced onshore.

8.3.2 Spectral analysis

Wave attenuation analysis for random waves is performed in terms of wave energy. Assuming linear wave theory, the evolution of random waves propagating through a vegetation field can be expressed in terms of the energy balance as (Jadhav et al., 2013):

$$\frac{\Delta\left(E_{S,j}C_{g,j}\right)}{\Delta X} = -S_{d,j} \tag{5}$$

where subscript j represents the jth frequency component of the wave spectrum, E is the spectral wave energy density, C_g is the group velocity calculated as $C_g = nc = (1/2)[1 + (2kh/sinh2kh)]\sqrt{(g/k)tanh(kh)}$, X is the cross-shore coordinate and S_d is the energy dissipation due to vegetation. The total energy dissipation is obtained by integrating the energy dissipation for each frequency along the spectrum frequency range. The incident spectrum energy density is obtained from the spectrum zero order moment, $m0$, for wave gauge 3.

In order to calculate the energy dissipation associated to each frequency component a set of frequency bands have been considered. Each frequency band has a width equal to $f_p/4$ where f_p is the peak frequency. The group velocity for the central frequency of each frequency band is obtained to calculate the energy dissipation. Figure 8.15 shows an example of this analysis for a target H_s=0.10 m and T_p=2s and the three water depths and configurations. The incident (gauge

3), transmitted (gauge 6) and dissipated root mean square wave height, H_{rms}, associated to each energy band is represented in the figure.

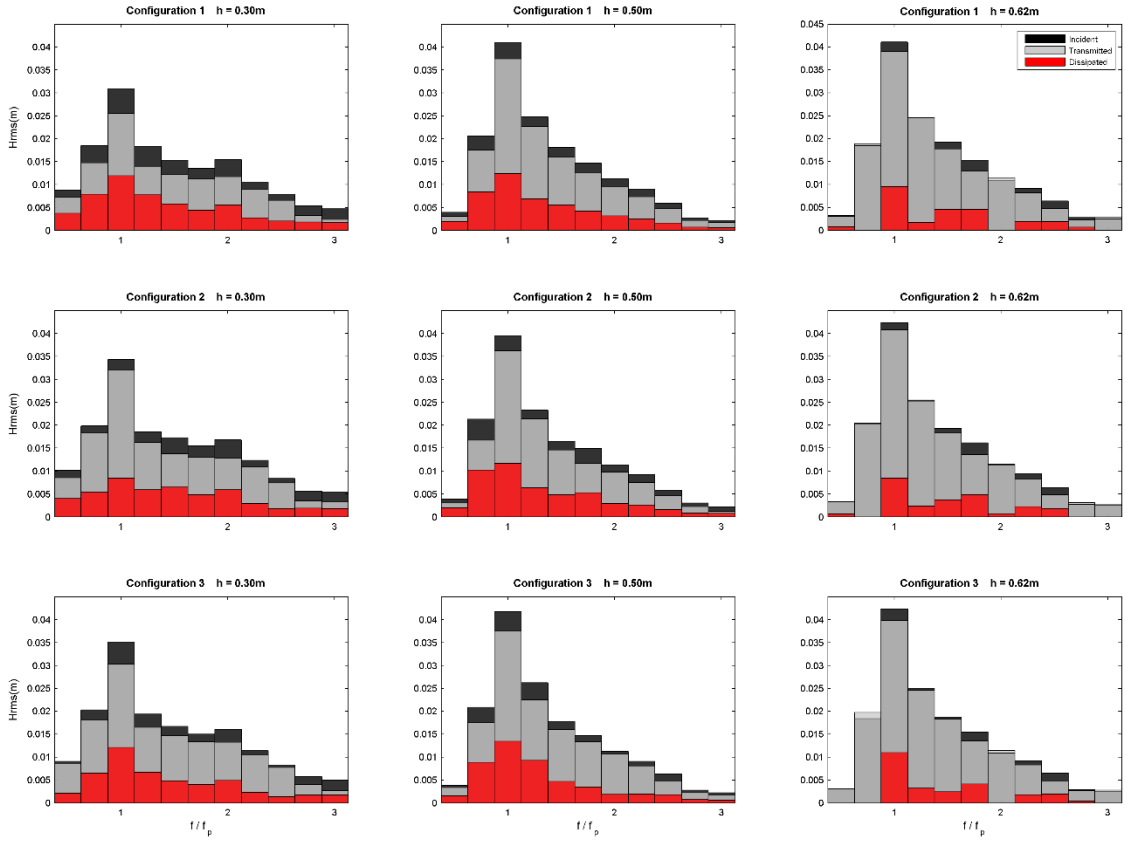

Figure 8.15 Energy spectrum (Hs = 0.10 m, Tp = 2 s) for the three configurations and water depths. Root mean square wave height associated to each frequency band is displayed.

The highest dissipation for the three configurations and the three water depths takes plottedy domain as has been expostitute of Technology.id cylinders.ue es uniforme es el flujo o la distribuciof waves and currenplace in the peak frequency band in agreement with previous studies (e.g.: Koftis et al., 2013; Jadhav et al., 2013). For emergent cases (h = 0.30 m) a second peak in the dissipation bands is observed at $2f_p$. Therefore, for the emergent cases the highest dissipation takes place around the peak frequency and the first superharmonic. The near emergent cases (h = 0.50 m) show again a higher dissipation for bands with higher energy density. However, submerged cases (h = 0.62 m) exhibit the highest dissipation in the peak frequency band. However, there is not dissipation in the $2f_p$ band and the second dissipation peak is observed around $1.5 - 1.75f_p$. Dissipation for these cases is small due to the low attenuation produced by the submerged field. Wave energy is not only dissipated by vegetation

but also redistributed in the frequency domain as has been explained by previous authors for low-crested structures (Garcia et al., 2004) or permeable structures (Lara et al., 2006).

In order to analyse the influence of the wave height, the relation between the relative energy dissipation ($S_d/m0$) and the incident relative root mean square wave height ($H_{i,rms}/h$) is plottedin Figure 8.16.

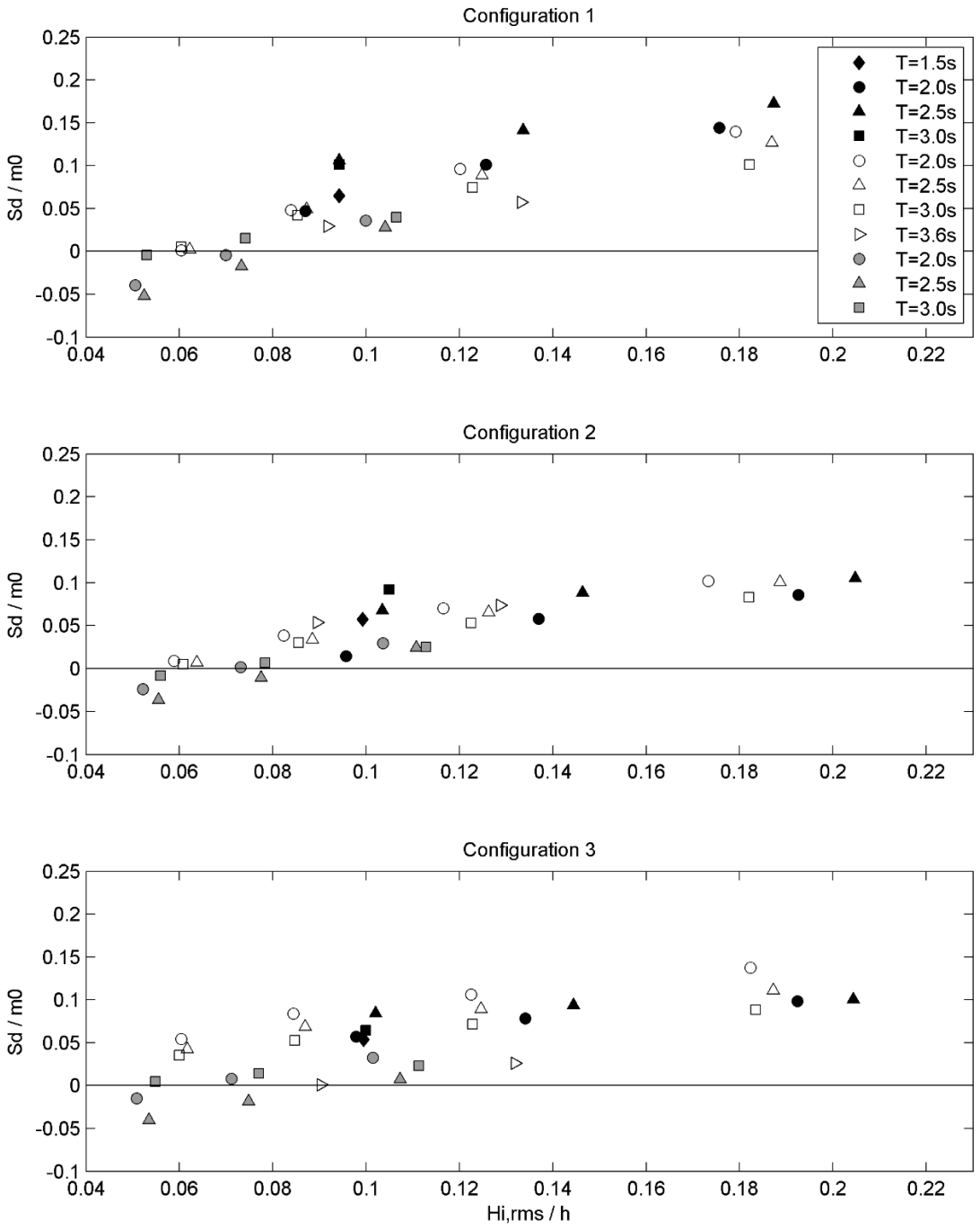

Figure 8.16 Relative energy dissipation as a function of relative root mean square wave height. Results for the three configurations and water depths: 0.30m (black solid symbols), 0.50m (black symbols) and 0.62m (gray solid symbols).

There is a direct relationship between the relative energy dissipation and the relative root mean square wave height for the three configurations (Figure 8.16). The highest dissipation values are

obtained for the smallest water depth and there is a wave enhancement along the field (negative dissipation values) for the submerged case with small relative wave heights. As has been shown in the regular waves analysis, wave attenuation is related to the depth wave number $k_p hSR$ calculated, in this case, considering the peak period. This relationship is shown in Figure 8.17.

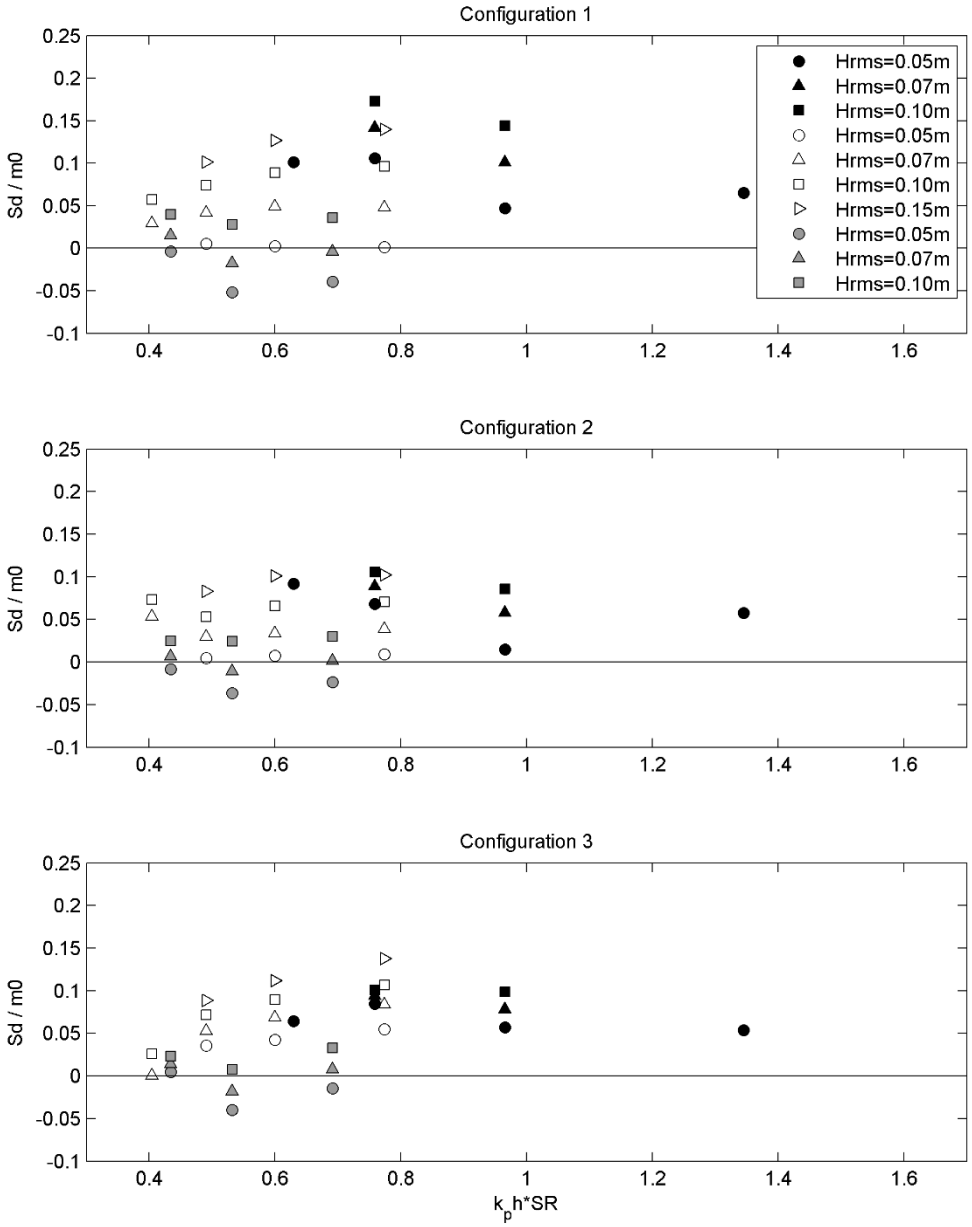

Figure 8.17 Relative energy dissipation as a function of relative peak wave number times the submergence ratio. Results for the three configurations and water depths: 0.30m (black solid symbols), 0.50m (black symbols) and 0.62m (grey solid symbols).

As a general trend Figure 8.17 shows a higher dissipation for higher $k_p hSR$ values. However, the data scatter is high according to the root mean square wave height, suggesting that dissipation is more strongly related to wave height than to wave number and therefore, wave period. Results for the three water depths are clearly different. Results for h = 0.30 m show a higher dissipation for longer wave periods. This is not in agreement with the trend observed for the other two water depths. For h = 0.50 and 0.62 m wave dissipation increases for shorter wave periods, as was observed for regular waves. Wave energy spectrum for h = 0.30 m reveal a wider energy distribution along the different frequencies (e.g.: Figure 8.15). The first superharmonic displayed in Figure 8.15 is produced for long waves (peak wave period higher than 2) and h = 0.30. This is shown in Figure 8.18 where the nondimensional energy spectra (S / Sp where Sp is the energy associated to the peak period) for two long waves (Hs = 0.10 m and Tp = 2 s and 2.5 s) are displayed for h = 0.30 m, 0.50 m and 0.62 m. Spectrum for h = 0.30 m shows a second energy concentration around $2f_p$ which is higher for longer wave periods. This is not observed for higher water depths (h = 0.50 m and 0.62 m). The energy associated to this second peak is strongly attenuated (as shown in Figure 8.15) and the resultant total dissipation is higher than for shorter waves.

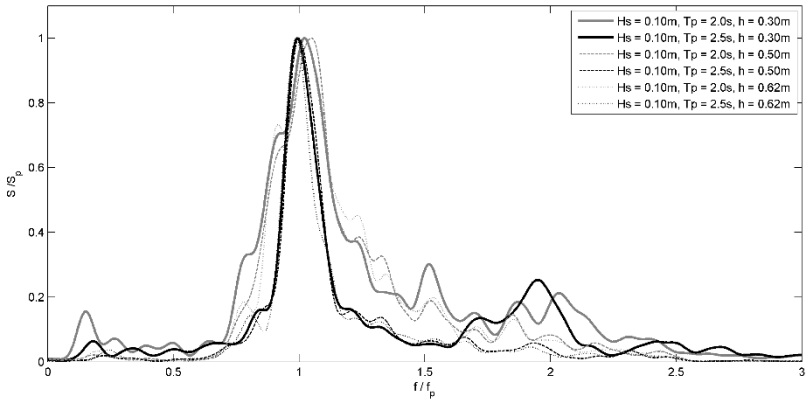

Figure 8.18 Wave energy spectrum for two wave conditions and two water depths.

The damping coefficient results for all random tests and the three configurations are displayed together in Figure 8.19 considering the field wave number.

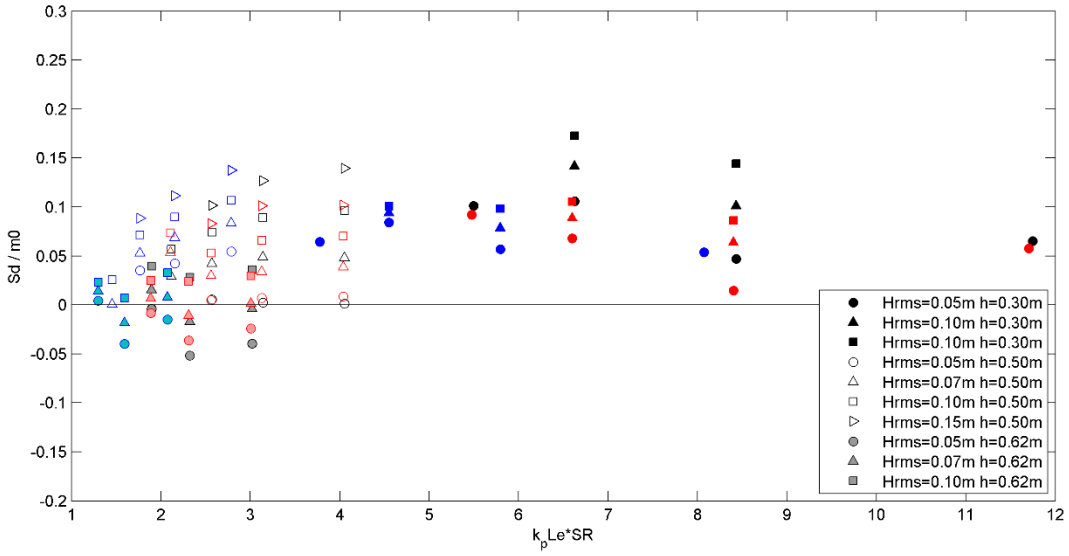

Figure 8.19 Relative energy dissipation as a function of the peak wave number times the submergence ratio and the equivalent field length for Configuration 1 (black), Configuration 2 (red) and Configuration 3 (blue). Different wave heights (symbols) and water depths (color intensity) are displayed.

Two clusters of data can be observed in Figure 8.19 regarding the water depth as has been discussed in Figure 8.17 and Figure 8.18. Lower dissipation obtained for Configuration 3 is related to lower $k_p Le * SR$ values, that is, for shorter waves and a submerged field as was observed for regular waves (Figure 8.11).

The relative dissipation obtained for all random wave cases is displayed as a function of the KC and the Re in Figure 8.20. Higher values of the KC number and the Re number results in a higher relative dissipation.

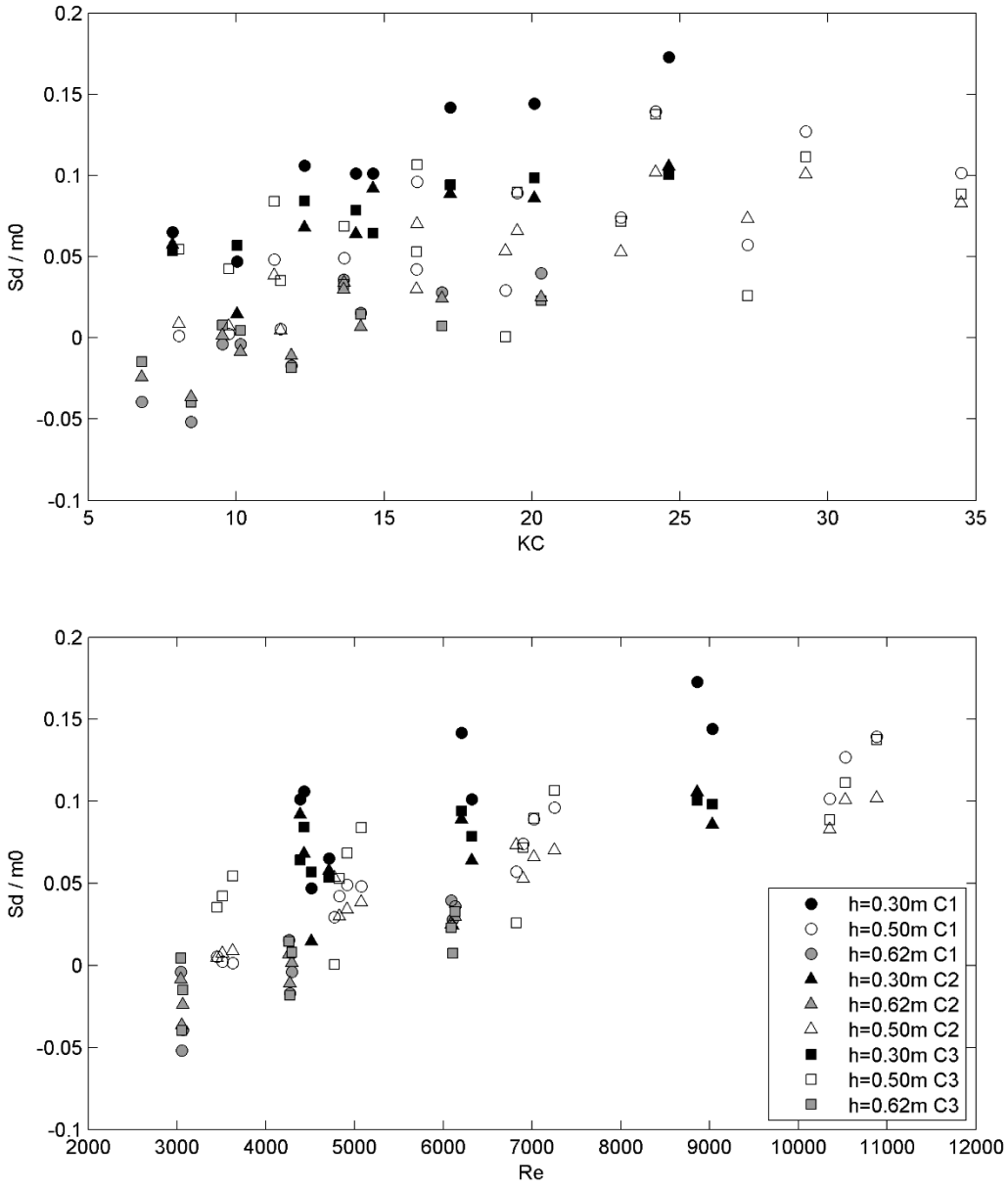

Figure 8.20 Relative energy dissipation as a function of the Keulegan-Carpenter number (top panel) and the Reynolds number (lower panel).

The relation of wave dissipation with these two nondimensional numbers follow the same trend for the three water depths, although three clusters can be differentiated attending to this parameter. Furthermore, for similar values of KC and Re results for the three configurations are distinguished.

Again the new Reynolds number defined in the regular wave section (Re_s^{Le}) is used to represent the relative dissipation rates obtained for random waves. The relationship between $Sd/m0$ and Re_s^{Le} is displayed in Figure 8.21.

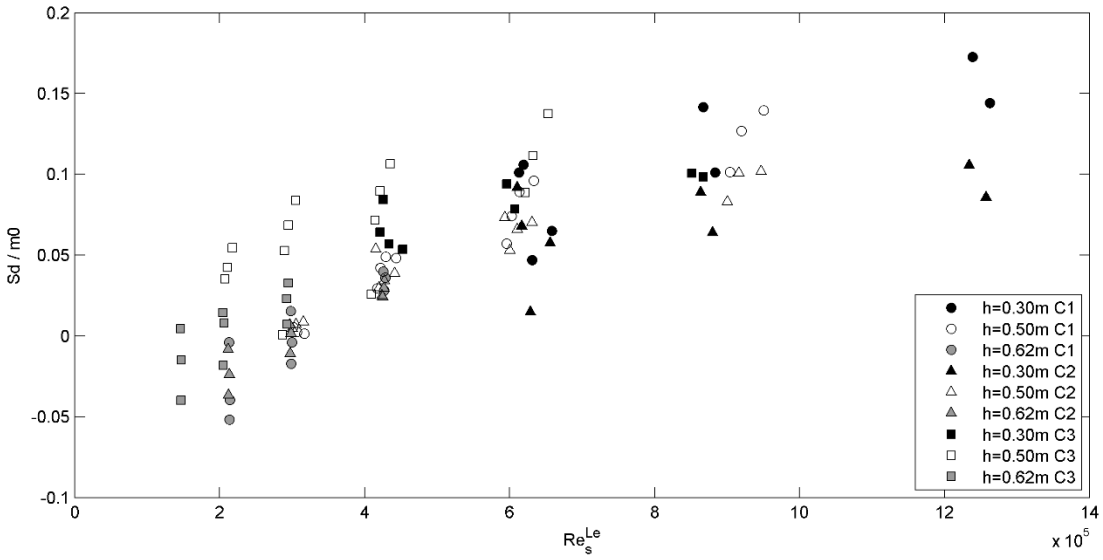

Figure 8.21 Attenuation coefficients for all random wave trains as a function of the field Reynolds number.

Figure 8.21 shows a direct relationship between the relative dissipation values and the field Reynolds number. Dissipation results are reorganized presenting the highest Re_s^{Le} those cases with high submergence values and long cylinders fields. Dissipation data is less scattered when it is related to Re_s^{Le} than when Re is used.

8.3.3 Solitary waves

Solitary wave analysis is performed by analysing the maximum wave height at each location. Again the relationship between wave attenuation and the wave parameters is analysed. Wave attenuation is represented in Figure 8.22 as a function of the maximum incident relative wave height for the three configurations.

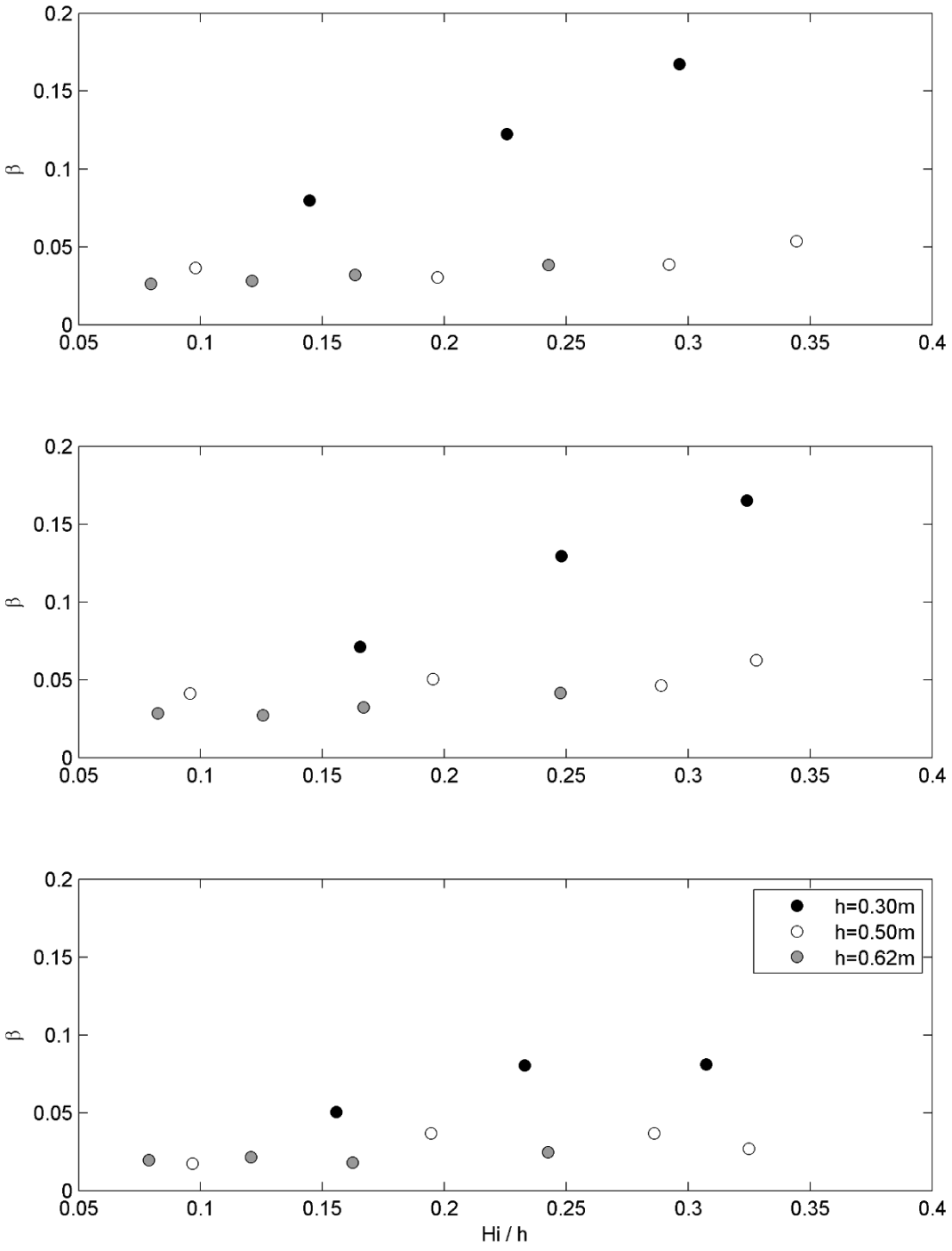

Figure 8.22 Wave attenuation as a function of relative wave height. Results for the three configurations and water depths: 0.30m (black solid symbols), 0.50m (black symbols) and 0.62m (gray solid symbols).

Wave attenuation increases with wave height and the influence of the submergence ratio is very important for these waves. Thus, emergent (h = 0.30 m) cases produce a much higher dissipation than the near emergent (h = 0.50 m) and the submerge cases (h = 0.62 m) as is shown in Figure 8.22. The difference between the three water depths increases with higher attenuation rates (Configurations 1 and 2). Therefore, both the submergence ratio and the field characteristics strongly influence wave attenuation. The influence of these two variables is analysed in Figure 8.23 by displaying the damping coefficients as a function of the field wave number, $kLe * SR$. The wave number, k, is obtained considering the solitary wave length values presented in Table 8.5, obtained following Dean and Dalrymple (1991).

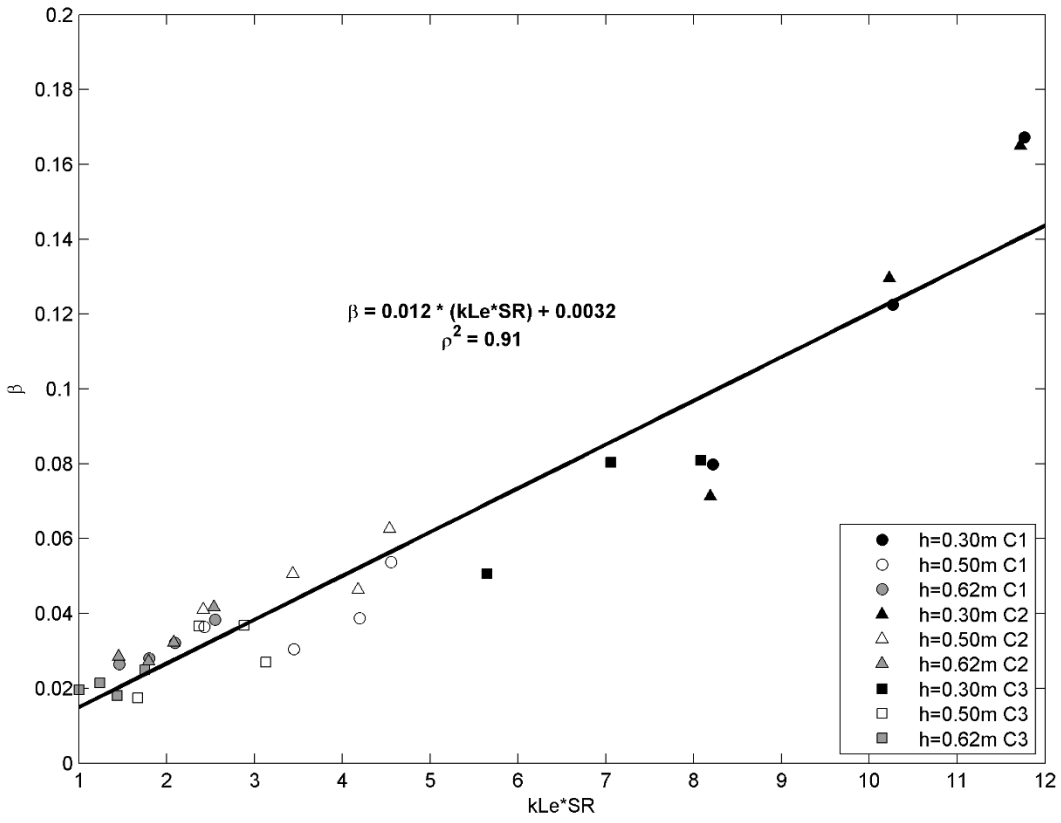

Figure 8.23 Wave attenuation as a function of the wave number times the submergence ratio and the equivalent field length for Configuration 1 (circles), Configuration 2 (triangles) and Configuration 3 (squares). Different water depths (color intensity) are displayed.

Figure 8.23 shows a linear relationship between wave attenuation and the field wave number. This relationship highlights the influence of these parameters on solitary waves attenuation revealing a higher attenuation for emergent (high SR) and long (high Le) fields.

Finally, the relationship between wave attenuation and Re is evaluated. This nondimensional number is obtained by considering the maximum solitary wave celerity as the characteristic velocity. This implies smaller Re numbers for smaller water depths although wave attenuation is higher for those cases. This can be observed in the top panel of Figure 8.24. Results for the same water depth displayed in the same figure show higher attenuation for higher Re. This is due to the wave height; a higher attenuation has been obtained for higher wave heights which correspond to higher Re. Therefore, it seems that for each water depth results follow a trend that opposes the general one. Dissipation coefficients are also displayed in the lower planel of Figure 8.24 as a function of the Re_S^{Le}, which includes the effect of the submergence and the cylinders distribution.

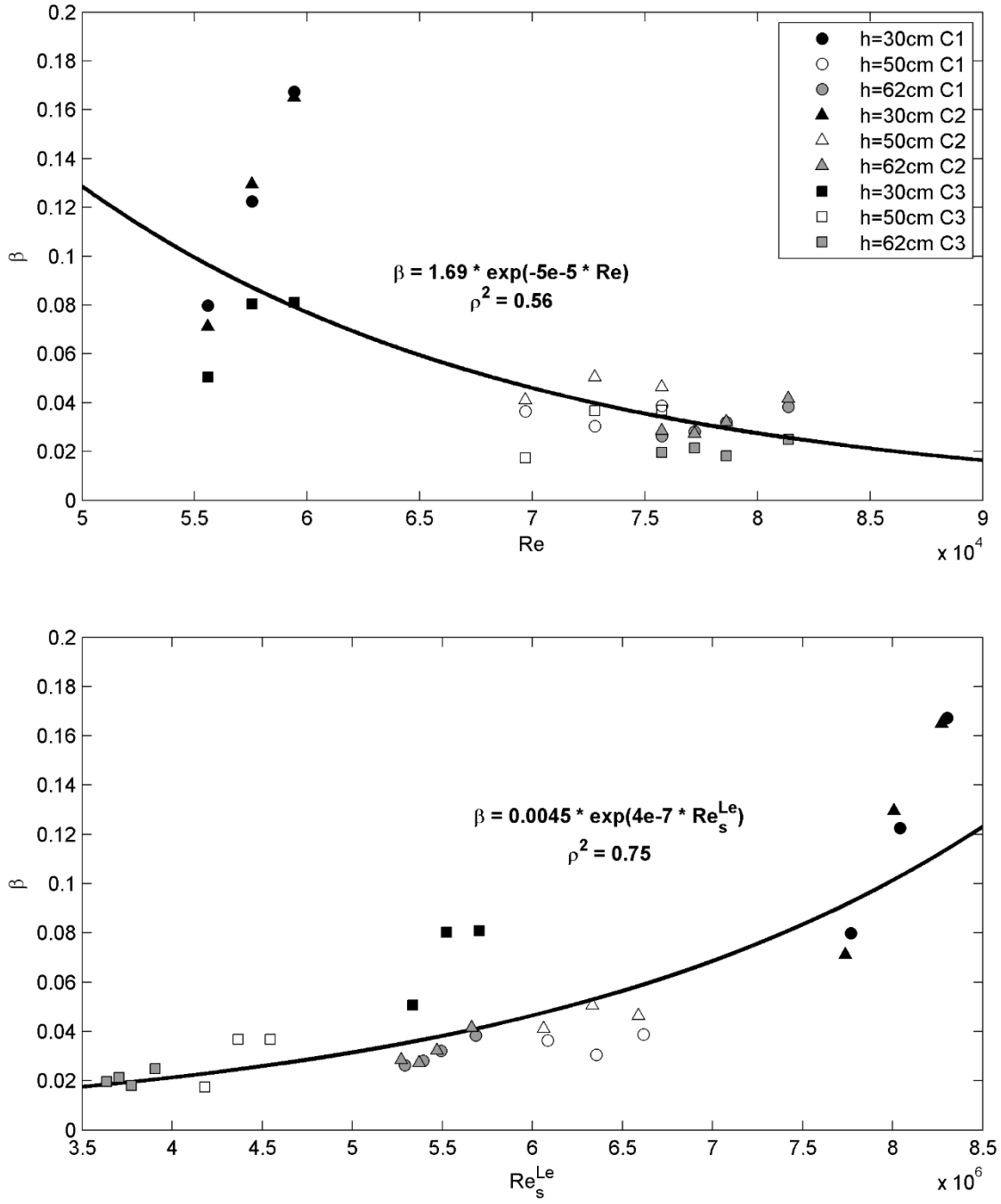

Figure 8.24 Wave attenuation as a function of Re (top panel) and Re_s^{Le} (lower panel).

The correlation coefficient found for the fitting obtained considering Re_s^{Le} is higher than the one obtained for Re (Figure 8.24). Furthermore, results as a function of Re_s^{Le} are well organized and increase constantly with it. Therefore, this new definition of the Reynolds number is better correlated to damping rates.

8.4 Numerical analysis

The experimental analysis has allowed the study different variables in the wave interaction with vegetation patches. In order to extend the knowledge about the flow - cylinders interaction, a set of numerical simulations are performed. These numerical tests provide detailed information with a high spatial resolution and allow analyzing variables not measured during the experiments.

The numerical model selected to perform the simulations is IHFOAM, presented in Chapter 7. The geometry of the three field configurations presented in Figure 8.2 is introduced in the model in order to reproduce the same experimental set-up. Three simulations are carried out considering the same solitary wave and the three geometric configurations. Tests run with a solitary wave of wave height (H) equal to 0.10 m over a water depth (h) of 0.30 m for the three configurations are selected. These cases are specified in Table 8.6.

Case	h (m)	H (m)	Configuration
Conf1_h30	0.30	0.10	1
Conf2_h30	0.30	0.10	2
Conf3_h30	0.30	0.10	3

Table 8.6 Experimental tests selected to perform the numerical simulations.

8.4.1 Mesh sensitivity analysis

A mesh sensitivity analysis is carried out in order to select the appropriate mesh discretization to run the simulations. Configuration 3 is selected to perform this analysis since it is the one with the smallest number of cylinders. Six mesh discretizations are tested (Figure 8.25). Their characteristics are specified in Table 8.7. Simulations are performed in a HPC machine (2.6 GHz).

Name	Δx and Δy range (m)	Δz range (m)	Points/ perimeter	Number of cells	Computational time (h)	Processors	Time (h) / processor
Mesh 1	0.014 – 0.0035	0.007 – 0.00175	26	15.474.001	34.2	128	0.27
Mesh 2	0.02 – 0.0067	0.01 – 0.0033	36	25.705.094	42.5	256	0.17
Mesh 3	0.016 – 0.0053	0.008 – 0.0027	44	43.644.988	84	256	0.33
Mesh 4	0.015 – 0.005	0.008 – 0.0027	48	26.522.430	66	256	0.26
Mesh 5	0.015 – 0.005	0.009 – 0.003	50	51.406.982	110	256	0.43
Mesh 6	0.012 – 0.0015	0.006 – 0.002	60	44.879.408	98	256	0.38

Table 8.7 Meshes used in the mesh discretization sensitivity analysis

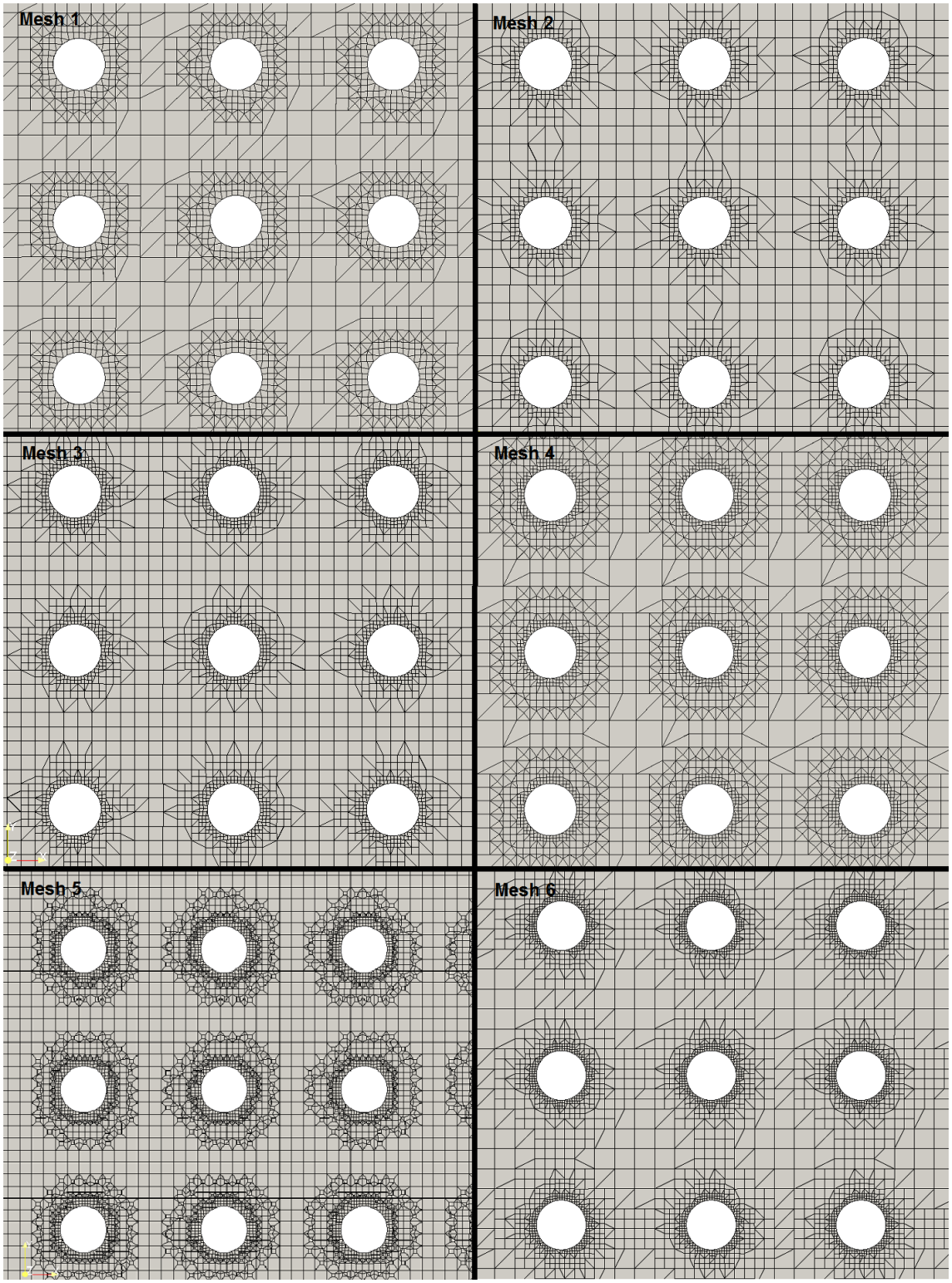

Figure 8.25 Meshes specified in Table 8.7 used to perform the mesh sensitivity analysis.

In order to compare the six meshes presented in Table 8.7 and Figure 8.25, wave height evolution along the field is compared for gauges located at Y = 0, 0.9, 1.17 and 2 m (Figure 8.2). Results for the different meshes and laboratory data are displayed in Figure 8.26.

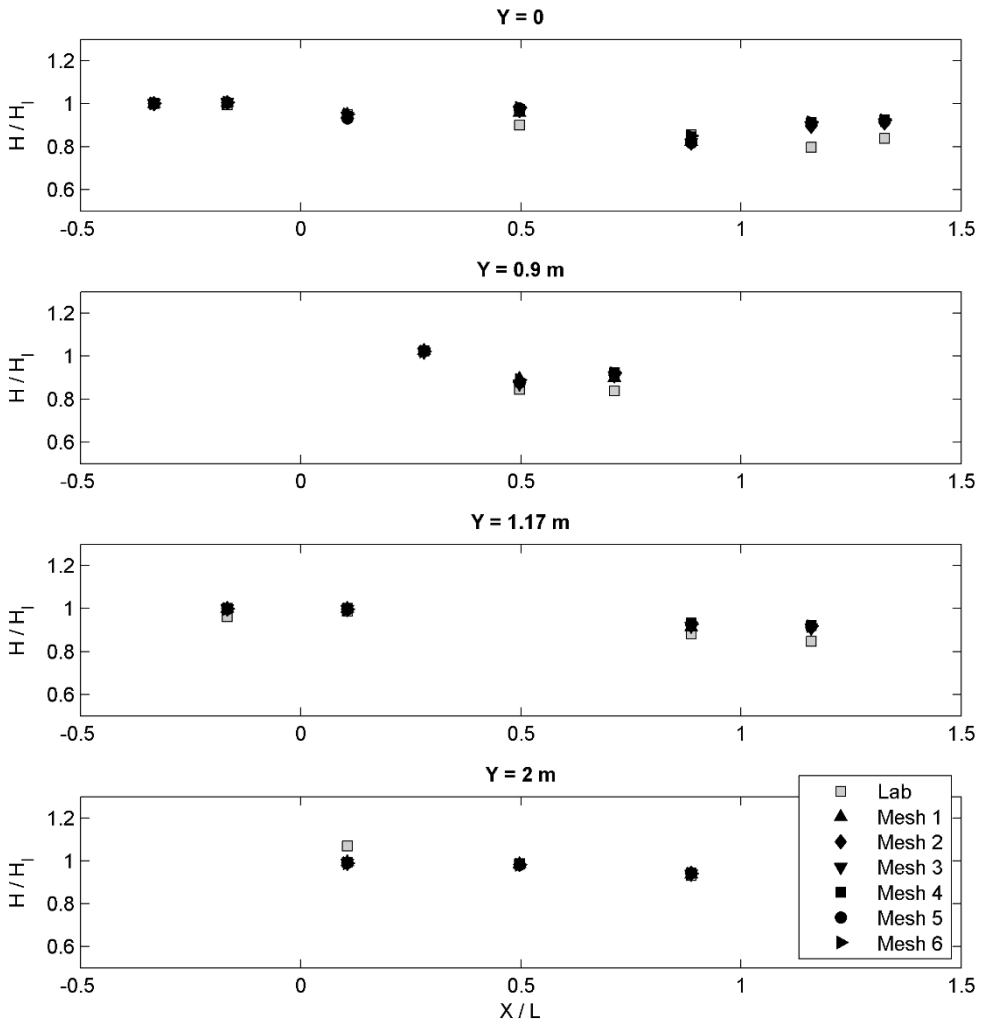

Figure 8.26 Wave height evolution for the six meshes presented in Figure 8.25 for different location along the field.

Regarding the wave height evolution along the meadow, Figure 8.26 shows almost the same results for the six meshes analyzed. This was also observed in the mesh sensitivity analysis carried out in Chapter 7. However, that analysis showed different results for wave exerted forces on the cylinders depending on mesh discretization. These forces are obtained as:

$$F_{max} = max\left(\int_0^{\eta}\left(p + \mu_{eff}\frac{\partial \bar{u}_i}{\partial x_i}\right)dA\right) \quad (6)$$

where η is the location of the free surface, p is the total pressure field, μ_{eff} is the effective kinematic viscosity, which includes the laminar and the turbulent contribution to shear stresses, $\bar{u}_i$ is the velocity field and *dA* the differential area along the cylinder. The maximum forces are normalized by $\rho g(h+H_l)A_w$ where A_w is the wet area of the cylinder. The comparison of the normalized maximum force exerted on the cylinders located at the central line of the field for the different meshes is displayed in Figure 8.27.

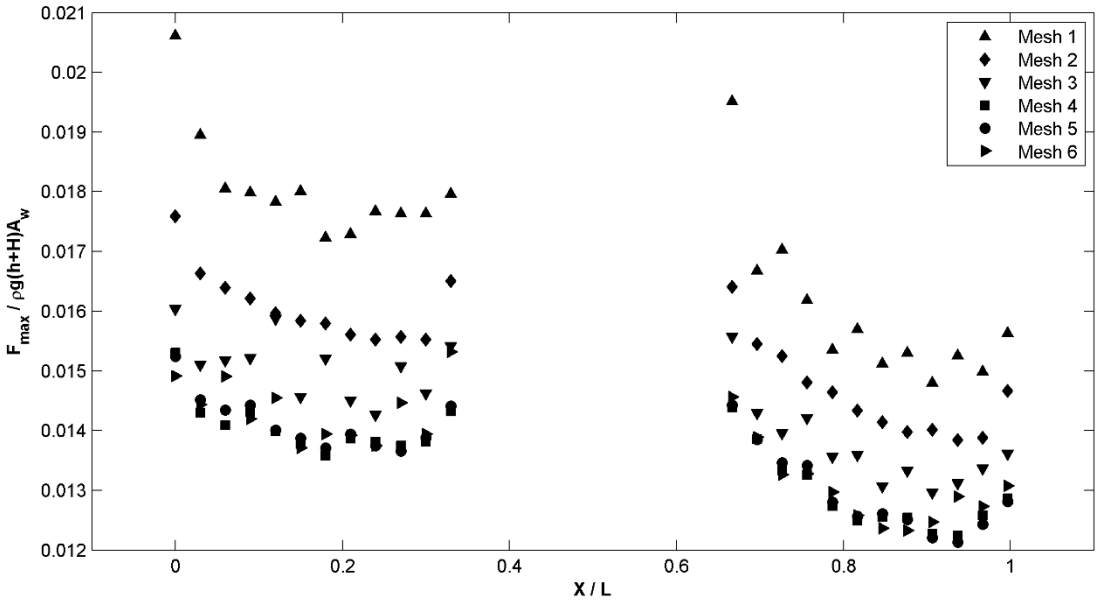

Figure 8.27 Maximum forces obtained for the field central line for the six meshes of Figure 8.25.

Numerical results for maximum forces presented in Figure 8.27 show different values depending on mesh discretization. Meshes 4, 5 and 6 show very similar results with differences below 6%. Consequently, the mesh selection is done attending to a balance between the computational cost and the accuracy of the numerical predictions. According to this, Mesh 4 is selected.

In order to validate flow velocities, the horizontal x-direction velocity component numerical results are compared with laboratory data measured by ADVs (Figure 8.2). For the two locations inside the meadow (X = 0.32 and 2.66 m) two velocity components were taken at two vertical positions (Z = 0.10 and 0.20 m) for h = 0.30 m. Furthermore, velocity was also measured at one point offshore and one onshore the field. Figure 8.28 shows the comparison between numerical results and experimental data.

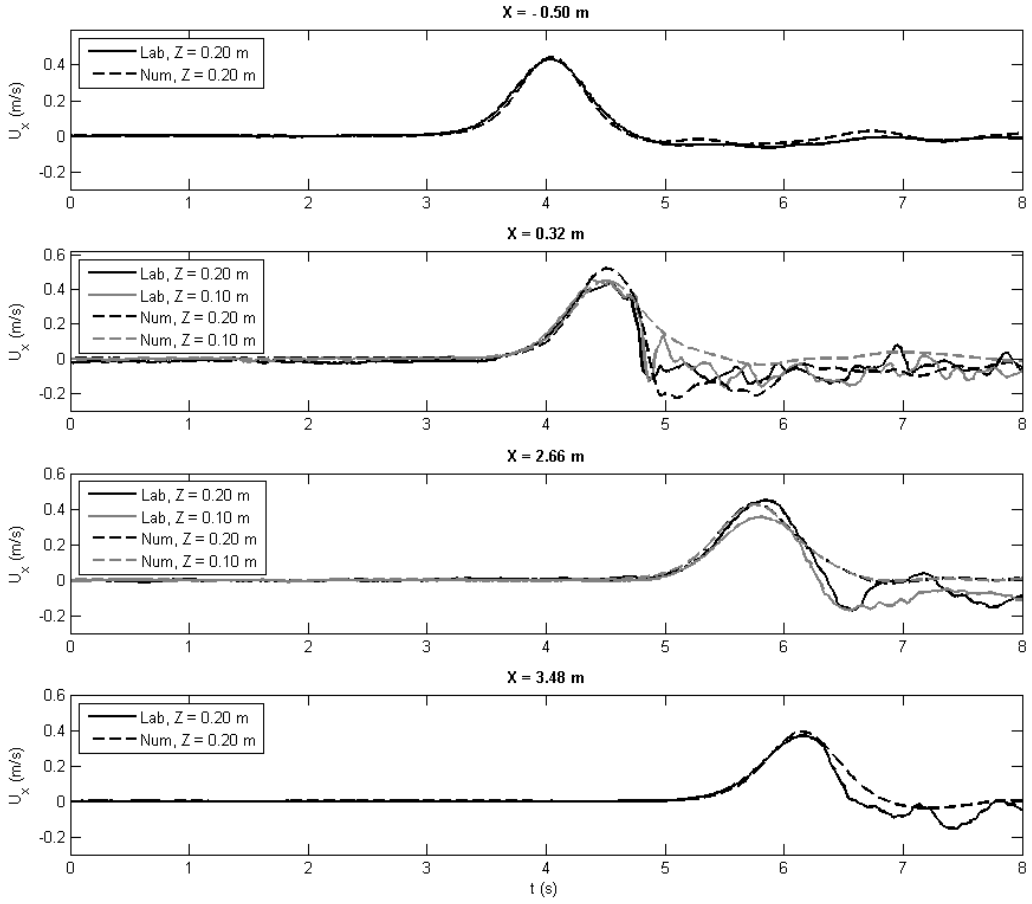

Figure 8.28 X velocity component results for Mesh 4 and laboratory data.

Figure 8.28 shows a good agreement between numerical and laboratory data for the different measurement points although some discrepancies are observed after the wave crest. The highest discrepancies are observed for points inside the meadow but even for those cases the maximum velocity is well approximated.

8.4.2 Spatial force distribution along the cylinders field

The numerical model allows obtaining the forces exerted on the individual cylinders. In order to analyze the spatial evolution of these forces along the cylinders field, the normalized maximum force value at each individual cylinder is displayed for the three configurations. Furthermore, the direction of these maximum forces is also studied. Results for Configuration 1 are shown in Figure 8.29. The maximum force values are displayed in the upper half of the figure and the force directional arrows in the lower half.

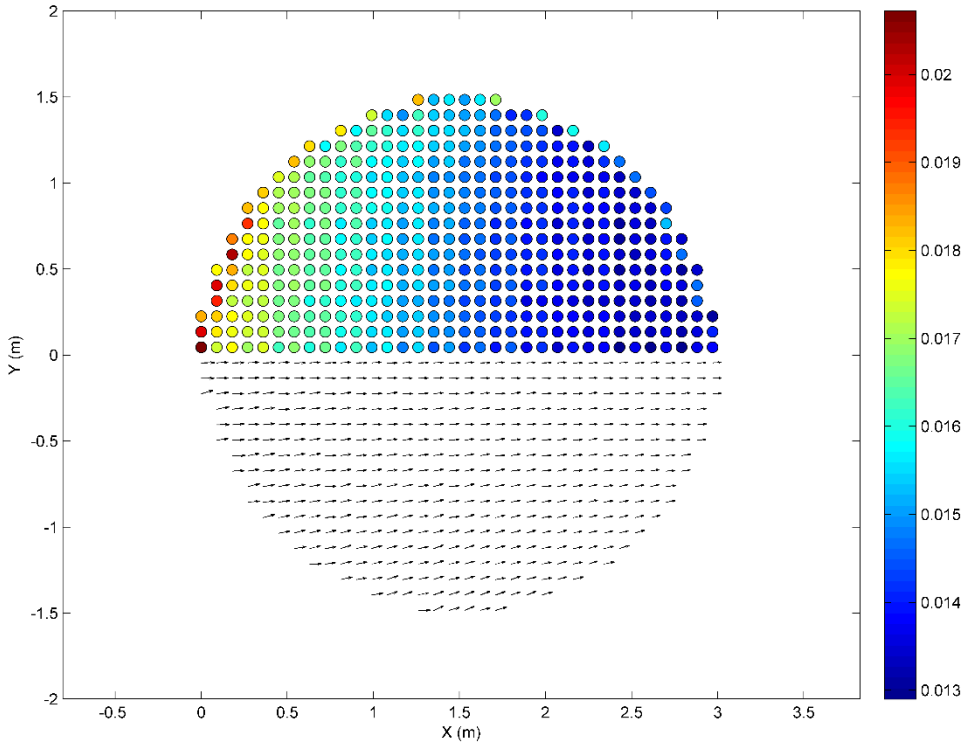

Figure 8.29 Maximum force value over each cylinder (upper half) and maximum forces directional arrows (lower half) for Configuration 1. Colorbar represents the normalized maximum force value.

As expected, Figure 8.29 shows a gradually reduction of the maximum force along the field (from left to right in the figure). It can be seen that the force exerted on the first cylinders row is much higher than the one recorded in the following rows. Cylinders located in the first rows, between two other cylinders, experience the highest forces whereas cylinders that have one of their sides free, suffer smaller forces. Arrows representing forces shown in the lower part reveals that the flow dominant direction is X-direction. A small deviation from the X-direction is observed around the field edges especially at the lateral edge (maximum Y in the field) where flow is slightly turned due to the circular shape of the meadow. The forces results obtained for Configuration 2 are shown in Figure 8.30.

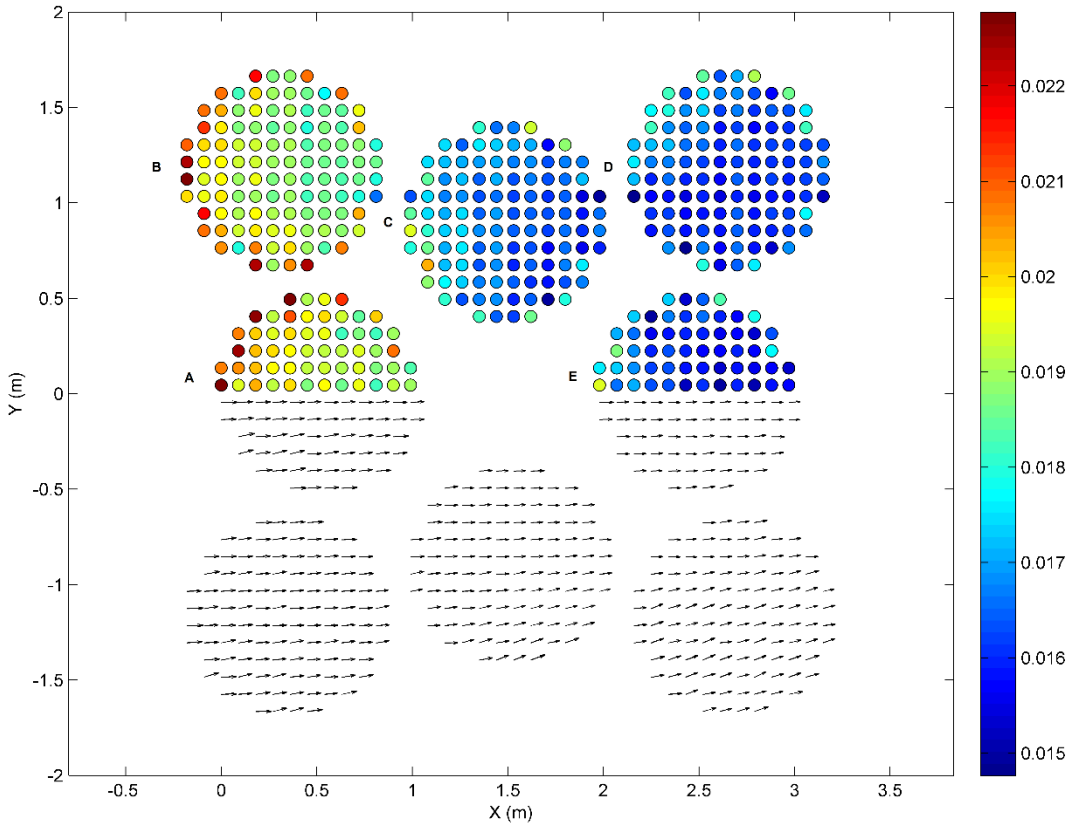

Figure 8.30 Maximum force value over each cylinder (upper half) and maximum forces directional arrows (lower half) for Configuration 2. Colorbar represents the normalized maximum force value.

Figure 8.30 also shows the highest normalized forces at the first rows of the field, which correspond to patches A and B. As observed in Configuration 1 cylinders at the first rows experience a higher force when they are surrounded by other cylinders. There is a flow concentration between patches A and B, which is reflected on the high force values recorded at cylinders located around those zones. Therefore, vegetation breaking or uproot can be enhanced in those preference flow channels where flow is focused. Patch C experiences the highest forces according to the flow concentration induced between patches A and B. The forces recorded in patches D and E show smaller values with the highest ones at the edges since previous patches have attenuated wave energy. Directional arrows representing forces show changes in the flow main direction corresponding to the patches disposition. Areas covered with cylinders produce a loss of momentum due to the induced drag force resulting in a wave height gradient around those areas. Finally, the same results are obtained for Configuration 3 and shown in Figure 8.31.

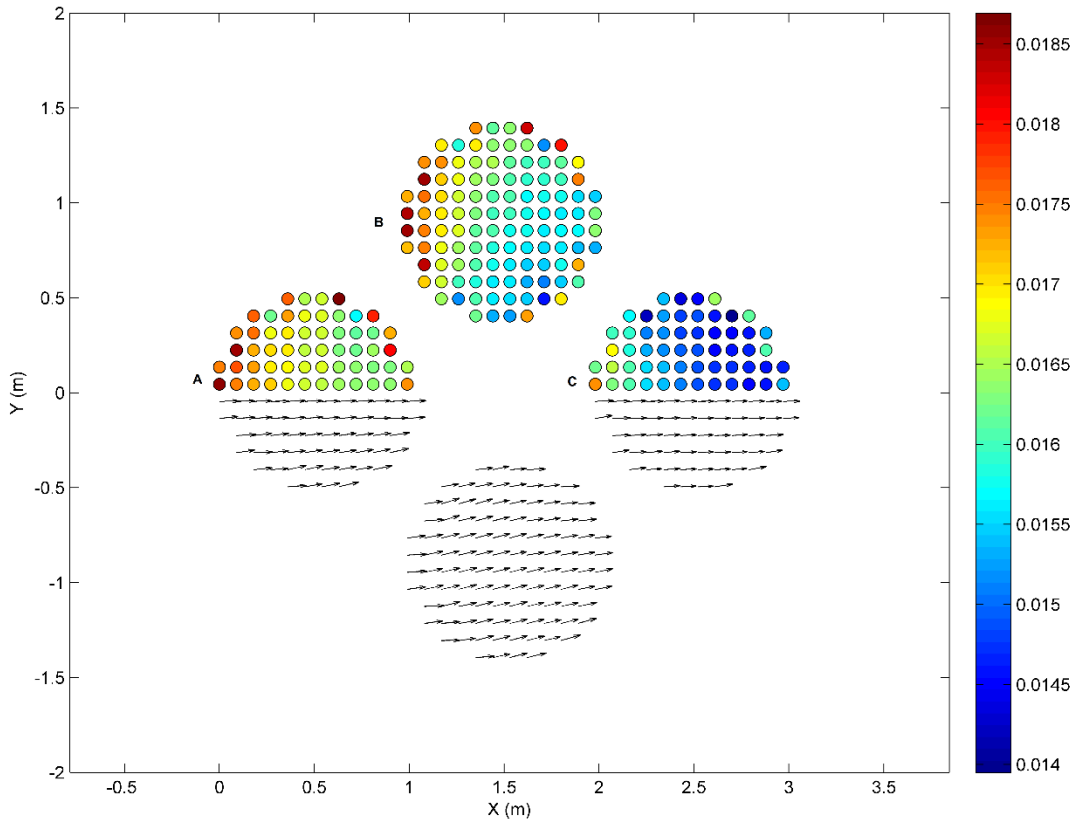

Figure 8.31 Maximum force value over each cylinder (upper half) and maximum forces directional arrows (lower half) for Configuration 3. Colorbar represents the normalized maximum force value.

Forces in configuration 3 show, consistently with previous configurations, the highest values in the first rows of patches A and B. As in Configuration 2, there is a flow concentration between patches A and B, which is noticed in the high force values recorded at the edge cylinders in the back side of patch A. Arrows show the change in the maximum force direction in patch B according to the wave height gradient induced by the attenuation produced by the cylinders field.

8.5 Conclusions

An experimental analysis has been conducted to assess the influence of wave parameters and cylinders distribution on wave attenuation. Different wave conditions, regular, random and solitary waves, and water depths have been tested. In order to understand the effect of the geometric distribution of vegetation patches, three cylinder configurations were tested under

these flow conditions. A total of 71 runs have been carried out for each configuration and the wave attenuation has been evaluated.

The study of the relative wave height influence reveals an increase in wave attenuation with wave height for the three wave types tested in the experiments. While regular and random wave results are well organized attending to relative wave height, solitary waves attenuation is strongly influenced by water depth. Consequently, emergent cylinders induced a much higher attenuation than near emergent or submerged ones.

The influence of the wave number is also studied. The relationship between wave attenuation and the relative wave number is analysed for regular waves. Results for the three water depths are clearly different and a common behaviour is not observed. A new nondimensional number, the depth wave number is defined by multiplying the submergence ratio by the relative wave. Damping coefficients are organized for this new parameter revealing a higher attenuation for higher $kh * SR$ values. The same trend is observed for random wave cases. In order to introduce the cylinders characteristics in the analysis the wave number is multiplied by the equivalent field length. This length is defined as a function of a benchmark field that considers the benchmark case cylinders spacing and porosity and it is related to the number of cylinders and porosity of each configuration. This new number called the field wave number introduces, both the horizontal and vertical lengths of the waves (h and L) and the field (h_v and Le). As a general trend, a higher value of $kLe * SR$ implies a higher wave attenuation. An emergent and long field under short waves induces higher attenuation rates. This parameter is linearly related to damping coefficients for solitary waves revealing the pronounced influence that this parameter has on wave attenuation for these flow conditions.

Keulegan-Carpenter and Reynolds numbers are also analysed. For both, regular and random waves, higher KC and Re imply higher attenuation values. A new Reynolds number based on field characteristics has been defined: Re_S^{Le}. This field Reynolds number allows relating the attenuation coefficients with not only flow but also field characteristics. Damping coefficients are better correlated according to this new number, especially for solitary waves. A new relationship between the damping coefficient and Re_S^{Le} is found for solitary waves.

Numerical simulations performed in the last section of this chapter allows studying the forces exerted on the cylinders for the three configurations. The obtained maximum normalized forces show the differences found between the cylinders configurations according to the patches disposition.

The different relationships shown in this work reveal the importance of both, waves and cylinders field characteristics on the induced wave attenuation. The equivalent field length can

be a good parameter to describe non-contiguous fields in terms of induced wave attenuation. The submergence ratio is a very important parameter and can better correlate wave attenuation results with flow parameters. It can concluded that nondimensional numbers including both, waves and field characteristics, such us the field wave number or the field Reynolds number, provide a better understanding of the wave attenuation produced under different wave conditions and non-uniform fields.

"What we know is a drop, what we don't know is an ocean"

Isaac Newton

9

CONCLUSIONS AND FUTURE RESEARCH

The main objective of the present thesis is to make a step forward in the analysis of coastal protection provided by vegetation. In order to achieve the main goal a set of secondary objectives have been set, namely: 1) The analysis of the role of flexible vegetation on wave attenuation; 2) Quantifying coastal protection provided by real salt marsh vegetation; 3) Semi-empirical modelling of wave and current attenuation by vegetation; 4) Advanced numerical modelling of emergent rigid vegetation and 5) The analysis of field vegetation large-scale characteristics on coastal protection. The accomplishment of these objectives has been achieved along the different chapters of this thesis. A detailed state of the art review of each specific topic has been presented at the beginning of every chapter in order identify present gaps in the literature.

A new two dimensional model for submerged flexible vegetation that solves the coupled movement between waves and flexible plants have been addressed. Later, the effort has been focus on the study of the coastal protection provided by salt marsh vegetation. This type of vegetation have been proven to contribute actively in flow energy attenuation. Therefore, a detailed experimental study of the interaction between waves and currents with two real salt

marshes have been presented. A new damping formulation for wave and current flow conditions have been developed based on these experimental data. After the analysis of the protection provided by salt marshes the study was focus on the development of a new three dimensional model able to reproduce the flow interaction with rigid elements that represented mangrove forests. This new model was later apply to extend the knowledge obtained from a new set of experiments run to study the influence of vegetation patches in waves attenuation.

All this work consequently constitutes a successful step towards a better characterization of flow-vegetation interaction and the coastal protection provided by vegetation ecosystems. This step forward has been addressed using analytical, numerical and physical models. A series of conclusions are presented in continuation. They aim to summarize the most important aspects already described along the document. After that a set of future research topics are presented.

9.1 Conclusions

Thanks to the integration of wave theory, experimental work and numerical modelling, in this thesis, several remarkable and innovatie results have been obtained contributing to the state of the knowledge of the flow-vegetation interaction and its implications on coastal protection. The different contributions can be summarized as follows.

Two dimensional model for flexible vegetation: to the author's knowledge, for the first time a two dimensional RANS model that solves the couple movement between flow and vegetation is presented. The model allows estimating the relative velocity developed between the flow and the plants and is able to reproduce the wave damping and the velocity fields inside and outside the vegetation meadow. These relative velocities have been used to define a new κ-ε turbulence model to represent the turbulence enhancement produced by vegetation. Furthermore, a new drag coefficient formula for flexible swaying vegetation that extends the Reynolds number range of previous studies has been derived.

Guidelines for physical modelling of real salt marsh hydrodynamics: a set of recommendations to develop physical experiments using real plants has been presented. These guidelines are based on the experience gained while carrying out the first large-scale wave basin experimental work using real vegetation and considering combined waves and current conditions. These recommendations cover, organize and prioritize the different aspects that must be taken into account when running experiments with real plants and complex hydrodynamic conditions. This kind of experimental work is expected to grow in the near future.

Quantification of the coastal protection provided by salt marshes: the development of the first large-scale wave basin experiments run with real salt marshes under waves and current conditions has also led to an experimental data base that allows the analysis of different flow and vegetation parameters. Some of the most relevant aspects observed when analyzing this data base are: a logarithmic law is found to explain the variation of wave damping with water depth; tests run with current following and opposing wave propagation direction reveal decreasing wave damping with wave following currents and decreasing damping in ht presence of an opposing current; for currents flowing with a 20º angle with respect to waves, wave damping increases; vegetation biomass strongly influences wave damping and a linear relation is obtained between both variables.

Semi-empirical modelling of wave and current attenuation by vegetation: a new formulation for wave damping under waves and current conditions has been presented. It is the first time that a formulation is derived for both, waves and following and opposing currents. Furthermore, the formulation is presented for both, regular and random waves. The experimental data from experiments carried out with real plants and waves and current conditions have been used to apply the new formulations in order to obtain new drag coefficient formulations.

Advanced numerical modelling of emergent rigid vegetation: to the author's knowledge, it is the first time that a three dimensional model based on Navier-Stokes equations is applied to wave and current interaction with vegetation, represented by rigid elements, comparing two approaches to account for the effect of vegetation in the equations. The first approach represents a direct simulation of the problem and allows evaluating the wave damping induced by the field, the flow between the elements and the forces exerted over them considering a κ-ω SST turbulence model. This approach requires a detailed description of the geometry of the vegetation field. The second approach reproduces the vegetation field by means of a drag force that induces a momentum loss along the vegetated area and requires a modified κ-ε turbulence model. This volume-averaged kind of approach, allows obtaining the wave damping induced by the field with a smaller computational cost. Pros and cons of the two different approaches are discussed and recommendations given, depending on the questions and applications to be made.

Analysis of plants spatial distribution on coastal protection: the three dimensional model developed to simulate flow interaction with rigid elements has been applied to simulate uniform and random plant distributions. The wave damping is not strongly influenced by plants disposition whereas it has been obtained that the forces exerted on the different elements are highly influenced by the different flow patterns developed attending to plants distribution.

Analysis of field vegetation large-scale characteristics on coastal protection: a new set of experiments to analyse vegetation patchiness influence on coastal protection has been performed. To the author's knowledge, it is the first time that three different patchiness configurations are tested under the same wave conditions and later compared. To perform this comparison a new nondimensional number to parameterize vegetation patchiness has been presented. This number allows finding a common relationship between flow parameters and wave damping for the three configurations. Meaningful relationships are found between wave damping and new parameters defined using this number. Additional advanced numerical simulations performed reproducing the physical experiments reveal a strong influence of patches disposition on the forces exerted over vegetation elements.

9.2 Ongoing and future research

9.2.1 Mechanical analysis of flexible vegetation under flow action considering large deformations

The model developed in Chapter 3 for vegetation movement under flow action considers a linear deformation of the plant. This assumption gives good results as soon as the vegetation deformation is not very large. However, for very flexible vegetation a model based on large deformations needs to be taken into account. That model would provide plant deformation for very flexible species and could be implemented in a hydrodynamic model, such as the IH-2VOF, to reproduce the coupled motion between flow and vegetation and the associated relative velocity.

A first approach to define a large deformation model has been developed based on a Lagrangian approach and considering the force balance in the group of elements the plant is divided into. In order to validate the model a set of flume experiments were performed at the University of Cantabria with mimics of flexible vegetation under the action of different wave conditions. The mimics reproduced *Posidonia oceanica* and two configurations were considered. The first one formed by 4 strips of different lengths inserted in a stiff rod and the second one considering only one of the short strips.

Plant movement was recorded by a 1 megapixel camera Marlin F131C of 8 bits of spectral resolution and with a frequency of 10Hz. The camera was positioned perpendicular to the plane of plant movement. Synchronous measurements of the wave height were made at the same distance from the paddle as the plant location and 4.65 m in front of this position, using wave

gauges measuring at 20Hz. The synchronization of both measurements was performed using a trigger at 10 Hz.

Wave period (T = 2, 3 and 4s) and height (H = 5, 10, 15 and 20cm) were combined giving a total of twelve different runs, all of them with an 80 cm water depth in the testing region. These wave conditions were designed attending to the Reynolds Keulegan-Carpenter and Cauchy numbers.

In order to characterize the periodic movement experienced by the *Posidonia oceanica* mimic due to flow action, the position of the mimic was analyzed at different wave instants. Figure 9.1 shows the mimic position for the wave up-crossing, crest, down-crossing and trough, points a, b, c and d, for the wave conditions with the highest wave height and period. Using a data phase averaging, the image above shows the free surface along a wave period and the image below the mimic position. In this second image positive values of x represent onshore and negative values offshore. The horizontal lines in each position show standard deviation of that position. In the same figure the moments of maximum and minimum displacement are represented in red by points e and f. As can be observed, these maximum amplitudes of movement are reached after the wave crest and wave trough. Therefore, there is a lag between maximum displacement onshore and offshore and the momentum when the wave crest and trough pass along the mimic. This lag is due to the inertia force produced on the plant due to flow accelerations. The maximum displacement values obtained onshore are greater than the values obtained offshore. This is due to wave asymmetry; the velocities at the wave crest are higher than velocities at the trough.

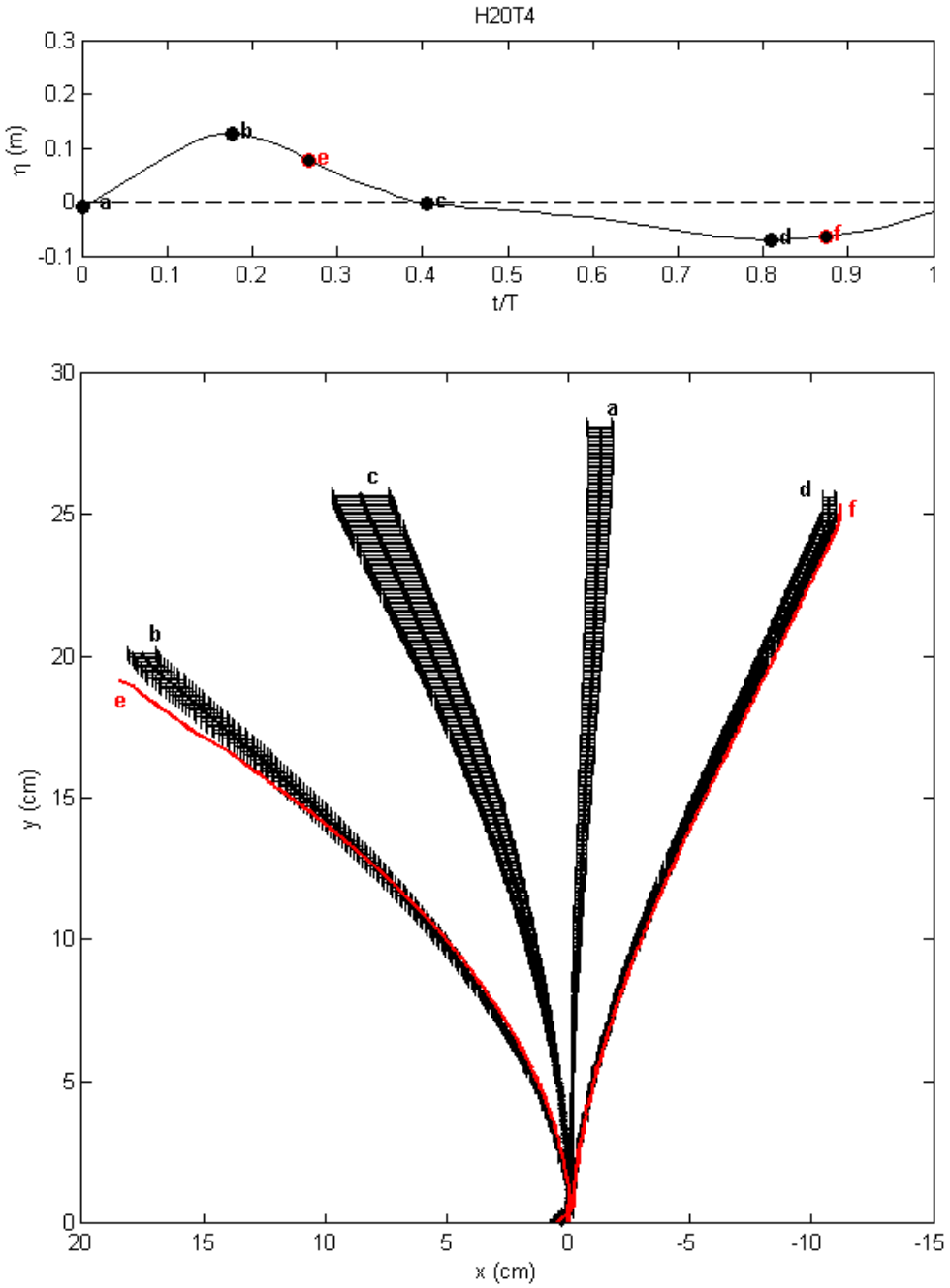

Figure 9.1 Representation of plant positions in (a) zero upcrossing, (b) wave crest, (c) zero downcrossing and (d) wave trough with their corresponding standard deviation and (e) maximum amplitude onshore and (f) maximum amplitude offshore. Run H20T4, H = 20cm and T = 4s for Configuration 1.

A set of numerical experiments was also carried out to validate the model. In order to validate the model it is necessary to evaluate the flow velocities that produce the mimic motion recorded

by the camera in the flume experiments. Since velocities were not measured in those experiments a numerical tool is used to obtain them. The numerical model IH-2VOF is used to infer these velocity values. Using this model a numerical experiment is performed for each of the flume experiments resulting in a total of 24 simulations (12 different wave conditions and two mimic configurations).

The deflection maximum shape obtained offshore and onshore with the model is displayed in Figure 9.2 Figure 9.2 for one of the tested wave conditions (H = 10 cm and T = 3 s). The deflected shape obtained with the small deformations model presented in Chapter 3 is also presented in the figure. Figure 9.2 shows a good agreement between the deformation shape taken by the camera and the one obtained with the model for large deformations along the full mimic length. For small deflections, the model allows obtaining the value of the free end displacement but does not reproduce the deformation along the mimic length. The improvement on the representation of the deformation shape by the model for large deformations provides the chance of estimating the forces along the full mimic length as well as the shaded areas resulting from vegetation bending.

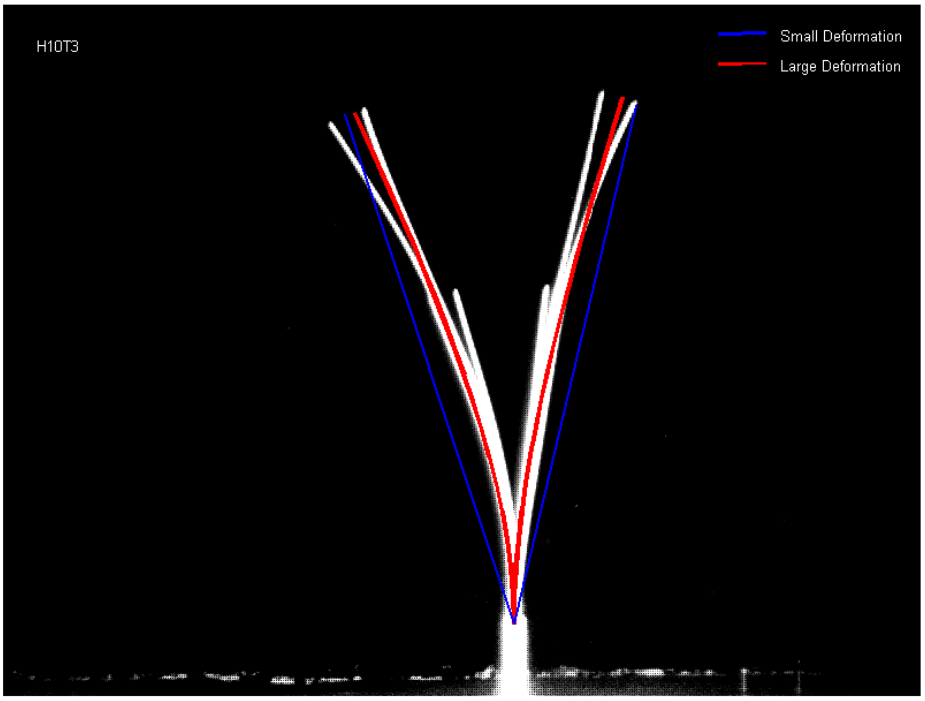

Figure 9.2 Solutions of mimic maximum deformation onshore (left) and offshore (right) obtained with both models, small deformations (blue) and large deformation (red).

9.2.2 Numerical model for wave-current-vegetation interaction

An analytical model for wave damping by vegetation under combined waves and currents have been presented in Chapter 6. Although this represents a good first approach, a numerical model that allows simulating waves and currents, considering different directions, interacting with vegetation is still necessary. This will represent a valuable tool to extend the understanding of the problem and to analyze wave damping under these conditions.

9.2.3 Real representation of mangrove forests and its implications on flow energy dissipation

Mangrove forests have been studied in this thesis by means of vertical rigid cylinders. Although this is a common practice in literature, mangroves have complex structures formed by aerial roots, trunks and branches. Therefore, it is important to study real geometries in order to assess coastal protection provided by these ecosystems. In order to make some progress on this aspect, a first attempt to reproduce the real geometry of a mangrove is ongoing. Among the mangrove species, *Rhizophora* is the one selected. *Rhizophora* plants occupy approximately 90% of the world mangrove distribution (Ohira et al., 2013). Furthermore, the vast majority of mangroves used for restorations are *Rhizophora* plants (Walters, 2000). They induce large friction on waves (further supported by Mazda et al., 1997b) due to their complex structure formed by aerial roots structures that contribute to higher drag coefficients (Sanit et al., 1992; Jayatissa et al., 2002).

Ohira et al. (2013) presented a stilt root morphology model taking the diameter of breast height (DBH) for assigning the hydraulic drag of *Rhizophora* plants. The stilt root morphology is modeled considering the relationships between DBH and the root parameters. This provides a three dimensional root layout. The highest root height and the total number of roots are obtained from the DBH value and with these values the root height, diameter, shape and length are determined. The sample trees used to develop this model had a DBH range from 0.03 to 0.28 m. As a first approximation, in this study a DBH = 0.20 m is chosen. This value corresponds to mature mangroves. The associated highest root height is H_{Rmax} = 2.012 m and the number of roots N = 24. The diameter of these roots range from 0.033 to 0.042 m and their shape is displayed in Figure 9.3.

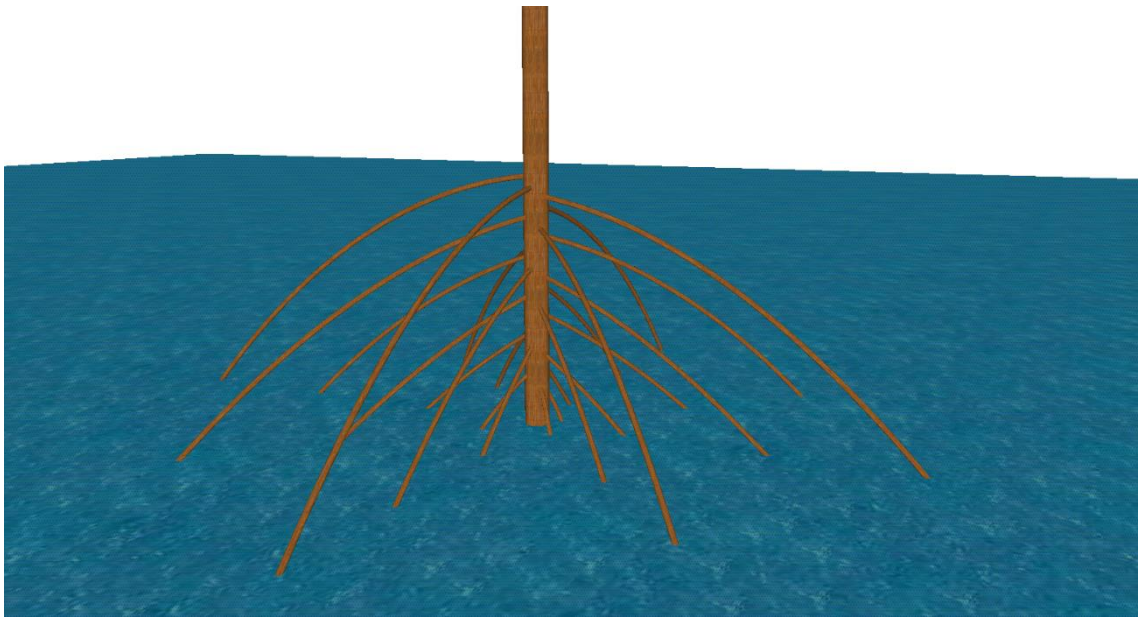

Figure 9.3 Representation of a real mangrove geometry

The mangrove model presented in Figure 9.3 is then used to create a mangrove forest in order to run simulations that allow the analysis of parameters such as wave attenuation, forces exerted on the vegetation elements or run-up on a beach slope. The density of a mangrove forest is determinant in the attenuation provided by them. Dense mangrove forests attenuate waves more effectively than low density forests (Alongi, 2008; Mazda et al., 1997a, b; Massel et al., 1999). The created mangrove model occupies an area of 7 x 7 m with 24 primary roots plus the central one. This geometry leads to a vegetation density about 0.5 stems/m^2. This is in agreement with previous works as the one presented by Tusinski (2012) which reports 0.3-0.35 stems/m^2. Therefore, the mangrove forest is created disposing the individual elements according to this density. Figure 9.4 shows the mangrove field created considering 53 mangroves distributed in 1500 m^2 (60m long and 25 m wide). This total area has been selected attending to computational resources and costs.

The slopes behind mangrove forests can be adjusted to a range between 1:10 and 1:50. These values are commonly used by previous researchers such as Hiraishi and Harada (2003), Harada and Imamura (2002), Yeh (1991) and Synolakis (1986). In order to reduce the numerical domain a slope of 1:10 is selected for this study. Figure 9.4 shows a top, lateral and frontal view of the mangrove forest created to run the simulations.

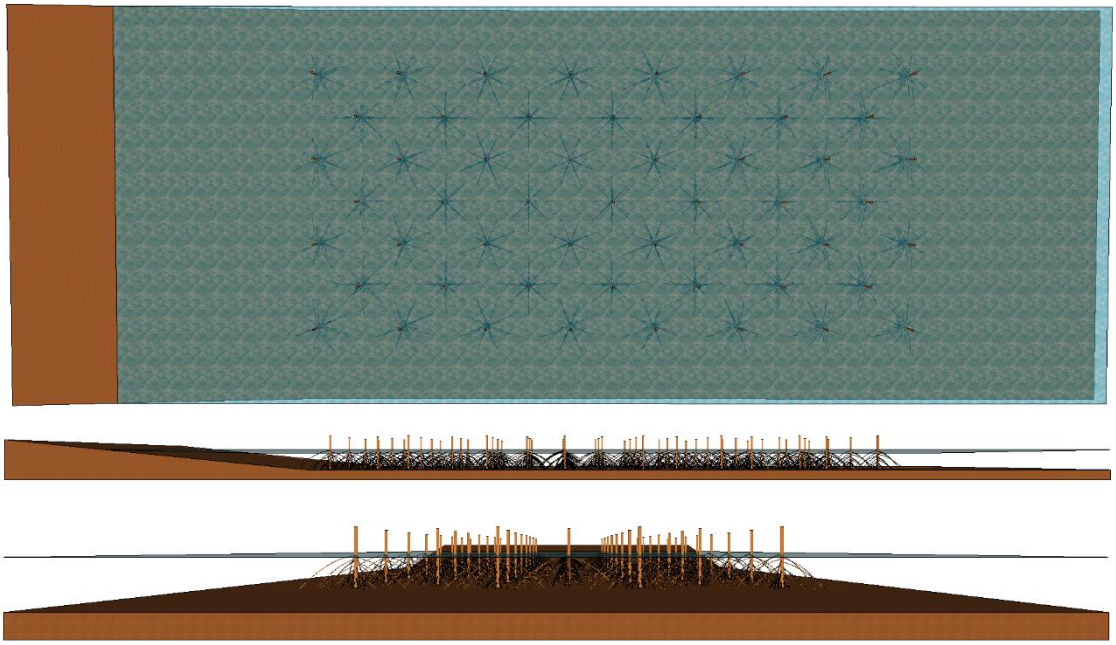

Figure 9.4 Top, lateral and front view of a numerical mangrove forest.

The three dimensional model presented in Chapter 7, IHFOAM, will be used to perform simulations considering the forest presented in Figure 9.4 and considering different hydrodynamic conditions.

9.2.4 Flow patterns and sediment transport

Section 7.4.2 in Chapter 7 and Chapter 8 have highlighted the strong influence that vegetation spatial distribution has on flow-vegetation interaction. Depending on this spatial distribution, the flow patterns developed around the vegetation elements or, at a higher scale, around vegetation patches are different. These flow patterns and the associated velocity fields induce different bottom shear stress values that strongly influence sediment transport. Therefore, a good definition of these flow variables can lead to predictions of potential erosion and accretion areas.

As a first attempt to identify potential sediment transport the two dimensional model IH-2VOF is used. The IH-2VOF model is able to provide the velocity field distribution not only around the vegetation field but also inside the meadow. It provides useful information to study flow patterns to later link them to ecological or morphological aspects, such as potential nutrients or sediment transport. Therefore, the developed flow patterns are analyzed by means of the mean velocity fields and the pathlines developed by numerical tracers that are introduced into the

domain. These numerical tracers move passively with the flow and are seeded around and inside the vegetation field in order to visualize their movement under wave flow action. Figure 9.5 shows the mean velocity fields (left panel) for two cases with the same regular wave conditions (H = 0.43 m and T = 3 s) and different water depths (h = 1.8 and 2.2 m). The vegetation meadow is simulated by considering *Posidonia oceanica* properties (defined in Chapter 3) and a meadow density of 360 shoots/m^2. The right panel of the same figure shows the pathlines developed for the numerical tracers in the two simulations.

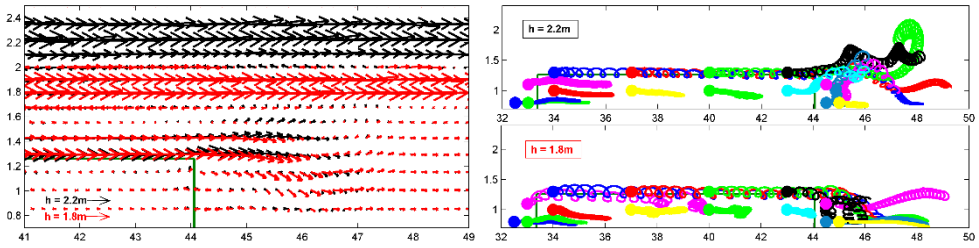

Figure 9.5 Mean velocity field and numerical tracers pathlines for two cases with different water depth.

The velocity fields associated to each case jointly with the pathlines described by the different tracers allow identifying zones of potential sediment loss and areas where accretion is expected.

In order to extend this analysis, different patches configuration are simulated. Figure 9.6 shows the mean velocity fields and the horizontal velocity profiles for three cases with different vegetation patchiness and subject to the same wave conditions (H = 0.43 m, T = 3 s and h = 2.4 m). The first case (A) is built of one 10.7 m long patch whereas cases B and C present two patches of 5 and 3.6 m, respectively.

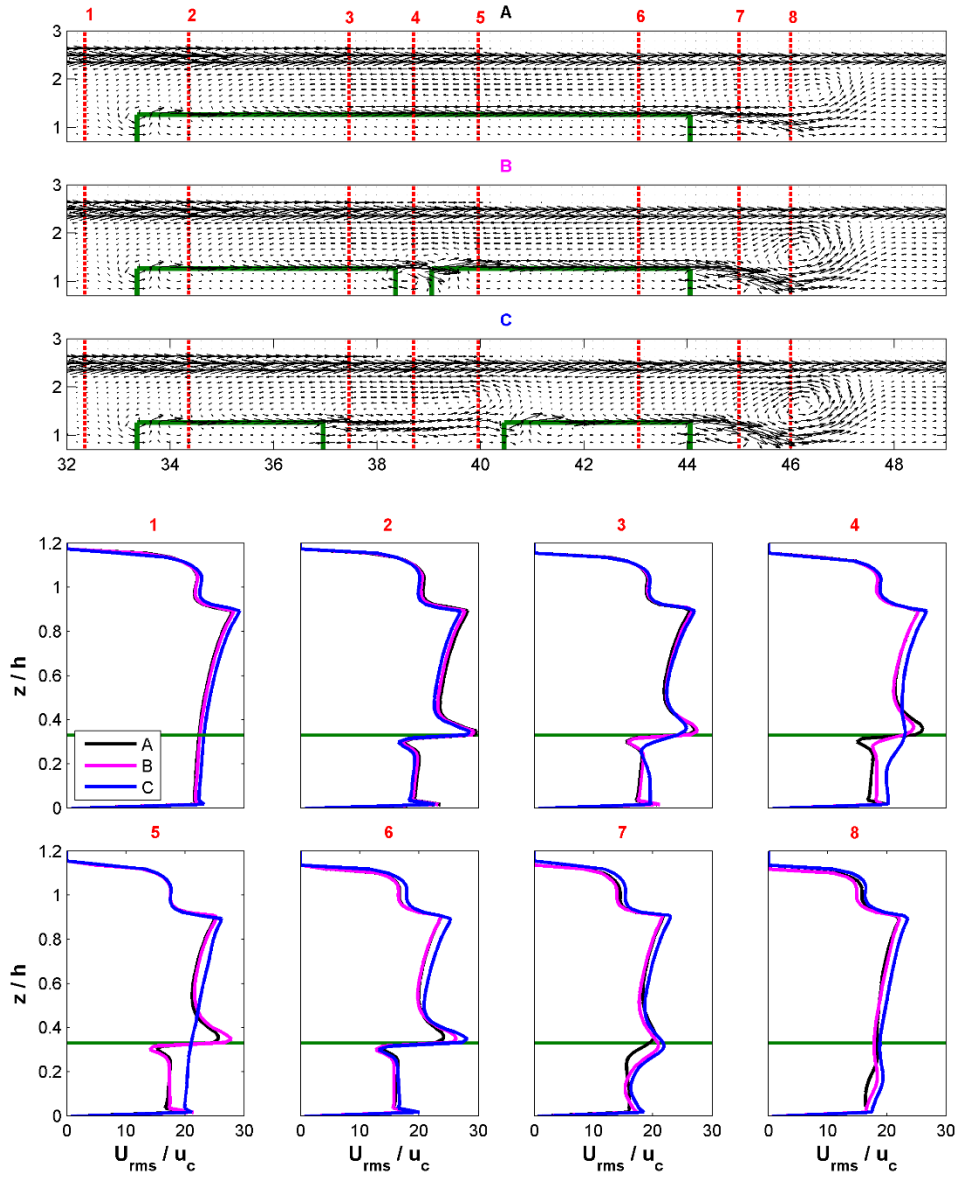

Figure 9.6 Mean velocity field and horizontal velocity profiles for three meadows with different patchiness. Green lines represent vegetation meadows.

Different simulations shown in Figure 9.6 reveal an acceleration of the flow at the top of the vegetation meadow. This is known as skimming flow and develops as a consequence of the drag force exerted by the plants. Although an upwelling motion is observed at the rear end of the vegetation field for all simulations, different recirculation patterns are associated to the different patchiness conditions. This is also observed in the velocity profiles recorded at sections 4 and 5 which are very different depending on the size of the gap between the vegetation patches.

Although this model can be useful in order to link hydrodynamic changes to potential ecological and morphological variations it only solves the hydrodynamics two dimensionally and does not consider sediment transport.

In order to complete the previous analysis, a three dimensional approach has been carried out analyzing the bottom shear stress obtained for the numerical simulations presented in Section 8.4 in Chapter 8. Preliminary results of the maximum shear stress obtained at each position for Configurations 2 and 3 are shown in Figure 9.7 and Figure 9.8.

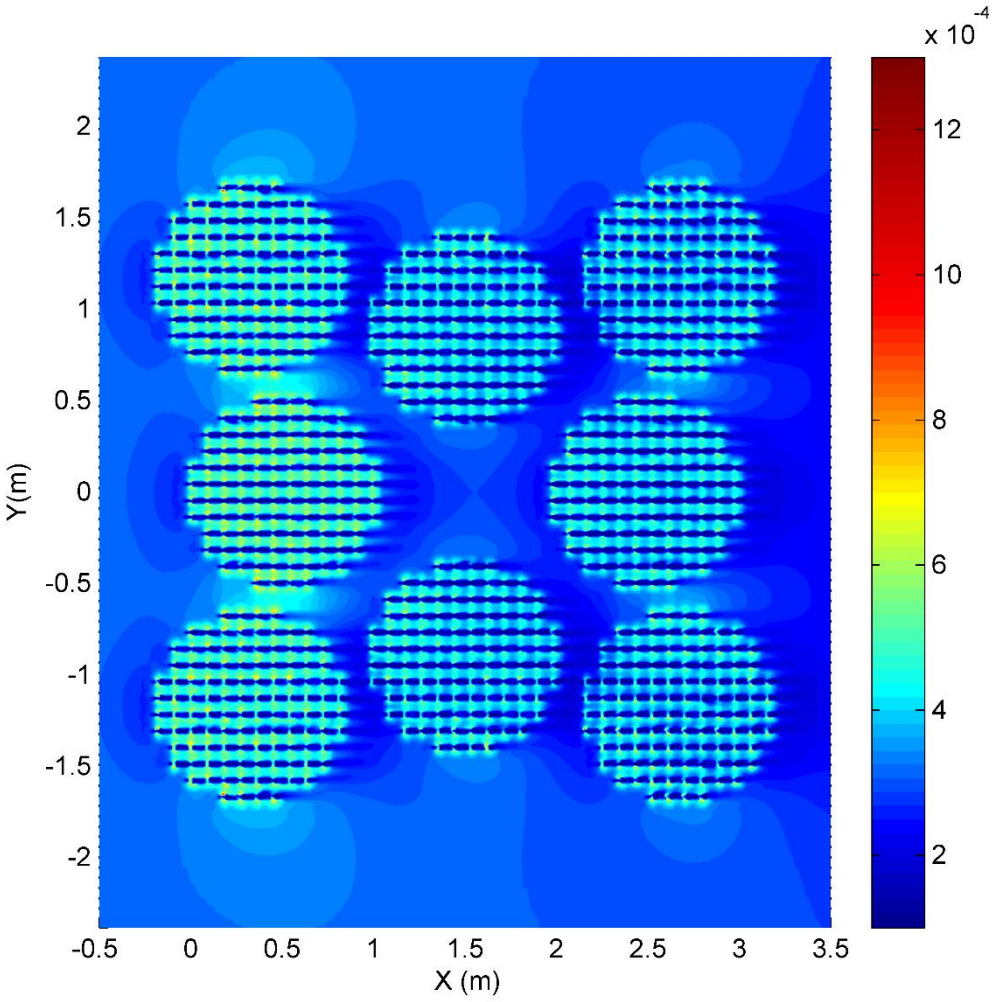

Figure 9.7 Maximum bottom shear stress for Configuration 2.

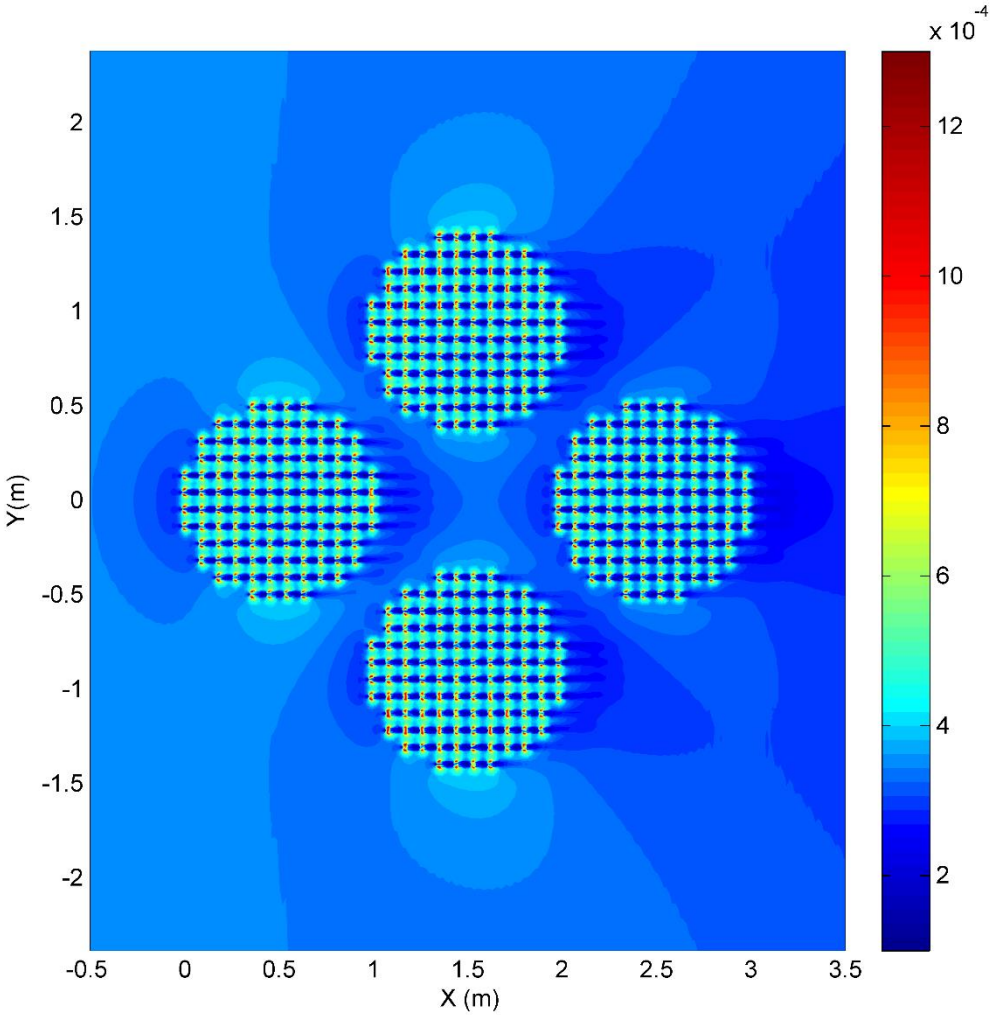

Figure 9.8 Maximum bottom shear stress for Configuration 3.

Figure 9.7 shows that the highest shear stresses are recorded among the front two lateral patches and the central one due to the flow focusing produced at that location. The same is observed with smaller values between the last three patches. For both configurations (Figure 9.7 and Figure 9.8), almost zero shear stresses are found onshore the different patches whereas the highest values are observed at the laterals. Regarding the individual elements, there is an increase of the shear stress at both sides of each individual cylinder. Conversely, preferred flow channels developed between cylinder rows lead to almost zero shear stresses behind the individual elements. These results can be related to potential sediment transport identifying areas of potential erosion or accretion.

Although the models presented before can be useful as a first approach, there is need for a model solving sediment transport in order to analyze the effect that vegetation meadows have on erosion protection.

REFERENCES

Allen, J.R.L. (2000). Morphodynamics of Holocene salt marches: a review sketch from the Atlantic and Southern North Sea coasts of Europe. Quat. Sci. Rev. 19, 1155-1231.

Alongi, D.M. (2002). *Present state and future of the world's mangrove forests*. Environmental Conservation, 29 (3), 331-349.

Alongi, D.M. (2008). Mangrove forests: Resilience, protection from tsunamis and responses to global climate change. Estuar. Coastal Shelf S., 76: 1-13.

Anderson, M. E. (2010). Measurements and linear wave theory based simulations of vegetated wave hydrodynamics for practical applications. Master's thesis, Texas A&M University.

Anderson, M.E., Smith, J.M. (2014). *Wave attenuation by flexible, idealized salt marsh vegetation.* Coastal Engineering, 83, 82-92.

Arkema, K.A., Guannel, G., Verutes, G. , Wood, S.A., Guerry, A., Ruckelshaus, M., Kareiva, P., Lacayo, M., Silver, J.M. (2013). *People and property shielded from sea level rise and storms by coastal habitats*. Nature Climate Change.

Asano, T., Tsutsui, S., Sakai, T. (1988).*Wave damping characteristics due to seaweed*. Proc. of the 35th Coastal Eng. Conf. in Japan (in Japanese), Japan Soc. of Civil Eng., Matsuyama, 138-142.

Asano, T., Setoguchi, Y. (1996). *Hydrodynamic effects of coastal vegetation on wave damping*. Hydrodynamics, 1051-1056.

Augustin, L.N., Irish, J.L., Lynett, P. (2009). Laboratory and numerical studies of wave damping by emergent and near emergent wetland vegetation. Coastal Engineering, 56, 332-340.

Baddour, R.E., Song, S. (1990). *On the interaction between waves and currents*. Ocean Eng., 17, 1-21.

Barbier, E.B., Koch, E.W., Silliman, B., Hacker, S.D., Wolanski, E., Primavera, J., Granek, E.F., Polasky, S., Aswani, S., Cramer, L.A., Stoms, D.M., Kennedy, C.J., Bael, D., Kappel, C.V., Perillo,

G.M. and Reed, D.J. (2008). *Coastal Ecosystem-Based Management with Nonlinear Ecological Functions and Values*. Science, 319, 321-323.

Barbier, E.B., Hacker, S.D., Kennedy, C.J., Koch, E.W., Stier, A.C. and Silliman, B.R. (2011). *The Value of Estuarine and Coastal Ecosystem Services.* Ecological Monographs, 81 (2), 169-193.

Borsje, B.W., van Wesenbeeck, B.K., Dekkerc, F., Paalvastd, P., Bouma, T.J., van Katwijk, M.M., de Vriesb, M.B. (2011). *How ecological engineering can serve in coastal protection*. Ecol. Eng. 37, 113-122.

Bouma, T.J., Vries, M.B., Low, E., Kusters, L., Herman, P.M.J., Tánczos, I.C., Temmerman, S., Hesselink, A., Meire, P., van Regenmorte, S. (2005a). *Flow hydrodynamics on a mudflat and in salt marsh vegetation: identifying general relationships for habitat characterisations*. Hydrobiologia, 540, 259 – 274.

Bouma, T.J., De Vries, M.B., Low, E., Peralta, G., Tanczos, I.C., van de Koppel, J. and Herman, P.M.J. (2005b). *Trade-offs Related to Ecosystem Engineering: A Case Study on Stiffness of Emerging Macrophytes.* Ecology, 86(8), 2187-2199.

Bouma, T.J., van Duren, L.A., Temmerman, S., Claverie, T., Blanco-Garcia, A., Ysebaert, T., Herman, P.M.J. (2007). Spatial flow and sedimentation patterns within patches of epibenthic structures: Combining field, flume and modelling experiments. Continental Shelf Research, 27, 1020–1045.

Bouma, T.J., De Vries,M.B., Herman, P.M.J. (2010). Comparing ecosystem engineering efficiency of two plant species with contrasting growth strategies. Ecology 91 (9), 2696-2704.

Bouma, T.J., Temmerman, S., van Duren, L.A., Martini, E., Vandenbruwaene, W., Callaghan, D.P., Balke, T., Biermans, G., Klaassen, P.C., van Steeg, P., Dekker, F., van de Koppel, J., de Vries, M.B., Herman, P.M.J. (2013). *Organism traits determine the strength of scale-dependent bio-geomorphic feedbacks: A flume study on three intertidal plant species*. Geomorphology, 180-181, 57-65.

Bouma, T.J., van Belzen, J., Balke, T., Zhu, Z., Airoldi, L., Blight, A.J., Davies, A.J., Galvan, C., Hawkins, S.J., Hoggart, S.P.G., Lara, J.L., Losada, I.J., Maza, M., Ondiviela, B., Skov, M.W., Strain, E.M., Thompson, R.C., Yang, S., Zanutigh, B., Zhang, L. and Herman, P.M.J., (2014). *Identifying knowledge gaps hampering application of intertidal habitats in coastal protection: opportunities & steps to take*. Coastal Engineering, 87: 147-157

Bradley, K., Houser, C. (2009). *Relative velocity of seagrass blades: Implications for wave attenuation in low-energy environments*. J. Geophysical Res. F: Earth Surface, 114, F01004.

Cavallaro L., Re, C.L., Paratore, G., Vvivano, A., Foti, E. (2010). *Response of Posidonia oceánica to wave motion in shallow-waters – preliminary experimental results*. Proc. 32nd Intern. Coastal Eng. Conf. Coas. Eng. Res. Council, 1-10.

Chakrabarti, S. K., (1987). *Hydrodynamics of offshore structures*. Computational Mechanics Publications and Springer, New York.

Chapman, V.J. (1974). *Salt marshes and salt deserts of the world*. 2nd edn. Verlag von J. Cramer, Lehre.

Chen, S.N., Sanford, L.P., Koch, E.W., Shi, F., North, E.W. (2007). *A nearshore model to investigate the effects of seagrass bed geometry on wave attenuation and suspended sediment transport*. Estuaries and Coasts, 30, 296-310.

Cheng N.S., Nyugen, H.T. (2011). Hydraulic radius for evaluating resistance induced by simulated emergent vegetation in open-channel flows. Journal of hydraulic engineering, 137, 995-1004.

Christiansen, T., Wiberg, P.L., Milligan, T.G. (2000). *Flow and sediment transport on a tidal salt marsh surface.* Estuarine, Coastal and Shelf Science 50, 315–331.

Cornelisen, C.D., Thomas, F.I.M. (2004). Ammonium and nitrate uptake by leaves of the seagrass Thalassia testudinum: Impact of hydrodynamic regime and epiphyte cover on uptake rates. J. Mar. Syst., 49, 177-194.

Costanza, R., d'Arge, R., Groot, R.d, Farber, S., Grasso, M., Hannon, B., Limburg, K., Naeem, S., O'Neill, R.V., Paruelo, J., Raskin, R.G., Sutton, P., Belt, M.v.d (1997). *The value of the world's ecosystem services and natural capital*. Nature 387, 253-260.

Belcher, S., Jerram, N., Hunt, J. (2003). *Adjustment of a turbulent boundary layer to a canopy of roughness elements.* J. Fluid Mechanics, 488, 369-398.

Bridges, K., Cox, D., Thomas, S., Shin, S., Rueben, M. (2011). *Large-scale wave basin experiments on the influence of large obstacles on tsunami inundation forces*. Proc. of the 6th International Conference on Coastal Structures, in Japan, D1-114.

Chen, W., Panchang, V., Demirbilek, Z. (2005). On the modelling of wave–current interaction usingthe elliptic mild-slope wave equation. Ocean Eng., 32, 2135-2164.

Dalrymple, R.A., Kirby, J.T., Hwang, P.A. (1984). *Wave Diffraction Due to Areas of Energy Dissipation*. J. Waterway, Port, Coastal & Ocean Eng., 110, 67-79.

Dean, R.G., Dalrymple, R.A. (1991). *Water wave mechanics for engineers and scientists*. Advanced Series on Ocean Engineering, 2, World Scientific.

del Jesus, M., Lara, J.L., Losada, I.J. (2012). Three-dimensional interaction of waves and porous coastal structures Part I: Numerical model formulation. Coastal Engineering, 64, 57–72.

Drew, M.C., Lynch, J.M. (1980). *Soil anaerobiosis, microorganisms, and root function*. Annual Review Phytopathology, 18, 37-66.

Duarte, C.M, Losada, I.J., Hendriks, I., Mazarrasa I., Marba, N. (2013) *The potential of coastal habitats for climate change mitigation and adaptation*. Nature Climate Change. Vol. 3, 961-968.

Dubi, A., Torum, A. (1995). *Wave damping by kelp vegetation*. Proc. of the 24th Coastal Eng. Conf. in New York, AM. Soc. of Civil Eng., 142 – 156.

Dubi, A., Torum, A. (1997). *Wave energy dissipation in kelp vegetation*. Proc. of the 25th Coastal Eng. Conf in Orlando, 3, 2626-2639.

DuPont, S., Gosselin, F., Py, C., de Langre, E., Hemon, P., Brunet, Y. (2010). Modelling waring crops using large-eddy simulation: comparison with experiments and a linear stability analysis. J. Fluid Mech., 652, 5 – 44.

Elwany, M.H.S., O'Reilly, W.C., Guza, R.T., Flick, R.E. (1995). *Effects of southern California kelp beds on waves*. J. Waterway, Port, Coastal & Ocean Eng., 121, 143-150.

Feagin, R.A., Irish, J.L., Möller, I., Williams, A.M., Colón-Rivera, R.J., Mousavi, M.E. (2011). *Short communication: Engineering properties of wetland plants with application to wave attenuation.* Coastal Engineering, 58, 251–255.

Ferrario, F., Beck, M., Storlazzi, C., Micheli, F., Shepard, C., Airoldi, L. (2012). *The effectiveness of coral reefs for coastal hazard risk reduction and adaptation*. Nature Communications 5. Article number 3789.

FitzGerald, D.M., Fenster, M.S., Argow, B.A., Buynevich, I.V. (2008*). Coastal impacts due to sea*-level rise. Annu Rev Earth Planet Sci, 36, 601–647.

Folkard, A.M. (2005). Hydrodynamics of model Posidonia oceanica patches in shallow water. Limnol. Oceanogr., 50, 1592-1600.

Fonseca, M.S., Zieman, J.C., Thayer, G.W., Fisher, J.S. (1983). *The role of current velocity in structuring eelgrass (Zostera marina L.) meadows.* Estuar. Coast. Shelf Sci., 17, 367-380.

Fonseca, M.S., Cahalan, J.A. (1992). *A preliminary evaluation of wave attenuation by four species of seagrass.* Estuarine, Coastal and Shelf Science, 35, 565-576.

Fonseca, M.S., Koehl, M.A.R. (2006). *Flow in seagrass canopies: the influence of patch width*. Estuarine, Coastal and Shelf Science, 67, 1-9.

Frostick, L. E., Thomas, R.E., Johnson, M.F., Rice, S.P., McLelland, S.J. (2014). Users Guide to Ecohydraulic Modelling and Experimentation: Experience of the Ecohydraulic Research Team (PISCES) of the HYDRALAB Network. IAHR Design Manual.

Gacia, E., Duarte, C.M. (2001). Sediment Retention by a Mediterranean Posidonia oceanica Meadow: The Balance between Deposition and Resuspension. Estuarine, Coastal and Shelf Science 52, 505-514.

Gaylord, B., Denny, M.W., (2003). *Modulation of wave forces on kelp canopies by alongshore currents*. Limnology and Oceanography, 48, 860-871.

Gedan, K.B., Kirwan, M.L., Wolanski, E., Barbier, E.B., Silliman, B.R. (2010). The present and future role of coastal wetland vegetation in protecting shorelines: answering recent challenges to the paradigm. Climatic Change, 106, 7-29.

Ghisalberti, M., Nepf, H.M. (2002). *Mixing layers and coherent structures in vegetated aquatic flows*. J. Geophysical Res. 107, C2.

Gishalberti, M., Nepf, H.M. (2005). *Mass transport in vegetated shear flows*. Environmental Fluid Mech., 5, 527 – 551.

Gishalberti, M., Nepf, H.M. (2006).*The structure of the shear layer in flows over rigid and flexible canopies*. Environmental Fluid Mech., 6, 277 – 301.

Granata, T.C., Serra, T., Colomer, J., Casamitjana, X., Duarte, C.M., Gacia, E. (2001). *Flow and particle distributions in a nearshore seagrass meadow before and after a storm*. Mar. Ecol. Prog. Ser., 218, 95 – 106.

Guanche, R., Losada, I.J., Lara, J.L. (2009) *Numerical modelling of coastal structures stability*. Coastal Engineering, 56(5-6), 543-558.

Hallegatte, S., Green, C., Nicholls, R.J., Corfee-Morlot, J. (2013). *Future flood losses in major coastal cities*. Nature Climate Change. Vol. 3, 802-806.

Harada, K., Imamura, F. (2002). E*xperimental study on the effect in reducing tsunami by the coastal permeable structures*. Paper presented at the Proceedings of the Twelfth (2002) International Offshore and Polar Engineering Conference, Kitakyushu, Japan

Harada, K., Imamura, F. (2003). *Evaluation of tsunami reduction by control forest and possibility of its use for mitigation*. Proc. of Coastal Engineering, Japan Society of Civil Engineers, 341-345. (In Japanese).

Hashim, A.M., Catherine, S.M.P., Takaijudin, H. (2013). *Effectiveness of mangrove forests in surface wave attenuation: a review.* Research journal of applied sciences, engineering and technology, 5, 4483-4488.

Hernandez-Soriano, M.C. (2012). *Evaluation of aluminum-saccharides complexes in solution by luminescence spectroscopy*. Communications in agricultural and applied biological sciences, 77 (1), 133-137.

Higuera, P., Lara, J.L., Losada, I.J. (2013a). Realistic wave generation and active wave absorption for Navier–Stokes models: application to OpenFOAM. Coastal Engineering, 71, 102–118.

Higuera, P., Lara, J.L., Losada, I.J. (2013b). *Simulating coastal engineering processes with OpenFOAM*. Coastal Engineering, 71, 119–134.

Higuera, P., Lara, J.L., Losada, I.J. (2014a). Three-dimensional interaction of waves and porous coastal structures using OpenFOAM. Part I: formulation and validation. Coastal Engineering, 83, 243–258.

Higuera, P., Lara, J.L., Losada, I.J. (2014b). Three–dimensional interaction of waves and porous coastal structures using OpenFOAM. Part II: Applications. Coastal Engineering, 83, 259–270.

Hiraoka, H., Ohashi, M. (2006). *A (k-ε) turbulence closure model for plant canopy flows.* Proc. of the 4th International Symposium on Computational Wind Eng. (CWE2006) in Yokohama.

Hiraishi, T., Harada, K. (2003). *Greenbelt tsunami prevention in south-pacific region*. Report of the Port and Airport Research Institute, 42: 1-23.

Hu, Z., Suzuki, T., Zitman, T., Uittewaal, W., Stive, M. (2014). *Laboratory study on wave dissipation by vegetation in combined current-wave flow.* Coastal Engineering, 88, 131-142.

Huang, Z., Yao, Y., Sim, S.Y., Yao, Y. (2011). *Interaction of solitary waves with emergent, rigid vegetation*. Ocean Engineering, 38, 1080-1088.

Ikeda, S., Yamada, T., Toda, Y. (2001). *Numerical study on turbulent flow and honami in and above flexible plant canopy*. Int. J. Heat Fluid Flow, 22, 252 – 258.

Infantes, E., Orfila, A., Simarro, G., Terrados, J., Luhar, M., Nepf, H. (2012). *Effect of a seagrass (Posidonia oceanica) meadow on wave propagation.* Marina Ecology Porgress series, 456, 63-72.

Irlandi, E.A., Peterson, C.H. (1991). Modification of animal habitat by large plants: mechanisms by which seagrasses influence clam growth. Oecologia, 87, 3, 307 – 318.

Irtem, E., Gedik, N., Kabdasli, M.S., Yasa, N.E. (2009). *Coastal forest effects on tsunami run-up heights.* Ocean Engineering, 36 313-320.

Ismail, H., Abd Wahab, A.K., Alias, N.E. (2012). Determination of mangrove forest performance in reducing tsunami run-up using physical models. Nat. Hazards, 63, 939-963.

Izaguirre, C., Méndez, F.J., Espejo, A., Losada, I.J., Reguero, B.G., (2013). *Extreme wave climate changes in Central-South America.* Climatic Change, 119, 277–290.

Jadhav, R., Chen, Q. (2012). *Field investigation of wave dissipation over salt marsh vegetation during tropical cyclone.* Proceedings of the 33rd International Conference on Coastal Engineering, Santander, Spain, 1-6 July 2012.

Jadhav, R.S., Chen, Q., Smith, J.M. (2013). *Spectral distribution of wave energy dissipation by salt marsh vegetation*. Coastal engineering, 77, 99-107.

Jayatissa, L.P., Dahdouh-Guebas, F., Koedam, N. (2002). *A review of the floral composition and distribution of mangroves in Sri Lanka*. Bot. J. Linn. Soc., 138: 29-43.

Jonsson, I.G., Arneborg, L. (1995). Energy properties and shoaling of higher-order stokes waves on a current. Ocean Eng., 22, 819-857.

Kandasamy, K., Narayanasamy, R. (2005). *Coastal mangrove forest mitigated tsunami.* Estuarine, Coastal and Shelf Science, 65, 601-606.

Knutson, P.L., Seeling, W.N., Inskeep, M.R. (1982). *Wave damping in Spartina alterniflora marshes.* Wetlands 2, 87–104.

Kobayashi, N., Raichle, A.W., Asano, T. (1993). *Wave attenuation by vegetation*. J. of Waterway, Port, Coastal and Ocean Eng., 119(1), 30-48.

Koch, D. L., Ladd, A. J. C. (1997). Moderate Reynolds number flows through periodic and random arrays of aligned cylinders. Journal of Fluid Mechanics, 349, 31-66.

Koch, E.W., Barbier, E.B., Silliman, B.R., Reed, D.J., Perillo, G.M.E., Hacker, S.D., Granek, E.F., Primavera, F.H., Muthiga, N., Polasky, S., Halpern, B.S., Kennedy, C.J., Kappel, C.V. and Wolanski, E. (2009). *Non-linearity in ecosystem services: temporal and spatial variability in coastal protection*. Frontiers in the Ecology and the Environment, 7(1), 29-37.

Koftis, T., Prinos, P., Stratigaki, V. (2013). *Wave damping over artificial Posidonia oceanica meadow: A large-scale experimental study*. Coastal Engineering, 73, 71-83.

Kronzucker, A. (2013). *Observing safety standards: A specialist for occupational safety must statutorily be included in all plants*. Fleischwirtschaft, 93 (2), 49-50.

Lara J.L., Losada I.J., Guanche, R. (2008). *Wave interaction with low-mound breakwaters using a RANS model*. Ocean Engineering, 35, 1388 – 1400.

Lara, J.L., Ruju, A., Losada, I.J. (2011). Reynolds averaged Navier–Stokes modelling of long waves induced by a transient wave group on a beach. Proceedings of the royal society A. 467, 1215-1242.

Leggett, D. J., Dixon. M. (1994). *Management of the Essex saltmarshes for flood defense*. Wetland Management. Thomas Telford, 232-245.

Leonard, L.A., Luther, M.E. (1995). *Flow hydrodynamics in tidal marsh canopies*. Limnology and Oceanography 40: 1474–1484.

Leonard, L., and Reed, D.J. (2002) *Hydrodynamics and sediment transport through tidal marsh canopies*. J. of Coastal Res. SI 36, 459–469.

Leonard, L. A., Ansley, P. A., Beavers, R.L. (2002). Flow dynamics and sedimentation in Spartina alterniflora and Phragmites australis marshes on the Chesapeake Bay. Wetlands 22, 415–424.

Lewis III, R.R. (2005) Ecological engineering for successful management and restoration of mangrove forests. Ecological Engineering, 24, 403-418.

Li, C.W., Yan K. (2007). *Numerical investigation of wave-current-vegetation interaction*. J. Hydraulic Engineering, 133, 794-803.

Liu, P.L.-F., Chang, C.-W., Mei, C.C., Lomonaco, P., Martin, F.L., Maza, M. (2015). *Periodic Water Waves through an Aquatic Forest*. Coastal engineering, 96, 100-117.

Longuet-Higgins, M. S., Stewart, R. W. (1960). *Changes in the form of short gravity waves on long waves and tidal currents.* Journal of Fluid Mechanics, 8, 565-583.

Longuet-Higgins, M. S., Stewart, R. W. (1961). *The changes in amplitude of short gravity waves on long waves and tidal currents*. Journal of Fluid Mechanics, 10, 529-549.

Losada, I.J., Lara, J.L., Guanche, R., Gonzalez-Ondina, J.M. (2008). *Numerical analysis of wave overtopping of rubble mound breakwaters.* Coastal Engineering, 55 (1), 47–62.

Lowe, R.J., Koseff, J.R., Monismith, S.G. (2005). *Oscillatory flow though submerged canopies: 1. Velocity structure*. J. Geophysical Res., 110, C10016.

Lowe, R.J., Falter, J.L., Koseff, J.R., Monismith, S.G., Atkinson, M.J. (2007). *Spectral wave flow attenuation within submerged canopies: Implications for wave energy dissipation*. J. Geophysical Res. C: Oceans, 112, C05018.

Luhar, M., Rominger, J., Nepf, H. (2008). *Interaction between flow, transport and vegetation spatial structure*. Environ. Fluid Mech., 8, 423-439.

Luhar, M., Coutu, S., Infantes, E., Fox, S., Nepf, H. (2010). *Wave-induced velocities inside a model seagrass bed*. J. Geophysical Res., 115, C12005.

Luhar, M., Nepf, H. (2011). Flow-induced reconfiguration of buoyant and flexible aquatic vegetation. Limnol. Oceanogr., 56, 2003-2017.

Ma, G., Kirby, J.T., Su, S.F., Figlus, J., Shi, F. (2013). *Numerical study of turbulence and wave damping induced by vegetation canopies.* Coastal Engineering, 80, 68–78.

Manca, E., Cáceres, I., Alsina, J., Stratigaki, V., Towenend, I., Amos, C.L. (2012). *Wave energy and wave-induced flow reduction by full-scale model Posidonia oceanica seagrass.* Cont. Shelf Res., 50-51, 110-116.

Massel, S.R., Furukawa, K., Brinkman, R.M. (1999). *Surface wave propagation in mangrove forests*. Fluid Dyn. Res., 24: 219-249.

Maza, M. (2012). Hydrodynamic study of Posidonia oceanica behaviour under oscillatory flow action. Master's thesis (in Spanish), Universidad de Cantabria.

Maza, M., Lara, J.L., Bouma, T.J., Ondiviela, B., Trinogga, J., Gordejuela, N., Losada, I.J. (2013). *Experimental analysis of three dimensional wave and current interaction with real salt marshes.* Internal report (Theseus project).

Mazda, Y., Magi, M., Kogo, M., Hong, P.M. (1997a). *Mangrove as a coastal protection from waves in the Tong King delta, Vietnam*. Mangroves Salt Marshes, 1: 127-135.

Mazda, Y., Wolanski, E., King, B., Sase, A., Ohtsuka, D., Magi, M. (1997b). *Drag force due to vegetation in mangrove swamps.* Mangroves and Salt Marshes, 1, 193–199.

Mazda, Y., Magi, M., Ikeda, Y., Kurokawa, T., Asano, T. (2006). *Wave reduction in mangrove forest dominated by Sonneratia sp.* Wetlands Ecol. Manag., 14, 365-378.

Mei C.C., Chan I.-C., Liu P.L.-F., Huang Z., Zhang W. (2011). *Long waves through emergent coastal vegetation.* J Fluid Mech 461, 461–491.

Mei, C.C., Chan, I.C., Liu, L.-F. P. (2013*). Waves of intermediate length through an array of vertical cylinders*. Environmental Fluid Mechanics, 14, 235-261.

Mendez, F.J., Losada, I.J., Losada, M.A. (1999). *Hydrodynamics induced by wind waves in a vegetation field.* J. of Geophysical Res., 104, 18383-18396.

Mendez, F.J., Losada, I.J. (2004). An empirical model to estimate the propagation of random breaking and non-breaking waves over vegetation fields. Coastal Engineering, 52, 103 – 118.

Menendez M., Woodworth, P.L. (2010). *Changes in extreme high water levels based on a quasi-global tide-gauge dataset*. Journal of Geophysical Research, 115, C10011.

Menter, F. R. (1992). Improved Two-Equation k-omega Turbulence Models for Aerodynamic Flows. NASA TM 103975.

Menter, F.R., (1994). Two-equation eddy viscosity turbulence models for engineering applications. AIAA Journal 32 (8), 1598–1605.

McGranahan, G., Balk, D., Anderson, B. (2007). The rising tide: assessing the risks of climate change and human settlements in low elevation coastal zones. Environ Urban, 19, 17–37.

McIvor, A., Möller, I., Spencer, T., Spalding, M. (2012a). *Reduction of wind and swell waves by mangroves. Natural Coastal Protection Series: Report 1*.The Nature Conservancy and Wetlands International.

McIvor, A., Spencer, T., Möller, I., Spalding, M. (2012b). *Storm surge reduction by mangroves. Natural Coastal Protection Series: Report 2*.The Nature Conservancy and Wetlands International.

Möller, I., Spencer, T., French, J.R. (1996). *Wind wave attenuation over saltmarsh surfaces: Preliminary results from Norfolk, England.* Journal of Coastal Research 12, 1009-1016.

Möller, I., Spencer, T., French, J.R., Leggett, D.J. (1999). *Wave transformation over salt marshes: A field and numerical modelling study from north Norfolk, England*. Estuarine Coastal and Shelf Science 49: 411-426

Möller, I. (2006). Quantifying saltmarsh vegetation and its effect on wave height dissipation: Results from a UK East coast saltmarsh. Estuarine Coastal and Shelf Science 69: 337-351

Möller, I., Kudella, M., Rupprecht, F., Spencer, T., Paul, M., van Wesenbeeck, B., Wolters, G., Jensen, K., Bouma, T.J., Miranda-Lange, M., Schimmels, S. (2014). *Wave attenuation over coastal salt marshes under storm surge conditions*. Nature Geoscience, 7.

Nagelkerken I. (2000). Importance of Mangroves, Seagrass Beds and the Shallow Coral Reef as a Nursery for Important Coral Reef Fishes, Using a Visual Census Technique. Estuarine, Coastal and Shelf Science, 51, 31-44.

Nehring, S., Adsersen, H. (2006*). NOBANIS – Invasive Alien Species Fact Sheet – Spartina anglica.* – From: Online Database of the European Network on Invasive Alien Species - NOBANIS www.nobanis.org.

Nepf, H. M. (1999). Drag, turbulence and diffusion in flow through emergent vegetation. Water Resources Reseach, 5(2), 479-489.

Nepf, H.M., Vivoni, E.R. (2000). *Flow structure in depth-limited, vegetated flow*. J. Geophysical Research, 105, C12, 28.547 – 28.557.

Nepf, H.M. (2012). *Flow and transport in regions with aquatic vegetation*. Annu. Rev. Fluid Mech., 44, 123-142.

Neumeier, U., Ciavola, P. (2004). Flow resistance and associated sedimentary processes in a Spartina maritima salt-marsh. Journal of Coastal Research 20: 435–447.

Ohira, W., Honda, K., Nagai, M., Ratanasuwan, A. (2013). Mangrove stilt root morphology modelling for estimating hydraulic drag in tsunami inundation simulation. Trees, 27, 141-148.

Ondiviela, B., Losada, Lara, J.L., I.J., Maza, M., Galvan, C., Bouma, T., van Belzen, J. (2014). *The role of seagrasses on coastal protection in a changing climate.* Coastal Engineering. 87, 158-168.

Osman, K. T. (2013). *Plant Nutrients and Soil Fertility Management*. Soils, pp. 129‑159.

Ota, T., Kobayashi, N., Kirby, J.T. (2004). *Wave and current interactions with vegetation*. Proc. of 29th Coastal Eng. Conf. in Singapore, 508–520.

Ozeren, Y., Wren, D.G., Wu, W. (2013). *Experimental investigation of wave attenuation through model and live vegetation*. J. Waterway, Port, Coastal, Ocean Eng., 04014019.

Paul, M., Bouma, T.J., Amos, C.L. (2012). Wave attenuation by submerged vegetation: combining the effect of organism traits and tidal current. Marine ecology progress series, 444, 31–41.

Penning, W.E., De Oude, R., Mynett, A. (2009). *The effects of macrophyte morphology and patch density on wave attenuation.* Proceedings of the 7th ISE and 8th HIC, 12-16 January 2009, Concepción, Chile.

Peregrine, D.H. (1976). *Interaction of water waves and currents.* Adv. Appl. Mech., 16, 9-117

Puijalon, S., Bornette, G., Sagnes, P. (2005). Adaptations to increasing hydraulic stress: morphology, hydrodynamics and fitness of two higher aquatic plant species. Journal of Experimental Botany, 56, 777–786.

Puijalon, S., Léna, J.P., Rivière, N., Champagne, J.Y., Rostan, J.C., Bornette, G. (2008). Blackwell Publishing Ltd Phenotypic plasticity in response to mechanical stress: hydrodynamic performance and fitness of four aquatic plant species. New Phytologist 177, 907–917.

Rodi, W., Constantinescu, G., Stoesser, T. (2013). *Large-eddy simulation in hydraulics*. IAHR book series.

Rosman, J.H., Koseff, J.R., Monismith, S.G., Grover, J. (2007). A field investigation into the effects of a kelp forest (Macrocystispyrifera) on coastal hydrodynamics and transport. J. of Geophysical Res., 112, C02016.

Ruju, A.,Lara,J.L., Losada, I.J. (2012). Radiation stress and low-frequency energy balance within the surf zone: A numerical approach. CoastalEngineering, 68, 44–55.

Rusche, H. (2002). *Computational fluid dynamics of dispersed two-phase flows at high phase fractions.* Ph.D. thesis, Department of Mechanical Engineering, Imperial College of Science, Technology & Medicine, London.

Sanit, A., Gordon, S.M., Sonjai, H., Somchai, P. (1992). *Plants in Mangroves*. Bangkok, pp: 120.

Sanz Elorza, M., Dana, M., Sobrino Vesperinas, E. (2004). *Atlas de las plantas alóctonas invasoras en España.* Dirección General para la Biodiversidad. Madrid, 342.

Shepard, C.C., Crain, C.M., Beck, M.W. (2011) The protective role of coastal marshes: a systematic review and meta-analysis. PLoS One 6, e27374.

Shi, Z., Pethick, J.S., Pye, K. (1995). Flow structure in and above the various heights of a saltmarsh canopy: a laboratory flume study. Journal of Coastal Research 11, 1204–1209.

Shuto, N. (1987). *The effectiveness and limit of tsunami control forest*. Coastal Engineering in Japan, 30, 143-153.

Snowball, K., Robson, A.D. (1991). *Nutrient Deficiencies and Toxicities in Wheat: A Guide for Field.* Identification, Mexico, D.F.: CIMMYT

Stratigaki, V., Manca, E., Prinos, P., Losada, I.J., Lara, J.L., Sclavo, M., Amos, C.L., Cáceres, I., Sánchez-Arcilla, A. (2011). *Large-scale experiments on wave propagation over Posidonia oceanica*. J. of Hydraulic Res., 49, 31-43.

Strusinska-Correia, A., Husrin, S., Oumeraci, H. (2013). *Tsunami damping by mangrove forest: a laboratory parameterized trees.* Nat. Hazards Earth Syst. Sci., 13, 483-503.

Sumer, B.M., Fredsoe, J. (2006*). Hydrodynamics around cylindrical structures*. Advanced series on ocean engineering, 26.

Suzuki, T., Zijlema, M., Burger, B., Meijer, M.C., Narayan, S. (2011). *Wave dissipation by vegetation with layer schematization in SWAN*. Coastal Engineering, 59, 64-71.

Tanaka, N., Sasaki, Y., Mowjood, M.I.M., Jinadasa, K.B.S.N., Homchuen, S. (2007). Coastal evegattion structures and their functions in tsunami protection: Experience of the re-cent Indian Ocean tsunami. Landscape Ecol. Eng., 3, 33-45.

Tanino, Y., Nepf, H. (2008). Laboratory investigation on mean drag in a random array of rigid, emergent cylinders. Journal of Hydraulic Engineering, 134, 34–41.

Tanino, Y., Nepf, H. (2009). Laboratory investigation of lateral dispersion within dense arrays of randomly distributed cylinders ar transitional Reynolds number. Physics of fluids, 21, 046603-1-046603-10.

Teh, S.Y., Koh, H.L., Liu, P.L.F., Ismail, A.I.M., Lee, H.L. (2009). *Analytical and numerical simulation of tsunami mitigation by mangroves in Penang, Malaysia*. Journal of Asian Earth Sciences, 36, 38-46.

Temmerman, S., Govers, G., Wartel, S., Meire, P. (2003). Spatial and temporal factors controlling short-term sedimentation in a salt and freshwater tidal marsh, Scheldt estuary, Belgium, SW Netherlands. Earth Surface Processes and Landforms, 28, 739-755.

Temmerman, S., Meire, P., Bouma, T.J., Herman, P.M.J., Ysebaert, T., De Vriend, H.J. (2013). *Ecosystem-based coastal defence in the face of global change*. Nature 493, 45–49.

Terrados, J., Duarte, C.M. (2000). Experimental evidence of reduced particle resuspension with invaseagrass (Posidonia oceanica L.) meadow. Journal of Experimental Marine Biology and Ecology 243, 45-53.

Torres-Freyermuth, A., Losada, I., Lara, J. (2007). Modelling of surf zone processes on a natural beach using reynolds-averaged navier-stokes equations. J. Geophysical Res., 112, L05601.

Torres-Freyermuth, A., Lara, J.L., Losada, I.J. (2009). *Numerical modelling of short- and long-wave transformation on a barred beach.* Coastal Engineering, 57 (3), 317–330.

Tschirky, P., Hall, K., Turcke, D. (2000). *Wave attenuation by emergent wetland vegetation*. Proc. 27th Intern. Coast. Eng. Conf., ASCE, 865-877.

Tusinski, A. (2012). The role of mangroves in the design of coastal dikes – hydrodynamics and cost related aspects. Master's Thesis, Delf University of Technology.

Valentine, J. R., Heck, K.L. (1999). *Seagrass herbivory: evidence for the continual grazing of marine grasses.* Mar. Ecol. Prog. Ser. 176, 291-302.

Vo-Luong, H.P., Massel, S.R. (2008). Energy dissipation in non-uniform mangrove forests of arbitrary depth. J. Mar. Syst., 74, 603-622.

Walters, B.B. (2000). Local mangrove planting in the Philippines: are fisherfolk and fishpond owners effective restorationists?. Restoration Ecology, 8 (3), 237-246.

Wayne, C.J. (1976). *The effects of sea and marsh grass on wave energy.* Coastal Research Notes 4: 6–8.

Weller, H.G., Tabor, G., Jasak, H., Fureby, C. (1998). A tensorial approach to computational continuum mechanics using object oriented techniques. Comput. Phys., 12 (6), 620–631.

Wilcox, D. C. (2006). *Turbulence Modelling for CFD*. 3rd edition, DCW Industries, Inc., La Canada CA.

Wong, P.P., Losada, I.J.,Gattuso, J.P., Hinkel, J., Khattabi, A., McInnes, K.L., Saito, Y., Sallenger, A. (2014). *Coastal systems and low-lying areas*. In: Climate Change 2014: Impacts, Adaptation, and Vulnerability. Fifth Assessment Report of the Intergovernmental Panel on Climate Change [Field, C.B. et al. (eds.)]. Cambridge University Press, Cambridge, United Kingdom and New York, NY, USA, (in press).

Yang, S.L., Li, H., Ysebaert, T., Bouma, T.J., Zhang, W. X., Wang, Y. Y., Li, P., Li, M., Ding, P.X. (2008) Spatial and temporal variations in sediment grain size in tidal wetlands, Yangtze delta: On the role of physical and biotic controls. Estuarine, Coastal and Shelf Science. 10.1016

Yang, S. L., Shi, B. W. , Ysebaert, T., Luo, X. X. (2012). *Wave attenuation at a salt marsh margin: A case study of an exposed coast on the Yangtze Estuary*. Estuaries and Coasts. 35, 169-182.

Yeh, H.H. (1991) *Tsunami bore run-up. In: Natural Hazards (vol 4).* Kluwer Academic Publisher, Dordrecht, The Netherlands.

Yoon, H.D., Cox, D., Albert, D., Mori, N., Smith, H., Zarnetske, J. (2011*). Ecological modelling of emergent vegetation for sustaining wetlands in high wave energy coastal environments*. Proceedings of the 28th International Conference on Coastal Structures, Yokohama, Japan, 5-9 September 2011.

Ysebaert, T., Yang, S.L., Zhang, L., He, Q., Bouma, T.J., Herman, P.M.J. (2011). *Wave Attenuation by Two Contrasting Ecosystem Engineering Salt Marsh*. Macrophytes in the Intertidal Pioneer Zone Wetlands, 31, 1043–1054.

Zhang, J.-S., Zhang, Y., Jeng, D.-S., Liu, P.L.-F., Zhang, C. (2014). *Numerical simulation of wave–current interaction using a RANS solver*. Ocean Eng., 75, 157-164.

Zong, L., Nepf, H. (2010). Flow and deposition in and around a finite patch of vegetation. Geomorphology, 116, 363-372.

Zou, Z.L., Hu, P.C., Fang, K.Z., Liu, Z.B. (2013). *Boussinesq-type equations for wave-current interaction*. Wave motion, 50, 655-675.